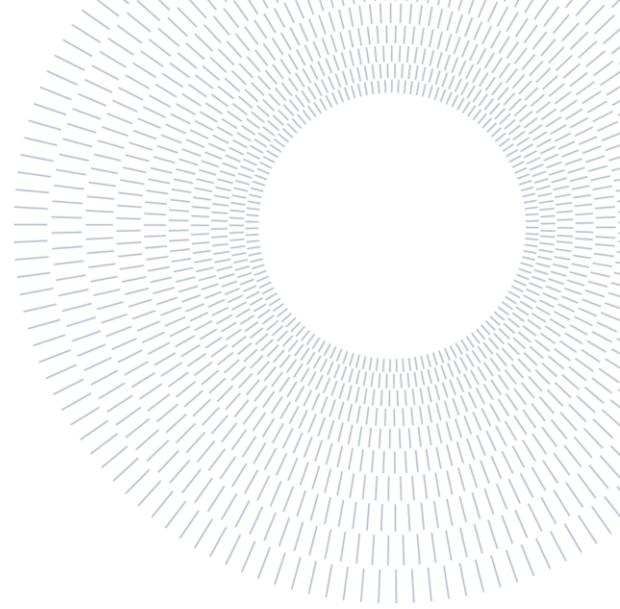




**POLITECNICO
MILANO 1863**

**SCUOLA DI INGEGNERIA INDUSTRIALE
E DELL'INFORMAZIONE**



EXECUTIVE SUMMARY OF THE THESIS

Nanophotonic waveguide enhanced Raman Spectroscopy for sensitive molecular fingerprinting.

TESI MAGISTRALE IN MATERIALS ENGINEERING AND NANOTECHNOLOGY- INGEGNERIA DEI MATERIALI E NANOTECNOLOGIE

AUTHOR: Giulio Benedini

ADVISOR: Carlo Casari

ACADEMIC YEAR: 2020-2021

1. Introduction

In the framework of photonics and enhanced Raman signal, waveguide enhanced Raman spectroscopy (WERS) has become a new trend in recent years (1). In WERS the enhancement is given by a nanophotonic WG fabricated on chip which has the scope of deliver pump and signal light between detectors and sample. The interaction with the sample is given by the evanescent field. It gives enhancement through increased probing length and waveguide (WG) enhancement (2). But the main advantage of WERS, over other technology, it is CMOS compatible, this result in possibility of low cost and reliable production.

The primary scope of this work is the understanding of the WERS limitation of the current design and individuate possible solutions for further improvements. Therefore, the work has been subdivided in smaller subobjectives.

The first one is to develop an adequate set up and coupling procedure for reliable and reproducible testing of WERS chips with implementation of automated scripts for data analysis of Raman spectra and scattering losses. Secondly, it has the objective to improve the existing theoretical and simulation models for enhanced understanding of

experimental results, and thereby informing the evolution of the next generation of devices. Thirdly, to critically review and experimentally evaluate two main challenges for WERS. The first one is regarding the background signal coming from silicon nitride strip waveguides. Therefore, a deep analysis of the Raman spectra has been studied. The study considers the most recent advancement of the theoretical background of these Raman spectra. Finally, this work has the objective to understand experimentally the optimal strip WG design of the current device and critically expose the current limitations for further improvements.

2. Chip design and set-up

The design of the chip was already made. It consisted by a SiO_2 cladded region with amorphous silicon nitride (a-SiN) strip WGs, with length L' (called not-probing length). It was designed to have even coupling objective-WG conditions at fixed cross section and then the width changes smoothly towards the probing region. This region is where the sensing occurs. It is consisted by 20 different spirals strip WGs at different probing length (L) and width (w). The height of the WGs was fixed at $0.3 \mu m$. Further

information can be found looking at Figure 1 and Table 1.

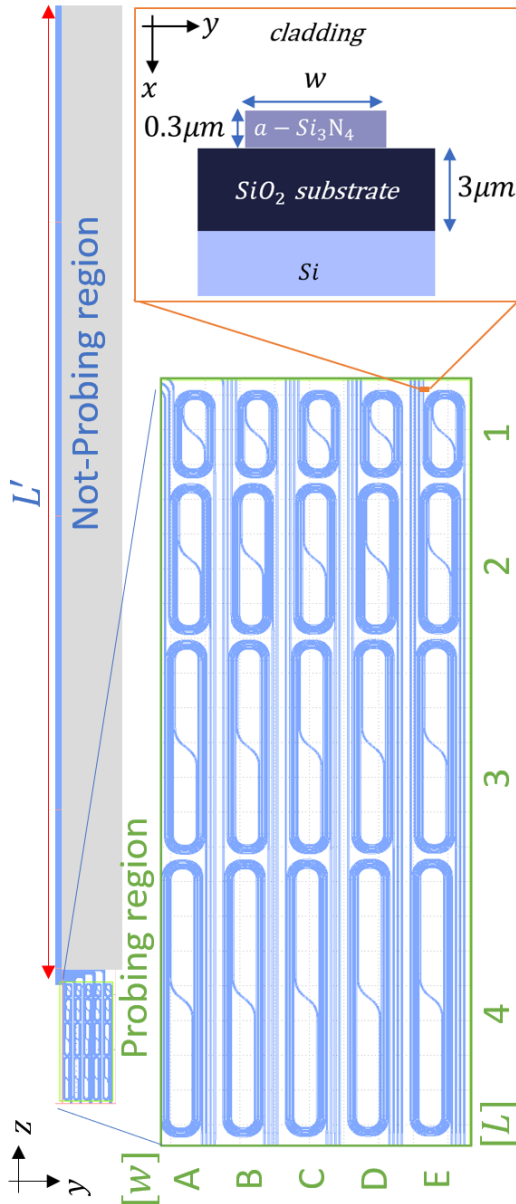


Figure 1: scheme of the chip design.

Table 1: Summary of the labels for different WGs geometries. Numbers correspond to different probing length L , and the letters to different WG width w .

w (μm)	letter	L (cm)	number
1,2	A	1.0	4
1	B	0.8	3
0,8	C	0.6	2
0,6	D	0.4	1
0,4	E		

The set-up consisted of a confocal Raman microscope to couple the light in the WGs and then collect back the scattered one (Figure 2). To improve the coupling procedure a camera observing the zy surface was added. The system to hold the chip under the objective it has been designed and produced. The main problem associated to Raman signal collections was the drift of the chip resulting in the de-coupling of the light in the chip. This was associated to mechanical instability and therefore after each chip is installed under the microscope a 12-hour rest time was usually applied (no studies regarding the exact amount of time were done).

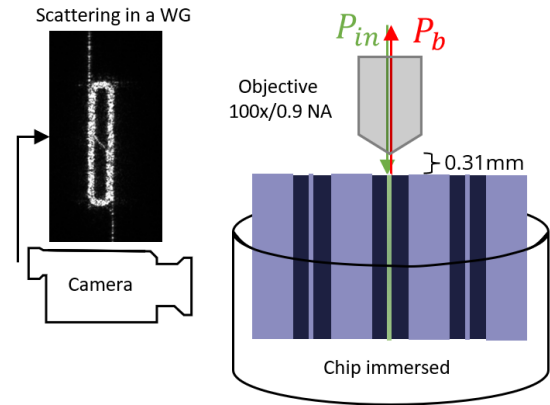


Figure 2: scheme of the design concept of the set-up (not in scale).

3. Background study

The first challenge of WERS devices is given by the background arising from the WG without the analyte. Since its major impact on the device performances a critical review of the peak assignments has been performed based on the studies (3, 4).

The waveguide Raman spectrum (S_{WG}) can be considered as the sum of different components:

$$S_{WG}(\tilde{\nu}) = P_{LFDC} + R_{core} + R_{sub} + F \quad 3.1$$

In which P_{LFDC} is the low frequency dominant component, R_{core} and R_{sub} are respectively the Raman signals coming from the core and the substrate and F is the residual noise.

It has been developed an almost fully automated fitting procedure for separation of the different components and full extraction of all the relevant parameters for the description of these spectra. The procedure is shown in Figure 3.

In accordance with (4), the P_{LFDC} is well fitted by an exponential decreasing function ($P_{LFDC} \sim e^{-\tau \cdot \omega}$, with

τ the characteristic time). This trend has been experimentally measured for similar strip WGs at different length and width ($\tau_{785nm} \in [12; 15]fs$). This behavior is recoded also by changing the pump power or the laser wavelength ($\tau_{633nm} = 11fs$). By the comparison between PMMA thin film Raman spectrum collected with laser beam perpendicular to the surface (i.e. not-guided light) or in parallel (i.e. guided light) it seems that P_{LFDC} appears if the light collected is guided. More quantitative studies on P_{LFDC} should be performed to understand if τ can be controlled.

An analysis of the $S_{WG}(\tilde{\nu}) - P_{LFDC}$ Raman signal has been performed. It has shown a good fit of the spectrum, and assignments of the different peaks has been performed. Peaks of interest are those associated to hydrogen impurities: Si-H stretching vibration at 2236 cm^{-1} , N-H₂ bending at 1549 cm^{-1} (3). These H-impurities increase the absorption of these WGs in the NIR range (5). Finally, comparing in the literature the spectral region $600\text{-}1300\text{ cm}^{-1}$ it cannot be excluded that some of the peaks are assigned to a-SiO₂, 740 and 1170 cm^{-1} (6), and they can have a non-negligible impact on the background. This is not completely in line on what shown by (3), where the model of the background was based on the hypothesis of neglecting the Raman signal of a-SiO₂.

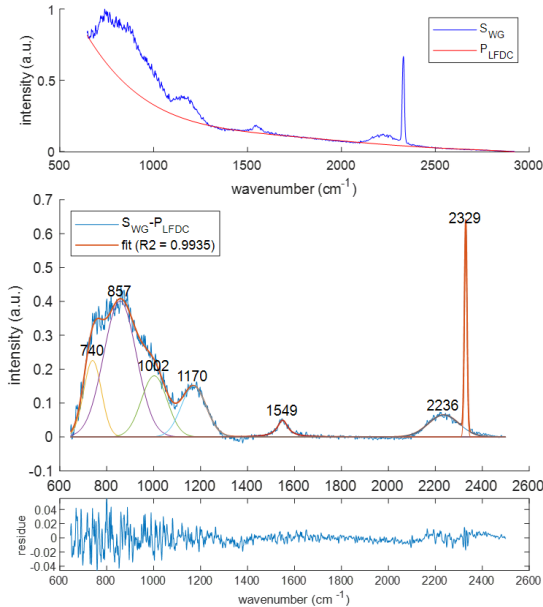


Figure 3: top figure: the normalized spectrum between $[0,1]$, S_{WG} , and the low frequency dominant component (P_{LFDC}). Center figure: the fit of the $S_{WG} - P_{LFDC}$ (blue line). The spectrum refers to the WG type 1E. The colored lines are the 7 peaks used in the fitting (Gaussian line shape). Bottom figure: the residue is reported.

4. Modeling

To critically understand the experimental results a model of the signal collected has been developed. As already said the WERS enhancement is composed by:

- increased probing length
- waveguide enhancement

The first mechanism is controlled by the losses present in the WGs. The n_w model (7) has been chosen to describe the trends of losses as function of different parameters (e.g. WG strip width and laser wavelength). It gives a relatively simple relation for scattering losses:

$$\alpha_R = A \frac{\partial n_{eff}}{\partial w} \quad 4.1$$

Where w is the WG width and n_{eff} is the effective refractive index. The factor A is WG width independent if sufficiently far from the mode cut-off (7).

The second enhancing mechanism is the WG enhancement. It is described by the so-called conversion efficiency η (sr.) (8). It considers how much the evanescent modes interact with the sample. It is given by (8):

$$\eta_i = \iint_{S_i} \frac{\lambda_s^2 \cdot n_g(\omega_p) n_g(\omega_s)}{\tilde{A}_{eff;p}(\vec{r}_0) \tilde{A}_{eff;s}(\vec{r}_0) n(\omega_s)} d\vec{r}_0 \quad 4.2$$

$$\tilde{A}_{eff;p} \equiv \frac{\int \int_{\infty} \epsilon_r(\vec{r}, \omega_p) |\vec{E}_m(\vec{r}, \omega_p)|^2 d\vec{r}}{|\vec{E}_m(\vec{r}_0, \omega_p)|^2} \quad 4.3$$

Where λ_s is the scattered wavelength, n_g is the group index of the WG, ω_p and ω_s are the angular frequency of pump and scattered light, $n(\omega_s)$ is the refractive index of the medium where the scattering particles are located and $\tilde{A}_{eff;p}(\vec{r}_0)$ is the effective mode area at the molecule position (\vec{r}_0) at the pump frequency, ϵ_r the relative dielectric constant, \vec{E}_m is the electric modal field and S_i is the integration surface over which the sample is present.

Signal to background ratio (SBR)

To compare experimental results with simulation results the SBR has been chosen. The advantage of using the SBR is that it should eliminate the uncertainty related to the coupling efficiency factor and because it is a more meaningful value, instead of comparing the actual signal intensity alone. To think in terms of SBR is better to approach the

problem, since to have improvements, the background can decrease.

The demonstration of the formula will be not reported. The final formula is quite complex since considers all the components shown in the chip design, and schematically reported in Figure 4:

$$SBR = \frac{\beta_{sample}}{\beta_{background}} \eta_{S/B} F_{np}(L, L') \quad 4.4$$

Where $\beta = \rho\sigma$, with ρ the density and σ the scattering cross section. The $\eta_{S/B} \equiv \frac{\eta_p(S_{clad})}{\eta_p(S_{core})}$ is the core-to-cladding conversion ratio (CCR), it is an important figure of merit which evaluates the sensitivity of the WG. It considers the ratio between the conversion ratio at the cladding area in the probing region $\eta_p(S_{clad})$ and the $\eta_p(S_{core})$ of the core area in the probing region.

The presence of a not-probing region (i.e. $L' \neq 0$), it results in an additional term of the SBR expression which has been called the not-probing factor:

$$F_{np} = \frac{1}{\frac{1}{\chi} \eta_{nP/P} \frac{\alpha_p}{\alpha_{np}} \frac{1 - e^{-2\alpha_{np}L'}}{1 - e^{-2\alpha_p L}} + 1} \quad 4.5$$

It considers the losses to deliver the power to the probing region, described by: $\chi \in [0,1]$. This factor is influenced by the bending losses, the discontinuity between the probing and not-probing region and the scattering losses of the not-probing region α_{np} and the not-probing length L' . From simulations the factor $\eta_{nP/P} \approx 1$ (i.e. $\eta(S_{core})$ is slightly influenced by cladding), therefore from now on will be neglected. Finally, F_{np} is influenced by the loss in the probing region α_p and length L .

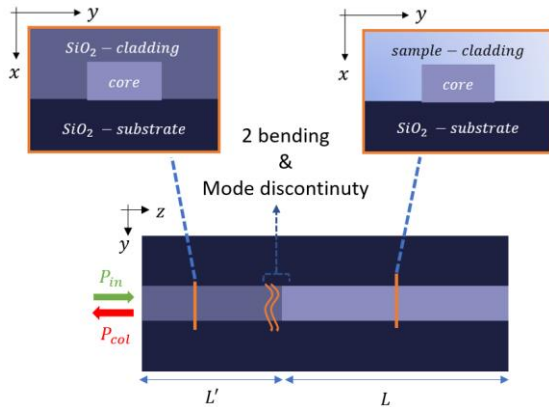


Figure 4: scheme of the chip design. L and L' are the probing and the not-probing length. P_{in} and P_{col} are the incoming and collected power respectively. On the left and right insets two cross section of the WG are represented to underline the difference of the two regions. In between these two regions it is underlined the presence of 2 bendings and mode discontinuity.

5. Raman measurements

It has been studied different chips with both isopropyl alcohol (IPA) and thin film spin coated poly(methyl methacrylate), PMMA. The SBR calculation procedure is reported in Figure 5.

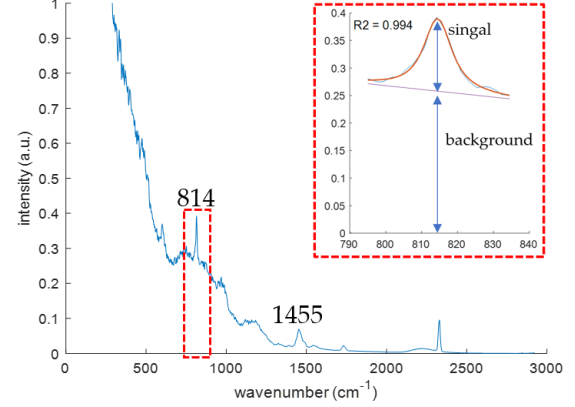


Figure 5: the Raman spectra obtained from 3C WG coated with PMMA (with 785nm laser, 100x/0.9NA objective, 55 mW and 0.005s accumulation time). The inset show the fitting procedure for the peak at 814 cm^{-1} .

Not-probing length influence on SBR

As it can be noticed in Figure 1, there is a long not-probing region, in which only background signal is collected. In our model if we simplify the all the losses terms (i.e. $\chi \approx 1$; $\alpha_{np} \approx 0$; $\alpha_p \approx 0$) it results:

$$SBR \propto F_{np} \approx \frac{L}{L' + L} \quad 5.1$$

It is simple to understand that we should decrease as much as possible L' . After cleavage of the chip, reducing L' from 1.7 cm to 0.3cm, it enabled to detect signal from IPA sample.

WG width influence on SBR

From this paragraph it will be presented experimental results with PMMA (spin coated film with thickness about 1 μm). The first parameter studied is the WG width. It should be expected that an optimal WG width result in the highest SBR, since as the width increases the losses should decrease (i.e. $SBR \uparrow$) but on the other hand the sensitivity should decrease (i.e. $SBR \downarrow$).

Simulations of both scattering losses and CCR has been performed with Lumerical mode solver. The estimation of the magnitude of the scattering losses in the n_w model relies on the evaluation of the side wall roughness, which is not simple to evaluate

experimentally. Therefore, losses have been measured with a simple method (9), exploiting the scattered losses observed by a camera. This method can be easily implemented during Raman measurements but suffer of low sensitivity. A simulation has been performed over the 814cm^{-1} peak, with 785nm laser wavelength, under the approximation of negligible bending losses and core-to-cladding losses (i.e. $\chi \approx e^{-2\alpha_{np}L'}$).

The comparison between the simulation results and experiments is shown in Figure 6. Even if the magnitude of the SBR is not well predicted there is a good agreement in the trend.

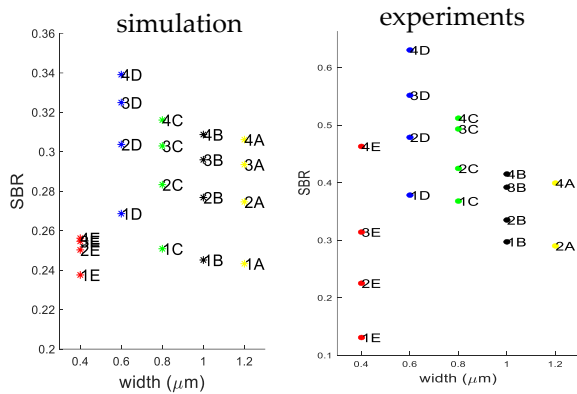


Figure 6: SBR as function of the WG width (each color defines the WG width), for different length WGs. On the left the simulations results and, on the right, the experimental one for PMMA cladding 814cm^{-1} peak.

Scattered and Laser wavelength influence on SBR

Further studies have been performed. In Figure 7 are shown the experimental results obtained from SBR for different peaks: 814cm^{-1} and 1455cm^{-1} .

The left plot shows that for peak at 814cm^{-1} (scattered wavelength around 839nm), the optimal WG width is $0.6\mu\text{m}$ (D WGs). But the right plot shows that for 1455cm^{-1} Raman shift (scattered wavelength of 886nm) the best WGs for Raman collection are the C WGs series (WG width = $0.8\mu\text{m}$). Therefore, there is a change in the optimal WG width as varying the scattered wavelength. This is a relevant result since it shows how each WG should be optimized for the specific wavelength region of Raman signal collection enhancement.

It is interesting to understand which could be to origin of the shift of the “peak” from WG width in Figure 7. The first two factors to check are the CCR and the WG losses. With the n_w it is possible to

estimate how the scattering losses changes as function of the wavelength. In accordance with (10), as we increase the wavelength the losses should decrease. There is not a significative variation between WGs with different width. Similar considerations can be done for the CCR.

Therefore, to justify this behavior it should be considered the losses associated to bending and core-to-cladding transition.

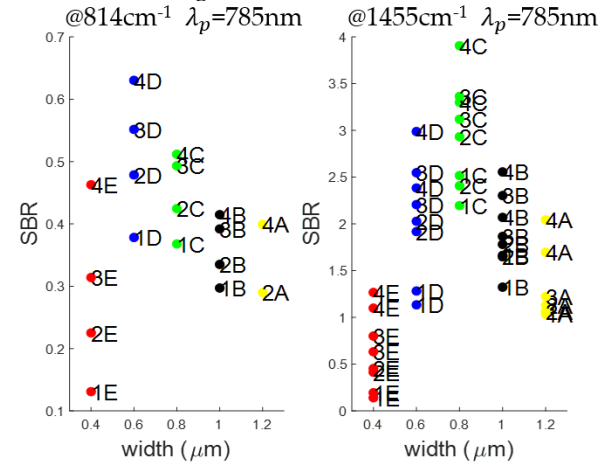


Figure 7: SBR trend with respect to the WG width with PMMA sample. On left the SBR of peak at 814cm^{-1} . On right the SBR of peak at 1455cm^{-1} .

6. Conclusions

In conclusion in this work the development of set-up, coupling procedure, data analysis software has been developed to collect Raman spectra and scattering losses pictures as experimental data. The programs developed offers the possibility to quickly study large number of spectra and collects the most meaningful data over the full range $0\text{-}3000\text{cm}^{-1}$.

In depth study of the background limiting signal have been performed showing the presence of signal coming from: exponential decreasing background, a-SiN WGs and a-SiO₂ substrate and cladding.

The influence of different parameters has been studied, the main of interest are the strip WG width, the pump wavelength and scattered wavelength. The critical review of different components of the current design have been done with conjunction with Lumerical simulation software. It has showed how the model developed can provides useful insights on the SBR trend and a good agreement has been reported in Figure 6.

The current design of the chip offered the possibility to highlight many improvements

strategy. The first one is to reduce the not-probing length by splitting the excitation and collection WG by introducing multi modal interferometer (MMI) (11) or using a 2x2 directional couplers (12). Secondly a better design of the bending and not-probing to probing transition is needed. Finally, it should be reported that up to now there is still not leading design strategy for WERS design (1) and a wide range of possible strategies are still unexplored.

Bibliography

1. Ettabib MA, Marti A, Liu Z, Bowden BM, Zervas MN, Bartlett PN, et al. Waveguide Enhanced Raman Spectroscopy for Biosensing: A Review. *ACS sensors*. 2021.
2. Michon J, Kita D, Hu J. Sensitivity comparison of free-space and waveguide Raman for bulk sensing. *JOSA B*. 2020;37(7):2012-20.
3. Dhakal A, Wuytens P, Raza A, Le Thomas N, Baets R. Silicon Nitride Background in Nanophotonic Waveguide Enhanced Raman Spectroscopy. *Materials*. 2017;10(2).
4. Thomas NL, Dhakal A, Raza A, Peyskens F, Baets R. Impact of fundamental thermodynamic fluctuations on light propagating in photonic waveguides made of amorphous materials. *Optica*. 2018 Apr;5(4):328-36.
5. Shaw MJ, Guo J, Vawter GA, Habermehl S, Sullivan CT. Fabrication techniques for low-loss silicon nitride waveguides. *Micromachining Technology for Micro-Optics and Nano-Optics III*; International Society for Optics and Photonics; 2005.
6. Yadav AK, Singh P. A review of the structures of oxide glasses by Raman spectroscopy. *RSC advances*. 2015;5(83):67583-609.
7. Melati D, Morichetti F, Melloni A. A unified approach for radiative losses and backscattering in optical waveguides. *Journal of Optics*. 2014;16(5):055502.
8. Dhakal A, Subramanian AZ, Wuytens P, Peyskens F, Le Thomas N, Baets R. Evanescent excitation and collection of spontaneous Raman spectra using silicon nitride nanophotonic waveguides. *Opt Lett*. 2014;39(13):4025-8.
9. Okamura Y, Yoshinaka S, Yamamoto S. Measuring mode propagation losses of integrated optical waveguides: a simple method. *Appl Opt*. 1983 Dec;22(23):3892-4.
10. Tyndall NF, Stievater TH, Kozak DA, Pruessner MW, Rabinovich WS, Fahrenkopf NM, et al. A low-loss SiN photonic integrated circuit foundry platform for waveguide-enhanced Raman spectroscopy. *Smart Photonic and Optoelectronic Integrated Circuits XXIII*; International Society for Optics and Photonics; 2021.
11. Reynkens K, Clemmen S, Raza A, Zhao H, Peñaranda JS, Detavernier C, et al. Mitigation of photon background in nanoplasmonic all-on-chip Raman sensors. *Opt.Express*. 2020 Oct;28(22):33564-72.
12. Kita DM, Michon J, Hu J. A packaged, fiber-coupled waveguide-enhanced Raman spectroscopic sensor. *Optics express*. 2020;28(10):14963-72.

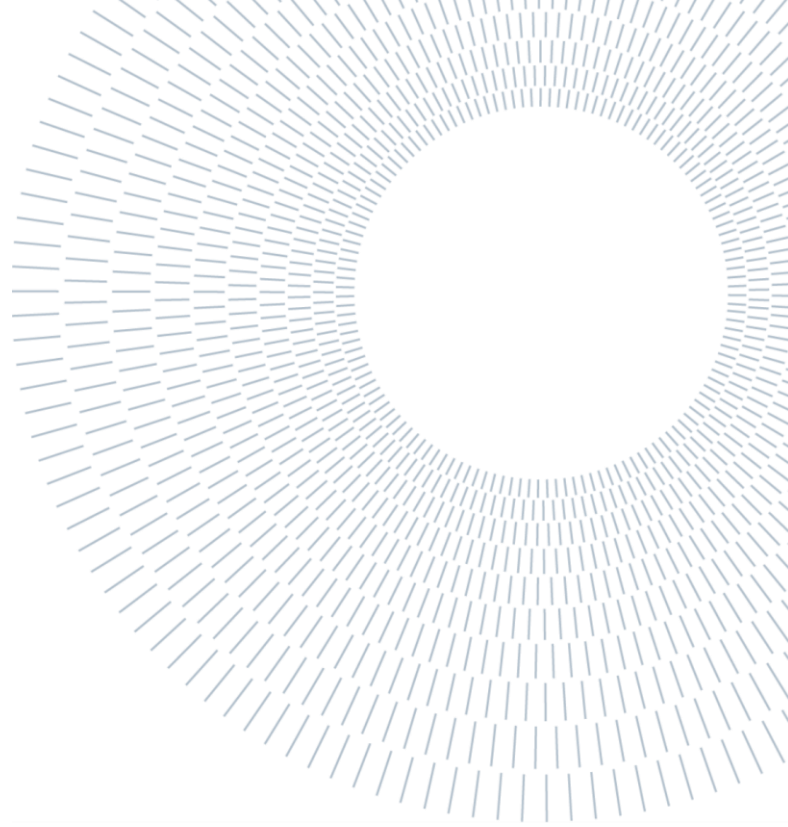
7. Acknowledgements

I thank Carlo Casari for his professionalism and patient support. Thanks to Aadhar Jain for the guidance given during my thesis work. Finally, I thank Pol Van Dorpe that gave me the possibility to work in imec.



POLITECNICO
MILANO 1863

SCUOLA DI INGEGNERIA INDUSTRIALE
E DELL'INFORMAZIONE



Nanophotonic waveguides enhanced Raman Spectroscopy for sensitive molecular fingerprinting

TESI DI LAUREA MAGISTRALE IN
MATERIALS ENGINEERING AND NANOTECHNOLOGY -
INGEGNERIA DEI MATERIALI E DELLE NANOTECNOLOGIE

Author: **Giulio Benedini**

Student ID: 10536718
Advisor: Carlo Casari
Co-advisor: Aadhar Jain and Pol Van Dorpe
Academic Year: 2020-2021

Abstract

Raman spectroscopy has a huge potential in material and bio-chemical science. Waveguide enhanced Raman spectroscopy (WERS) is a promising technique that can further solve the current limitations of Raman spectroscopy. It combines Raman spectroscopy and it replace the expensive objectives with a chip of a 1 mm² size produced with CMOS technology. At the same time, it can increase the signal collected, as compared with free-beam space collection. Up to now, WERS performances are limited by the background signal and losses. In this work, the background Raman signal, strip waveguide (WG) width and other relevant parameters that affects WERS performances are studied. The WERS performances has been evaluated in terms of signal to background ratio (SBR).

The first challenge was the creation of a set-up and coupling procedure for reliable testing of the chip combined with the creation of almost automated data elaboration script. Within this environment it has been performed accurate studies of the background signal. Modelling the background can open the possibility of artificial background removal for bulk sensing that can further decrease the detection limit.

The second part of the study has been mainly developed on the evaluation of the influence of strip WG width on the WERS performance. It has been developed a model to predict the trend of SBR as varying the strip WG width. Similar trend between model and experiments has been found showing that for the current design the best WG width is 0.6 μm in TM mode. In the end a review of all the possible solutions for improving the current design has been proposed for next generation devices.

Key-words: Waveguide enhanced Raman spectroscopy, Silicon nitride photonics, dielectric channel waveguides, biosensing, Raman sensor.

Abstract in italiano

La spettroscopia Raman ha un enorme potenziale nella scienza dei materiali e biochimica. La spettroscopia Raman potenziata da guida di luce (WERS) è una tecnica promettente che può risolvere le attuali limitazioni della spettroscopia Raman. WERS sostituisce i costosi microscopi con chip da 1 mm² prodotti con tecnologia CMOS. Inoltre, può aumentare l'intensità del segnale. Al momento WERS è limitato dalla presenza del segnale di fondo proveniente dal nucleo e dalle perdite di potenza. In questo lavoro vengono studiati il segnale Raman di fondo, la larghezza della guida d'onda di luce (WG) per una striscia in nitruro di silicio e altri parametri rilevanti che influenzano le prestazioni WERS. Queste ultime sono state valutate in termini di rapporto segnale/fondo (SBR).

La prima sfida è stata la creazione di un adeguato set-up sperimentale ed una procedura di accoppiamento della luce laser nel chip. Inoltre, è stato creato un programma che permetta la veloce elaborazione dei dati attraverso una elaborazione quasi automatica. Con lo sviluppo di questi strumenti sono stati eseguiti studi accurati del segnale di fondo. La modellazione di questo può aprire la possibilità di rimozione artificiale del segnale di fondo che può ridurre ulteriormente il limite di rilevamento.

La seconda parte dello studio è stata principalmente incentrata sulla valutazione dell'influenza della larghezza della striscia WG sulle prestazioni del WERS. È stato sviluppato un modello per prevedere l'andamento del SBR al variare della larghezza della WG. Si è trovato un andamento simile tra modello e dati sperimentali che dimostrano che per l'attuale chip la migliore larghezza per la striscia di WG è 0,6 μm (per il modo TM₀₀). Infine, possibili strategie per migliorare il design attuale sono state proposte a fronte di successivi dati sperimentali che ne esaltavano le sue limitazioni.

Parole chiave: spettroscopia Raman potenziata a guida d'onda di luce, fotonica al nitruro di silicio, guide d'onda a canale dielettrico, biosensori, sensore Raman.

Contents

Abstract	3
Abstract in italiano.....	4
1 Introduction to Waveguide enhanced Raman spectroscopy.....	9
1.1 Research framework overview	9
1.1.1 Photonics: a “key enabling technology”	9
1.1.2 Raman spectroscopy: its major challenge.....	10
1.1.3 Waveguide enhanced Raman spectroscopy	12
1.2 State of the art	14
1.2.1 Historical introduction and main applications.....	14
1.2.2 WERS challenges.....	15
1.3 Thesis outline	21
2 Theoretical background	22
2.1 Spontaneous Raman scattering	22
2.1.1 Classical theory for diatomic molecule.....	22
2.1.2 Quantum theory of Raman scattering.....	25
2.1.3 Raman scattering intensity and scattering cross section.....	28
2.1.4 Raman selection rules and shape of the Raman peaks	29
2.2 Some basis of waves in the waveguide: optical confinement.....	32
2.2.1 WG modes.....	32
2.2.2 WG losses	34
2.3 Signal collection by a WG	37
2.3.1 One molecule scattering.....	37
2.3.2 Ensemble of particles.....	38
2.4 Intensity collected by the CCD camera	41
3 Materials and methods	42
3.1 Confocal Raman microscope	42
3.1.1 Working principle confocal Raman microscope	46
3.2 Thor Camera.....	47
3.3 Epilog Laser cutter	47
3.4 Chip design.....	48
3.4.1 xy plane	48

3.4.2	zy plane	49
4	Optical set up and SiN WG Raman spectra	51
4.1	Chip cleavage procedure.....	51
4.2	Optical set-up.....	53
4.3	Procedure for spectrum acquisition	56
4.3.1	Influence on the laser spot position	56
4.3.2	Data acquisition and Drift.....	58
4.4	No analyte Raman measurements.....	61
4.4.1	One single WG study with 785nm laser wavelength	61
4.4.2	Multiple WGs Raman spectra	64
4.4.3	Influence of power intensity on the spectra	65
4.4.4	One single WG study with 633nm laser wavelength	66
5	Parameters that influence the signal collection	68
5.1	Strip waveguides realistic design model.....	68
5.1.1	Recall of the main theoretical results	73
5.2	Conversion efficiency calculation	75
5.2.1	Simulation results for IPA	77
5.2.2	Simulation results for PMMA.....	79
5.3	Scattering losses	80
5.3.1	Theoretical prediction of scattering losses	80
5.3.2	Measurements of scattering losses	82
5.3.3	Comparison n_w model to scattering losses trends	84
5.4	Influence of the probing length and cladded length on the SBR.....	86
5.4.1	Theoretical prediction	86
5.4.2	Raman spectra from IPA sample.....	87
5.5	WG width influence on the SBR.....	89
5.5.1	Simulation	89
5.5.2	Experimental results	91
5.6	Influence of the scattering wavelength.....	94
5.6.1	Experimental results	94
5.6.2	Simulation	95
5.6.3	Additional losses.....	97
5.7	Influence of the laser wavelength	98

6	Conclusion and Prospective	101
6.1	Set-up designs.....	101
6.2	Background signal Raman spectrum	102
6.3	Optimal WERS design	103
6.4	Next generation samples	105
6.5	Final overview on the thesis work	105
	Bibliography.....	106
A.	Appendix A.....	117
A.1	Electromagnetic spectrum	117
A.2	Overlap analysis for waveguide-objective coupling.....	118
A.3	Conversion efficiency (Lumerical).....	120
A.3.1	Convergence testing.....	120
A.3.2	Additional simulations	122
A.3.3	Script: conversion efficiency probing region	124
A.3.4	Script: conversion efficiency for not-probing region	126
A.4	Scattering losses	128
A.4.1	Experiments procedure	128
A.4.2	Comparison nw model with volume-current method.....	131
A.4.3	WG losses simulation for not-probing region	132
A.5	Raman spectra of PMMA.....	134
A.5.1	Height of PMMA spin coated film.....	134
A.5.2	Thin film PMMA Raman spectrum	135
A.5.3	PCA for extraction PMMA signal.....	137
A.5.4	Standard procedure for evaluation the SBR	140
A.6	Additional observation during experiments.....	142
A.6.1	Slot WGs Raman spectra.....	142
A.6.2	Strange coupling effect	143
	List of figures.....	144
	List of tables.....	153
	List of symbols and Abbreviations	154
	Acknowledgements	155

1 Introduction to Waveguide enhanced Raman spectroscopy

1.1 Research framework overview

1.1.1 Photonics: a “key enabling technology”

Photonics is the science of creating, moving, and detecting photons (2). There is vast array of applications, going from displays, lasers, LED, camera sensors and optical fibers. The tremendous growth started from the 20th century of electronic manufacturing process led to the improvements in the fabrications process of chips towards 10 nm precision in nowadays (3). This incredible development opened the possibility to integrated photonics technology to be accessible. Integrated photonics is an emerging branch of photonics in which structures are built on a chip to manipulate light, instead of electrons, but with similar production process (e.g. lithography) proper the electronics field. In integrated photonics structures the absolute dimension must be precisely controlled. This indicates that despite the relatively large dimensions (e.g. μm) of the waveguides, extreme accurate lithography is needed (roughness in the order of nm is desired).

The digital revolution changed the human life drastically. The developments of technologies such as television, computers, and smartphones are clear sign of it. Nowadays, photonics has a huge potential comparable to electronics. In the EU Photonics21 roadmap (4) have been established eight thematic roadmaps including fields of information and communication, industrial manufacturing and quality and life science and health. The healthcare is one of the largest markets among photonics but also one of the more rapidly expanding sectors (Figure 1).

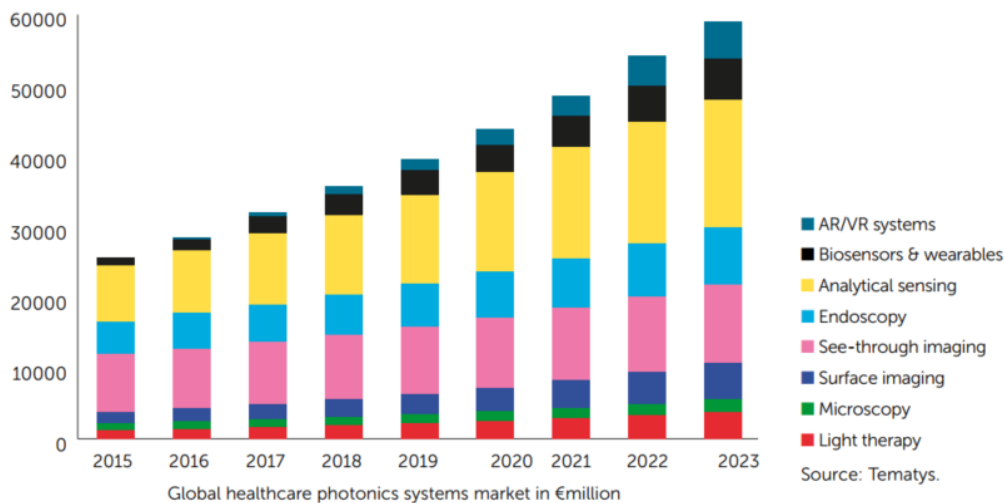


Figure 1: Global Market of Healthcare Photonics Systems. TBN Raman spectroscopy can be allocated in the analytical sensing field.

The pervasive character of photonics results in a crucial “building blocks of the next digital revolution” (5). Therefore, these kinds of technology are recognized as Key Enabling Technologies. This master thesis will dive into one of these technologies that has been opened thanks to the advancement in integrated photonics.

1.1.2 Raman spectroscopy: its major challenge

Raman spectroscopy is a technique that has the potential to detect molecules through their characteristic vibrations. It has a huge potential in material and bio-chemical science. Particular interest is the so-called fingerprint region (Figure 2) of the spectrum where the major assignments related to glycogen, proteins, lipids, and nucleic acids are highlighted (6).

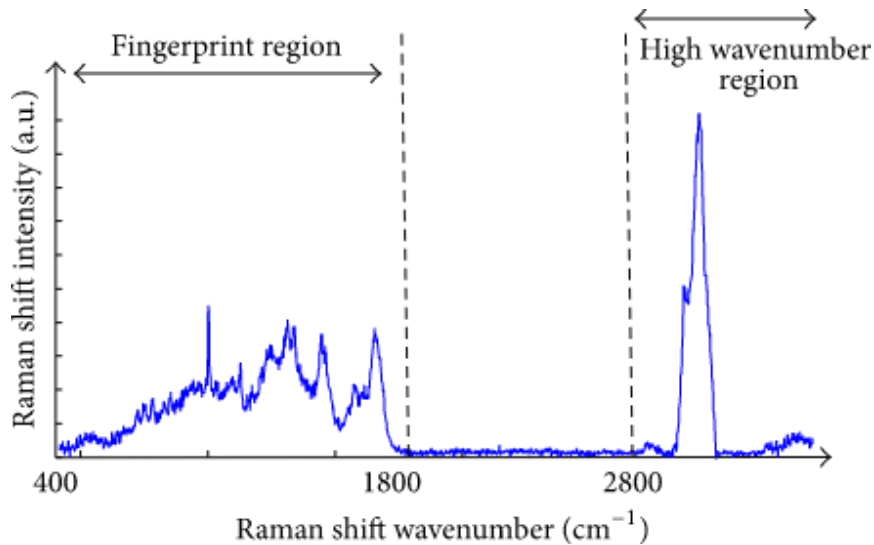


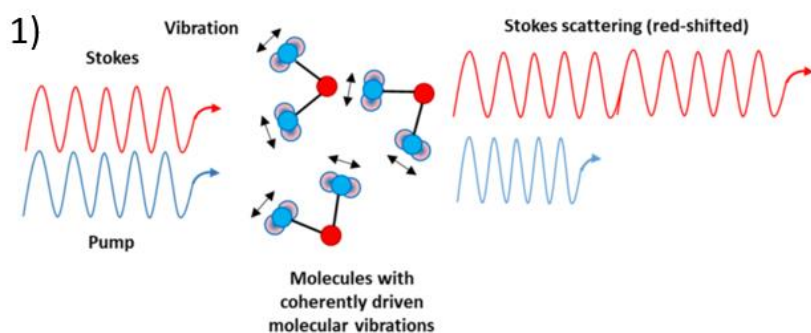
Figure 2: Raman spectrum example to highlight the two different regions of it. Fingerprint region is one of the most of interest in drug monitoring field (6).

The major limitation of this technique is the weak signal intensity and the complex and expensive tools used for detection. Therefore, it has not found yet widespread use outside of specialized labs. Many methods have been applied to improve the signal and make cheaper the measurements (7-10). For example:

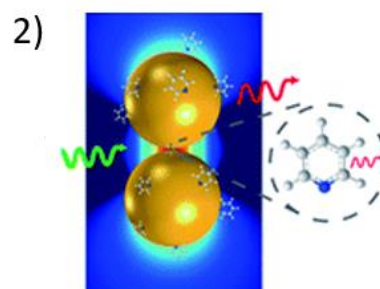
- Resonant Raman scattering and Coherent Raman scattering (CRS, Figure 3-1), exploits respectively one or two lasers with tuned frequency such that enhancement of the Raman signal occurs (10).
- Surface enhanced Raman scattering (SERS Figure 3-2), the “conventional one”, exploit the use of a nanostructured metallic substrate, over which the sample is deposited, to have a great enhancement of the signal (11). This has been attributed to different factors (12): electromagnetic enhancement associated to surface plasmon excitations; chemical enhancement, due to chemical interaction with substrate-analyte; and presence of “hot spot”, local interaction between nanoparticles of the substrate (13). It should be mentioned also tip-enhanced Raman spectroscopy (TERS) which is a combination of SERS and atomic force microscopy. With TERS is possible to overcome the optical microscope limitations (14).
- Photonic crystal enhancement Raman scattering (PC-RS Figure 3-3) given by the increase of apparent interaction thickness due to slow light (9).
- Fiber enhanced Raman spectroscopy (FERS, Figure 3-4) exploits the light confinement given by total internal reflection to increase the interaction length (15). Similarly, photonic

crystals fibers for Raman spectroscopy (PCF-RS, Figure 3-5) increases the volume of interaction but the light confinement is achieved with the creation of a photonic band gap associated to Bragg reflection (16, 17).

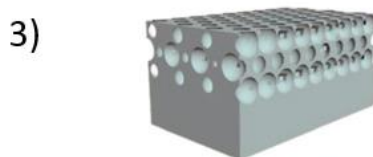
Combinations between previous techniques have been also demonstrated. For example, it has been studied CRS combined with PC or PCF (18, 19), or SERS combined with PCF (20, 21). It should be noted that not always a combination of different techniques results in an advantage, for example combining PCF with SERS (16). It can be understood since on one had the PCF advantage is the increase of sensing length, on the other hand if nanoparticles are distributed along the fiber, the absorption associated to surfaces plasmons strongly reduces the propagation length and increases the complexity of the device.



Ferrara et al. *Micromachines* 11.3 (2020)

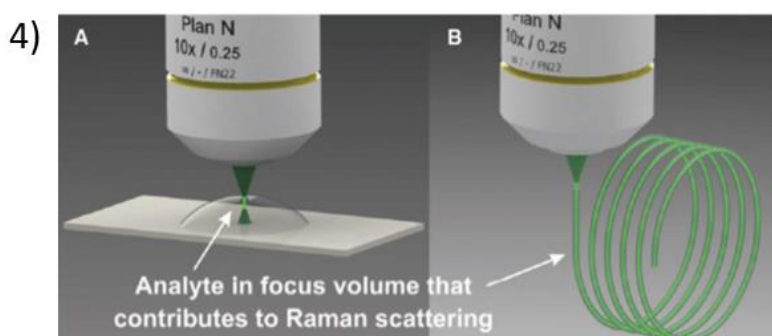


Pérez-Jiménez et al. *Chemical science* 11.18 (2020): 4563-4577.

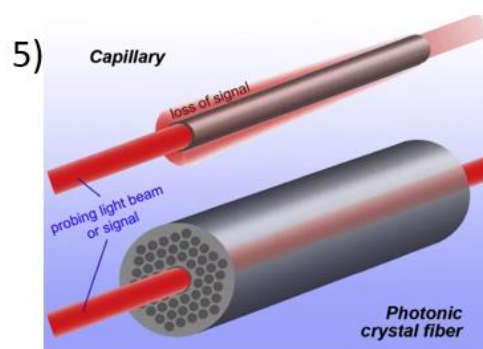


Inverse ETPTA PhC

Ashurov et al. *Physical Chemistry Chemical Physics* 22.17 (2020): 9630-9636.



Frosch. Et al. *Nanophotonics*, vol. 9, no. 1, 2020, pp. 19-37.



Markin et al. *TrAC Trends in Analytical Chemistry* 88 (2017): 185-197.

Figure 3: collection of figures for each techniques: 1) Coherent Raman scattering (10); 2) Surface enhanced Raman scattering (22); 3) Photonic crystal for enhancement Raman scattering (9); 4) Fibre enhanced Raman spectroscopy (15) and 5) photonic crystals fibers for Raman spectroscopy (16).

1.1.3 Waveguide enhanced Raman spectroscopy

In the framework of photonics and enhanced Raman signal, waveguide enhanced Raman spectroscopy (WERS) has become a new trend in recent years (Figure 4). In WERS the enhancement is given by a nanophotonic WG fabricated on chip which has the scope of deliver excitation and signal light between detectors and sample. The interaction with the sample is given by the evanescent field. Similarly, to FERS, it gives enhancement through increased probing length and WG enhancement.

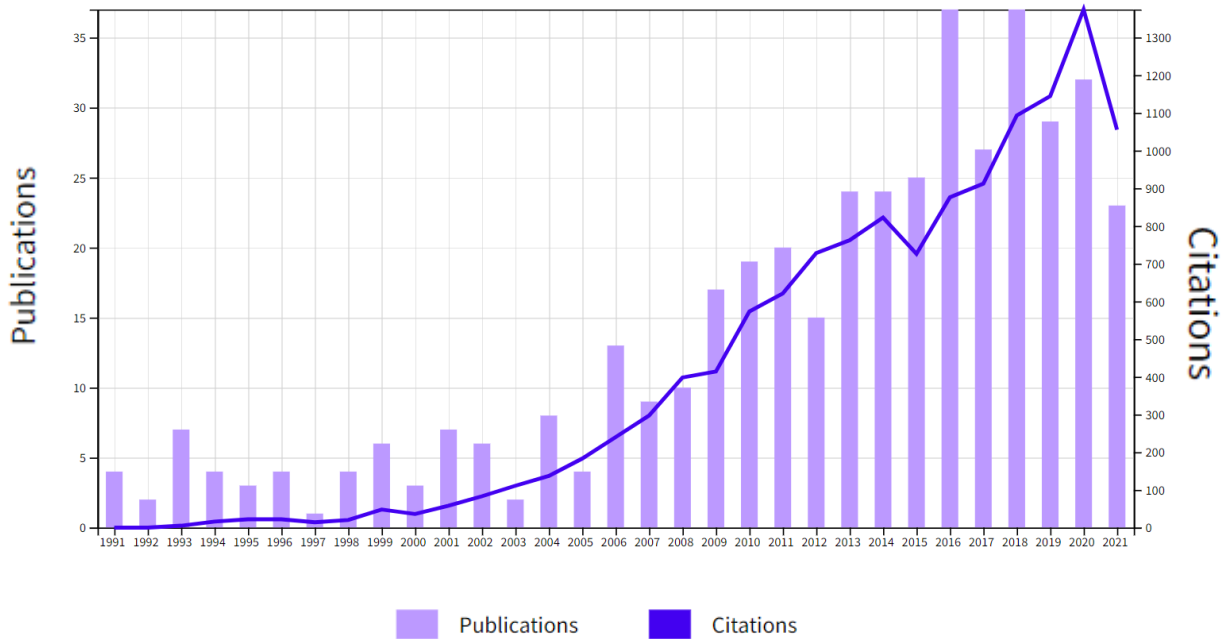


Figure 4: citation and publications per year. Results taken from Web of Science by searching: "Waveguide Enhanced Raman".

But the major advantage of WERS is that is CMOS compatible, i.e. it relies on well-established production process. This result in huge advantages over other techniques in terms of scalability and low-cost production (23). WERS research can be well combined with other research lines to achieve a full Raman system on a nanophotonic chip, including lasers and filters spectrometers (24), Figure 5.

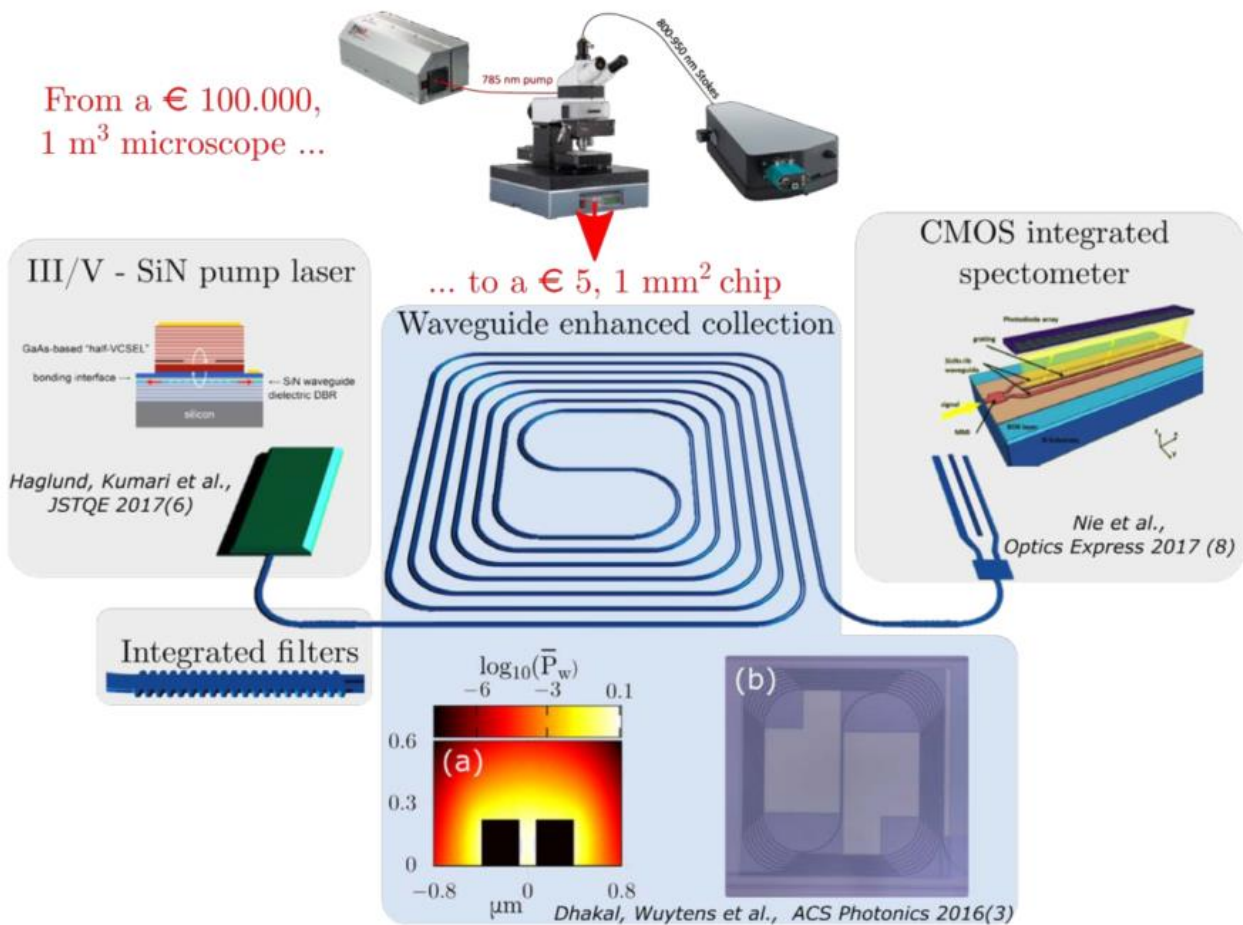


Figure 5: Image and text caption taken from (25). "Conceptual view of a fully integrated Raman system on a nanophotonic chip. Insets (a) and (b) show the two contributions to the waveguide enhanced excitation and collection: An efficient coupling of dipole radiation to the waveguide and the collection of Stokes power over a long interaction length".

1.2 State of the art

In this chapter a review of the WERS field is exposed. It is mainly based on well done other reviews, please refers to them for others information (23, 24, 26, 27).

1.2.1 Historical introduction and main applications

The WERS enhancement mechanism is equivalent to FERS and it has been demonstrated in 1972 by Walfren et al. (28). They used hollow core optical fibers in which the laser light propagates in the core filled sample. Waveguide enhanced Raman spectroscopy was demonstrated in 1974 by Levy et al. (29). They have used a slab waveguide of thin film ($1\mu\text{m}$) of methyl-methacrylate film to study Raman spectra of methyl-methacrylate thin film itself. Therefore, they have probed the material of the WG itself. In 1996, Kanger et al. (30) has been demonstrated WERS using a ZnO slab WG (2D geometry) to collect Raman signal through its evanescent field (i.e. the sample is not the WG material itself). They have been shown dynamic measurements of protein binding in Raman regions between $[900; 3100] \text{ cm}^{-1}$. The authors have been pointed out what is one of the main challenges for these devices: the Raman background from the WG core could limit the detectability of weak signals.

Recent improvements in nanofabrication techniques lead to improvement of WG losses, opening the possibility to 1D WG geometries (rib, strip and slot designs). In 2014 Dackal et al. (31) developed the theory on which most of the works nowadays are based on and it will be exposed in chapter 37. The advantages of WERS have been demonstrated for both detection of bulk materials and thin films (31, 32).

There is a very interesting research line in which it has been shown a possible combination of WERS with other techniques. For example, combined WERS and SERS (33-36). A comparison between different design strategies to reproducible plasmonic structures on the WGs and the resulting Raman signal has been done by Turk et al. (37). It has been shown that still improvements are needed in terms of signal enhancement with respect to free space beam collection (37). It has been shown the possibility to combine WERS and CRS (38). There have been conducted also a study of combined WERS, SERS and CRS (39).

In terms of detection capability there were many demonstrations of the potentials of WERS. Dhakal et al. demonstrated the capability of WERS for real-time detection of DNA hybridization (40), by using slot WG: PEVEC Si_3N_4 with height = 220 nm; width $w = 850 \text{ nm}$; slot width $s = 150 \text{ nm}$; length 1 cm; in forward signal collection, 785nm laser and TE polarization. WERS has been applied also for gas detection. Holmstrom et al. reported the first measurements of trace of gases with WERS (41). They used a coated (with hypersorbent polymer) slab WG: LPVCD Si_3N_4 with height = 175 nm; width $w = 2 \mu\text{m}$; etch = 100 nm; length 1 cm; in forward signal collection, 1064nm laser and TE polarization. Zhao et al. have been shown the possibility to detect volatile organic compounds through functionalized slot WGs with mesoporous silica (42). The chip design consisted in a slot WG of PEVCD Si_3N_4 with height = 300 nm; width $w = 700 \text{ nm}$; slot $s = 150 \text{ nm}$; length 8 mm; backward signal collection, 785nm laser. With similar design, Liu et al. (43) demonstrated its application for detection of organic compounds in water solutions.

1.2.2 WERS challenges

One of the major challenges in WERS is the correct choice and design of the device. To subdivide this bigger problem in smaller-interconnected tasks, it is useful to understand the travel that laser light follows to interact with the analyte molecule and then how the Raman signal is collected back to be analyzed. A scheme of the process is reported in Figure 6.

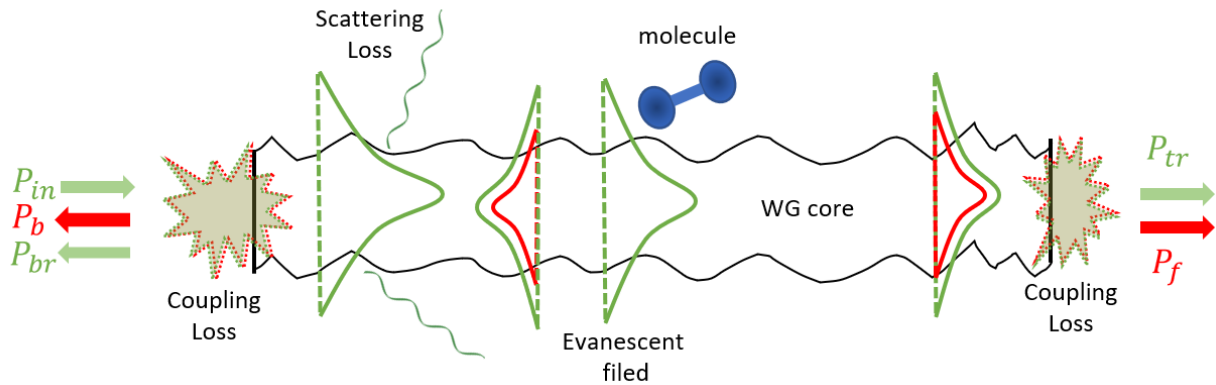


Figure 6: scheme of the light path into the WG for Raman detection. In red the Raman scattered light and green the laser light. P_{in} is the input power, P_b is the backward Raman scattered power and P_{br} is the backward scattered power, P_{tr} is the power transmitter at pump wavelength and P_f is the forward power Raman scattered.

The first challenge is the **coupling** of the laser power in the WG (Figure 6). This is a delicate process during testing, usually relying on expensive stages and time-consuming procedures. For future application it will need to be highly reliable and quick. There have been shown multiple possibilities in literature: the most common is by using microscope objective (44, 45) or aspheric lenses, with coupling efficiency ranging from 3 to 8 dB/facet (Figure 7a). For slab WG it is possible to use prism coupling (Figure 7b), with minimum losses of 5 dB/facet (46). Another possibility is the use of grating couplers which greatly simplify the coupling procedure, increasing the translational tolerances and possibility to reduce the insertion losses to 1 dB (23). Studies have been done for tantalum pentoxide WGs by Ettabib et al. (47) and for silicon nitride WGs by Subramanian et al. (48). It should be mentioned the main limitation of grating couplers is the narrow bandwidth since the scattered wavelength in Raman is shifted from pump wavelength also by 300 nm which limits their application to only pump in coupling. Kita et al. (49) have been shown the possibility to couple directly fibre to strip WGs and bonding fibre and strip together (Figure 7c), losing the possibility to change multiple chips but on the other hand eliminating misalignment problems associated to mechanical instability for example.

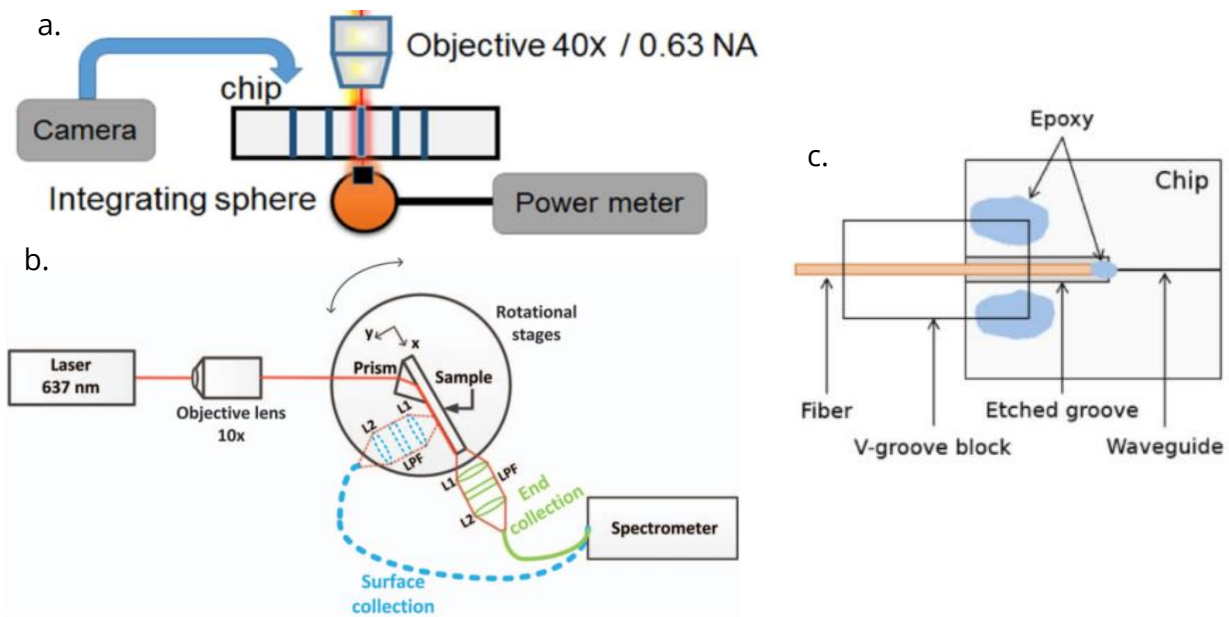


Figure 7: a) schematic of a fraction of the setup with objective coupling (50). b) Experimental apparatus with prism coupling in a slab WG. Broken blue lines: waveguide surface collection configuration; solid green lines: waveguide end collection configuration. L1 and 2, lenses; LPF, long pass filter (46). c. top-view schematics of the fiber-bonding region. The glass V-groove block is bonded to the chip with epoxy at the tip of the fiber in the etched groove, and with larger volumes of cured epoxy on the sides of the block for improved robustness. Image and caption taken from (49).

After coupling light in the WG it can be added **extra components** such as pump rejection filters, in order to separate pump laser light from the WG when this is no more needed. This device has been studied by Nie et al. (51) and they have shown high extinction ratio (68.5 dB). Strip or slab WGs are commonly used for coupling with outside coming laser sources, but if a strip WG is used for the sensing region, a strip to slot mode converter is needed. There have been shown two possible designs for this scope: one proposed by Mere et al. (52) consisting in a balanced 50/50 power splitter and tuneable phase matched taper combiner; the second one is a MMI shown by Deng et al. (53). The second one has been demonstrated for silicon nitride WGs and seems the more compact solution.

Once the light is coupled, it should be delivered to the analyte, but **losses** can limit the efficiency of this process. Many factors can determine the losses. Materials and process production are strictly related. For example, a promising WERS material is TiO_2 but nowadays silicon nitride is still the best choice mainly due to the high losses of TiO_2 WGs (23). Another important parameter is the WG type (rib, strip, slot) and dimension. Finally, it should be taken into account the laser wavelength and polarization. A rule of thumb is that higher the power is at the side wall and higher the scattering losses are. In 2015 Subramanian et al. (54) had calculated scattering losses for PEVEC silicon nitride strip WGs varying the WG width, pump wavelengths and cladding material (silicon dioxide or not). For pump wavelength at 780nm they measured losses below 1 dB/cm for cladded WGs and in the range of 1-3 dB/cm for uncladded WGs. In 2021 Tyndall et al. (55) have been performed a similar study on silicon dioxide cladded silicon nitride WGs comparing annealing and PEVEC and LPCVD production process. In particular in the band 700-

1000 nm they have measured WG losses of 0.5 dB/cm for not annealed and 0.4 dB/cm annealed chip, thus suggesting that WGs long as 10 cm can be used.

While the pump light is travelling it also interacts with the materials. Through its evanescent tails (Figure 6) light excites the molecules such that they emit Raman signal. A fraction of that couples back in the WG. The efficiency in the excitation and collection is given by the **conversion efficiency** parameter (η). Which is a measure of the sensitivity of the WG. Theoretical and experimental studies have been done to see how it is influenced by the WG geometries, pump wavelength and light polarization (31, 56). In these studies, it has been shown that in general strip WGs have higher η in TM mode with respect to TE. Slot WGs perform better of strip one in TE mode. The values of η can goes from 0.01 to 0.5 sr. it has been studied theoretically the influence of the Raman shift over the η . Dhakal et al. (31, 56) had developed the theory for η in which this phase shift is taken into account. Simulations results of η as function of the scattered wavelength have been reported by Stievater et al. (57).

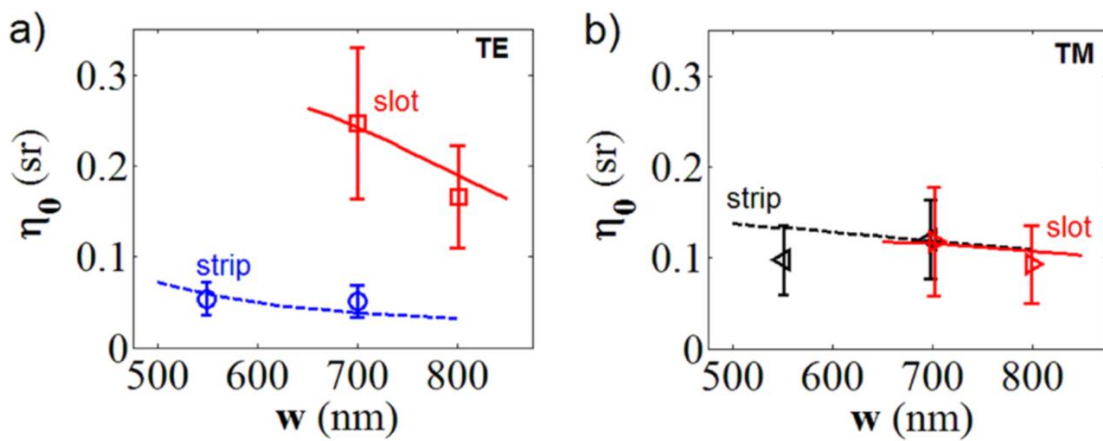


Figure 8: Theoretical and experimental values of η obtained for (a) TE modes and (b) TM modes of Si_3N_4 waveguides. The markers represent the estimated experimental values obtained from the least square error fit of the experimental data. The error bars represent the measurement and estimation errors. Lines represent the theoretical curves. The red solid lines are the theoretical curve for slot waveguides with $s = 150$ nm. The blue and black dashed lines are the theoretical curves for TE and TM polarizations, respectively, for strip waveguides. Circle: TE polarization, strip waveguides. Left-handed triangles: TM polarization, strip waveguides. Right-handed triangles: TM polarization, slot waveguides. Square: TE polarization, slot waveguides. Image and caption taken from (58).

It should be noted that while the evanescent tail interacts with the analyte, a major fraction of the power is confined in the core WG. The interaction between the core material and the pump laser result in the generation of the **Raman background**. This result in the ultimate limitation of the sensitivity for WERS devices (27, 59, 60). The background generation is influenced by the material type as have been shown by Raza et al. (44) in which they studied four WG materials: Al_2O_3 , Si_3N_4 , Ta_2O_5 and TiO_2 (Figure 9). A second work done by Lee et al. (61) they have been studied Al_2O_3 , Si_3N_4 and TiO_2 WG materials. Similar results have been obtained from both groups, where Si_3N_4 WGs seems to be the best choice at this current moment. But as pointed out by (23) differences in WG geometry and loss between the different WGs in both studies “make firm conclusions elusive”. In background Raman spectra of different WGs it can be easy to recognize a common feature, which can be well described by and exponential decreasing

function. This is quite peculiar behaviour and very few papers have been pointed out this. Dhakal et al. (59) have been done the first in depth studies, showing that the exponential decreasing background signal with high probability can be associated to core WG Raman signal. It has been shown that by changing laser wavelength the exponential decreasing feature does not change significantly. Since it is a common feature with other materials its origin has been associated to amorphous material. Thomas et al. (27, 60) have been proposed a theory in which this signal could be originated from intrinsic thermal fluctuations, which results in fluctuation in the refractive index resulting in exponential decreasing Raman spectrum. Therefore, a solution to this problem could be to create crystalline WGs.

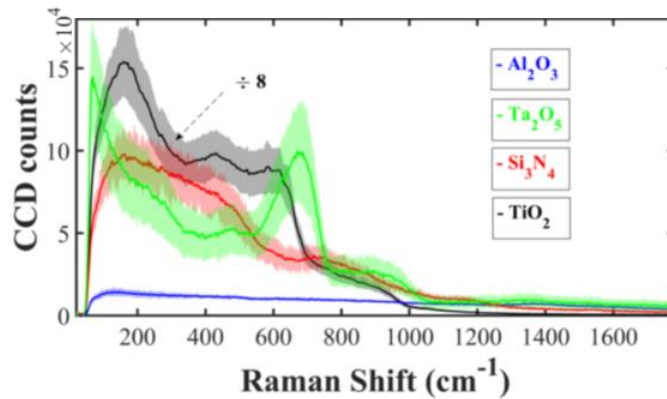


Figure 9: Background scattering spectra for the four material platforms studied by (44).

Then the Raman signal travels in the WG. The **losses** are associated to a **different wavelength**. The only experiments which report extensively the evolution of the scattering losses as function of different wavelengths it was done by Tyndall et al. (55). They have shown how the annealing process and how the production process can influence the scattering losses.

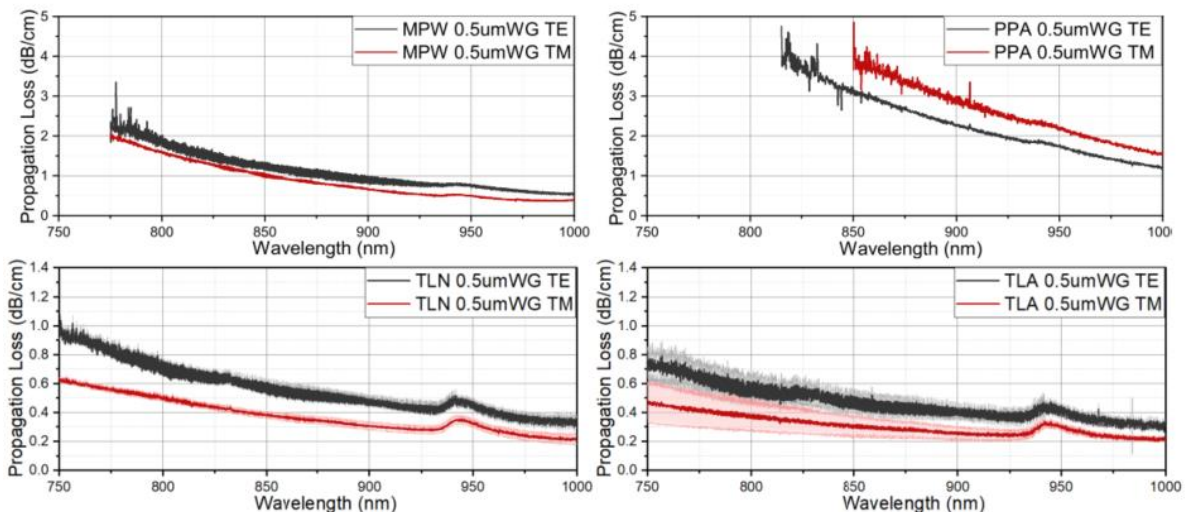


Figure 10: Propagation loss vs. wavelength for the TE_{00} and TM_{00} modes in the i/z bands (750 nm to 1000 nm) of four wafer builds: MPW, PPA, TLN, and TLA (the first letter refers to the production process of the SiO_2 : P=PEVEC and T=Thermal, M=P+T; the second letter refers to the production process of SiN: L=LPCVD and P=PEVEC; the third letter refers if it is annealed or not: A=yes, N=no, W=N+A). The light gray and light red shaded regions indicate the standard error in the linear fit. Note the different y-axis scales in the plots. Image and caption taken from (55). The WGs used were 220 nm thick, 0.5 μm width and top and bottom cladding are 5 μm thick.

Finally, the scattered light should be **collected out** towards the spectrometer. Since the scattered is subdivided equally (for isotropic materials) there are two different possibilities of collection: forward or backward (in chapter 2.3.2 there is the theory that explain the difference). The difference in the collection design has been pointed out by Raza et al. (44), showing clear advantage toward backward collection. In particular for backward collection it has been shown possible strategies to reduce the background signal. Kita et al. (49) have been designed a 2x2 directional couplers to reduce the background signal coming from not probing region, on the other hand Reynkens et al. (62) have studied the use of multi-mode interferometer for this scope.

The WG type and geometry influence both losses, collection efficiency and background collection efficiency, which are the three main parameters to consider for WERS device. It should be noted that as the mode is less confined, the losses are higher as well as the WG sensitivity (63) as shown in Figure 11 at the bottom. There have been some works showing how slot WG are the best design since both increase the sample conversion efficiency and at the same time have reduced background (59), Figure 11 on top. But recently in some papers have suggested that strip WGs have lower losses with respect to the slot WGs resulting in lower losses that can allow to longer WGs (49, 64). For longer WGs both signal and background increase linearly but since the main parameter to be optimized is the signal to noise ratio (SNR), in which for shot noise limited noise it is given by $N_{shot\ noise} = \sqrt{S}$, it can be understood that an increase of the WG length (L) have a beneficial effect of the SNR proportional by a factor of $\frac{S}{\sqrt{S}} = \sqrt{S(L)}$.

Up to now no clear leading approach has been emerged for WERS design (23). In this master thesis one objective is to critically understand the influence of some WGs parameters that should be taken into account for WERS design.

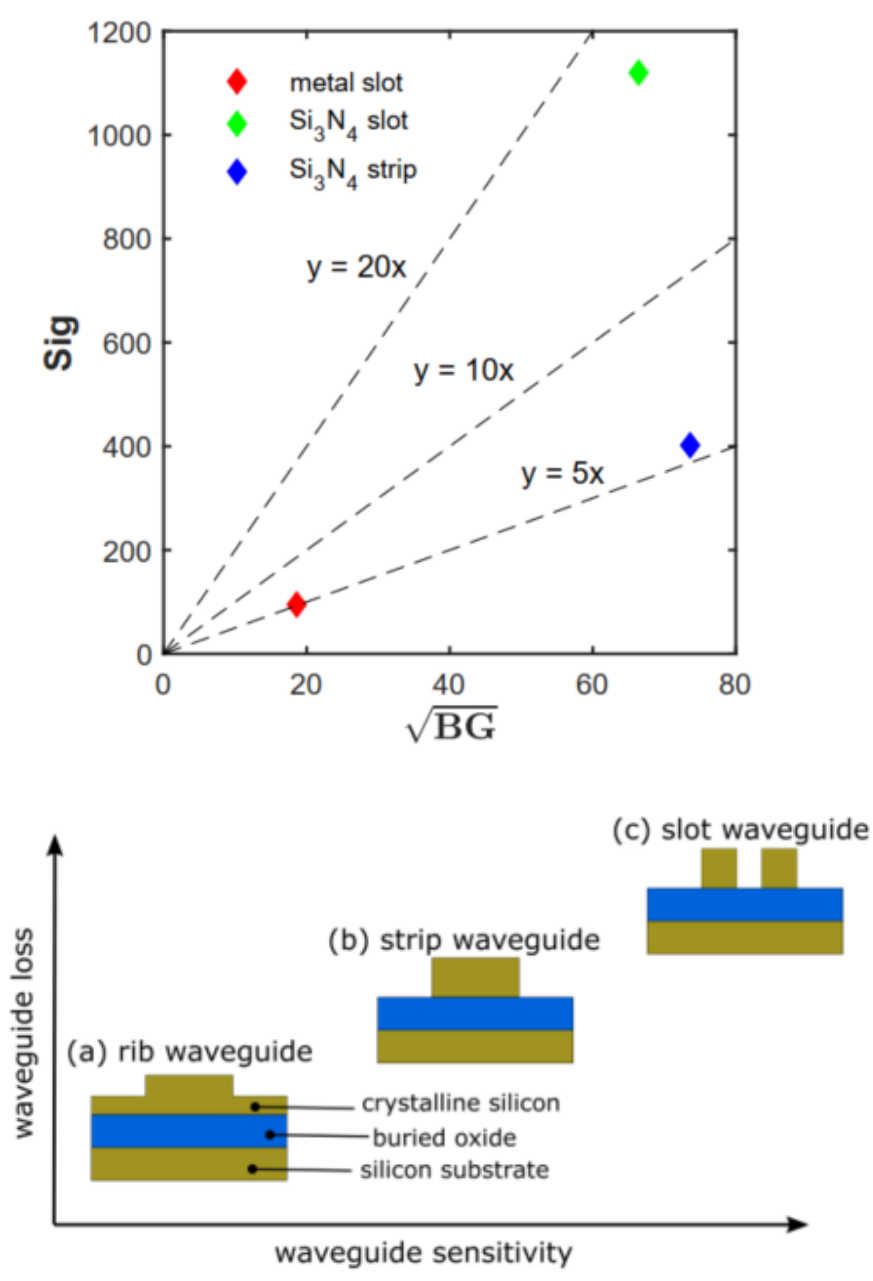


Figure 11: on the top: comparison between slot, strip and WERS-SERS (metal slot) WGs signal vs shot noise (65). on the bottom influence of the WG on the waveguide sensitivity and loss (63).

1.3 Thesis outline

The primary scope of this master thesis is to develop an adequate set up and coupling procedure for reliable and reproducible testing of WERS chips with implementation of automated scripts for data analysis of Raman spectra and scattering losses. Secondly, it has the objective to improve the existing theoretical and simulation models for enhanced understanding of experimental results, and thereby informing the evolution of the next generation of devices. Thirdly, to critically review and experimentally evaluate two main challenges for WERS. The first one is regarding the background signal coming from silicon nitride strip waveguides. Therefore, a deep analysis of the Raman spectra has been studied. The study considers the most recent advancement of the theoretical background of these Raman spectra. Finally, this thesis work has the objective to understand experimentally the optimal WG design for next generation devices.

This thesis is subdivided in 5 chapters. The first one is the introduction to WERS research.

In the second chapter of this thesis there is summarized the theoretical background on which this thesis is based. The study of WERS need a deep understanding of Raman scattering theory, WG theory and the theoretical framework characteristic of WERS devices. The third chapter exposes the instrumentation used and the current chip design.

In the fourth and fifth chapters expose the results of my research. The fourth chapter shows the developments regarding the first two objectives of this master thesis. Some of the major problems associated to the set-up design and data collection procedure have been reported and solution to those have been developed and tested. Then the results of a deep study of Raman background spectra have been shown. It has been developed an almost fully automated fitting procedure for full extraction of all the relevant parameters for the description of these spectra (i.e. peak hight, FWHM, peak position, and exponential decreasing signal). It has been collected these spectra under different conditions such as varying pump power, laser wavelength and WG strip width and length.

The last chapter shows the development of an improved model for deep understanding of the current device, and it has been validated by experimental results. Regardless its complexity it offers a deep understanding of most of the design parameters. The signal to background ratio (SBR) has been chosen as a figure of merit for this device. It has been simulated the WG losses, coupling efficiencies and conversion efficiency via Lumerical mode solver. Finally, it is presented a critical discussion of the experimental results regarding the WG width influence on the signal to background ratio. From those results it can be pointed out additional components that can influence the efficiency of these devices: the scattered wavelength and the not-probing length.

2 Theoretical background

In this chapter the main theoretical background is described. I will not report the full derivation of any formula but only the main passages and hypothesis. For more information, look at the references that are reported in each paragraph. The first chapter will describe the fundamentals of Raman scattering. The second and third one describes the waveguides and WERS theory.

2.1 Spontaneous Raman scattering

In this chapter the theoretical background for Raman scattering is briefly introduced on (66).

Raman spectroscopy is an analytical technique used to measure the vibrational energy modes of a sample (i.e. atomic vibrations). Raman spectroscopy exploits the phenomena discovered in 1928 by the Indian physicist C.V. Raman (67), Nobel prize 1931, which consists in the use of a monochromatic incident radiation to analyze the resulting inelastic scattered light after the interaction with the material under examination. The analyte diffuses electromagnetic waves with frequencies equal, higher or lower to the excitation line: the first case is called Rayleigh elastic scattering, then for the second and the third we have inelastic scattering that are called respectively: anti-Stokes and Stokes (Figure 12).

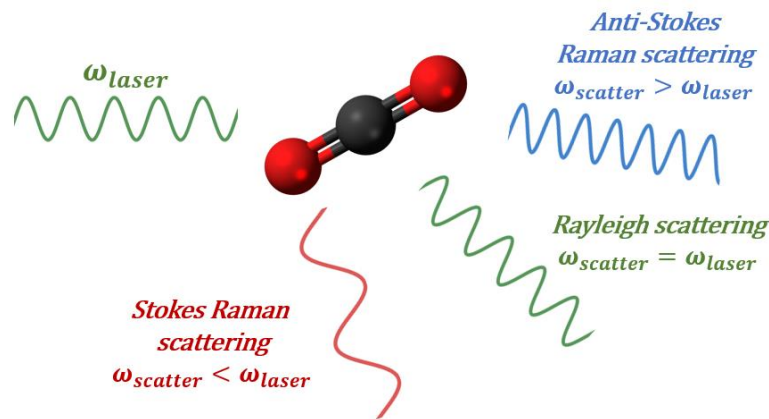


Figure 12: Scheme of Raman scattering process.

Raman scattering can be described considering both a classical and, more accurately quantum approach.

2.1.1 Classical theory for diatomic molecule

In classical theory the vibrations of a diatomic molecule can be obtained by solving the Hamilton's equations of motion (68):

$$\begin{cases} \frac{\partial H}{\partial p_i} = \dot{x}_i \\ -\frac{\partial H}{\partial x_i} = \dot{p}_i \end{cases} \quad 2.1$$

Where p_i , x_i are momentum and position of the atom i and \dot{p}_i, \dot{x}_i their derivative with respect to time. The Hamiltonian of the system is given by the sum of the kinetic energy (T) and the potential (V) $H = T + V$. In the hypothesis of small oscillations, i.e. near to equilibrium, the potential can be approximated with a harmonic one:

$$V \approx V(R_{eq}) + \left. \frac{\partial V}{\partial R} \right|_{eq} (R - R_{eq}) + \frac{1}{2} \left. \frac{\partial^2 V}{\partial R^2} \right|_{eq} (R - R_{eq})^2 \quad 2.2$$

Where R is the absolute distance between the two nucleus and R_{eq} is the equilibrium distance. Since $V(R_{eq})$ can be arbitrary defined as equal to zero and at equilibrium $\left. \frac{\partial V}{\partial R} \right|_{eq} = 0$, it results:

$$V \approx \frac{1}{2} k (R - R_{eq})^2 \quad 2.3$$

Where we define the force constant as: $k = \left. \frac{\partial^2 V}{\partial R^2} \right|_{eq}$. By solving the Hamilton's equations of motion, we obtain:

$$R(t) = R_{eq} + A \cos(\omega_{vib} t) \quad 2.4$$

A can be obtained from the initial conditions (we should also consider a phase shift ϕ that is set equal to zero to simplify the notation). The characteristic vibrational frequency of the diatomic molecule is:

$$\omega_{vib} = \sqrt{\frac{k}{\mu}} \quad 2.5$$

Where μ is the reduced mass defined as: $\mu = \frac{m_1 m_2}{m_1 + m_2}$, with m_1, m_2 are the mass of the two atoms. Therefore, we can notice how the characteristic vibrational frequency depends on the elastic constant and on the reduced mass of the system.

In more general terms we can introduce the normal coordinates, Q_{vib} , each one of those is characterized by a specific vibrational frequency, ω_{vib} and their associated eigenvector which represent how the atoms vibrates in the molecule (direction and relative verse). For the case of the diatomic molecule there is only one normal coordinate, which is the stretching mode (Figure 13). It corresponds to the oscillation of the two nuclei around the equilibrium distance position, therefore from equation 2.4:

$$Q_{vib}(t) = R(t) - R_{eq} = A \cos(\omega_{vib} t) \quad 2.6$$

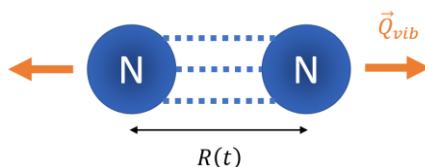


Figure 13 Schematic representation of the normal stretching mode of nitrogen molecule (\vec{Q}_{vib}), with $R(t)$ nuclei distance.

Now we can introduce incoming light:

$$E(t) = E_0 \cos(\omega_L t) \quad 2.7$$

The oscillating field polarizes the electronic cloud of the molecule, leading to its oscillation which in turn re-emits the energy according to the normal modes that are excited.

At the molecular level, polarization is described by an induced dipole moment $p(t)$, which is a function of the incoming electric field and material dependent, given by the polarizability: α . In general, it can have a non-linear tensorial form but we can introduce a linear and isotropic approximation, so the polarizability can be considered a scalar obtaining that the induced dipole moment is:

$$p = \alpha \cdot E \quad 2.8$$

Polarizability is a function of charges distribution in the molecule and the characteristic resonance frequency of the molecule. Since the molecule is vibrating also the polarizability is influenced by this motion, therefore the polarizability can be described with a Taylor expansion with two components: the static polarizability, α_0 , and a dynamic component. The last one can be described by a summation over the set of normal coordinates. The total polarizability is (66):

$$\alpha = \alpha_{eq} + \sum_j \left(\frac{\partial \alpha}{\partial Q_j} \right)_{eq} Q_j + \dots \quad 2.9$$

For small displacements it can be assumed simple harmonic motion, the time dependence of Q_j can be written as $Q_j = Q_{j0} \cos(\omega_j t)$. Considering only a normal coordinate, neglecting second order terms, or higher, the polarizability becomes:

$$\alpha_{vib} \approx \alpha_{eq} + \left(\frac{\partial \alpha}{\partial Q} \right)_{eq} Q_0 \cos(\omega_{vib} t) \quad 2.10$$

Where Q_0 is the normal coordinate amplitude. By combining the equations 2.7 and 2.10 the induced dipole moment becomes:

$$p = \left(\alpha_{eq} + \left(\frac{\partial \alpha}{\partial Q} \right)_{eq} Q_0 \cos(\omega_{vib} t) \right) \cdot E_0 \cos(\omega_L t) \quad 2.11$$

By the application of Werner's formulae we find three different components:

$$p = p_{\omega_L} + p_{\omega_L - \omega_{vib}} + p_{\omega_L + \omega_{vib}} \quad 2.12$$

Respectively each term is related to different scattering phenomena: elastic scattering and two inelastic scattering (Stokes and anti-Stokes):

$$p_{\omega_L} = \alpha_{eq} E_0 \cos(\omega_L t) \quad 2.13$$

$$p_{\omega_L - \omega_{vib}} = \frac{1}{2} \left(\frac{\partial \alpha}{\partial Q} \right)_{eq} Q_0 E_0 \cos((\omega_L - \omega_{vib})t) \quad 2.14$$

$$p_{\omega_L + \omega_{vib}} = \frac{1}{2} \left(\frac{\partial \alpha}{\partial Q} \right)_{eq} Q_0 E_0 \cos((\omega_L + \omega_{vib})t) \quad 2.15$$

For a medium with some significant degree of molecular order, the elastic scattering in equation 2.13, in the absence of absorption (i.e. $\omega_L \neq \omega_{molecule}$), is in-phase with the incident light, therefore it corresponds to the forward propagation of light. The random positioning of the scattering molecules (e.g. due to amorphous phases and temperature) leads to an incoherent addition of scattered light that leads to the so called Rayleigh scattered light (69).

The two last equations are of our interest since they contain molecular information related to its vibrational frequencies. From those equations we can introduce the first selection rule to have Raman scattering:

$$\left(\frac{\partial\alpha}{\partial Q}\right)_{eq} \neq 0 \quad 2.16$$

Therefore, a normal mode Q to be Raman-active should have nonzero rate change of polarizability, α , with the vibration around its equilibrium position.

2.1.2 Quantum theory of Raman scattering

To describe intensity of Raman scattering it is necessary to describe the matter with quantum mechanics formalism. The Schrödinger equation for a harmonic oscillator is given by:

$$\left[-\frac{\hbar^2}{2\mu}\frac{\partial^2}{\partial R^2} + \frac{1}{2}k(R - R_{eq})^2\right]\psi = E\psi \quad 2.17$$

The solutions of the equation are reported in Figure 14. The energy is given by:

$$E_n = \left(\frac{1}{2} + n\right)\hbar\omega \quad n = 1, 2, \dots \quad 2.18$$

From equation 2.18 we can introduce one of the main differences with respect to the classical description, which consist in the quantization of the energy of the harmonic oscillator in discrete energy levels. For the harmonic oscillator, these energy levels are equispaced by $\hbar\omega$.

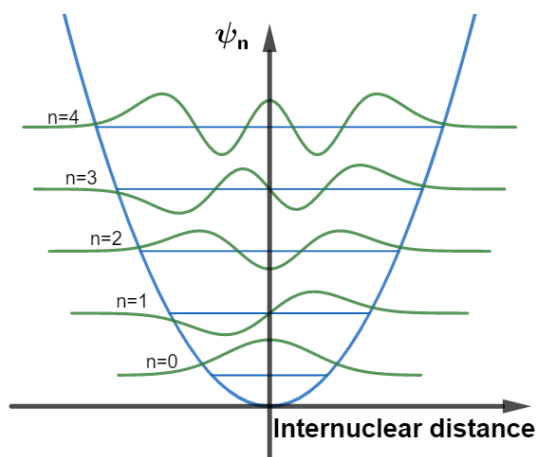


Figure 14 representation of the solutions of the quantum harmonic oscillator for one vibrational mode.

The introduction of anharmonic terms gives a more realistic description in which the energy levels are no more equispaced (Figure 15). This can be useful in the description of those process in which high vibrational levels are involved such as fusion where the thermal energy breaks the intermolecular interactions.

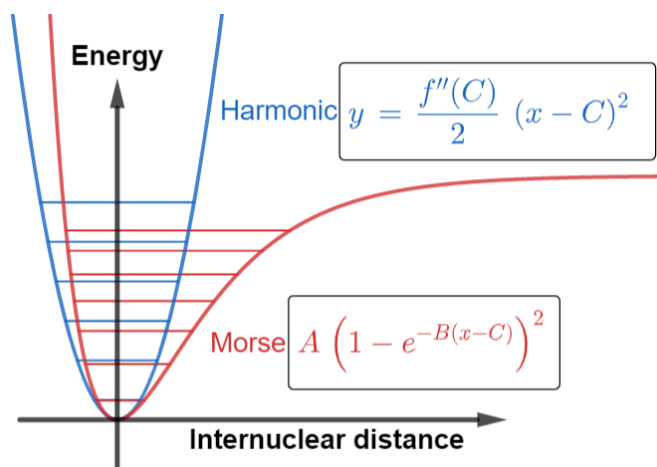


Figure 15: Comparison between a harmonic potential (blue) and anharmonic potential (red). Where A , B and C are constants. As can be noticed the energy levels are no more equidistant.

The vibrational energy of a molecule is characterized by discrete energy levels, therefore we can describe scattering process as a transition that start from a certain vibrational level, then the molecule is excited to a virtual energy level (annihilation of a photon) and a suddenly decay to a vibrational level (creation of a photon). For inelastic scattering, the initial and final vibrational energy levels are different. As we can see in Figure 16, anti-Stokes scattering starts from a higher vibrational level, with respect to the Stokes scattering. Since the number of phonons in a molecule is governed by the Bose-Einstein distribution, it is less probable to find a molecule with higher vibrational energy state. Therefore, the relative intensity of the two phenomena should considered this difference which it was not considered by the classical theory. As we can see in Figure 16, at room temperature the Stokes scattering intensity is 10^3 higher with respect to the anti-Stokes scattering (if we consider a Raman shift of 2500 cm^{-1}), as it can be calculated from:

$$\frac{I_{Stokes}}{I_{anti-Stokes}} \propto \left(\frac{\omega_L - \omega_{vib}}{\omega_L + \omega_{vib}} \right)^4 \exp\left(\frac{\hbar\omega_{vib}}{kT} \right) \quad 2.19$$

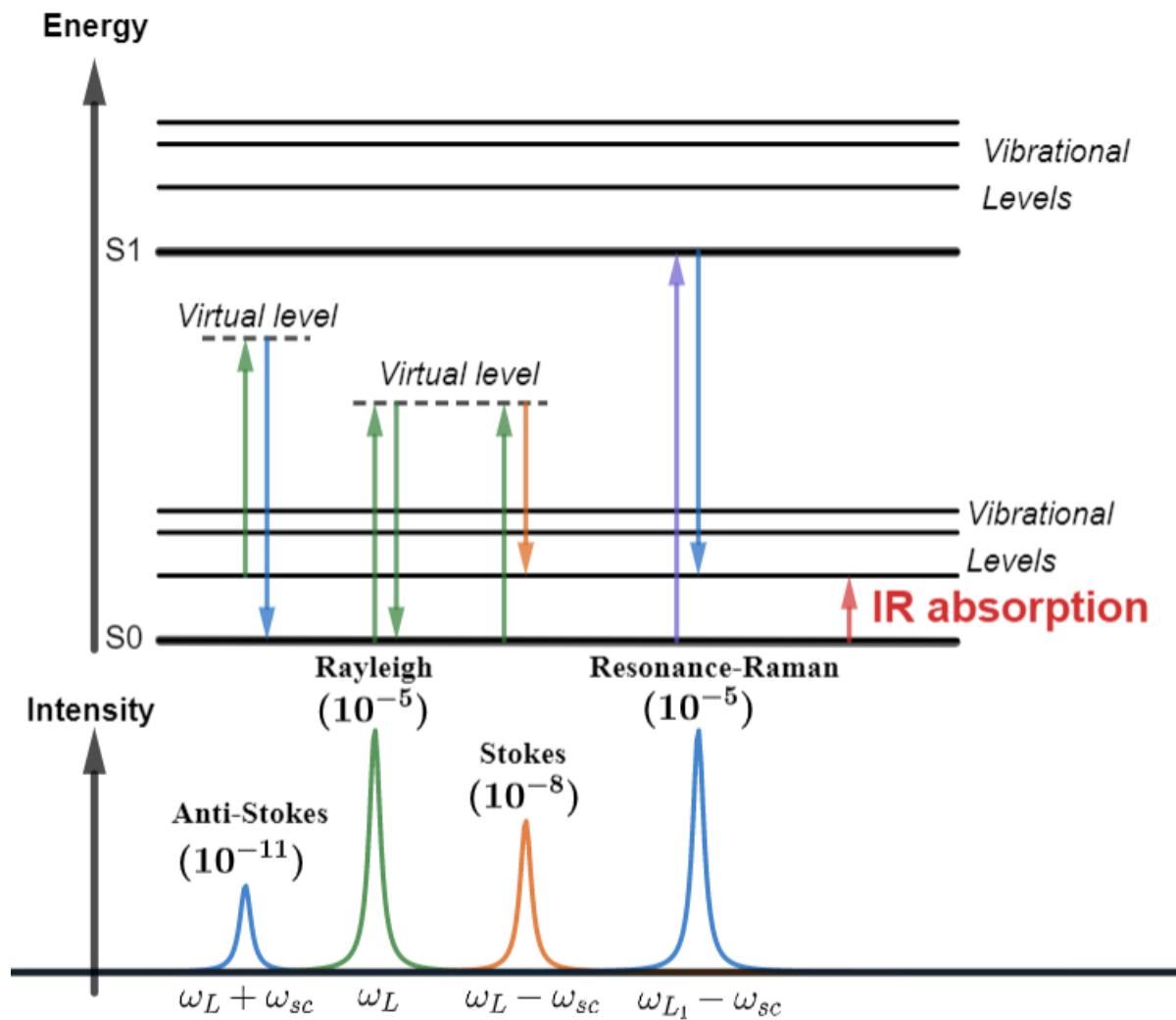


Figure 16: Scheme of the transitions involved in Raman anti-Stokes, Rayleigh, Raman Stokes, Resonance Raman scattering and IR absorption. The last phenomena is characterized by photon energies in the order of the electronics transitions ($S_0 \rightarrow S_1$) and this leads to an increase of the Raman scattering intensity in the order of $10^3 - 10^5$. In the schematic spectrum at the bottom is reported also the intensities normalized to the incident radiation (image inspired by (69)).

2.1.3 Raman scattering intensity and scattering cross section

The radiation intensity of Stokes Raman scattering is proportional to the square of the second derivative of the induced dipole moment (equation 2.14):

$$I_{Stokes} \propto \frac{1}{4} \left(\frac{\partial \alpha}{\partial Q} \right)_{eq}^2 Q_0^2 (\omega_L - \omega_{vib})^4 \cdot I_L \quad 2.20$$

From this equation we can see that the Stokes scattering intensity is mainly influenced by: the 4th power of the scattering frequency: $\omega_{sc} = \omega_L \pm \omega_{vib}$; by the 2nd power of the variation of the polarizability along one specific normal mode and by the incident intensity, I_L .

Here it can be underlined how the intensity of the Raman scattering is influenced by the incoming light through the laser frequency and the laser intensity.

- The choice of the laser power is not so simple since although it is preferable to increase it to have higher signal, there is an upper limit due to other phenomena: the degradation of the material, due to thermal heating, the presence of second order phenomena, more relevant at higher intensity and the possibility of saturation of the CCD camera, especially in the presence of high background signal.
- The choice of the laser frequency, it should be preferable to use low laser wavelength for Raman detection. But it is also important to take into account other two factors in the pump wavelength choice. The presence of fluorescence could cover completely the Raman signal, due to its higher scattering cross section. It should take into account Resonance Raman effect, when the laser photon energy match the electronic transition leading to a further increase of the Raman intensity. For our purpose we should also consider the requirements and limitation of using the waveguide to "deliver" the light and transport back the signal to the detector.

It can be introduced the differential Raman scattering cross section, σ , defined by:

$$\sigma \equiv \frac{\# \text{ photons emitted per unit of time in } \Omega}{\text{incident flux}} \left[\frac{\text{cm}^2}{\text{sr} \cdot \text{molecule}} \right] = \frac{I_{Stokes}}{J} \quad 2.21$$

Where J is the irradiance and Ω is the solid angle. Comparing the two equations 2.20 and 2.21 it is easy to understand the relation:

$$\sigma = \frac{\pi^2 \alpha_{tr}^2}{\varepsilon_0^2 \lambda_s^4} \quad 2.22$$

Where λ_s is the scattered wavelength and α_{tr} is the transition polarizability. Raman scattering cross section will be useful for next chapters.

2.1.4 Raman selection rules and shape of the Raman peaks

With a similar approach of classical theory, knowing that the frequency dependent intensity is obtained by the Fourier transform of the equation 2.14, so it is intuitive the resulting formula:

$$I_{Stokes} \propto \left(\frac{\partial \alpha}{\partial Q} \right)_{eq}^2 \delta(\omega_s - \omega_L + \omega_{vib}) \quad 2.23$$

The conditions for Raman scattering process can be summarized in two points:

- Conservation of energy and of momentum.
- General Raman selection rule: at least one component of the polarizability tensor should change during the oscillation of that mode to be Raman active. These can be evaluated by with group theory, if the polarizability belongs to the same symmetry species of that one of the vibration the mode is Raman active (66).

From equation 2.23 we can see that the expected line shape of the Raman spectrum should be composed by Dirac delta. By the introduction of a dumping factor (i.e. phonon finite lifetime) it leads to Lorentzian shape (66):

$$I_{Stokes}(\omega) \propto \frac{1}{2\pi} \frac{\Gamma}{(\omega - (\omega_L - \omega_{vib}))^2 + \Gamma^2/4} \quad 2.24$$

Where Γ is the full width half maximum (FWHM). At a simple level it corresponds to the inverse of the effective lifetime τ .

Experimentally the peak line shape could be more complex with respect of a simple Lorentzian function (70). It should be taken in consideration that the Raman spectrum is generated by an ensemble of molecules which are interacting with the surrounding. Therefore, each vibrational mode is characterized by a slightly different vibrational frequency and the sum of all the scattering phenomena affect the line shape of the peak. It should be considered that if all the molecules emit incoherently all the signals interfere destructively leading to no signal. Therefore, what we have introduced as effective lifetime τ it is composed by two contributions: amplitude correlation lifetime τ_a , i.e. the lifetime of the excited state, and the coherence lifetime τ_c , i.e. the time after which the vibrations lose their coherence. We can now distinguish three different cases:

- If $\tau_a \gg \tau_c$ the coherence is lost more rapidly, and it is the dominant loss mechanism. This is the case of gases and the resulting line shape, as already mentioned, is Lorentzian (70).
- If $\tau_a \ll \tau_c$ the main loss process is related to relaxation of the molecules. This model is suitable for solids and due to the statistical distribution of the environments, the peak has a Gaussian profile (70).
- Liquids are in between these two limiting cases and their line shape is mostly described by a combination of Gaussian and Lorentzian profile, such as Voigt profile. The Voigt profile is characterized by 4 parameters: the first three are in common with the other

curves (location, height and line width of the peak), the 4th parameter specifies the Lorentzian character.

It is worth to differentiate the Raman spectra of amorphous materials and crystalline ones. As reported by Shuker and Gammon (71) the distinction between them is the extension of the correlation length compared to the wavelength of light. The lack of translational symmetry in amorphous materials results in a relaxation of the crystal momentum selection rule. For solids the Raman scattering involves the center of the Brillouin zone but for amorphous materials the spectrum is influenced by the phonon density of states of the band ($G_b(\omega)$) as shown in the formula:

$$I_{Stokes}(\omega) = \sum_b \frac{n(\omega) + 1}{\omega} C_b(\omega) G_b(\omega) \quad 2.25$$

Where $C_b(\omega)$ is the coupling factor related to the band b and $n(\omega)$ gives the number of phonons.

One peculiarity of glasses is the presence of the so-called Boson peak (72). The peak is asymmetric and, more importantly, seems to have a universal shape for many different glasses, when normalized by peak position and height (73). An example of the boson peak is reported in Figure 17 in can be seen the spectrum of a-SiO₂ characterized by the Boson peak at wavenumbers lower than 200 cm⁻¹.

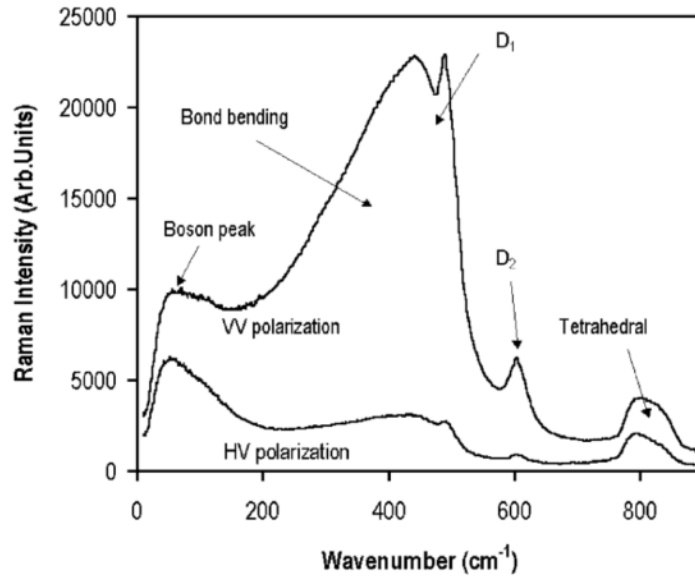


Figure 17 Characteristic features in the polarized Raman spectra of a-SiO₂ (73). The peaks D1 and D2 are the defects bands.

Recently, in the article (60) it was discussed the origin of an exponential decreasing line shape Raman spectrum coming from a-SiN, $S_{SiN}(\Omega)$. The main result from this publication was:

$$S_{SiN}(\Omega) = 4\pi^2 A_0^2 \langle \delta n^2 \rangle \frac{Ll}{\lambda_0^2} \frac{l^2}{l^2 + 2W^2} \tau e^{-\tau|\omega|} \quad 2.26$$

With:

- $\langle \delta n^2 \rangle$ is composed by the refractive index fluctuation, δn , associated to the temperature fluctuation in the material. It can be estimated by: $\langle \delta n^2 \rangle = \left(\frac{\partial n}{\partial T} + n_\phi \alpha_L \right)^2 \langle \delta T^2 \rangle$. With n_ϕ the effective index, α_L the linear thermal expansion coefficient.
- L is the length of the WG.
- A_0 is the amplitude of the electromagnetic mode propagating with a wavelength λ_0 .
- l is the characteristic length at which the fluctuation occurs. For a-SiN was calculated that $l \in [145; 300]nm$ (60).
- W is the radial half-width of a gaussian approximated mode profile.
- τ is the characteristic time associated to the power spectrum line shape and it influences the exponential decay of $S_{SiN}(\Omega)$. It can be calculated form:

$$\tau = \frac{\sqrt{l^2 + 2W^2}}{\sigma_v \sqrt{2}} \quad 2.27$$

the dynamics of the fluctuations of the refractive index field follows a Gaussian probability distribution function, with a standard deviation σ_v (60). It has been estimated a value of $1.3 \cdot 10^{-3} \mu m/fs$ (60).

The major hypothesis for equation 2.26 are (27):

- negligible losses of the WG. Otherwise, it should be considered a correction factor for the power collected.
- The propagating electromagnetic field overlaps with all the medium. This is valid for strip WG, but for more complex shape as the slot WG this assumption does not hold any more.
- The viscous effects are neglected by cancelling the viscous pressure tensor of the medium. This could have an impact on the correlation length l (27).
- The polarization due to the interaction with the pump power does not perturb the random heat flux dynamics. This assumption is valid only for coupled continuous power of few milliwatts.

Figure 18 is an example of the exponential decreasing line for two different laser pump wavelengths: 785 nm and 633 nm.

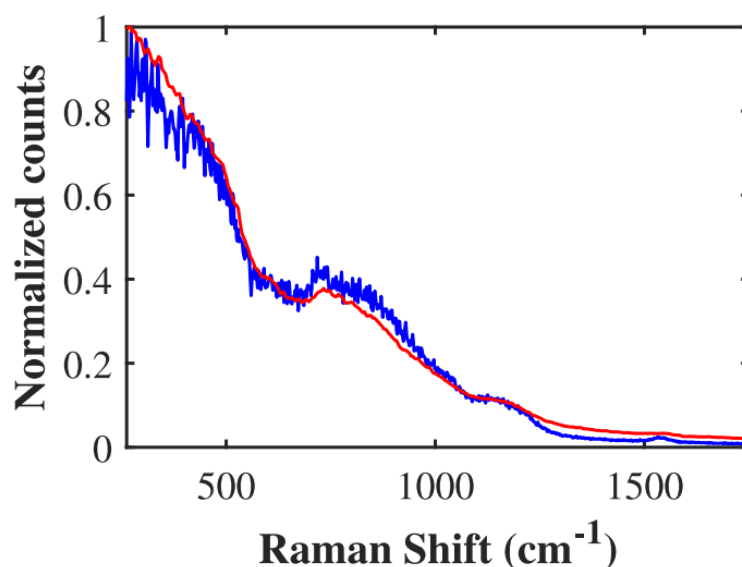


Figure 18: a-SiN background Raman signal coming from a WG with different pump laser wavelength: 633nm in blue and 785 nm in red. The plot is taken from (44).

2.2 Some basis of waves in the waveguide: optical confinement

The term optical waveguides (WG) it is referred to any structure capable of confining and guiding an electromagnetic radiation in the wavelength of the light (74, 75). Of our interest are the amorphous silicon nitride (a-SiN) waveguides patterned on an amorphous silicon dioxide (a-SiO₂) thermally grown on a Si wafer (an example is reported in Figure 19 of a strip WG).



Figure 19: scheme of the cross section of strip WG (translationally invariant on the not shown direction). The refractive index of the WG made by a-SiN is $n_w = 1.852$, then we distinguish two region s: the cladding (n_c : H₂O = 1.3296 PMMA = 1.4850281701926) and the substrate (if SiO₂ $n_s = 1.454$).

2.2.1 WG modes

In ray optics the confinement of light in WGs is based on the phenomena of total internal reflection (TIR). The light is trapped in the WG only if the incident angle at the interface between two transparent materials is lower than the critical angle θ_c . The critical angle can be obtained from the Snell law and it results in the first condition to have guided light: $n_w > n_c$ & $n_w > n_s$. To have a propagating wave, a second condition should be satisfied: phase matching. This condition considers different paths of the ray light with same wavelength in the WG, to have propagation constructive interference should occur (Figure 20).

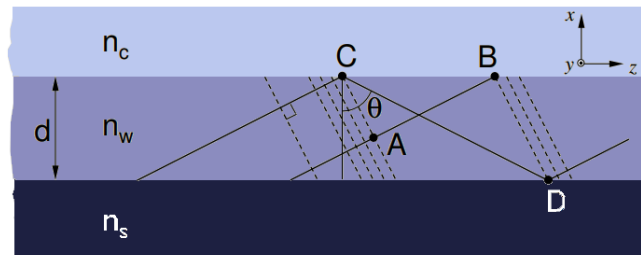


Figure 20: lateral view of a WG and representation of two confined waves in the ray theory. To have propagation, the phase shift related to AB segment should be equal to that on related to CD segment (considering the phase shift due to reflection).

Combining these two conditions it follows that only a discrete number of so-called modes are allowed into the WG. These modes are characterized by their wavelength λ , polarization and wavevector β . It exists a frequency cut-off below which no modes are allowed in the WG given by $k_0 n_s$ (if $n_s > n_c$), with $k_0 = 2\pi/\lambda$ is the vacuum wavenumber. Therefore, to have confinement and propagating mode two conditions should be respected (if $n_c < n_s$):

$$\begin{cases} \theta_c < \theta < \pi/2 \\ k_0 n_s < \beta < k_0 n_w \end{cases} \quad 2.28$$

The second condition can be rewritten in terms of effective index ($n_{eff} = \beta/k_0$): $n_s < n_{eff} < n_w$.

In order to compute the waveguide modes in a more rigorous way a electromagnetic treatment is needed. This can be achieved by using the Finite Difference Eigenmode solver (or FDE solver) in Lumerical software, based on the theory exposed by Zhaoming Zhu and Thomas G. Brown in their paper (76).

The program solves the Maxwell's equations at a single frequency with no sources:

$$\nabla \times \vec{E} = -\frac{\partial \vec{B}}{\partial t} \quad 2.29$$

$$\nabla \times \vec{H} = \frac{\partial \vec{D}}{\partial t} \quad 2.30$$

For isotropic and linear medium: $\vec{D} = \epsilon \vec{E}$ and $\vec{B} = \mu \vec{H}$. Assuming the fields have dependence:

$$E, H \sim \exp[i(\beta z - \omega t)] \quad 2.31$$

From the differential equations 2.29 and 2.30, after some algebra, we obtain an eigenvalue equation in terms of transverse electric fields:

$$\begin{bmatrix} P_{xx} & P_{xy} \\ P_{yx} & P_{yy} \end{bmatrix} \begin{bmatrix} E_x \\ E_y \end{bmatrix} = \beta^2 \begin{bmatrix} E_x \\ E_y \end{bmatrix} \quad 2.32$$

$$\begin{bmatrix} Q_{xx} & Q_{xy} \\ Q_{yx} & Q_{yy} \end{bmatrix} \begin{bmatrix} H_x \\ H_y \end{bmatrix} = \beta^2 \begin{bmatrix} H_x \\ H_y \end{bmatrix} \quad 2.33$$

The solver creates a 2D rectangular mesh to discretize the cross section of the waveguide, therefore E_i , P_{ij} and Q_{ij} are matrices. P_{ij} and Q_{ij} matrices depend by the mesh size Δx and Δy , by the boundary conditions and the materials property (i.e. the dielectric permittivity). Although they also depend by the $k_0 = 2\pi/\lambda$. For further information about P_{ij} and Q_{ij} matrices can be found in (76).

By solving the equations 2.32 and 2.33 we obtain the mode profiles E and H and the propagation constant of the mode, β . Furthermore, the fields are normalized such as the maximum electric field intensity, $|E|^2$ is 1.

For a WG the guided modes ($\vec{E}_m; \vec{H}_m$) are evaluated. If two different WGs are connected, it is possible to evaluate the losses associated to the change in guiding modes (77). This can be achieved by using the overlap function, which measures the fraction of electromagnetic field that overlap between two fields profiles, which correspond to the fraction of power that is converted from the incoming mode (P_{in}) to mode(m) (P_m). The overlap function is given by:

$$\frac{P_m}{P_{in}} = Re \left[\frac{(\int \vec{E}_m \times \vec{H}_{in}^* \cdot d\vec{S})(\int \vec{E}_{in} \times \vec{H}_m^* \cdot d\vec{S})}{\int \vec{E}_m \times \vec{H}_m^* \cdot d\vec{S}} \right] \frac{1}{Re(\int \vec{E}_{in} \times \vec{H}_{in}^* \cdot d\vec{S})} \quad 2.34$$

Where $Re(\int \vec{E}_{in} \times \vec{H}_{in}^* \cdot d\vec{S}) \cdot \frac{1}{2} = P_{in}$. The calculation of the electric field mode profile it will be useful to evaluate the integrated-luminosity of the waveguide coefficients, which we will see it is an important parameter in the photonics for Raman application field.

2.2.2 WG losses

Each wave that propagates in the region of a WG can be described as a superposition of the solutions of the wave equations, which can be subdivided in the guided mode (\vec{e}_m) and the radiative modes (\vec{e}_R):

$$\vec{E}(x, y) = \sum_m a_m \vec{E}_m(x, y) + \int_0^\infty a(\beta) \vec{e}_R(\beta; x, y) d\beta \quad 2.35$$

In which a_m and $a(\beta)$ are the modal coefficients. The excitation of the radiative or lossy modes results in power loss and it is typically associated to the presence of discontinuities in the WG.

Assuming a weak attenuation, the power loss of a waveguide of length L can be written as:

$$\frac{I_{out}}{I_{in}} = \exp(-\alpha L) \quad 2.36$$

Where α is the loss coefficient in cm^{-1} . Usually, α is reported in dB/cm the conversion factor is: $cm^{-1} = 0.23 \cdot dB/cm$.

The loss coefficient can be described as separated in three components (78):

$$\alpha = \alpha_a + \alpha_R + \alpha_b \quad 2.37$$

Which are: α_a absorption loss, α_R , radiation loss and α_b backscattered loss.

Absorption loss, α_a . It is determined by the type of material used. For silicon nitride core WG the absorption losses are negligible if compared to other losses.

Radiation loss, α_R , takes into account all the possible phenomena in which part of the power is coupled with radiative modes (Figure 21). It is influenced by the refractive index contrast $\Delta n = \frac{n_{core} - n_{clad}}{n_{core}}$. We can distinguish different origin: scattering losses, losses related to WG bends.

Scattering losses, originated by not homogeneous refractive index of the WG. In the bulk of the WG it can be originated from contamination, voids, and density discontinuity (like crystalline domains). The major contribution is given by the surface scattering losses originated by the surface roughness. These losses influenced by the fabrication process. There are many models proposed to describe scattering losses (64, 79, 80). The n_w model (78) has the advantage to highlight the interaction between the sidewall roughness and the modal field. It is given by:

$$\alpha_R = A \frac{\partial n_{eff}}{\partial w} \quad 2.38$$

Where w is the WG width and n_{eff} is the effective refractive index, given by $n_{eff} = \beta/k_0$. This model considers “how easily” the guided modes couples out to radiative modes. It neglects the losses associated to top and bottom scattering of the WG, this is usually true due to the much lower roughness of these two surfaces compared to the lateral one. The side wall roughness is heavily affected by the etching step after the deposition of the thin film of the core material for the WG. The n_w model is in well accordance with Lacey and Payne model (79). In n_w model it is supposed that the side wall roughness can be described with an exponential correlation function $R(z) = \sigma^2 \exp(-z/L_c)$ where σ is the root mean square roughness and L_c is the correlation length, above which the surface profile is random. The factor A is WG width independent if sufficiently far from the mode cut-off (78). A coefficient takes into account the side wall roughness and the wavelength influence. A coefficient formula has been well rewritten by Wang et al. (81):

$$A = \sigma^2 L_c k_0^2 \frac{n_{core}^2 - n_{clad}^2}{n_{core}^2} n_{eff} \tilde{f} \quad 2.39$$

$$\tilde{f} = \sqrt{\frac{\sqrt{y} + 1 - L_c^2 k_0^2 (n_{eff}^2 - n_{clad}^2)}{y}} \quad 2.40$$

$$y = \left(1 + L_c^2 k_0^2 (n_{eff}^2 - n_{clad}^2)\right)^2 + 16 L_c^2 k_0^2 n_{clad}^2 \quad 2.41$$

Where $k_0 = 2\pi/\lambda_p$ is the vacuum wavenumber, n_{eff} is the effective refractive index, L_c is the correlation length and σ is the root mean square roughness (Figure 21), n_{core} and n_{clad} are the core and cladding refractive indexes respectively.

Losses related to WG bends. The bending losses are influenced by the bend radii:

$$\alpha_{R-bend} = \frac{C_1}{\sqrt{R}} e^{-C_2 R} \quad 2.42$$

Where C_2 increases (i.e. α_{R-bend} decreases) if the index contrast increases and if the WG width increases (for a slab WG). New types of bends using hybrid circular and seminatural spline shapes curves (82) or simulation-based inverse design geometries (83) have been developed.

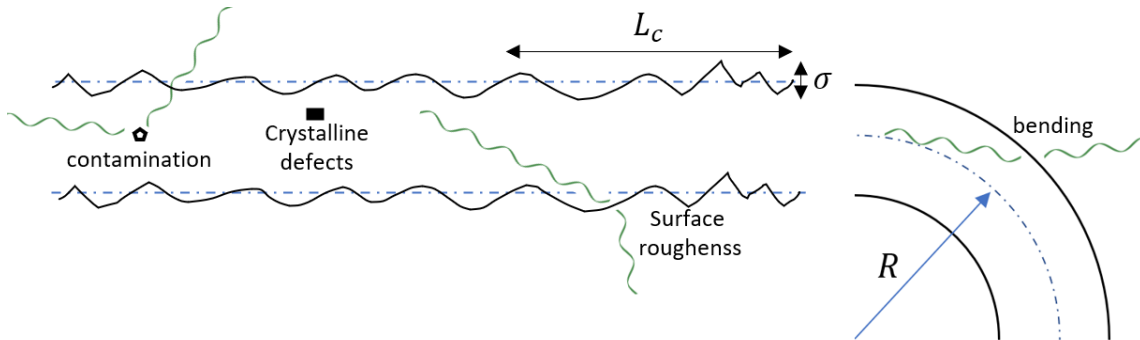


Figure 21: representation of many possible radiation losses in the WG due to contamination, crystalline defects, surface roughness and bending (R is the bending radius). A model for describing surface roughness is given by the exponential correlation function: $h(z) = \sigma^2 \exp(-z/L_c)$ where σ is the standard deviation of the surface with respect to the mean line (blue dotted line on the left figure) and L_c is the correlation length, above which the surface profile is random. L_c and σ are shown in the figure.

Backscattered losses, α_b . A fraction of the power is coupled into the guiding mode with opposite propagation direction. This loss type is still originated by sidewall roughness, but it is much less relevant with respect to radiation losses: $\alpha_b \approx 10\% \alpha_r$ (78). The n_w models can describe this type of loss:

$$\alpha_b = B \left(\frac{\partial n_{eff}}{\partial w} \right)^2 \quad 2.43$$

Where B factor expression can be found in D. Melati et al. paper (80).

It is interesting to introduce now the working principle of the device studied. It consists in an a-SiN WG on a a-SiO₂ substrate which delivers power to a sample in the cladding region (Figure 22). The interaction is through the evanescent tail of the guided modes. Then the inelastically scattered light by sample is coupled back into the WG. Therefore, the fraction of light that is recorded represents the inelastic scattered light losses.

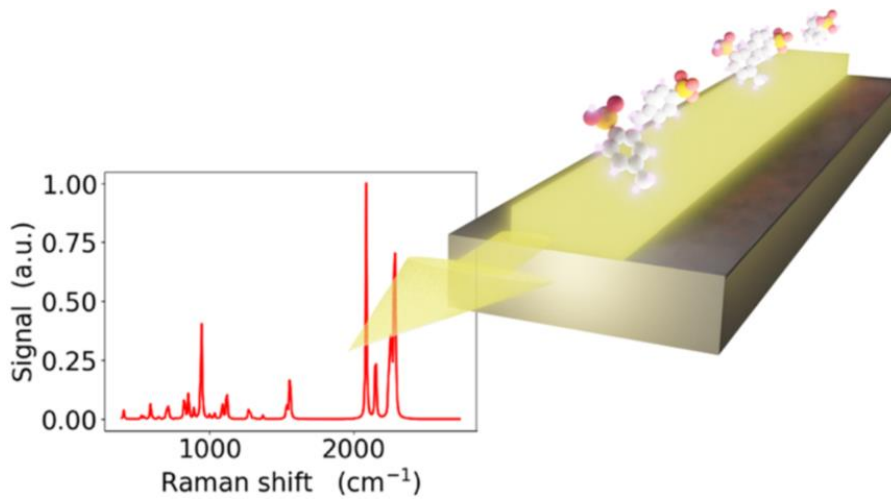


Figure 22: schematic working principle of WERS (23).

On the other hand, side wall roughness produces scattering losses, therefore the power guided in the WG decreases along the WG. It can be seen like a molecule that is excited consequently emits light. In some papers (84, 85) is reported this analogy where the side wall roughness can be described by an oscillating dipole. It is an interesting point of view, if compared to that one given by the n_w model, in which the roughness is seen as a change of WG width that results in coupling with radiative modes.

2.3 Signal collection by a WG

It will be introduced the main equations at the basis to describe the experimental data. In chapter 2.3.1 describes the signal collection of the WG from a single molecule. In chapter 2.3.2 it will be considered the overall contribution of the scattered power collected from all the waveguide with length L . At the end the difference between a backscattered and forward scattered collection system is explained.

2.3.1 One molecule scattering

This theoretical approach was proposed by Ashim Dhakal et al. in their paper (56). We consider a molecule at position \vec{r}_0 near or inside a single mode waveguide as represented in the figure below (Figure 23).

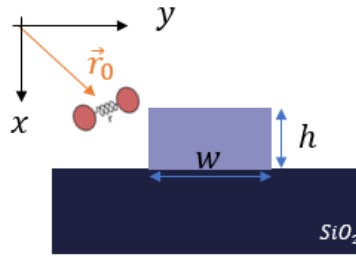


Figure 23: scheme of a α – SiN strip WG on SiO_2 substrate and a diatomic molecule in harmonic approximation.

Taking into consideration the process of excitation of the molecule by the guided electric field (with power P_{in}), the subsequent emission by the excited molecule (at frequency ω_s) and the coupling back of the light into the WG, we can evaluate the power collected into the waveguide, $P_{wg}(\vec{r}_0, \omega_s)$ by:

$$P_{wg}(\vec{r}_0, \omega_s) = \Lambda_{wg}(\vec{r}_0, \omega_p, \omega_s) \sigma(\omega_p, \omega_s) P_{in} \quad 2.44$$

Where $\sigma(\omega_p, \omega_s)$ is the scattering cross section at a given pump frequency ω_p and Λ_{wg} as the integrated-luminosity of the WG:

$$\Lambda_{wg}(\vec{r}_0, \omega_p, \omega_s) = \frac{\lambda_s^2 \cdot n_g(\omega_p) n_g(\omega_s)}{\tilde{A}_{eff}(\vec{r}_0, \omega_p) \tilde{A}_{eff}(\vec{r}_0, \omega_s) n(\omega_s)} \quad 2.45$$

It gives a measure of the fraction of power scattered back to the waveguide for a given particle in its surrounding taking into account the WG enhancement effects (56). It is influenced by the scattered wavelength (λ_s), the group index of the WG (n_g), the refractive index of the medium where the scattering particles are located n and the effective mode area at the molecule position given by:

$$\tilde{A}_{eff}(\vec{r}_0, \omega_p) \equiv \frac{\int \int_{\infty} \varepsilon(\vec{r}, \omega_p) |\vec{E}_m(\vec{r}, \omega_p)|^2 d\vec{r}}{|\vec{e}_d(\vec{r}_0) \cdot \vec{E}_m(\vec{r}_0, \omega_p)|^2} \quad [\text{m}^2] \quad 2.46$$

With $\varepsilon(\vec{r}, \omega_p)$ the relative dielectric constant and $\vec{E}_m(\vec{r}_0, \omega_p)$ is the electric modal field. The index m stays for the mode number. The mode area is a quantitative measure of the area which a

waveguide mode effectively covers in the transverse dimension. It is obtained by the integrated energy density divided by the maximum energy density (86). In this case we call it effective mode area since its definition is slightly different. At the denominator in equation 2.46, instead of the maximum energy density position, the molecule position \vec{r}_0 and the orientation vector $\vec{e}_d(\vec{r}_0)$ of their dipole moment are considered.

2.3.2 Ensemble of particles

Now we should consider the presence of a random ensemble of particles emitting incoherently (Figure 24). It is important to underline that the Raman signal of interest is generated from the cladded area, but it is collected the signal coming from the $a - SiN$ core WG and the $a - SiO_2$ substrate too.

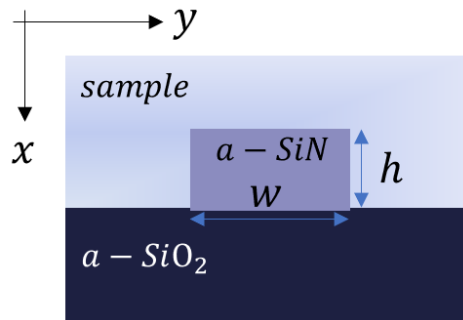


Figure 24: Strip waveguide made by amorphous silicon nitride with uniformly distributed molecules in the cladding.

In a similar treatment done in the article (58) we are going to evaluate the power collected in the WG in a region dz :

$$\frac{dP_{col}(\omega_s)}{P_{in}} \equiv \frac{1}{2} dz \sigma \rho \iint \Lambda_{wg}(\vec{r}, \omega_p, \omega_s) d\vec{r} \quad 2.47$$

In which the $\frac{1}{2}$ is introduced since in our set up we record only the backward light (considering the direction of propagation of the light z). This implies the consideration that the backward and forward direction collect equally amount of scattered light, and this is reasonable thanks to the isotropic nature of the dipole emission (58). In the formula $\rho \left[\frac{\text{molecule}}{\text{cm}^3} \right]$ is the molecules density.

We can define the Raman conversion efficiency as:

$$\eta_i \equiv \iint_{S_i} \Lambda_{wg}(\vec{r}, \omega_p, \omega_s) d\vec{r} \quad 2.48$$

Which is a characteristic parameter related to the geometry of the waveguide, the excitation line, the scattered frequency, and the integration area over which the analyte is present S_i (of our interest are the N_2 , $a - SiN$ in the WG core or the sample in the cladded area). The unit of measure of η_i is in sr .

Therefore, the total power collected is given by:

$$\frac{P_{col}}{P_{in}} \equiv \int_L \frac{1}{2} \sigma \rho \eta_i f(\alpha, z) dz \quad 2.49$$

Where $f(\alpha, z)$ is a function of the losses of the waveguide and L is the detection length.

By considering η_i not dependent by the waveguide length (i.e. the detection region has constant modal properties), the total power collected from the objective is:

$$\frac{P_{col}(\omega_s, L)}{P_{in}} \equiv \xi = \frac{1}{2} \rho \sigma \eta_i \cdot LF_j \quad 2.50$$

We have defined the ratio power collected over guided power as ξ and it is a measure of the collection efficiency of Raman signal by the waveguide. In particular:

- $\rho \sigma$ product is dependent by the analyte and its concentration, and the scattering cross section is dependent by the scattered frequency for Raman signal.
- $\eta_i = \eta_i(S_i, \omega_p, \omega_s)$ depends by the pump frequency as well as the scattered one, but it considers the design of the waveguide (geometry and cladding material, i) and detection area too (S_i).
- The last term $LF_j(\alpha_s, \alpha_p, L)$ is the length factor which is influenced by the length of the detection region, L , and the losses due to the propagation of the scattered and pump light, α_s and α_p . It is also influenced by the experimental set up which determines where the collection occur (forward, LF_f or backward collection, LF_b or both).

In previous work (44) it has been shown the difference in the backward and forward collection, that is shown in Figure 25. In our set up we collect light in backward configuration. It is important to understand the difference between these two designs, therefore I will briefly describe them.

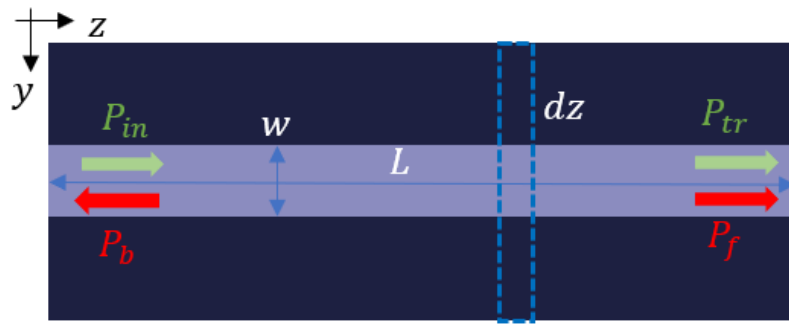


Figure 25 zy sketch of a generic waveguide of length L and width w . In a backward configuration we collect the power, P_b , from at the same side of the incoming power, P_{in} . At the end of the WG it can be collected the transmitted power P_{tr} and the forward Raman scattered signal P_f .

For backward collection, the length factor is:

$$LF_b = \int_0^L e^{-\alpha_p z} e^{-\alpha_s z} dz = \frac{1 - e^{-(\alpha_p + \alpha_s)L}}{\alpha_p + \alpha_s} \quad 2.51$$

On the other hand, for the forward collection, the length factor is:

$$LF_f = \int_0^L e^{-\alpha_p z} e^{-\alpha_s(L-z)} dz = e^{-\alpha_s L} \frac{1 - e^{-(\alpha_p - \alpha_s)L}}{\alpha_p - \alpha_s} \quad 2.52$$

A reasonable consideration is that the two loss coefficients are almost equal, $\alpha_s(\omega_s) \approx \alpha_p(\omega_p)$, since $\omega_s \approx \omega_p$. Therefore, we can simplify the two previous equations as:

$$LF_b = \frac{1 - e^{-2\alpha L}}{2\alpha} \quad 2.53$$

$$LF_f = L e^{-\alpha L} \quad 2.54$$

Where $\alpha = (\alpha_s + \alpha_p)/2$, typical values for α for uncladded waveguides $\alpha_{air} \in [0.5, 5] \text{ dB} \cdot \text{cm}^{-1}$ and for SiO_2 cladding $\alpha_{\text{SiO}_2} \in [0.1, 1.5] \text{ dB} \cdot \text{cm}^{-1}$ (87). If we convert in exponential units:

$$\alpha_{air} \in [0.12, 1.15] \text{ cm}^{-1} \quad \alpha_{\text{SiO}_2} \in [0.02, 0.35] \text{ cm}^{-1}$$

The difference between forward and backward collection can be seen comparing these two equations, and it is well shown in Figure 26. As we can see the backward collection at increasing the length of the WG the LF_f goes to a plateau equal to $1/2\alpha$. On the other hand, in forward collection configuration there is an optimal length to maximize the length factor.

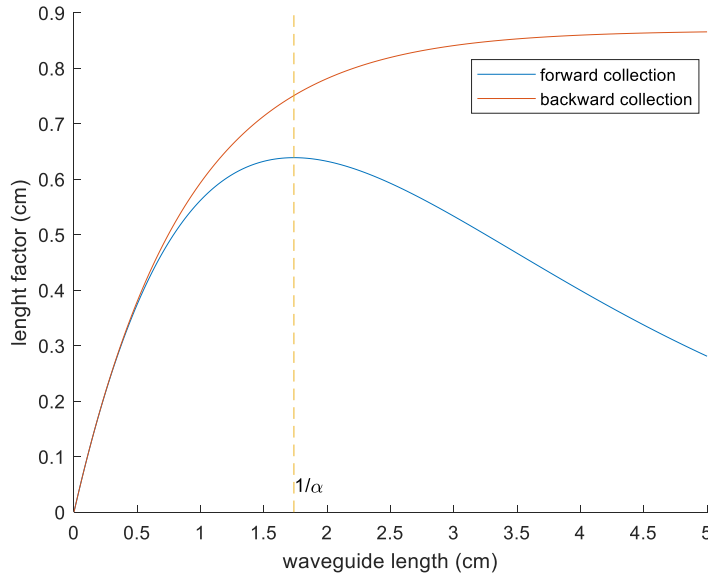


Figure 26 length factor in function of the waveguide length with $\alpha = 2.5 \text{ dB} \cdot \text{cm}^{-1}$. It is also reported $1/\alpha$ line which correspond to the saturation limit or maximum LF for respectively the backward and forward collection.

The length factor for the backward collection should be maximized taking into account possible drawbacks of infinite extended WG, like costs for example, but to have a rule of thumb if $L = 1/\alpha$ the $LF_b(L = 1/\alpha) = 85\% LF_b(L \rightarrow \infty)$ and for $L = 2/\alpha$ the length factor is almost equal to its plateau value. We define $1/\alpha$ as saturation length above which an increase of L has an almost negligible impact on the increase of the length factor.

2.4 Intensity collected by the CCD camera

In the end it is useful to introduce some parameters to evaluate the actual signal given by the spectrum in counts per unit time (CCD/s). Therefore, it should be considered all the losses due to the coupling efficiency γ , the losses in the microscope optics, T_{MO} (the presence of the pinhole and filters) and the spectrometer transmissions, T_{spec} (this approach is similar in the appendix of (65)). The Stokes power reaching the detector surface is given by:

$$P_{DS} = \gamma_{in}(\omega_p, \vec{r}_{obj}) \cdot \gamma_{out}(\omega_s, \vec{r}_{obj}) \cdot T_{MO} \cdot T_{spec} \cdot \xi \cdot P_{pump} \quad 2.55$$

Here it has been introduced $\gamma_{in}(\omega_p, \vec{r}_{obj})$ and $\gamma_{out}(\omega_s, \vec{r}_{obj})$ which are the coupling coefficients between the WGs modes and the laser beam coming from the objective and coming out from the WG. They depend by the pump and scattered frequency ω_p and ω_s but also by the relative position in xy plane of the objective with respect to the waveguide cross section \vec{r}_{obj} (Figure 27).

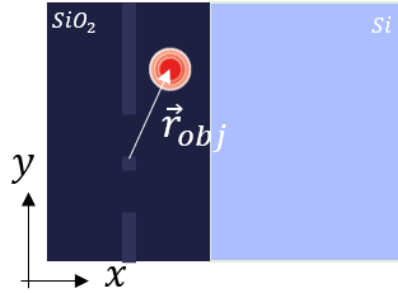


Figure 27: schematic of the xy plane of the chip, i.e. the cleaved face. The lighter blue is Si, then the SiO_2 is the darkest blue and then there is the $a-SiN$ waveguides. The vector \vec{r}_{obj} connects the $a-SiN$ WG to the laser spot.

Now we should correlate the P_{DS} with the CCD counts per second (C_s/t) which is given by:

$$P_{DS} = \frac{C_s}{t} \cdot \frac{hc}{\lambda_s} \cdot \frac{\psi}{QE(\lambda_s)} \quad 2.56$$

Where $QE(\lambda_s)$ is the quantum efficiency of the detector (number of electrons/photon) and ψ is the CCD sensitivity (number of electrons/count). Combining the two equations we get:

$$\frac{C_s}{t} = \xi \cdot \frac{\lambda_s}{hc} \cdot P_{pump} \cdot \gamma_{in} \cdot \gamma_{out} \cdot T_{MO} \cdot T_{spec} \cdot \frac{QE(\lambda_s)}{\psi} = \xi \cdot C_{ext} \quad 2.57$$

Where C_{ext} collects all the external factors of the signal collection not associated to the chip. ξ is the collection efficiency of the waveguide.

3 Materials and methods

3.1 Confocal Raman microscope

For the analysis we have used the Witec R300 confocal Raman spectrometer, Figure 28. It combines a highly efficient Raman spectrometer with high resolution confocal optical microscope. The main components are (88):

- Multi-mode optical fiber (core diameter: $50\mu\text{m}$ for 633nm laser and $100\mu\text{m}$ for 785 nm laser) (E1)
- Single-mode optical fiber with polarization maintaining (E2)
- Laser (E3)
- Spectrometer and CCD detector (E4)
- XY positioner (U1)
- Scan stage (U2)
- Objective turret with objectives (U3)
- Binocular tube with ocular camera (U6)
- Fiber coupling unit optical output (U8)
- Filter slider unit (U10)
- Microscope Z stage with stepper motor (U14)

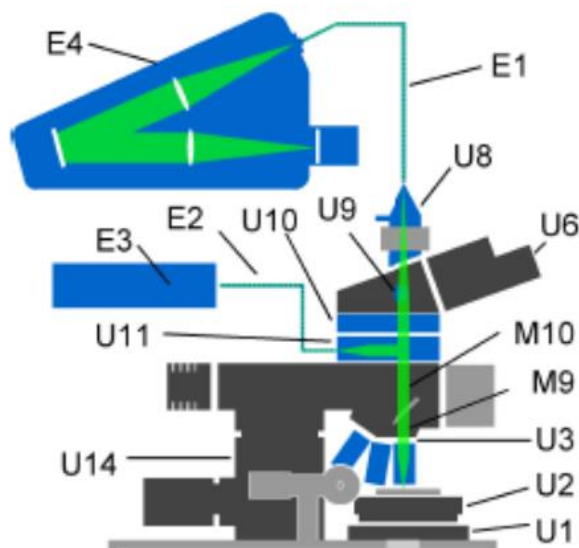


Figure 28 Schematic illustration of the beam path for Confocal Raman Microscopy in green (88). The main components are highlighted in blue. Scattered and pump light are unfortunately shown with the same colour: green.

The working principle of this Raman spectrometer is composed by the laser generation and delivery to the sample through the single-mode polarization maintaining optical fiber. The scattered light is collected by the objective and the Rayleigh component is filtered out by a notch filter. Then the light is coupled in the multi-mode optical fiber (confocal microscope) that deliver the signal to the spectrometer and CCD detector (Charged Coupled Device).

It is also possible to switch to camera mode to inspect the sample with a white lamp. In this case the notch filter is removed, and the light is delivered to the binocular tube with ocular camera.

The available **laser** are reported in the table below:

Table 1 laser property.

Laser	Wavelength	Fiber power
Diode laser	785 nm	>200mW
HeNe	633 nm	>10mW

Spectrometer: it has a Czerny Turner design (Figure 29) composed by two reflecting mirrors and a diffracting grating. The spectral resolution in a dispersive Raman spectrometer is determined by four main factors:

- Spectrometer focal length (the distance between the dispersing grating and detector): if longer the spectral resolution is higher (from 200 mm, for low/medium resolution, to 800 mm, for high resolution).
- Diffraction grating: it is characterized by the groove density (measured as number of grooves per millimeter, gr/mm). Typical gratings used for Raman vary from 300 gr/mm (low resolution) through to 1800 gr/mm (high resolution).
- Laser wavelength: the spectral resolution decreases as the laser excitation wavelength decreases.
- Detector: composed by pixel. The smaller the pixel the higher the achievable spectral resolution.

In our current instrumentation with 785nm and 633nm lasers with grating groove density of 600 g/mm the spectral resolution is respectively 1.18 and 1.98 cm^{-1} (focal length of 400 mm for 785nm laser).

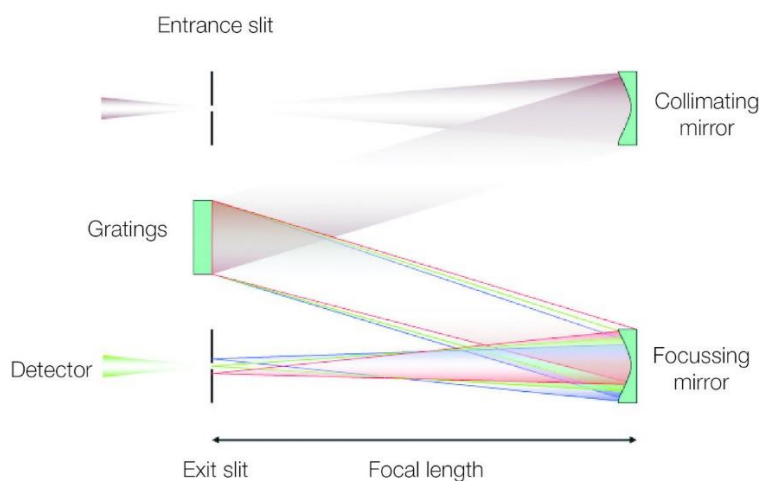


Figure 29: Czerny Turner design (89).

Detectors: there are two detectors for NIR and VIS ranges. Both detectors are back-illuminated CCD. A CCD consists in an array of photosensitive elements, each radiation of a certain wavelength hits the CCD at different and determined positions to obtain the sample spectrum. The back-illumination design involves the removal of the bulk silicon substrate, allowing direct exposure of the active photosensitive region to the incoming photons (more info refers to (90, 91)).

It is reported below a well written explanation of the noise associated to a CCD camera taken from the Witec manual (88). The sources of noise in the CCD camera are:

- The shot noise. It is the ultimate limitation in the reduction of the noise. The origin of the shot noise comes from the statistic of the photons detected by the CCD camera: Poisson statistic. The shot noise corresponds to the square root of the signal.
- Thermally generated carriers within the CCD chip are responsible for the dark noise. These can be reduced through efficient cooling and high-quality CCD cameras will have a thermal dark current below 0.01 electrons/pixel/s at -60 °C (88).
- The read-out noise is associated to the process of conversion of electrons into digital counts. It is directly linked to the read-out speed used (88). The read-out noise can be decreased by increase of the integration time. However faster Raman collection spectra are desirable, especially in confocal Raman imaging. For example: *"if a readout noise of 10 electrons is assumed, every signal below 100 electrons/pixel will be readout limited (Poisson noise = readout noise)"* (88).

Objective turret with objectives can hold up to 5 objectives and has a positioning repeatability better than $2\mu m$. For a confocal system, if the pinhole radius is set smaller than Airy disk, the XY spatial resolution can be calculated by (92):

$$d \approx 0.8 n \frac{\lambda}{NA}$$

For a confocal system, the pinhole only allows light from a much shorter vertical distance to pass through to the detector so the depth of field (*d. o. f.*) can be calculated by:

$$d. o. f \approx 1.4 n \frac{\lambda}{NA^2}$$

Where NA is the numerical aperture, λ is the laser wavelength and n is the refractive index of the medium between the objective and the sample.

The possible objectives available and their specifics have been calculated and reported in Table 2.

Table 2: summary of the objective specifications for confocal Raman.

<i>magnification</i>	NA	Working distance	Spatial resolution (μm)		Depth of focus (μm)	
			633nm	785nm	633nm	785nm
100x	0.9	0.31mm	0.6	0.7	1.1	1.4
50x	0.7	0.95 mm	0.7	0.9	1.8	2.2
40x	0.65	0.6 mm	0.8	1.0	2.1	2.6
10x	0.25	9 mm	2.0	2.5	14	18

The microscope is connected to a camera which allows to observe the image of the sample on the screen if the shutter is open. A lamp allows the correct illumination of the focused zone.

XY positioner (or manual stage) is positioned under the piezoelectric scan stage and two micrometres are used to move the sample. The main properties are sum up in Table 3. It is important to underline the internal coordinate system of the positioner in Figure 30.

Scan stage (or piezo-stage) mounted on XY positioner uses a piezoelectrically driven 3-axis flexure stage to scan the sample. The flexures provide zero stiction, friction or backlash, combined with ultra-high resolution and exceptional guiding precision (88).

Table 3 xy positioner and scan stage properties.

<i>property</i>	Xy positioner	Scan stage
<i>XY travel and resolution</i>	20 mm ($<1\mu\text{m}$)	100 μm ($<1\text{nm}$)
<i>Z travel and resolution</i>	/	20 μm ($<0.1\text{nm}$)
<i>graduation</i>	5 μm	/
<i>Backlash</i>	$<5\mu\text{m}$	no
<i>Maximum load</i>	400 N	50 N

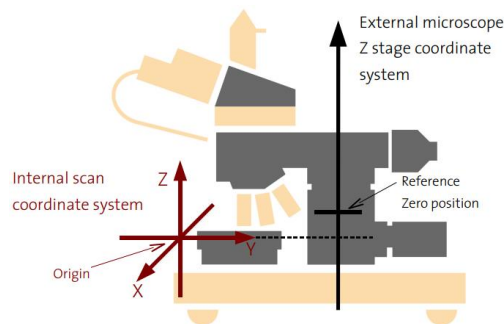


Figure 30 Internal and external coordinate systems in WITec Control (88).

3.1.1 Working principle confocal Raman microscope

In this section, a brief theoretical background of the confocal microscopy will be provided and it is mainly based on the book (92).

The main innovation of a confocal microscopy is the introduction of a spatial pinhole to block out-of-focus light in image formation, which is illustrated in Figure 31a. The laser beam passes through a beam splitter with high reflectivity at the non-design wavelengths. A microscope objective focusses the incident beam into the sample, the spatial extension of the focus spot, for a gaussian beam, is given by the Airy disk on the sample:

$$D = 1.22 \frac{\lambda}{NA}$$

which is determined by the wavelength λ and the numerical aperture NA of the objective. The image spot is then focused through the same lens onto the pinhole, which in our case is given by the fiber section itself. The pinhole removes the aberrations in the beam, filtering them out as shown in the sketch in Figure 31b. Therefore, light collected at the detector comes from the focal plane.

The main advantages are:

- the increased image contrast and with a proper selection of the pinhole size, thanks to the reduced depth of focus (i.e. axial resolution).
- Additionally, by choosing an appropriate pinhole diameter, the lateral resolution can be increased by up to a factor of $\sqrt{2}$.

This leads to the possibility of three-dimensional imaging of the sample. This is not possible in conventional microscopy.

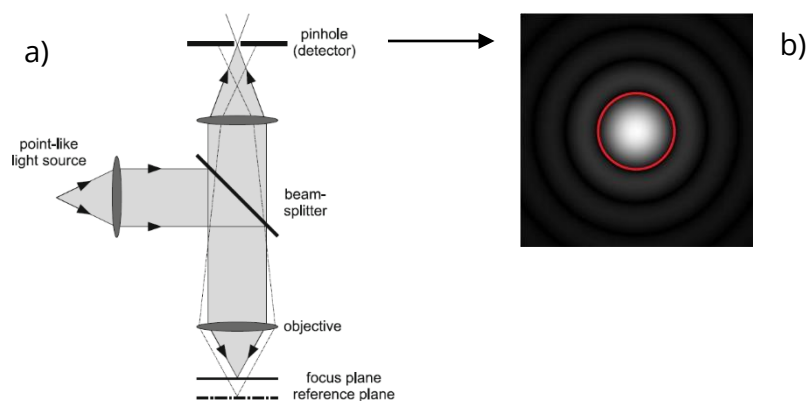


Figure 31 a) Principal setup of a confocal microscope (92) b) Pinhole diameter and diffraction pattern, the red circle indicates a circular pinhole adjusted to 1 Airy Unit (93).

The pinhole size is very important in confocal Raman experiments. On one hand the signal should be as high as possible, while on the other hand we want to have as much as possible high resolution for a good objective-WG coupling and without collecting the Raman signal from silicon dioxide of the cladding.

3.2 Thor Camera

The Thor Camera is used in our set up to have a visualize the zy surface of the chip during the experiments and to measure the scattering losses. It is composed by:

- a CCD camera (CS165MU Specifications).
- an objective with a DL Doubler. The DL Doubler has the function to increase the field of view.

The main properties of the camera are listened in the Table 4.

Table 4 Property of Thor Camera.

property	values
<i>Working Distance</i>	44 mm
<i>field of view</i>	3.20 mm
<i>with DL Doubler (mm)</i>	Horizontal Fields of View.
<i>Magnification</i>	2x
<i>Numerical Aperture (NA)</i>	0.068
<i>Resolution (microns)</i>	5 μm
<i>Lines per Millimeter (l/mm)</i>	204
<i>Depth of Field (DOF) (mm)</i>	0.118

3.3 Epilog Laser cutter

FusionPro Laser System (Model 16000) was used to create the chip set-up. It is composed by a CO₂ laser system operating at wavelength of 10.6 μm (94). The machine include: a camera positioning system allowing to precise material placement and an automated focusing procedure. The laser has two basic operating methods: vector, used for cutting achieved with slow speed and high-power cutting property, and engraving, applied for marking.

Acrylic 3mm plate was used for chip set up production. Laser cutting produces good edge quality without the need of polishing or secondary clean up. Combination of power, speed, cycles number and resolution determine the quality of the cut or for trench formation. In Table 5 below are summarized the two settings for trench and cut for Acrylic 3mm plate.

Table 5: summary of the settings for Epilog laser cutter.

Cut type	Process type	Resolution	Speed	Power	Frequency
<i>Cut acrylic 3mm</i>	vector	//	7%	100%	100%
<i>Trench 1mm depth acrylic</i>	engrave	1200	10%	100%	//

3.4 Chip design

3.4.1 xy plane

The waveguides studied are made of two different types: strip and slot waveguides. The main difference can be seen in Figure 32. As we can see the strip waveguides are characterized by a rectangular cross-section with a variable width, w . On the other hand, the slot waveguides are composed by two smaller slot waveguides separated by a distance s one to each other and occupying in width w as in Figure 32 on the right. The waveguides are made by amorphous silicon nitride $a - SiN$ (Si_xN_y with $x \sim 3$ and $y \sim 4$). They are deposited on a SiO_2 film of $3\mu m$ thick grown on monocrystalline Si wafer.

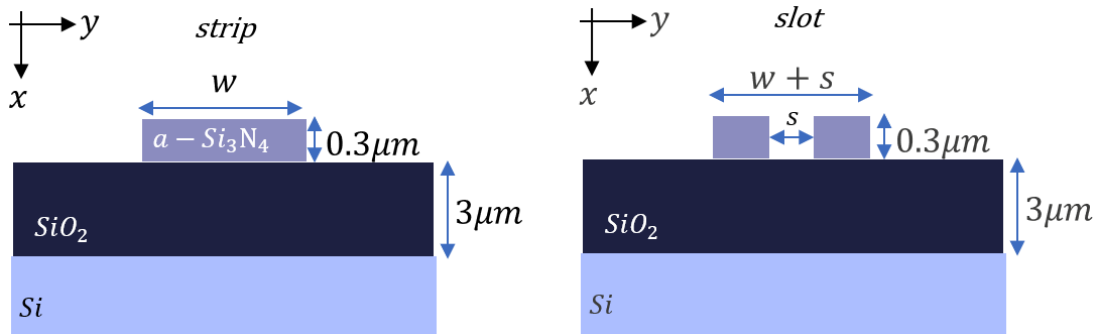


Figure 32 scheme of an ideal strip waveguide on the left, and of an ideal slot waveguide on the right. The thickness are not in scale.

The last interesting cross section of the waveguides is where the coupling between the objective and the WG occurs. These waveguides are cladded by SiO_2 . In this region there a strip WG with a standard width of $0.7\mu m$ (Figure 33).

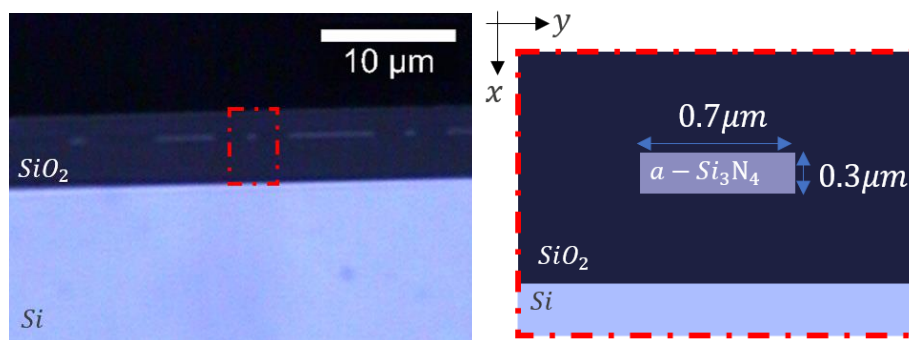


Figure 33 On the left the real image of a xy cleaved surface taken with the microscope with a $100\times/0.9NA$ objective. We can notice that between each waveguides of our interest (small dots) there is a $a - SiN$ slab waveguide much wider that is not designed for guiding the light to the probe region. On the left the scheme of the crosssection of the coupling region of the red dotted region.

After the coupling occurs, the light is delivered to the probing regions and the cross sections of the WGs is slowly changed and the final width is in between $0.4 - 1.3\mu m$.

3.4.2 zy plane

The chip design under study is reported in Figure 34. We can see the top view of the zy plane. The dimension of the chip is about 2.2x0.5 cm, but it can vary depending on the cleavage (process in which a clean xy surface is created by brittle fracture).

The light is coupled in a SiO_2 cladded WG with cross section equal between all the WGs. Then the WG slowly change the cross section till arriving to the probing regions in green in which each WG is characterized by different cross section and probing length (green areas in Figure 34). The probing regions are characterized by the absence of SiO_2 cladding, therefore the WGs can go directly in contact with the analyte. Therefore, for each WG it can be introduced the presence of a SiO_2 cladded region, with length L' and a probing region where the WG probing length is L .

There are two probing regions, corresponding to two different designs that we will define as T1 and T2. We now specify in more details these two different designs.

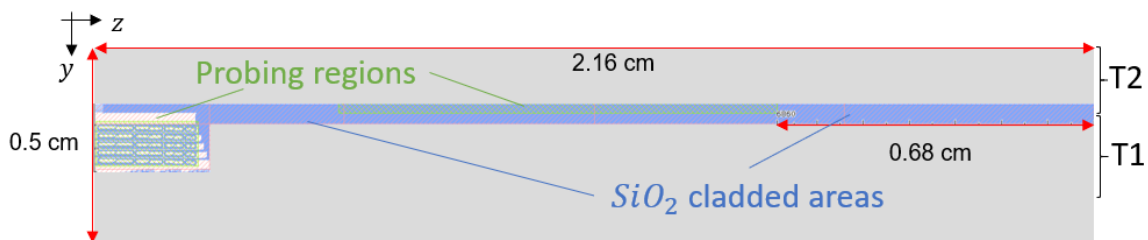


Figure 34: scheme of the chip used in the experiments with some details regarding its dimensions and regions: probing regions in green and SiO_2 cladded areas in blue.

The T1 design is characterized by a long SiO_2 cladded WG that can be at maximum 2 cm long. The probing region is constituted by 20 strip waveguides each one of them is characterized by a specific width and length, as shown in Figure 35. These waveguides are grouped with 4 different probing lengths: [0.4, 0.6, 0.8, 1.0] cm (labels by numbers) and 5 different width waveguides: [0.4, 0.6, 0.8, 1.0, 1.2] μm (labels by letters). For more information look at Table 6. All the WGs are designed to have minimized the bending losses.

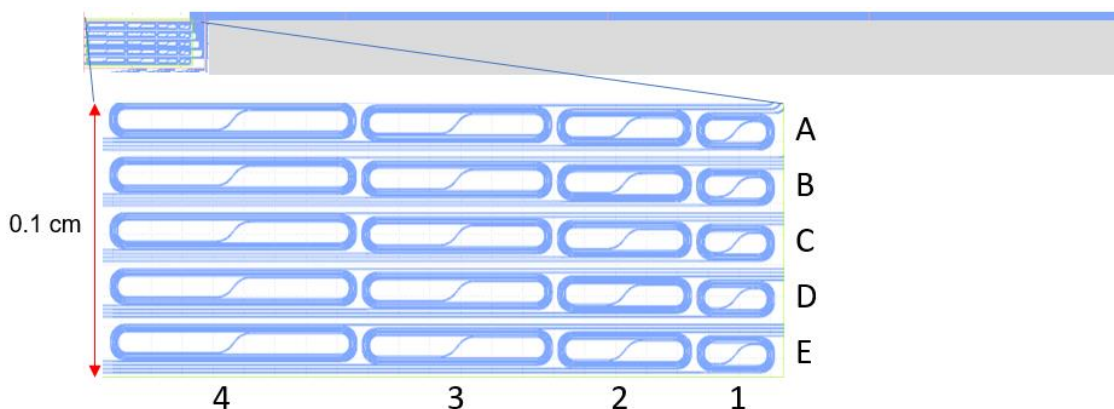


Figure 35: T1 design. With capital letter we distinguish the difference in width and with numbers the different probing length. The spirals bends have bending radius of 35, 40, 45, 50, 55 μm .

Table 6: Summary of the geometries of the T1 design.

T1 design			
strip			
width (μm)	letter assigned	Probing Length (cm)	number assigned
1,2	A	1.0	4
1	B	0.8	3
0,8	C	0.6	2
0,6	D	0.4	1
0,4	E		

The T2 design is characterized by WGs with a constant probing region 1cm long. The probing region is constituted by 16 waveguides, where half of them are strip (with label the letter a) and half of them are slot (with label the letter b), Figure 36. For each slot WG there is a strip waveguide with the same w value. Each slot waveguide differs one to each other for different s distance, $[0.15, 0.25]\mu m$, and in width, $[0.5, 0.7, 0.9, 1.1]\mu m$. For more information look at Table 7.

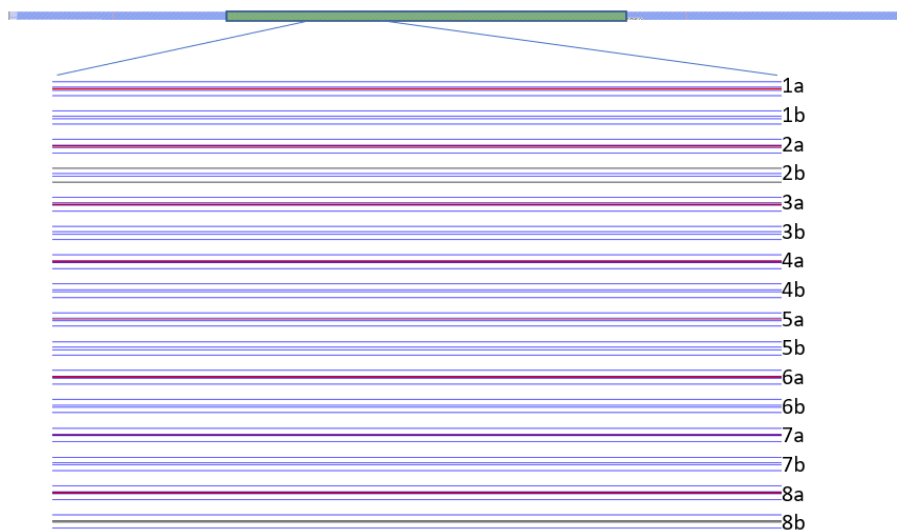


Figure 36: T2 design. With letter we distinguish between slot and strip and with numbers the different geometry.

Table 7: summary of the geometries of the T2 design.

T2 design (Probing length = 1 cm)			
number assigned	slot (letter assigned = a)		strip (letter assigned = b)
	width (μm)	separation (μm)	width (μm)
1	1,2	0,25	1,1
2	1	0,25	0,9
3	0,8	0,25	0,7
4	0,6	0,25	0,5
5	1,2	0,15	1,1
6	1	0,15	0,9
7	0,8	0,15	0,7
8	0,6	0,15	0,5

4 Optical set up and SiN WG Raman spectra

The first challenge in my thesis work is the design of the experiments. It includes the chip preparation (chapter 4.1), the creation of an optical set up to hold under the microscope the chip-sample system (chapter 4.2) and the procedure for coupling the light in the WGs and Raman collection. Finally, in chapter 4.4 it will be analyzed in depth the Raman spectra intrinsic of the chip. To analyse these spectra a peak fitting procedure has been developed in quasi-automated manner and the major step for data evaluation are reported in chapter 4.4.

4.1 Chip cleavage procedure

To couple the light in the WGs the xy chip surface needs to be as much as possible flat and smooth. Therefore, the cleavage procedure of the die to produce clean edges is a key process. The procedure that was applied is:

- Under a fume hood a diamond pen is used to scribe one straight line on the wafer surface with the support of a ruler. This will favor the brittle fracture of the wafer along [001] plane from that point.
- The fracture is obtained with a cleabreak pliers positioned on the scratch previously obtained. The position of the fracture can vary and determine the not-probing length L' (Figure 37 on the right there is a sketch of where the cleavage on the chip is usually performed).

The process results in high quality, clean samples that can be used for further analysis. There are other different process to cleave the die, such as laser scribe based or saw based (95), but they do not result in clean edges. The simple tool needed for this procedure are shown in Figure 37 on the left.

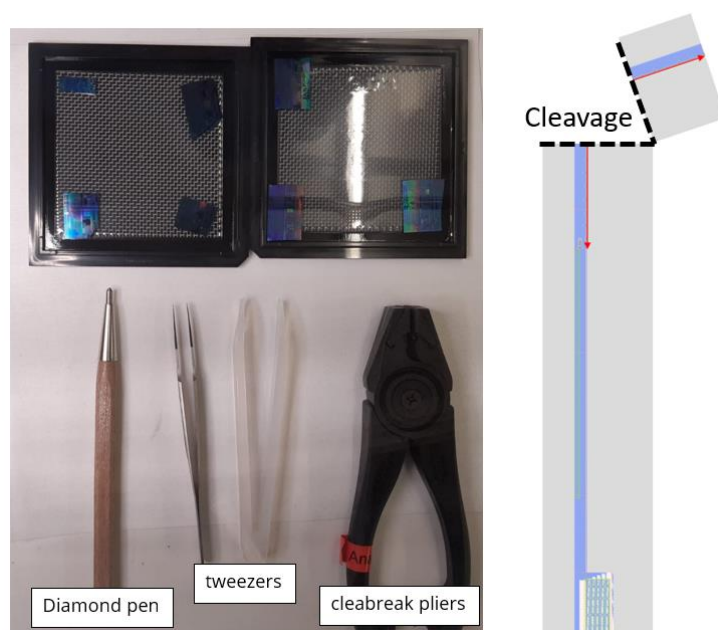


Figure 37: instruments for cleavage the chips.

Critical aspect of this process is the quality of the cleaved surface where the coupling occurs. This can be evaluated in terms of straight line cutting in the zy plane and surface smoothness in the xy plane, both influence the coupling of the laser in the WG. Therefore, a check on the microscope is needed. Here it has been reported two examples of cleaved chips (Figure 38):

- chip1 has got a better quality in terms of straightness in the zy plane, but from an inspection on the xy plane we can see that the cut was obtained not by a brittle fracture but by means of diamond saw. By trying to couple the light inside it is not possible.
- chip2 is characterized by some defects that can be detected in the zy plane (red circles in Figure 38) but the flatness of the xy surface leads to still possible coupling in some of the WGs. Even if the cleavage is not optimal, is still possible to couple the light inside.

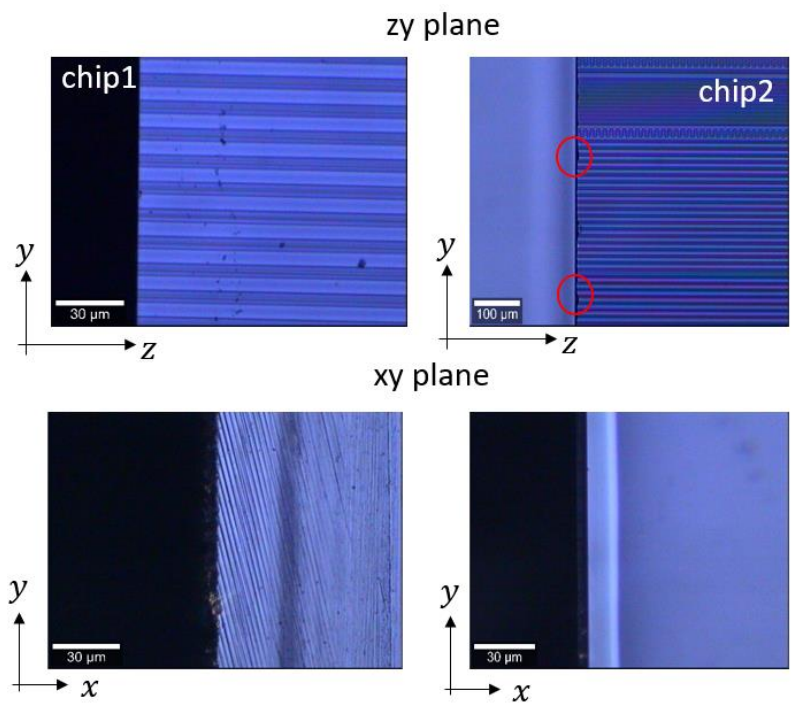


Figure 38: difference between 2 cleavage procedure: diamond saw for chip1 and diamond tip for chip2. Pictures taken with 40x objective except for the chip2-xy plane taken with 10x, to show better the presence of defects highlighted with red circles. Both cannot be used in the experiments.

Haupt et al. (96) shown the side wall roughness is influenced by the cleaving direction (Figure 39). Therefore, the appearance on the microscope of the xy face can give insight on the straightness of the zy cut.

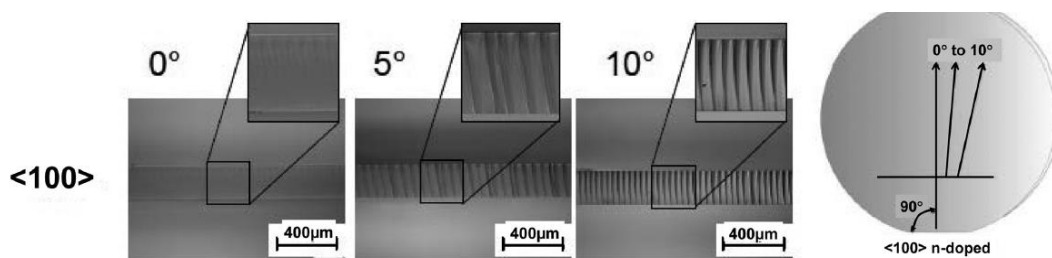


Figure 39: appearance of the side wall of the cleaved die form a (100) wafer at different angles. Taken form article (96). To be noted the length scale of these two phenomena.

4.2 Optical set-up

Here it is presented briefly the three main set-ups created for experiments. It is important to understand that one challenge in this research field is the appropriate design and construction of set up that hold the chip and sample. I will not describe in depth all the design parameters, but the most important details are shown in the images themselves. An example of the set-up is reported in Figure 40. Figure 41 there is scheme of the Raman spectrum acquisition.

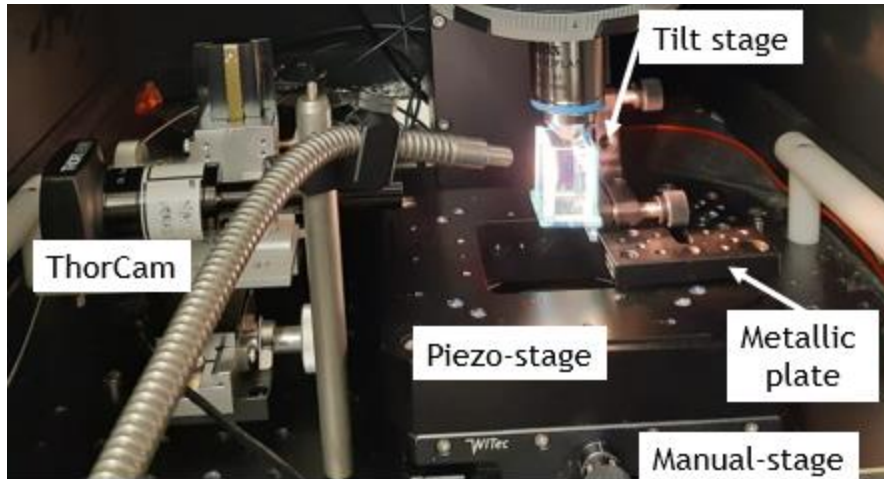


Figure 40: example of complete set up for a general experiment.

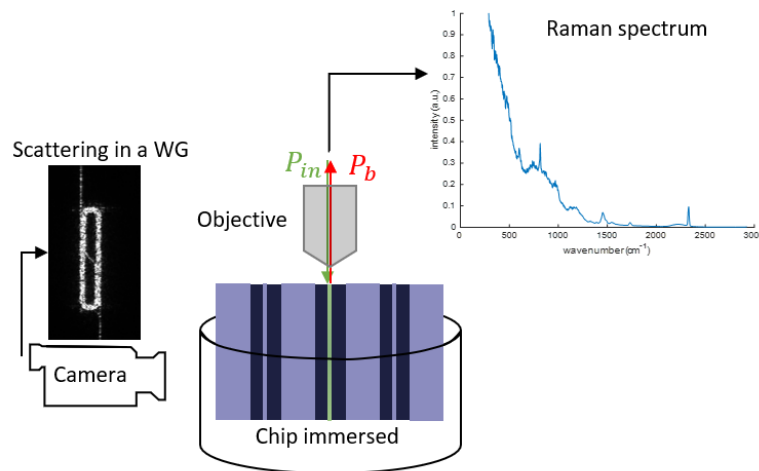


Figure 41: scheme of the how measurements are done. P_{in} is the incoming power and P_b is the backscattered collected power.

The main constrains for the chip design are:

- Chip support.
- Liquid sample container and chemical compatibility.
- Transparency of the container to observe the WGs with a top camera.
- XY constrain: the chip can be positioned only in a limited region where the objective can be positioned (2cm x 2cm).
- Z constrain: the maximum height for the chip position is 5 cm.
- Maximum load on the piezo-stage: 50N.
- Anchoring system sufficiently stable avoiding any drift.

Some of these constraints can be evinced from the cad images in Figure 42. The set-up was modeled using SolidWorks software.

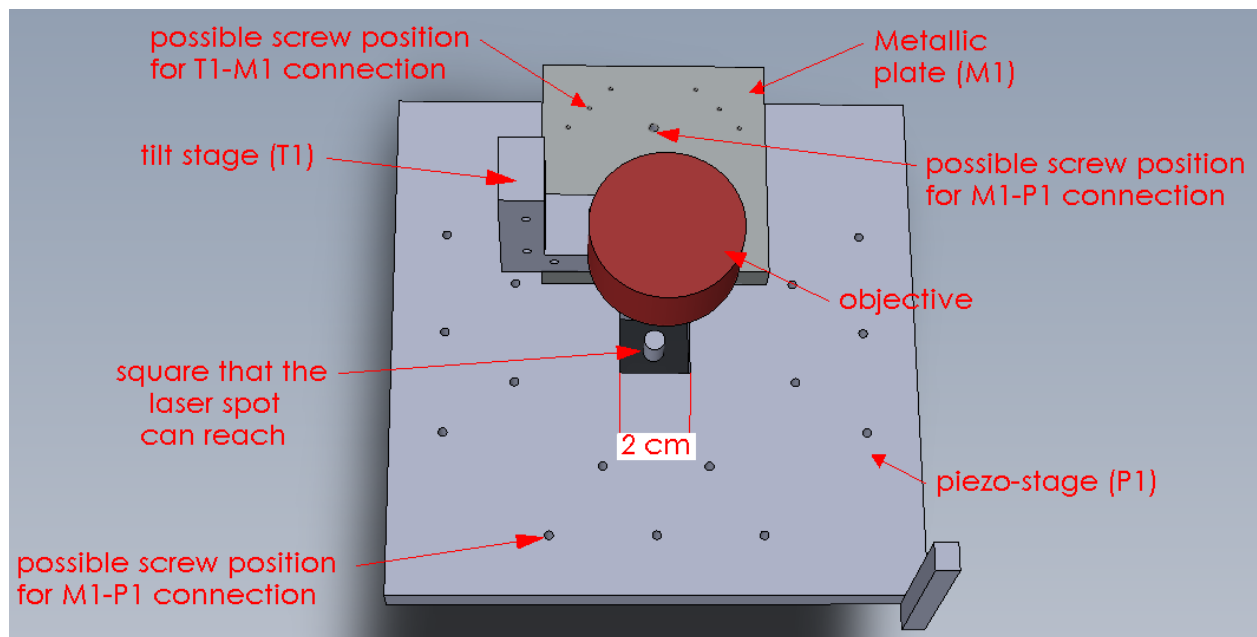
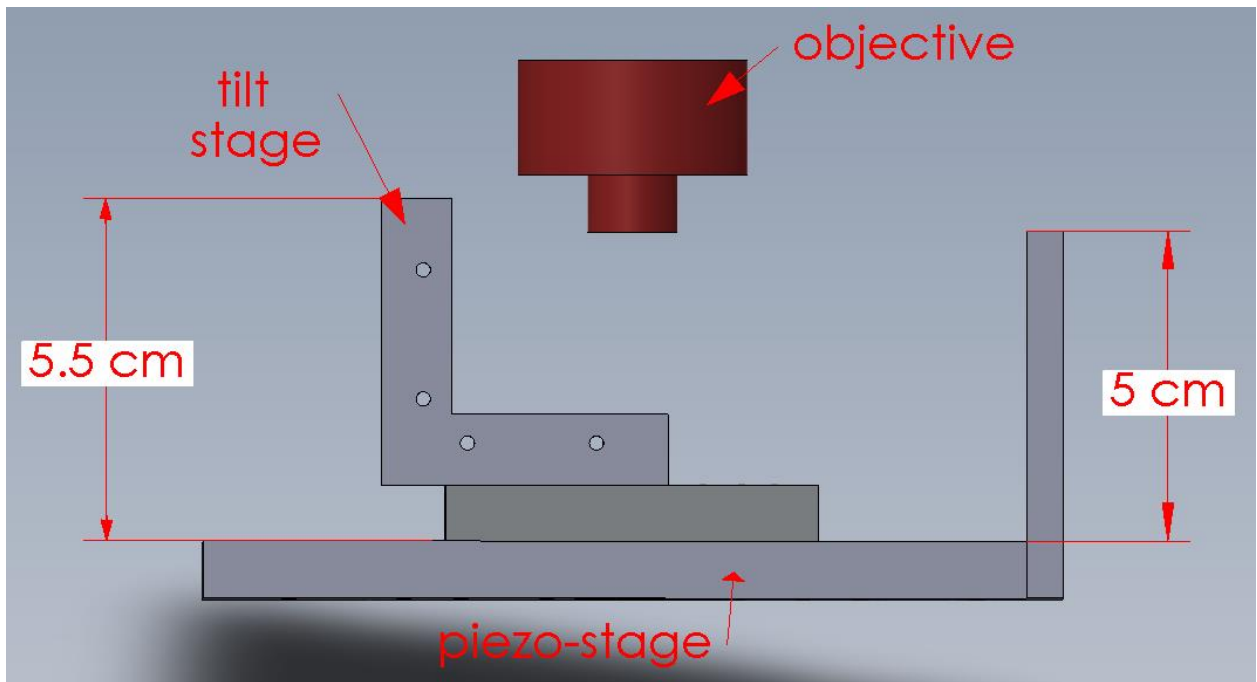


Figure 42: images of the space near by the objective with two additional components used for building the set up: the metallic plate and the tilt stage. The last one was not used in all the set up. On the top image the 5 cm refers to the constraints of the maximum height reachable by the objective.

The three main chip designs are: set up N0, set-up N1 (Figure 43) and set-up N2 (Figure 44). The main advantage in using the set-up N1 is the possibility to easily change the chip. On the other hand the set-up N2 is designed to have easier sample filling and smaller sample volume. But for N2 the chip change is a more complicate procedure. The set-up N0 it is almost equivalent to set-up N2 but without any closed channels, it is suitable for initial no-sample testing or for solid-coated samples.

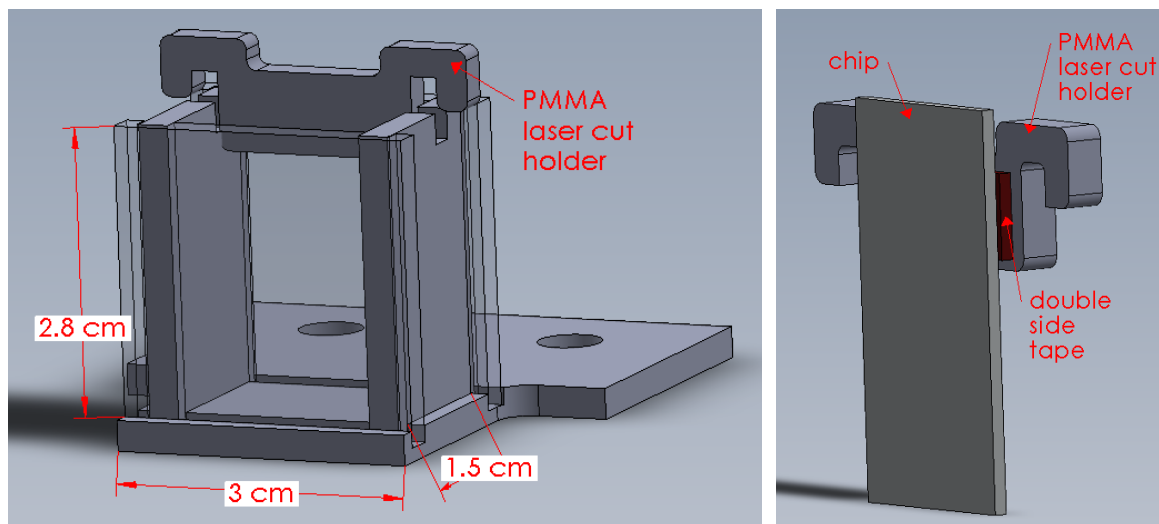


Figure 43: complete set up N1 on the left. On the right image is shown how the chip is anchored to the PMMA laser cut holder that subsequently will be inserted in the set up N1. Therefore, it is very important the accurate study of all the tolerances. This set up is directly mounted on the metallic plate.

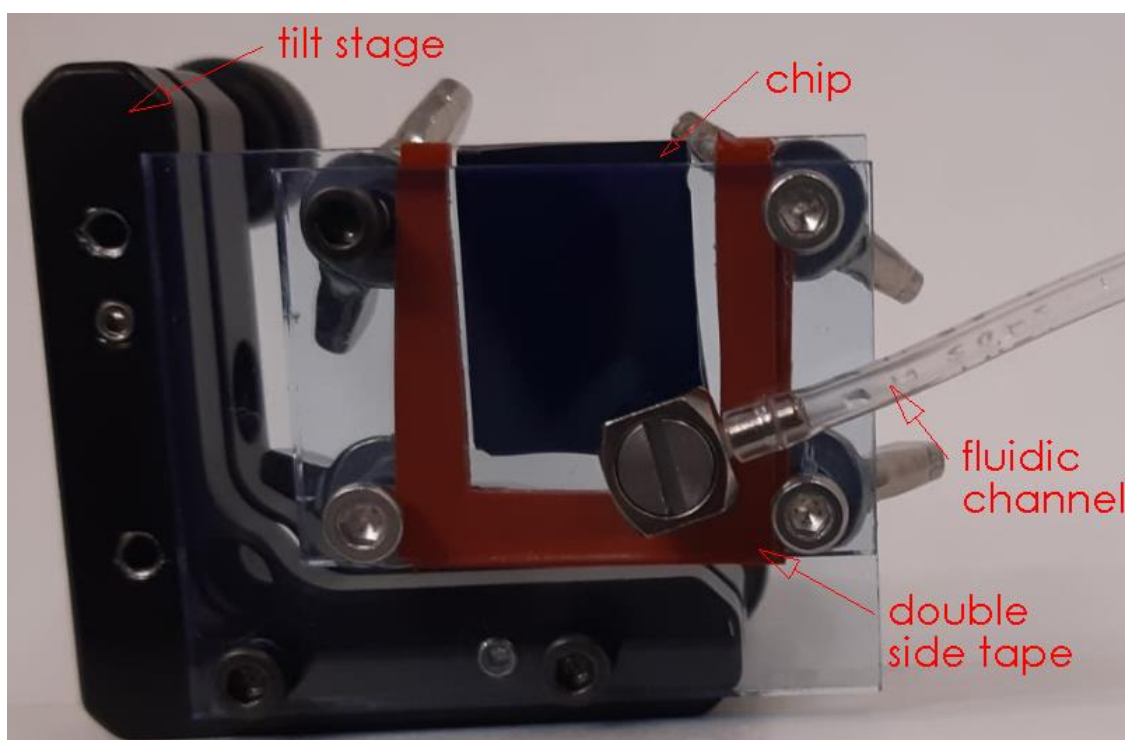


Figure 44: set up N2. It is composed by two plane of acrylic, allowing light transmission, connected by 2 layers of double side tape and 4 screws. A fluidic channel is built for liquid sample delivery. A tilt stage is used to connect the box to the metallic plate.

4.3 Procedure for spectrum acquisition

4.3.1 Influence on the laser spot position

It is worth to look at Raman mapping of the chip reported in Figure 45.

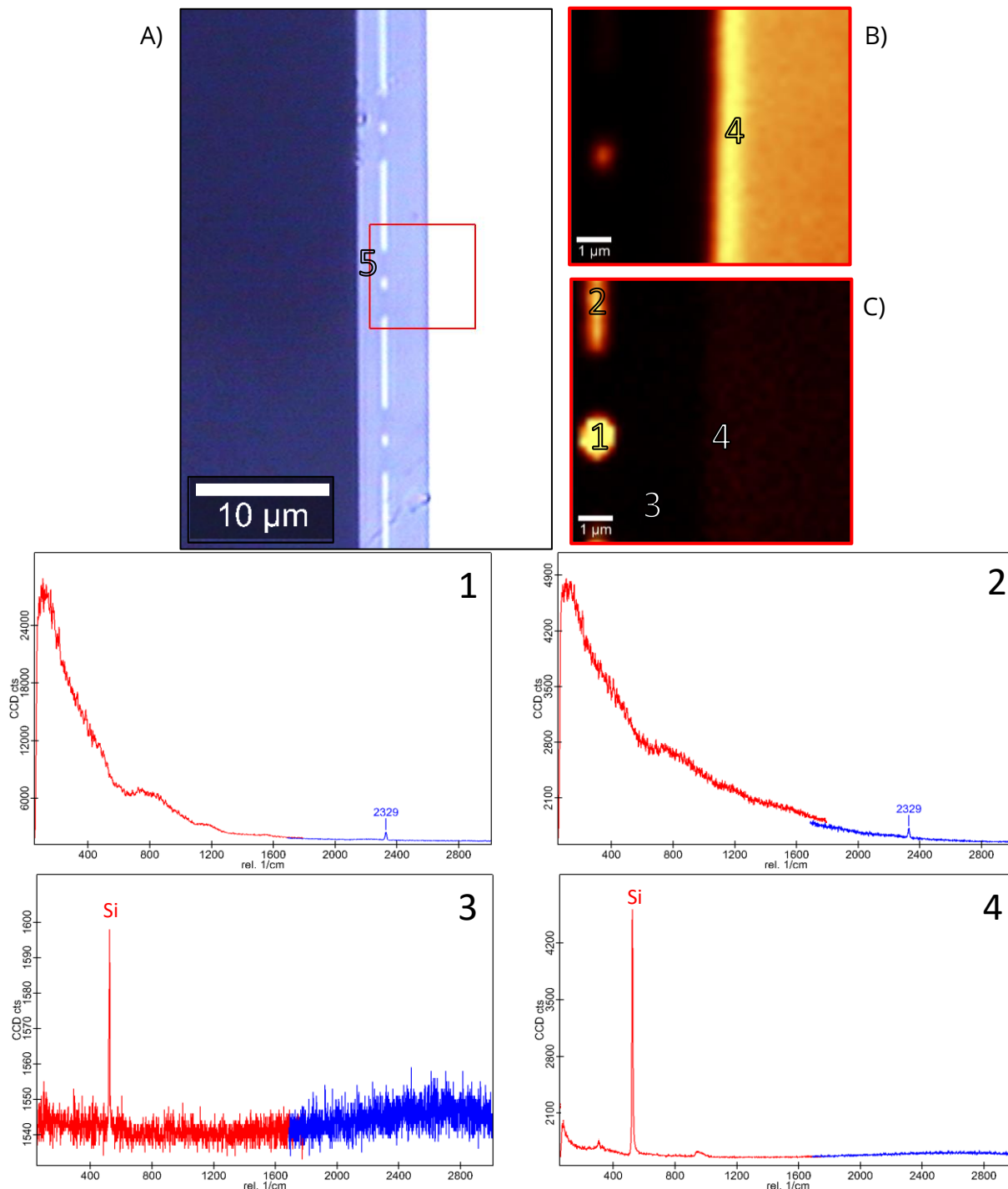


Figure 45: the image A) is the xy surface where is indicated the region where scan image was done. On the top right there are two scan images (B and C) with two different filters, i.e. the colour of the images range from 0 to 1 intensity of a certain quantity, in this case is the standard deviation with centre at Si peak (B image) and N_2 at 2329 cm^{-1} (C image). The four spectra reported are numbered and their position is shown in the scan images (A, B, C). Raman acquisition with excitation wavelength: 785 nm , integration time: 0.005 s , objective $100\times/0.9$.

It can be noticed the main difference between the four spectra: when the laser is well coupled in a WG as in the spectrum 1 the resulting signal is more than five times more intense with respect to the slab region, spectrum 2. The Raman spectra of SiN WG will be discussed in more detail in chapter 4.4, but it can be already spotted some characteristic features: in the region $[0;1200]$ cm^{-1} there is an intense broad peak and at 2329 cm^{-1} the characteristic peak of N_2 incorporated in the WG during the production process (97).

The spectrum 4 (Figure 46- look at B and C for scan images) clearly correspond to Si signal associated to transverse optic (TO) phonon mode (98-101).

On the other hand, the spectrum 3, which should be assigned to amorphous SiO_2 is too noisy and the only clear feature is the Si peak which should be characteristic of Si crystalline substrate. Therefore, I have decided to take a spectrum at position 5 (moved more far from Si substrate) that is reported in Figure 46. As we can see there is still the Si peak therefore can be the result of presence of Si-Si bonds in the amorphous network. The peak at 609 cm^{-1} is characteristic of a-SiO_2 , and it is usually assigned to defects of the network (73, 102, 103). Then it can be distinguished at low wavenumbers, below 200 cm^{-1} the Boson peak (or more in general an exponential decreasing trend) which it seems at much higher intensity with respect to the a-SiO_2 spectra founded in other papers (73, 104), and it covers the main band for a-SiO_2 at $400\text{-}500 \text{ cm}^{-1}$, attributed to bending motion of Si-O-Si unit (102, 103). The increased intensity could be related to the effect of confinement (105) but further studies should be done to understand better the spectrum features. Finally, there are two less intense peaks at 812 cm^{-1} and 981 cm^{-1} . The first one is assigned to the so-called Si stretching motion ($\leftarrow \text{SiO} \rightarrow \leftarrow \text{Si}$) (102, 106). The peak at 981 cm^{-1} is assigned to Si-OH stretching motion (102, 103).

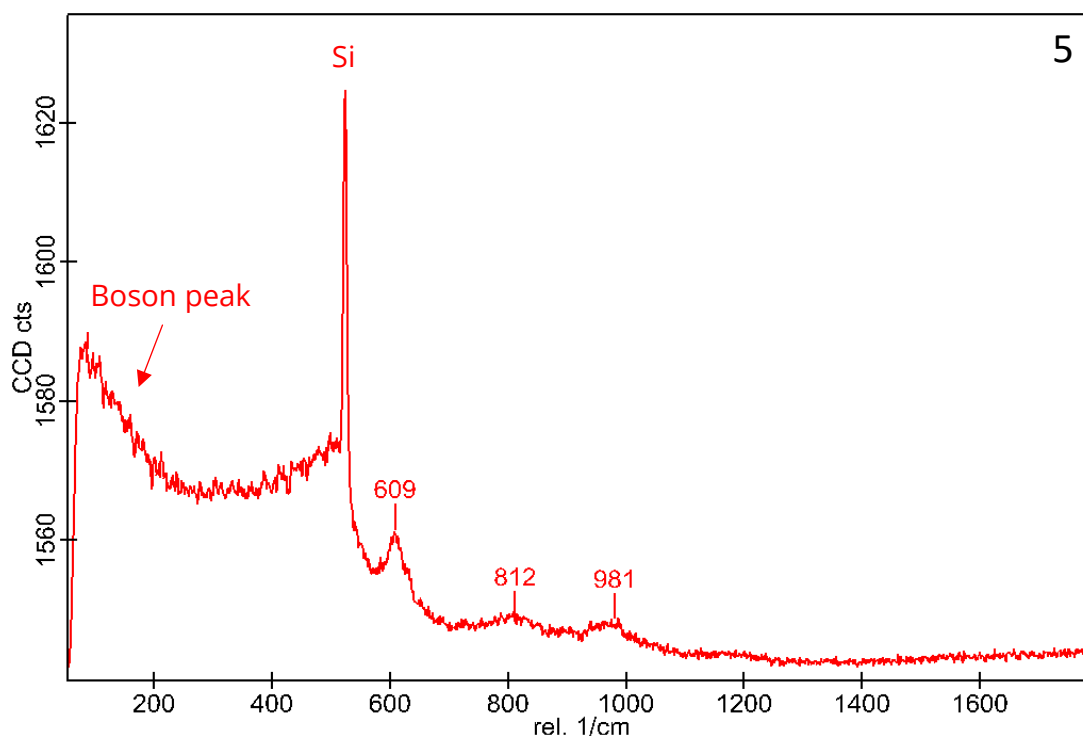


Figure 46: a spectrum taken at position 5 of Figure 45-A) with laser 785nm with 55mW power, integration time of 0.1s and accumulation number of 100. As we can see the clear peak of Si-Si stretching and a peak at 609 cm^{-1} it could be related to defects in the a-SiO_2 network.

4.3.2 Data acquisition and Drift

The data acquisition procedure consists in:

1. Load of the set up and the chip. Observation of the quality of the cleavage of the chip.
2. Alignment of 10x objective with the manual xy stage by observing the 633nm laser spot on the Thor camera.
3. Focus with 10x. Change of the objective to 40x or 100x and observation of the xy surface quality. For example, in Figure 47 we can see the difference between a xy surface dirty and damaged with respect to one well cleaned and uniform.

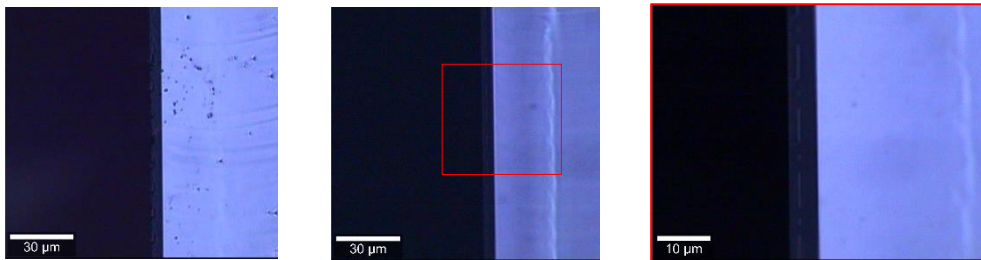


Figure 47 Pictures of a chip xy surface. The two images on the left were taken with 40x objective of two different chip, one of them not well cleaned and with some cladding of the slab WG broken. On the right image is the same chip of the central image but taken with 100x objective.

4. Alignment of the laser spot with the WG interested in the study. The best procedure is to observe in the camera mode and switched laser coupler to edge filter on as in Figure 48, in this way you can clearly distinguish the difference between the slab and strip WG.

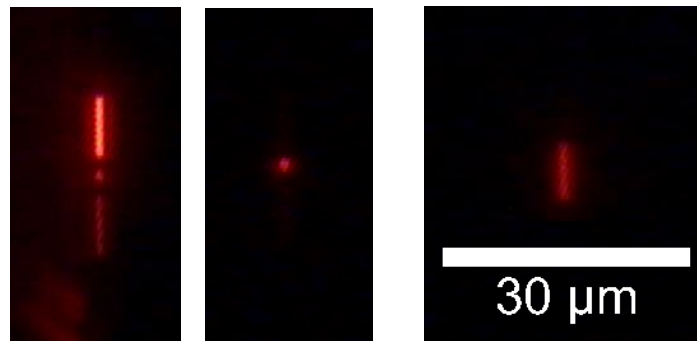


Figure 48 images obtained with 40x objective in camera mode and edge filter on for 633nm laser.

5. Switch to the oscilloscope mode and maximize the peak intensity around 2330 cm^{-1} by controlling the chip position with the piezoelectric stage with a precision of $0.1\mu\text{m}$ in the xy plane. Also optimize the z-position.

It is important to underline the influence of the x position of the laser spot on the resulting Raman signal collected. Therefore, in Figure 49 it is reported 5 different Raman spectra. The first one (labeled by $x = 0.0\mu\text{m}$) comes from one SiN strip WG air cladded at optimal position of the laser spot. The optimal position is characterized by the highest intensity of N_2 peak at 2329 cm^{-1} (i.e. the maximal coupling efficiency). The other spectra are collected at different x-chip position with respect to $x = 0.0\mu\text{m}$. As we can see there is a very high sensitivity of the measurements to the x-position in the order of $0.1\text{-}0.2\mu\text{m}$ with the objective $40\times/0.65\text{NA}$. This is much lower with respect to the laser spot dimension of $r = 1.22 \frac{\lambda}{NA} \approx 1.5\mu\text{m}$.

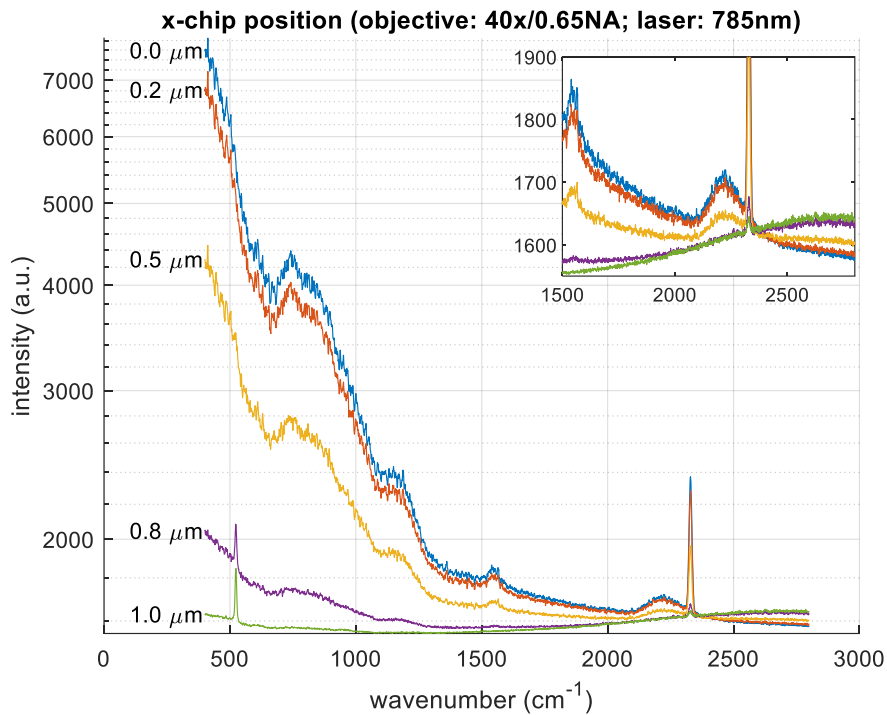


Figure 49: Raman spectra of collected at different position on the x axis from the SiN WGs air cladded maximum intensity. The pump laser wavelength is 785 nm.

During the first experiments it was reported a variation during time of the spectra recorded. The origin could be attributed to drift of the chip-microscope alignment or in a change of the focus. This problem occurs at apparently random occasion and its probing was of difficult detection. It ruined many experiments. The possible sources could be:

- The set up that holds the chip.
- The anchoring system of the chip to the set up.
- Drift in the xy manual stage. The origin could be the polymer creep phenomena.
- Drift due to the piezoelectric stage.
- Drift of the objective tower in z direction. The origin could be a T change that result in an expansion or contraction of the metallic part of the objective tower.
- Possible external vibrations.

Therefore, there were made different experiments changing different set up and 2 different holding systems and recording if there is a drift observing the change in camera mode with a 100x objective. Firstly, it was noted that the drift involves only the xy directions and no variation in the z distance was reported. In Figure 50 it is reported one example of the recorded drift on the xy plane. The mean velocity in the two directions were in the order of $5 \cdot 10^{-3} \mu\text{m}/\text{s}$.

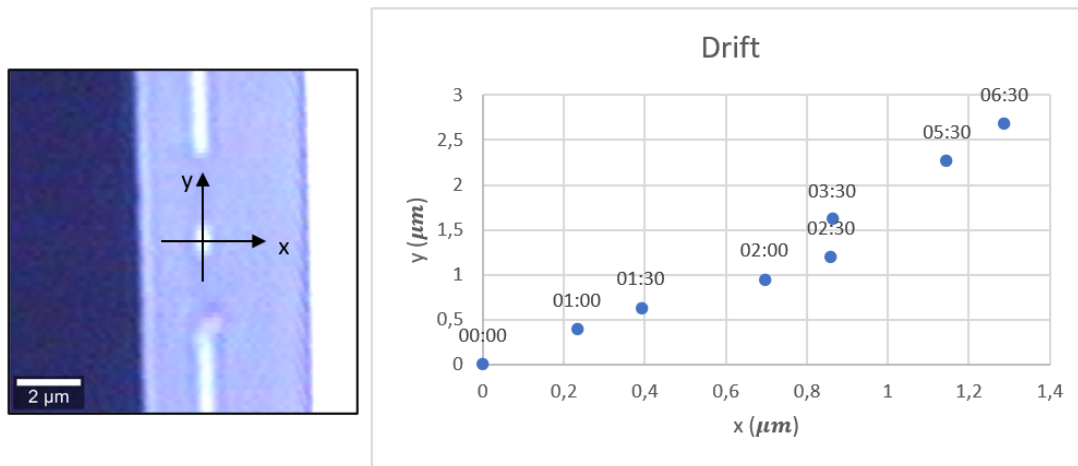


Figure 50 on the left one picture of the xy plane captured with 100x objective. On right the position map on the xy plane of one feature of the chip, each point is labelled with the time at which was recorded, and is reported in [mm:ss].

The main hypothesis of the origin due to this drift was related to mechanical instability. Therefore, the best experimental procedure that adopted was to separate the “loading procedure”, steps 1, 2 and 3, to the “Raman spectra collection”, steps 4 and 5, by certain amount of time. In my case it was decided to switch the experimental schedule to prepare the set up at the end of one day and the day after taking the measurements.

4.4 No analyte Raman measurements

This chapter it will be described the Raman spectrum of the a-SiN strip WG without analyte. This signal is the background of the analyte spectrum once the chip is loaded, and it ultimately limit the efficiency of the device (59). The analysis will consider the most recent models (60) to decompose these spectra in relevant components.

4.4.1 One single WG study with 785nm laser wavelength

The waveguide Raman spectrum ($S_{WG}(\tilde{\nu})$) can be considered as the sum of different components:

$$S_{WG}(\tilde{\nu}) = P_{LFDC}(\tilde{\nu}) + R_{core}(\tilde{\nu}) + R_{sub}(\tilde{\nu}) + F(\tilde{\nu})$$

In which $P_{LFDC}(\tilde{\nu})$ is the low frequency dominant component, $R_{core}(\tilde{\nu})$ and $R_{sub}(\tilde{\nu})$ are respectively the Raman signals coming from the core and the substrate and $F(\tilde{\nu})$ is the residual noise.

First it is estimated the $P_{LFDC}(\tilde{\nu})$ by using 5th order polynomial that fit the Raman spectrum with an asymmetric truncated cost function ('atq') (107). It's origin was shown to be related to the dielectric amorphous core of the waveguide (60), which should be distinguished from $R_{core}(\tilde{\nu})$, i.e. the Raman spectrum local bonding phenomena in the core. It was demonstrated that due to its origin should follow an exponential decay. As shown in the Figure 51 on the top subplot the spectrum and the P_{LFDC} , on the bottom of the subplot it is reported $S_{WG}(\tilde{\nu}) - P_{LFDC}(\tilde{\nu})$. By fitting the P_{LFDC} polynomial with an exponential decay the background has an exponential behavior. In the Figure 51 is reported the result of the fitting between the 5th order polynomial and the exponential with the error $R^2 \equiv 1 - \frac{\sum(y_i - y_{i,fit})}{\sum(y_i - \bar{y})}$. The characteristic frequency is given by: $\frac{1}{0.0023} = 435\text{cm}^{-1}$ which can be converted in characteristic time with a value of 12.4 fs.

The resulting spectrum given by the difference $S_{WG}(\tilde{\nu}) - P_{LFDC}(\tilde{\nu})$, which will be composed by $R_{core}(\tilde{\nu})$, $R_{sub}(\tilde{\nu})$ and $F(\tilde{\nu})$. To extract the $F(\tilde{\nu})$ the spectrum is fitted with 7 peaks (look at Figure 52) taking into account the risks of overfitting the data explained in (70). The peaks assignment is given:

- the core of the waveguide $R_{core}(\tilde{\nu})$ composed by peaks that have been found also in Raman and IR spectra of a-SiN thin films (108-113). It can be distinguished Si-H stretching vibration at 2236 cm^{-1} , N-H₂ bending at 1549 cm^{-1} , Si-N stretching 846 cm^{-1} . The peak at 2329 cm^{-1} it has been assigned to N₂ incorporated in the WG during the production process (97).
- The spectral region in between $600\text{-}1300\text{ cm}^{-1}$ it is decomposed in three different peaks: at 740 , 1007 and 1170 cm^{-1} (excluding the already assigned peak at 857 cm^{-1}). The assignment to these peaks is not straightforward. For example around 1170 cm^{-1} in the literature was found signals coming from both a-SiO₂ (104, 114-116) and a-SiN, N-H bending (110-112). The peak 1002 cm^{-1} can be assigned to Si-N bond with an hydrogen atom back bonded to the silicon atom (109, 113) and on the other hand the peak at 740 cm^{-1} can be assigned to Si-O bending of a-SiO₂ (102, 117).

From all the considerations said before the WG Raman spectrum without analyte is mainly composed by spectra coming from a-SiN, N₂ and the exponential decay signal. It is also not possible to exclude the Raman signal originated from a-SiO₂ and it have an impact on the background signal. This is not completely in line on what shown by A. Dhakal et al. (59), where the model of the background was based on the hypothesis of neglecting the Raman signal of a-SiO₂. In chapter 5.1 it will be explained what change under the assumption of not negligible a-SiO₂ Raman signal.

The presence of hydrogen impurities has been easily detected. These impurities of the WG core as well as in the substrate affects in the WG absorption losses in the NIR range (118-120). Usually with an annealing step these impurities are greatly reduced (113, 121, 122), and therefore should not possible to detect them but the WG enhancement in this case greatly increase the intensity of these signals. It would be interesting to studying how the process parameters influences the SiN Raman signal.

In Figure 53 is reported the original spectrum coming from the WG 3D and the fit, given by the sum of the different components evaluated previously (with R²=0.9987). In the bottom subplot is shown the residue and it is also reported the mean standard deviation of the residue, equal to 359 CCD cts, and the mean shot noise, evaluated as square root of the original spectrum ($\sqrt{S_{WG}}$) equal to 87 CCD cts. Therefore, the noise in our experimental spectra is more than 3 times higher than the shot noise (lower limit to the noise). It is interesting that even increasing the number of accumulations the noise does not change. If comparing to other papers (41, 44), the background signal measured in Figure 53 has much higher noise. This behavior is not recorded if we make measurements with a free space beam Raman signal collection system with same objective on common glass or water glucose solution samples. Therefore, one hypothesis is that this high noise could be influenced by the design of the WG or the production process of the WG. Further experiments should be needed on different WGs to appreciate this difference.

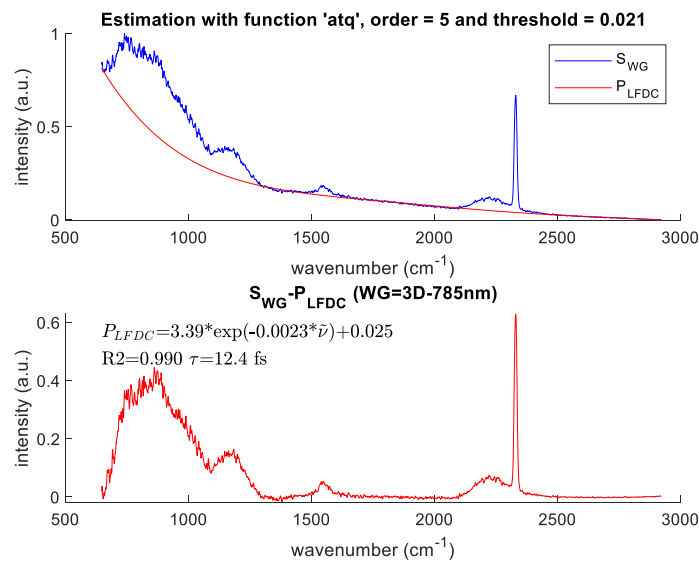


Figure 51: on the top figure, the normalized spectrum between [0,1], S_{WG} , and the low frequency dominant component. P_{LFDC} . P_{LFDC} is estimated by a 5th order polynomial with an asymmetric truncated quadratic cost function ('atq') with threshold 0.021 (reported in the title). In the bottom the difference is reported. The result of the fitting of the 5th order polynomial with an exponential function is written in the bottom subplot along with the characteristic time τ of the fluctuations of the refractive index.

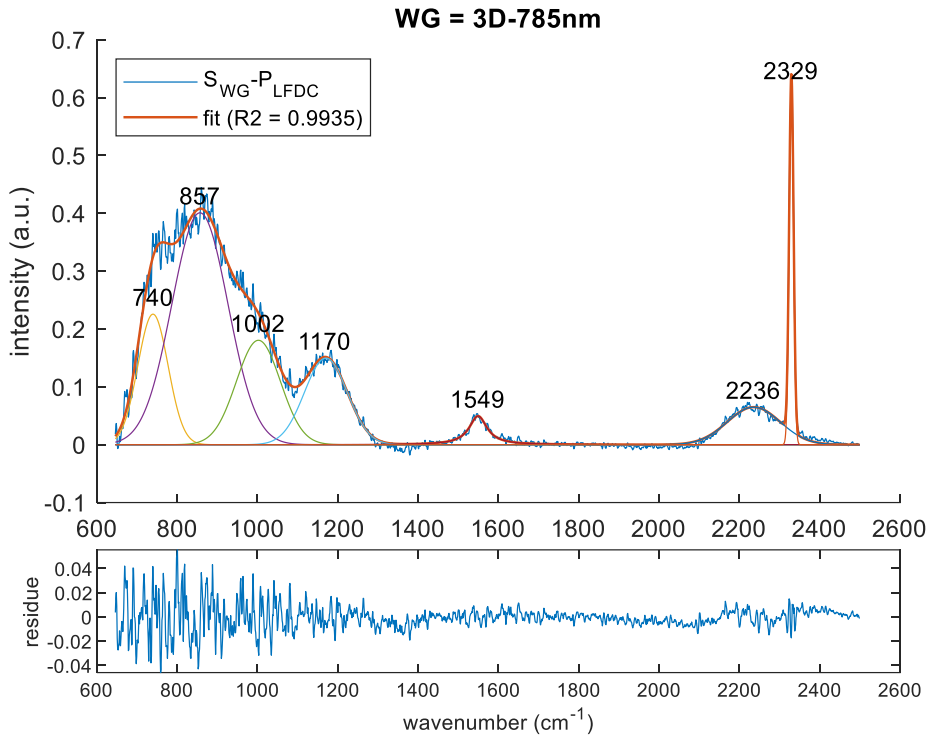


Figure 52: fit of the resulting spectrum after low frequency dominant component subtraction $S_{WG}(\tilde{\nu}) - P_{LFDC}(\tilde{\nu})$. The spectrum refers to the WG type 3D. In the bottom figure the residue is reported. The coloured lines are the 7 peaks used in the fitting.

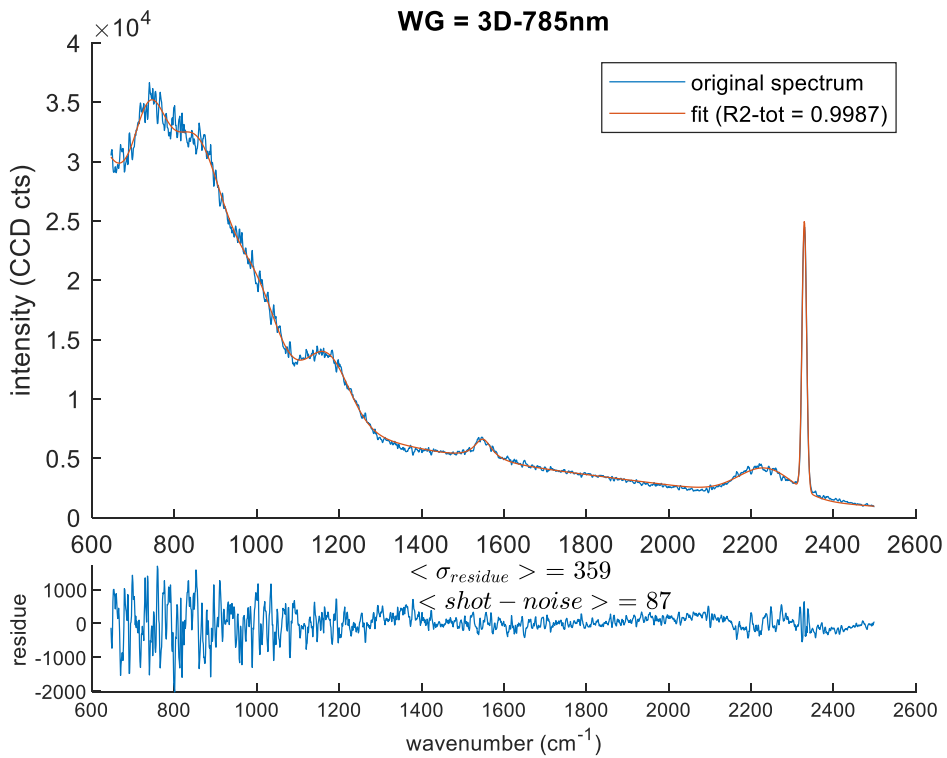


Figure 53: original spectrum obtained from 3D waveguide with 40x objective, 785 nm laser, 0.3s integration time and 20 accumulation number. in orange the total fit curve is represented. In the bottom subplot the residue is given by the fit and experimental data difference.

4.4.2 Multiple WGs Raman spectra

An almost fully automated script has been written to fit over many different spectra. It combines the programs already mentioned and a further script written by Thomas Nuytten. Therefore, the fitting procedure has been repeated for 20 times on different spectra. First on 4 equivalent spectra collected from the 4D WG, to evaluate the possible experimental errors involved in this procedure. These experimental errors are comparable to those associated to the fitting procedure therefore it will be not reported to reduce the amount of information's. These errors should be taken as reference since each single WG differs in length and width between each other and therefore the experimental error should be performed for each single WG. The remaining 16 WGs (labeled with 1 to 4 and B to E). Results are reported in Table 8 and Figure 54.

Table 8: mean values of the fit of 16 WGs with their standard deviation and relative error. For each spectrum a fit is performed. For example, the $FWHM_{ij}$ of the spectrum i and peak j and the fitting error $FitErr_{ij}$ are evaluated. For each peak is reported the mean FWHM over all the spectra and the associated standard deviation in the form: $\langle FWHM_{ij} \rangle_i \pm std(FWHM_{ij})_i$. In the row below is also reported the relative error in %: $std(FWHM_{ij})_i / \langle FWHM_{ij} \rangle_i$ and in the parenthesis is reported the mean of the fitting error over all the spectra divided by $\langle FWHM_{ij} \rangle_i$ in %: $(\langle FitErr_{ij} \rangle_i / \langle FWHM_{ij} \rangle_i)$. For peak Center is not reported the fitting error since is negligible. (n.u.= normalized units).

	Gaussian	Gaussian	Gaussian	Gaussian	Gaussian	Gaussian	Gaussian	P_{LFDC} (exp)
Center (cm^{-1})	736±3	846±14	989±27	1170±4	1550±1	2237±2	2330±0	A_{exp} (CCD cts) 1.6e+05±9.2e+04
FWHM (cm^{-1})	84±8	163±23	137±36	134±16	50±7	157±7	13±1	τ_{exp} (fs) 13.2±1.6
	10%(3%)	14%(6%)	26%(5%)	12%(2%)	15%(7%)	5%(2%)	4%(1%)	
Area (n.u.)	18±4	63±18	25±8	19±5	3±1	11±3	9±2	
	23%(7%)	29%(2%)	34%(7%)	24%(1%)	28%(5%)	29%(2%)	27%(1%)	

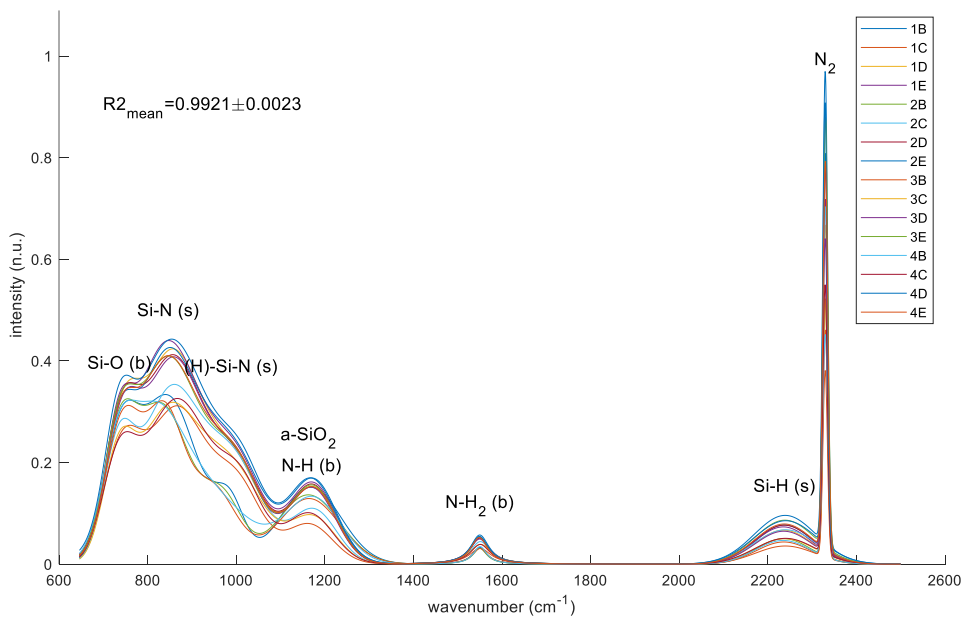


Figure 54: The total fitting spectrum for each WG. There are also reported the assignments where (s), (b) stays for stretching and bending vibrations. The mean R2 value and standard deviation over all the spectra are reported in the top left of the graph. The spectra have been taken at 785nm laser wavelength, full power, 40x objective and 0.3s of accumulation time

As can be seen the main difference between all the spectra is related to the peak area. This variation is much higher than the experimental and fitting errors and therefore are significant. It would be interesting to see the correlation between the areas and the WG design parameters such as width and probing length. But the not-probing region has not a constant cross-section (if $L' > 0.2 \text{ cm}$) and therefore a not direct correlation can be drawn. It is still interesting to see that the fitting procedure is consistent and gives good R2 values for multiple WGs. Almost all peaks' centres do not vary considerably which should be an indication of a good procedure. The only two considerably big variation in the peak centres are associated to Si-N stretching mode around 846 cm^{-1} and (H)-Si-N stretching at 989 cm^{-1} . This can be associated to the influence of the environment in which the bonds are. But it should not be excluded the possibility to add new components and therefore this shift could actually result in the change of intensity of 2 different bands. To appreciate and support this hypothesis more study should be needed.

4.4.3 Influence of power intensity on the spectra

To understand the influence of the power intensity on the background three different spectra were taken at respectively 12mW, 28mW and 55mW with 785nm laser wavelength. There are some main aspects to take into consideration:

- The Raman signal scales linearly with the power, therefore higher power and accumulation times should result in higher signal.
- High power intensity can introduce degradation of the sample or nonlinear effect. As it can be seen from Figure 55, second order phenomena are not registered, the spectra are equivalent and differs only by a scaling factor.
- High power or accumulation time can lead to saturation of the CCD camera. This limits the maximum power and integration time, especially when a high background is present.
- Lastly higher time of the measurements can be disadvantageous because it is time consuming. High accumulation times can be critical also when the set-up is not well stable. It could happen that due to mechanical instability the chip drift, therefore higher is integration time and there is much higher possibility to have a significant drift leading to out-coupling of the laser.

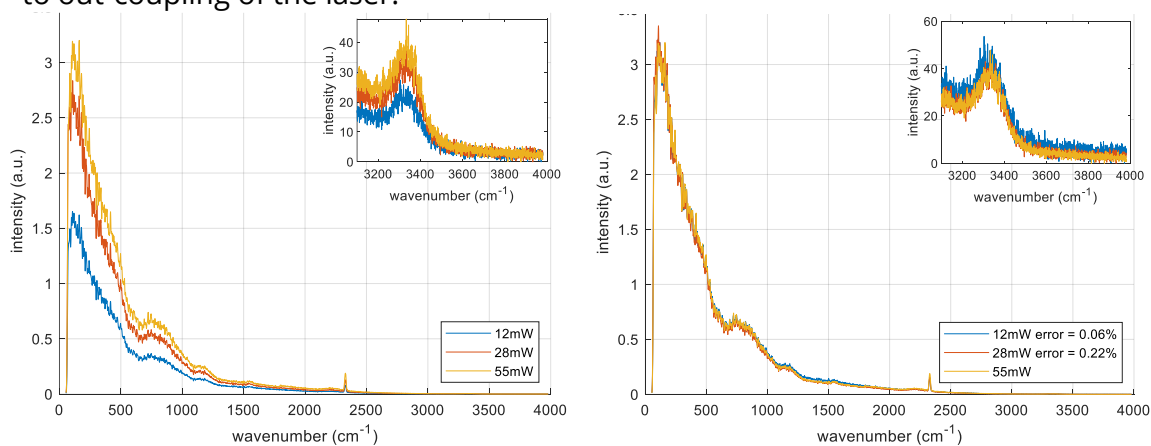


Figure 55: on the left: different spectra of SiN coming taken with different pump power. On the right: rescaled spectra by a coefficient to the 55mW spectrum as reference. The mean distance between 55mW and the rescaled spectra is also reported in % in the labels of the right image.

4.4.4 One single WG study with 633nm laser wavelength

It is interesting to report an example obtained with 633nm laser. The spectrum comes from a 3D WG with 100x/0.9NA objective, 0.1s integration time and 9.5mW power. In Figure 56, Figure 57 and Figure 58 the result of the spectrum fitting is reported and they are completely equivalent to Figure 51, Figure 52 and Figure 53. It should be noted the first difference between 785nm and 633nm is the great enhancement of the N_2 peak at 2330 cm^{-1} .

In Figure 56 it is interesting to notice that low frequency dominant background is still well approximated by an exponentially decreasing function. This reinforces the consideration that the signal is not fluorescence. By comparing the characteristic time there is a decrease from $\tau_{exp}(785nm) = 12.4\text{ fs}$ to $\tau_{exp}(633nm) = 11.2\text{ fs}$.

In Figure 56 are reported the results of the curve fitting. All the peak centres are comparable on what found with 785nm laser (Figure 52). The $R^2=0.9879$ (fitting error) is not an optimal value even if it can be related to the high noise of the spectrum. From the results shown in Figure 58 the $\langle\sigma_{noise}\rangle/\langle shot - noise \rangle \approx 7$, much higher with respect to what found with 785nm laser.

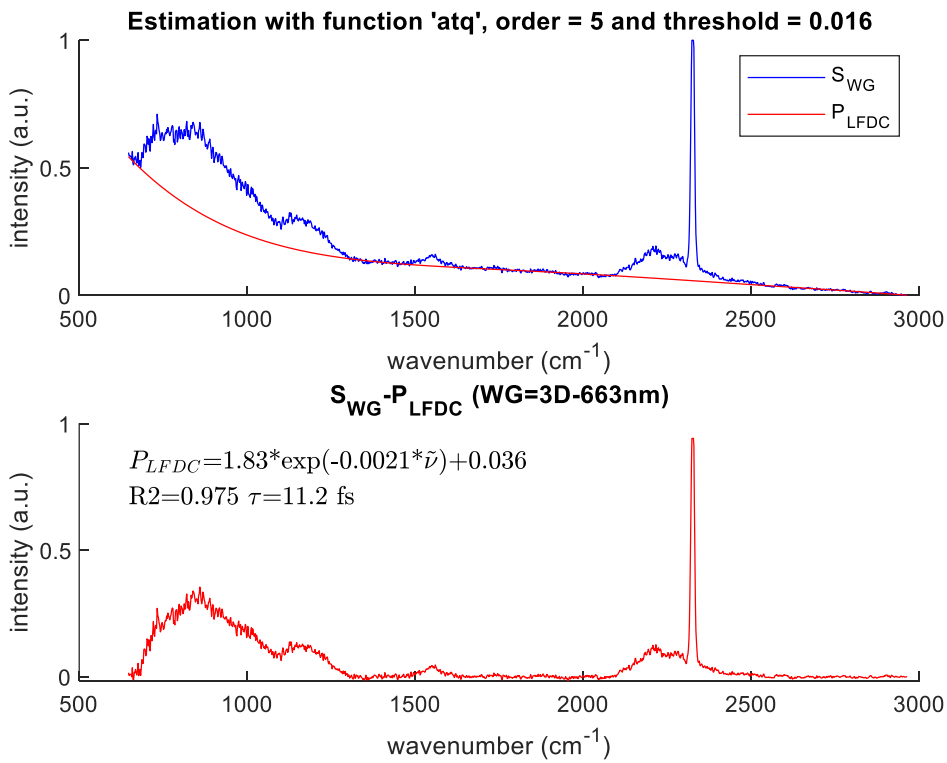


Figure 56: estimation of the P_{LFDC} with a 5th order polynomial fitted with an asymmetric cost function with threshold=0.016. in the bottom subplot the resulting spectrum obtained from the subtraction of $S_{WG} - P_{LFDC}$. The text shows results of the fitting of the P_{LFDC} with an exponential decreasing function.

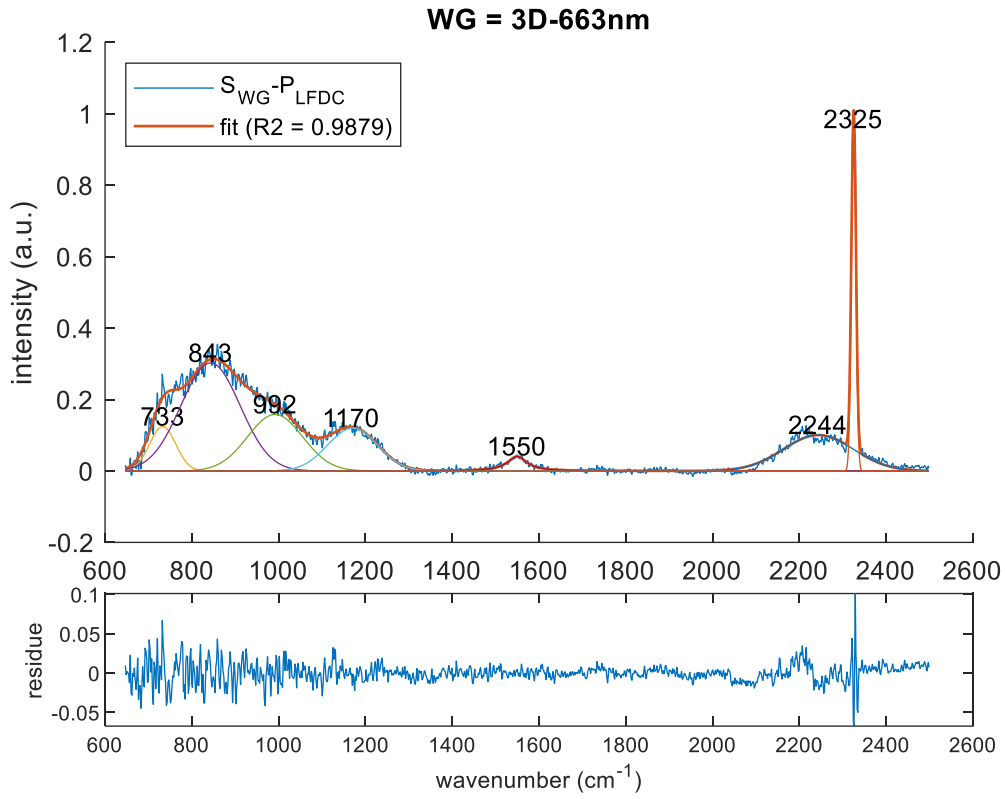


Figure 57: results of the fitting of the spectrum $S_{\text{WG}} - P_{\text{LFDC}}$. In the bottom subplot the residue is shown.

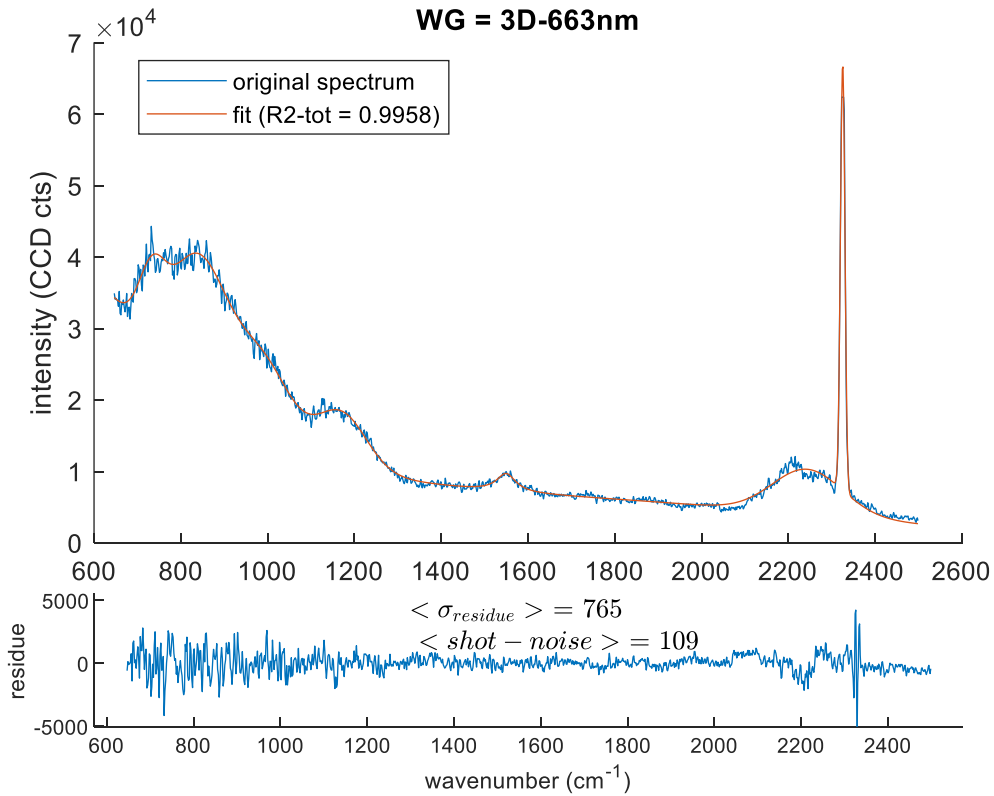


Figure 58: original spectrum obtained from 3D waveguide. in orange the total fit curve is represented. In the bottom subplot the residue is given by the fit and experimental data difference.

5 Parameters that influence the signal collection

In this chapter it is presented the influence of the SiO_2 cladded length and WG width on the Raman signal. First, it will be derived the model that should be more appropriate for describe our designs. Then it will be shown the main simulation results obtained with Lumerical mode solver. Finally, it will be compared the simulation results with the experimental one.

5.1 Strip waveguides realistic design model

The Raman scattering power collected by the waveguides with backward collection is now evaluated. Firstly, it will be considered a simpler design without cladding length ($L' = 0$), and then is introduced the presence of the cladded length as shown in Figure 59. It is defined L as the detection length and L' is the SiO_2 cladded length (or not-probing region).

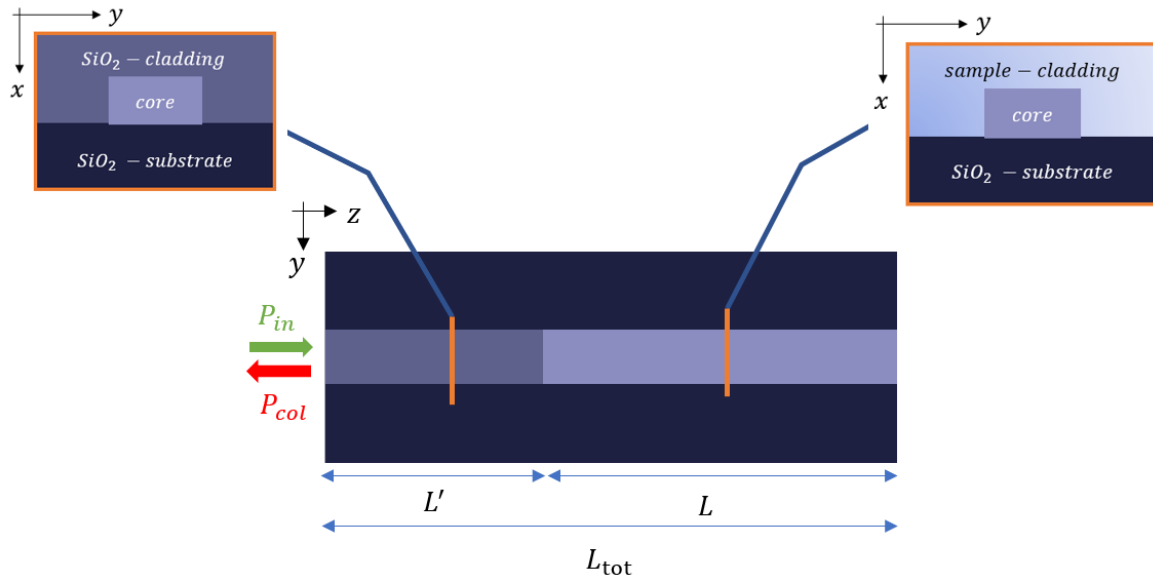


Figure 59: scheme of the chip design. L_{tot} is the total length, L is the probing length and L' is the not-probing SiO_2 cladded length. P_{in} and P_{col} are the incoming and collected power respectively. On the left and right insets two cross section of the WG are represented in order to underline the difference of the two regions and recall the different regions: cladding, core and substrate.

Similarly, as done by Ali Raza et al. (44) for a WG with $L' = 0$ and translational symmetry along the z direction, the conversion efficiency ξ of the cladding region can be calculated from equation 2.49. The result is:

$$\xi(\text{clad})|_{L'=0} = \frac{1}{2} \rho_{\text{clad}} \sigma_{\text{clad}} \eta(S_{\text{clad}}) \cdot \frac{1 - e^{-2\alpha_p L}}{2\alpha_p} \quad 5.1$$

If we are referring to the Raman signal coming from the WG core we should consider:

$$\xi(\text{core})|_{L'=0} = \frac{1}{2} \rho_{\text{core}} \sigma_{\text{core}} \eta(S_{\text{core}}) \cdot \frac{1 - e^{-2\alpha_p L}}{2\alpha_p} \quad 5.2$$

The ratio between the two is given by:

$$\frac{\xi(clad)}{\xi(core)} \Big|_{L'=0} = \frac{\rho_{clad}\sigma_{clad}\eta(S_{clad})}{\rho_{core}\sigma_{core}\eta(S_{core})} \quad 5.3$$

Where $\rho_{clad}\sigma_{clad}$ are related to the analytes and $\rho_{core}\sigma_{core}$ are associated to the core signal. If we neglect the signal coming from the SiO_2 substrate the ratio between the two conversion efficiencies corresponds to the signal to background ratio (SBR) recorded by the Raman spectrometer:

$$\frac{\rho_{clad}\sigma_{clad}\eta(S_{clad})}{\rho_{core}\sigma_{core}\eta(S_{core})} \approx SBR|_{L'=0} \quad 5.4$$

It is interesting that the length factors in the SBR are canceled out. Therefore, SBR is influenced by the Raman conversion efficiency factor and on $\rho\sigma$. The SBR is constant for any WG probing length. Figure 60 shows the SBR ($R_{S/B}$) experimentally evaluated as function of the probing length (59).

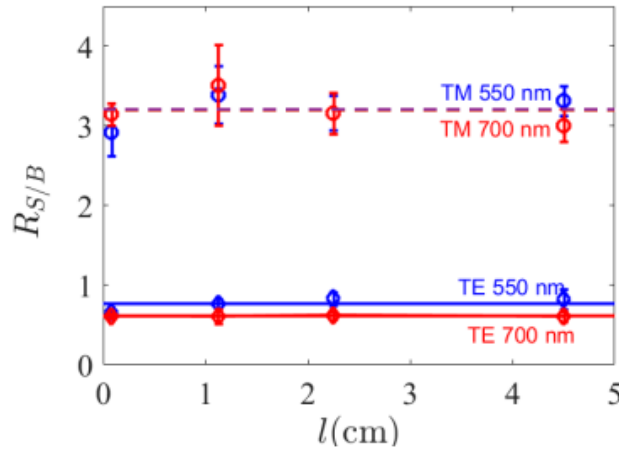


Figure 60: the SBR ($R_{S/B}$) experimentally evaluated as function of the probing length (59).

Equation 5.4 is valid in the assumption that SiO_2 signal is negligible. This hypothesis was introduced by Ashim Dhakal et al. (59) and they justified it by noticing that with laser wavelength of 785nm and 633nm the Raman signal of the SiO_2 is negligible with respect to the signal coming from the WG core. In that article they have evaluated experimentally the spectrum $\beta_{BG}(\tilde{\nu}) \approx \rho_{core}\sigma_{core}$ from an air cladded WG. It is a useful parameter to estimate the SBR. But the assumption of neglecting SiO_2 Raman signal is not trivial. As we have shown in chapter 4.4.1 in the region 700-1000 cm^{-1} the SiO_2 Raman signal cannot be excluded. Therefore, $\beta_{BG}(\tilde{\nu})$ should be associated to the SiO_2 substrate too and not only to the $a - SiN$ core. To be precise:

$$\begin{aligned} SBR|_{L'=0} &= \frac{\xi(clad)}{\xi(core) + \xi(sub)} \Big|_{L'=0} = \frac{\rho_{clad}\sigma_{clad}\eta(S_{clad})}{\rho_{core}\sigma_{core}\eta(S_{core}) + \rho_{sub}\sigma_{sub}\eta(S_{sub})} = \\ &= \frac{\rho_{clad}\sigma_{clad}\eta(S_{clad})}{[\rho_{core}\sigma_{core} + \rho_{sub}\sigma_{sub}\eta(S_{sub})/\eta(S_{core})]\eta(S_{core})} = \frac{\rho_{clad}\sigma_{clad}\eta(S_{clad})}{\beta_{BG}(\tilde{\nu})\eta(S_{core})} \end{aligned} \quad 5.5$$

Therefore: $\beta_{BG}(\tilde{\nu}) = \rho_{core}\sigma_{core} + \rho_{sub}\sigma_{sub}\eta(S_{sub})/\eta(S_{core})$. To still use $\beta_{BG}(\tilde{\nu})$ the assumption that should be made for strip WGs is that the ratio $\eta(S_{sub})/\eta(S_{core})$ is constant with respect to changes in WG width and cladding material. Therefore, with the introduction of $\beta_{BG}(\tilde{\nu})$ we have:

$$\frac{\rho_{clad}\sigma_{clad}\eta(S_{clad})}{\beta_{BG}(\tilde{\nu})\eta(S_{core})} = SBR|_{L'=0} \quad 5.6$$

In our design the presence of SiO_2 cladded length $L' \neq 0$ influence the Raman conversion efficiency. Since the equation 2.49 can be applied only for translationally invariant WG, knowing that $\xi = P_{out}/P_{in}$ the conversion efficiency of the not-probing region is given by:

$$\xi_{np} = \frac{1}{2} (\sigma\rho)_{np}\eta_{np} \frac{1 - e^{-2\alpha_{np}L'}}{2\alpha_{np}} \quad 5.7$$

Then for the probing region we should add an extra term related to the losses of travelling two times in the not probing region:

$$\xi_p = \frac{1}{2} (\sigma\rho)_p\eta_p\chi \frac{1 - e^{-2\alpha_pL}}{2\alpha_p} \quad 5.8$$

In presence of the not-probing region ξ_p shows an extra loss factor: $\chi \in [0,1]$. This factor is influenced by different contributions, associated to the design of the WG design of our chip:

- The bending losses of the two bends in the not-probing region. The bends should be designed to have as much as reduced losses.
- The coupling factor associated to the discontinuity between the probing and not-probing region.
- the scattering losses of the not-probing region α_{np} (it should be noticed α_{np} is the mean between the loss coefficient at pump and scattered frequency) and the not-probing length L' , which can express as $L' = xL$, where x is the length ratio.

If only the scattering losses are not negligible $\chi \approx e^{-2\alpha_{np}L'}$ and only if $\alpha_{np} \rightarrow 0$ we would have $e^{-2\alpha_{np}L'} \rightarrow 1$ and the losses would be negligible.

The second effect of the introduction of the not-probing region is the increase of the background signal. Therefore, the SBR is reduced. The complete evaluation is given by:

$$SBR = \frac{\xi_p(clad)}{\xi_p(core) + \xi_p(substrate) + \xi_{np}(clad) + \xi_{np}(core) + \xi_{np}(substrate)} \quad 5.9$$

To simplify the expression, in order to understand the main impact of the presence of the not-probing region, the SBR expression can be approximated by neglecting the Raman signal coming from amorphous SiO_2 , $\xi_p(substrate)$, $\xi_{np}(clad)$, $\xi_{np}(substrate)$:

$$SBR = \frac{\xi_p(clad)}{\xi_p(core) + \xi_{np}(core)} \quad 5.10$$

This approximation can be valid if the Raman cross section of amorphous SiO_2 is considerably lower with respect to the sample and core material at the wavenumber considered. The extended SBR writes:

$$SBR = \frac{(\sigma\rho)_{sample}\eta_p(S_{clad})e^{-2\alpha_{np}L'}\frac{1-e^{-2\alpha_pL}}{2\alpha_p}}{(\sigma\rho)_{core}\left[\eta_{np}(S_{core})\frac{1-e^{-2\alpha_pL'}}{2\alpha_p} + \eta_p(S_{core})e^{-2\alpha_{np}L'}\frac{1-e^{-2\alpha_pL}}{2\alpha_p}\right]}$$

By grouping out the properties related to the two materials, sample and WG core, and the two-conversion efficiency of the probing regions (η_p) the SBR becomes:

$$SBR = \frac{\rho_{sample}\sigma_{sample}\eta_p(S_{clad})}{\rho_{core}\sigma_{core}\eta_p(S_{core})}F_{np}(L, L') \quad 5.11$$

Where it has been introduced the not-probing factor, F_{np} . From the comparison with equation 5.3, we can see that equation 5.11 is a generalized case in which the upper limit for F_{np} is 1. The not-probing factor can be written as:

$$F_{np} = \frac{\eta_p(S_{clad})e^{-2\alpha_{np}L'}\frac{1-e^{-2\alpha_pL}}{2\alpha_p}}{\left[\eta_{np}(S_{clad})\frac{1-e^{-2\alpha_{np}L'}}{2\alpha_{np}} + \eta_p(S_{clad})e^{-2\alpha_{np}L'}\frac{1-e^{-2\alpha_pL}}{2\alpha_p}\right]} \quad 5.12$$

It can be simplified recognizing that the numerator is equal to a part of the denominator:

$$F_{np} = \frac{1}{e^{2\alpha_{np}L'}\frac{\eta_{np}(S_{core})}{\eta_p(S_{core})}\frac{\alpha_p}{\alpha_{np}}\frac{1-e^{-2\alpha_{np}L'}}{1-e^{-2\alpha_pL}} + 1} \quad 5.13$$

It is interesting that with the introduction of the not-probing region the SBR is no more a constant function with respect to the probing length L .

If we take as a reference $\alpha_p = 2.5 \text{ dB/cm}$, $\alpha_{np} = 0.6 \text{ dB/cm}$ and $\eta_{np}(S_{core})/\eta_p(S_{core}) = 1.05$ (obtained from simulation done in next chapter considering $w = 0.6\mu\text{m}$) the resulting F_{np} as function of L and L' are reported in Figure 61. The highlighted point data correspond to the detection length in our chips. In the Figure 61 on the left it shows three curves associated at three cases on which $L' = [0.2, 0.5, 1.7] \text{ cm}$. The presence of cladded WGs contribute to F_{np} decrease affecting the maximum achievable as shown by the orange arrow.

In the Figure 61 on the right is shown again the decrease as function of the L' . The maximum cladded length for our chip design corresponds to $L' = 1.7\text{cm}$ which has a very low F_{np} in the order of 0.25. If by cleavage we reduce the chip cladded length to 0.2 cm the F_{np} should became 3 times larger.

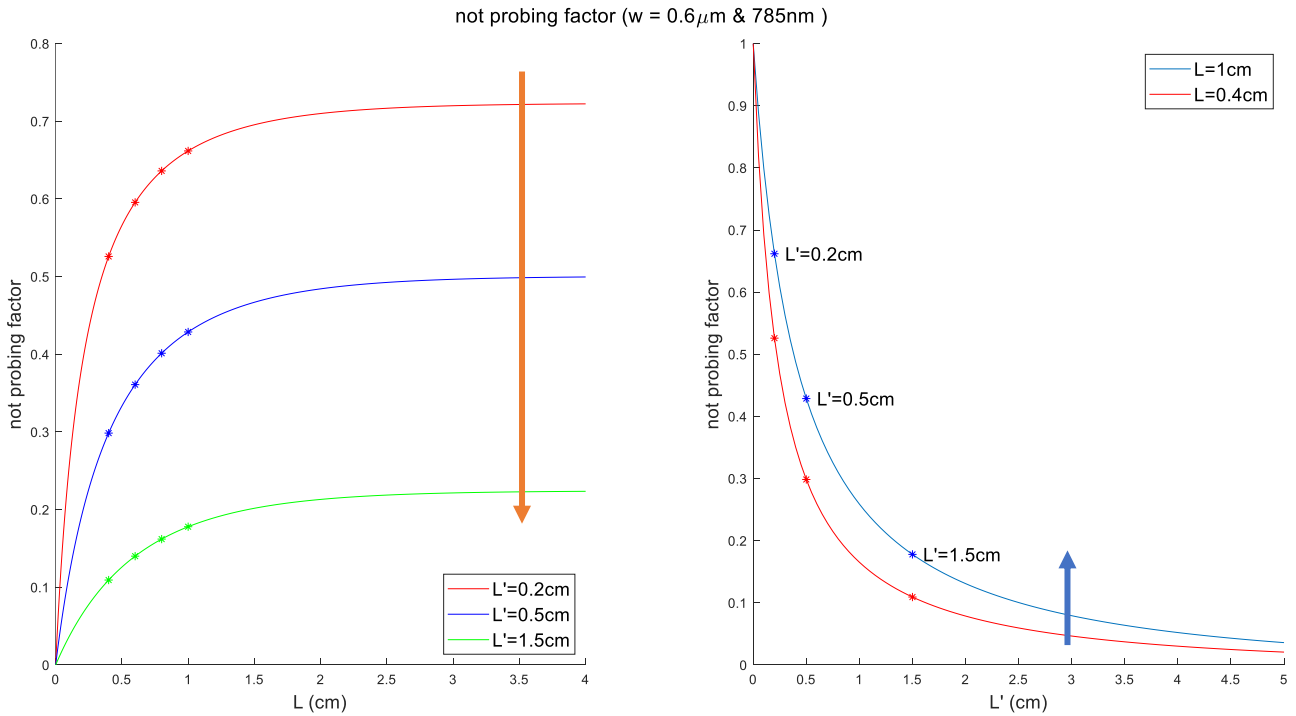


Figure 61 on the left not-probing factor (F_{np}) as function of the detection length (L). The arrows show the trend due to the increase of L' , the decrease of the plateau limit is shown with an orange arrow. On the right image F_{np} as function of the SiO_2 cladded length (L') for two different probing length. It clearly shows the exponential decrease of F_{np} vs L' . The blue arrow highlights the effect of the increase of L . It is important to remind that $\text{SBR} \propto F_{np}$.

If both α_p and α_{np} are negligible the loss factor $1/\chi \approx e^{+2\alpha_{np}L'} \approx 1$ and the length factors simplifies as $\frac{(1-e^{-2\alpha x})}{2\alpha} \approx x$ the not-probing factor becomes simply:

$$F_{np} = \frac{1}{\frac{\eta_{np}(S_{core})}{\eta_p(S_{core})} \frac{L'}{L} + 1} = \frac{L}{\frac{\eta_{np}(S_{core})}{\eta_p(S_{core})} L' + L} \quad 5.14$$

Equation 5.14 underline the second contribution of the not-probing length on the SBR. It is associated to the generation of an extra contribution on the background signal. If the losses are negligible the plot in Figure 61 on the right should result in a hyperbolic trend.

Therefore, it has been shown how the not-probing factor, which determines the SBR, it is a key parameter in the chip design, and this was not taken into account in the current design.

By looking at equation 5.9 if we do not neglect the SiO_2 Raman signal and take into account that from the literature can be evaluated $\beta_{BG}(\tilde{\nu})$, the not approximated SBR formula becomes:

$$SBR = \frac{\rho_{sample}\sigma_{sample}\eta_p(S_{clad})}{\beta_{BG}\eta_p(S_{core})} F_{np}(L, L') \quad 5.15$$

Where the resulting not-probing factor becomes:

$$F_{np} = \frac{1}{1 + \frac{1}{\chi} \left[\frac{(\rho\sigma)_{SiO_2}}{\beta_{BG}} \frac{\eta_{np}(S_{clad})}{\eta_p(S_{core})} + \frac{\eta_{np}(S_{core})}{\eta_p(S_{core})} \right] \frac{\alpha_p}{\alpha_{np}} \frac{1 - e^{-2\alpha_{np}L'}}{1 - e^{-2\alpha_p L}}} \quad 5.16$$

as we can notice if we need to consider SiO_2 we should add an extra term in the square parentheses.

5.1.1 Recall of the main theoretical results

There are two different strategies in order to compare the data between the theoretical model and the experimental data with the backward configuration.

The first one consists in the evaluation of the actual signal intensity of the analytes and compare it with the spectrum obtained after subtraction. I recall the main formulas from the previous chapters here:

$$\frac{C_s}{t} = \xi \cdot C_{ext} \quad 2.57$$

Where:

$$C_{ext} = \frac{\lambda_s}{hc} \cdot P_{in} \cdot \gamma_{in} \cdot \gamma_{out} \cdot T_{MO} \cdot T_{spec} \cdot \frac{QE(\lambda_s)}{\psi} \quad 2.57$$

C_{ext} is given by γ_{in} and γ_{out} are the coupling coefficients between the WG-objective coming in and out from the WG; the losses in the microscope optics, T_{MO} (the presence of the pinhole and filters) and in the spectrometer transmissions, T_{spec} ; the power coming from the objective P_{in} , the CCD counts per second (C_s/t), the $QE(\lambda_s)$ is the quantum efficiency of the detector (number of electrons/photon) and ψ is the CCD sensitivity (number of electrons/count).

$$\xi = \frac{1}{2} \rho_{sample} \sigma_{sample} \eta_p(S_{clad}) \cdot \frac{1 - e^{-2\alpha_p L}}{2\alpha_p} \chi \quad 5.8$$

The collection efficiency ξ is influenced by the scattering cross section σ_{sample} and density ρ_{sample} , the conversion efficiency of the cladding region $\eta_p(S_{clad})$, the losses in the probing region α_p and the probing length L and the extra loss factor χ .

Another way it is possible to evaluate the signal to background ratio. From equation 5.16 in the approximation that $\chi \approx e^{-2\alpha_{np}L'}$ and neglecting the signal coming from the cladding in the not-probing region, this is valid as far as: $(\rho\sigma)_{SiO_2} < \beta_{BG}$ and $\eta_{np}(S_{clad}) < \eta_p(S_{core})$:

$$SBR = \frac{\rho_{sample}\sigma_{sample}\eta_p(S_{clad})}{\beta_{BG}\eta_p(S_{core})} \frac{1}{e^{2\alpha_{np}L'} \frac{\eta_{np}(S_{core})}{\eta_p(S_{core})} \frac{\alpha_p}{\alpha_{np}} \frac{1 - e^{-2\alpha_{np}L'}}{1 - e^{-2\alpha_p L}} + 1} \quad 5.17$$

Each strategy takes a similar amount of effort since for both cases we need to estimate α_{np} , α_p and $\eta_p(S_{clad})$. But in the first case we should estimate $\gamma_{in}\gamma_{out}$ and on the second case we need to evaluate $\eta_{np}(S_{core})$ and $\eta_p(S_{core})$. From the literature and manuals ρ_{sample} , σ_{sample} , β_{BG} and C_{ext} can be found.

The advantage of using the SBR is that it should eliminate the uncertainty related to the coupling efficiency factor and also because it is a more meaningful value, instead of comparing the actual signal intensity alone. To think in terms of SBR is better to approach the problem, since to have improvements, the background can decrease. Therefore, SBR has been chosen as the figure of merit for this device.

Therefore, it should be summarized the main factors influencing the SBR. If $L' = 0$ there are two factors to consider:

- The WG losses of the probing region α_p .
- The ratio of Raman conversion efficiencies of the probing region in the cladding area and the core one, $\eta_p(S_{clad})/\eta_p(S_{core})$, defined as core-to-cladding conversion ratio (CCR): $\eta_{C/B}$.

With the introduction of the not-probing region the not-probing factor $F_{np} < 1$ should be considered. This factor is not constant with respect to the probing length and therefore SBR becomes function of L . The two main factors that decrease F_{np} are:

- The increase of the background signal associated to the not-probing length L' .
- The loss factor χ associated to local losses due to bindings and change of the fundamental guiding mode, and the scattering losses.

In the next chapters will be evaluated the Raman conversion efficiency (by simulation) and the scattering losses of the probing region (experimentally estimated). From those data can be obtained an estimation of the SBR which would be useful to critically discuss the experimental results. In particular the influence of the not-probing length will be analyzed and then discussed the influence of the WG width on the SBR. The WG width will influence both losses and collection factor.

5.2 Conversion efficiency calculation

The η_i can be evaluated summing up the previous equations: 2.45, 2.46 and 2.48. It is obtained:

$$\eta_i = \iint_{S_i} \frac{\lambda_s^2 \cdot n_g(\omega_p) n_g(\omega_s)}{\tilde{A}_{eff}(\vec{r}_0, \omega_p) \tilde{A}_{eff}(\vec{r}_0, \omega_s) n(\omega_s)} d\vec{r}_0 \quad 5.18$$

$$\tilde{A}_{eff}(\vec{r}_0, \omega_p) \equiv \frac{\int \int_{\infty} \varepsilon_r(\vec{r}, \omega_p) |\vec{E}_m(\vec{r}, \omega_p)|^2 d\vec{r}}{|\vec{E}_m(\vec{r}_0, \omega_p)|^2} \quad 5.19$$

Where λ_s is the scattered wavelength, n_g is the group index of the WG, ω_p and ω_s are the angular frequency of pump and scattered light, $n(\omega_s)$ is the refractive index of the medium where the scattering particles are located and $\tilde{A}_{eff}(\vec{r}_0, \omega_p)$ is the effective mode area at the molecule position (\vec{r}_0), $\varepsilon_r(\vec{r}, \omega_p)$ the relative dielectric constant, $\vec{E}_m(\vec{r}, \omega_p)$ is the electric modal field and S_i is the integration surface. Form these two equations we obtain:

$$\eta_i = \lambda_s^2 \cdot \frac{n_g(\omega_p) n_g(\omega_s)}{n(\omega_s)} \frac{1}{\text{integral1}|_{\omega_p}} \frac{1}{\text{integral1}|_{\omega_s}} \text{integral2} \quad 5.20$$

In which:

$$\text{integral1}|_{\omega_p} = \iint_{\infty} \varepsilon_r(\vec{r}, \omega_p) |\vec{E}_m(\vec{r}, \omega_p)|^2 d\vec{r} \quad 5.21$$

$$\text{integral1}|_{\omega_s} = \iint_{\infty} \varepsilon_r(\vec{r}, \omega_s) |\vec{E}_m(\vec{r}, \omega_s)|^2 d\vec{r} \quad 5.22$$

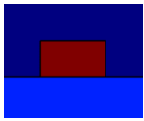
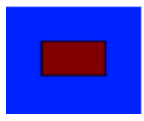
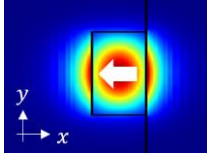
$$\text{integral2} = \iint_{S_i} |\vec{E}_m(\vec{r}, \omega_p)|^2 |\vec{E}_m(\vec{r}, \omega_s)|^2 d\vec{r} \quad 5.23$$

Where: $n_g = \text{group index of the mode}$, $n = \text{refractive index at the location of the molecule}$, and ω_p and ω_s is the pump and scattered frequency. To evaluate *integral1* and *integral2* we need to evaluate the supported modes in the waveguide, \vec{E}_m . FDE Lumerical simulation find n_g and \vec{E}_m , the input needed for the simulation are:

- The specifics of the physical problem: the geometry of the waveguide: $w \times h$. The pump wavelength, λ_p and Raman shift recorded $\tilde{\nu}_s$. The refractive index map: $n_{analyte}$, n_{SiN} and n_{SiO_2} . The integration area over which the Raman signal is generated (S_{core} or S_{clad}). The mode selected for the Raman conversion efficiency evaluation is the TM01 mode since all the experiments are done with TM polarized source.
- The input for the simulation region: mesh size: Δy and Δz . Simulation region dimension: FDE y_span and z_span . The boundary conditions are set on absorbing boundaries (PML). They simulate an infinite space within a finite computational grid. These boundaries attempt to absorb all incident fields, without creating any back reflection. The only exception is for the boundary condition "z min bc" set on "Symmetric" (in our reference system is the \hat{u}_y direction that is set symmetric). The symmetric boundary condition allows to reduce the calculation time and exclude the calculation of the fundamental TE mode.

$\eta_p(S_{clad})$, $\eta_{np}(S_{core})$, $\eta_p(S_{core})$ and $\eta_{np}(S_{clad-sub})$ are evaluated for the different WGs geometry. In Table 9 is reported the resume of all the parameters. The material dispersion relations are reported in Figure 65. The script used can be found in chapter A.3. From now on we will refer $\eta_p(S_{clad}) = \eta_{analyte}$, e.g. η_{IPA} .

Table 9: Input for evaluation of the Raman conversion efficiency η . Each column shows which are the values used, some of the values are in common therefore for some rows, the columns are joint.

	$\eta_p(S_{clad})$	$\eta_p(S_{sub})$	$\eta_p(S_{core})$	$\eta_{np}(S_{core})$	$\eta_{np}(S_{clad-sub})$
Plot name	$\eta_{analyte}$	η_{SiO_2}	η_{SiN}	η_{SiN}	η_{SiO_2}
h [μm]	0.3				
w [μm]	[0.4, 0.6, 0.8, 1.0, 1.2]				
λ_p [nm]	[785, 633]				
$\tilde{\nu}_s$ [cm^{-1}]	822 (IPA) 814 (PMMA)				
refractive index map	$n_{SiO_2}(\lambda), n_{SiN}(\lambda)$ and $n_{analyte}(\lambda)$			$n_{SiO_2}(\lambda)$ and $n_{SiN}(\lambda)$	
	 <p>Figure 62: refractive index map of probing region in brown a-SiN, light blue is SiO₂, in blue the analyte</p>			 <p>Figure 63: refractive index map of not-probing region.</p>	
Integration area	S_{clad}	S_{sub}	S_{core}	S_{core}	$S_{clad} + S_{sub}$
Mode	TM01 mode ($\vec{E}_{TM} \perp \hat{u}_y$ & $\vec{E}_{TM} // \hat{u}_x$)				
	 <p>Figure 64: E map of TM01 mode. The arrows indicate the major E-field direction.</p>				

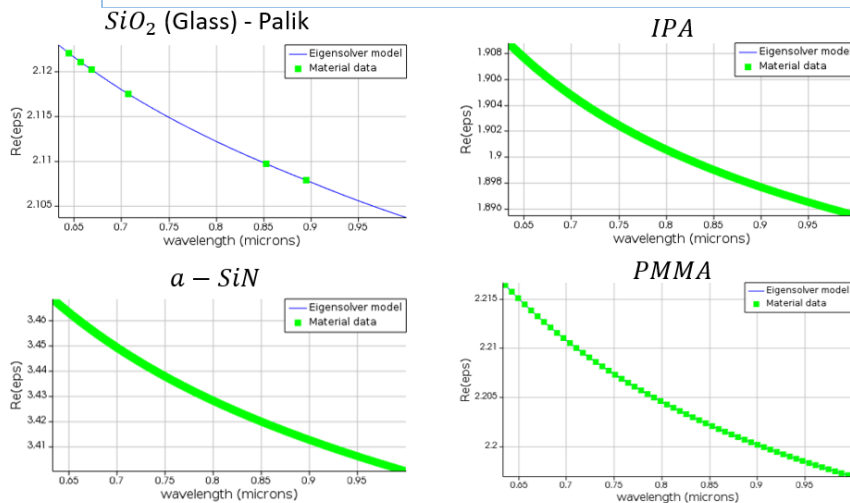


Figure 65: materials dielectric coefficients real components of silicon dioxide (Material data taken from Lumerical library), IPA and PMMA (Material data taken from (123, 124)) and silicon nitride (Material data taken from imec library). For the simulation a polynomial fit of the Material data is performed in order to obtain the Eigensolver model (blue line). The mean refractive index are: $n_{SiO_2} = 1.46$, $n_{SiN} = 1.85$, $n_{IPA} = 1.38$ and $n_{PMMA} = 1.48$ ($n_{H_2O} = 1.33$).

5.2.1 Simulation results for IPA

In Figure 66 it is reported the Raman conversion efficiency obtained from the simulation, with isopropyl alcohol (IPA) as analyte, as function of the WG width. In both plots (left and right) there is a general trend over which by increasing the waveguide width there is a decrease of the Raman conversion efficiency. As we can see in Figure 66 on the plot on the left (about the probing region):

- the η_{core} is much higher with respect to the η_{IPA} for the cladding region since the modal field is confined in the core of the waveguide. This is generally true for any strip WGs.
- for high widths the $\eta_{core}(785nm)$ is comparable to $\eta_{core}(633nm)$. But in the region lower than $0.8\mu m$ the $\eta_{core}(785nm)$ trend changes and at $0.4\mu m$ the $\eta_{core}(633nm)$ is 25% higher with respect to $\eta_{core}(785nm)$.
- Finally comparing η_{SiO_2} with η_{IPA} we can see that for a fixed waveguide width and pump wavelength the η_{SiO_2} is higher than η_{IPA} . The source of this difference is related to the difference in refractive index, since SiO_2 has higher refractive index with respect to IPA (1.38 for IPA and 1.46 for SiO_2).

The Figure 66 on the right shows the Raman conversion efficiency the not-probing region (SiO_2 cladded). By comparing η_{core} on the left and right plots of Figure 66 (the $\eta_{np}(S_{core})$ and $\eta_p(S_{core})$), the η_{core} of the not-probing region is lower with respect to that one of the probing region. This is associated to the higher mode confinement in the not-probing region.

Looking at the equations 5.11 and 5.13 it is interesting to plot two different ratios: $\eta_{nP/P} \equiv \eta_{np}(S_{core})/\eta_p(S_{core})$ (probing to not-probing conversion ratio, PCR) and $\eta_{S/B} \equiv \eta_p(S_{clad})/\eta_p(S_{core})$ (core to cladding conversion ratio, CCR) as function of the waveguide width and pump wavelength (Figure 67). It is important to underline their effect on the SBR here reported:

$$SBR \uparrow \text{ if } \eta_{S/B} \uparrow \text{ or } \eta_{nP/P} \downarrow \quad 5.24$$

Therefore, comparing the Figure 67 and equation 5.24 we can see that in terms of η it is more efficient a WG width of $0.4\mu m$. Looking at the Figure 67 on the left:

- for pump frequency of 785nm, comparing the values for waveguides width of 1.2 and $0.4\mu m$, the variation of the PCR is about 5%. Therefore, PCR dependence on the WG width is negligible.
- the variation between the same WGs but at different pump wavelength is about 2%.

Looking at the Figure 67 on the right:

- for pump frequency of 785nm, comparing the values for waveguides width of 1.2 and $0.4\mu m$, the variation of the CCR is about 36%.
- at 785nm CCR is around 2.5 times higher to that one at 633nm.

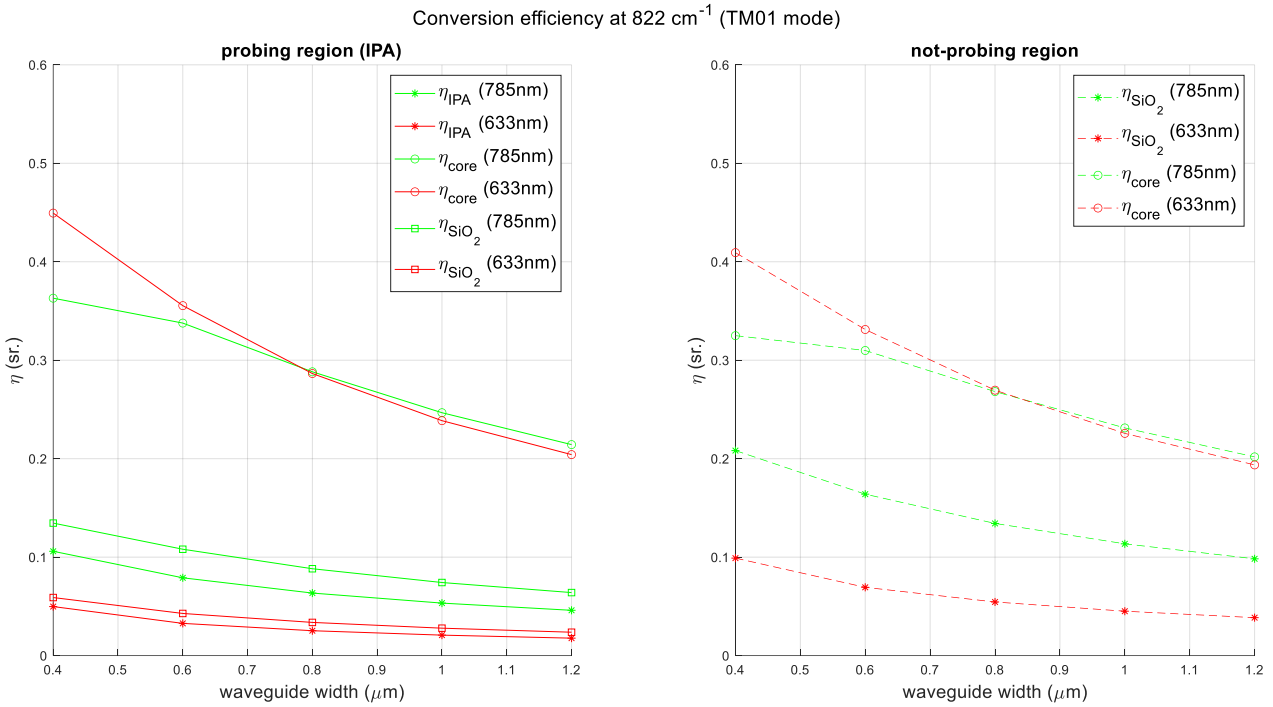


Figure 66: two plots of Raman conversion efficiency evaluated at 822 cm^{-1} Raman shift with light in TM01 polarization mode. On left the plot of η for the probing region with IPA on upper cladding in function of the waveguide width. On right the plot of η for the SiO_2 cladding region in function of the waveguide width. In each plots the η are evaluated for pump wavelength of 785nm and 633nm. Near the titles of the graphs on the top right and top left there are the two representations of the two regions respectively the SiO_2 cladding region and the probing region with IPA. These are simulation results.

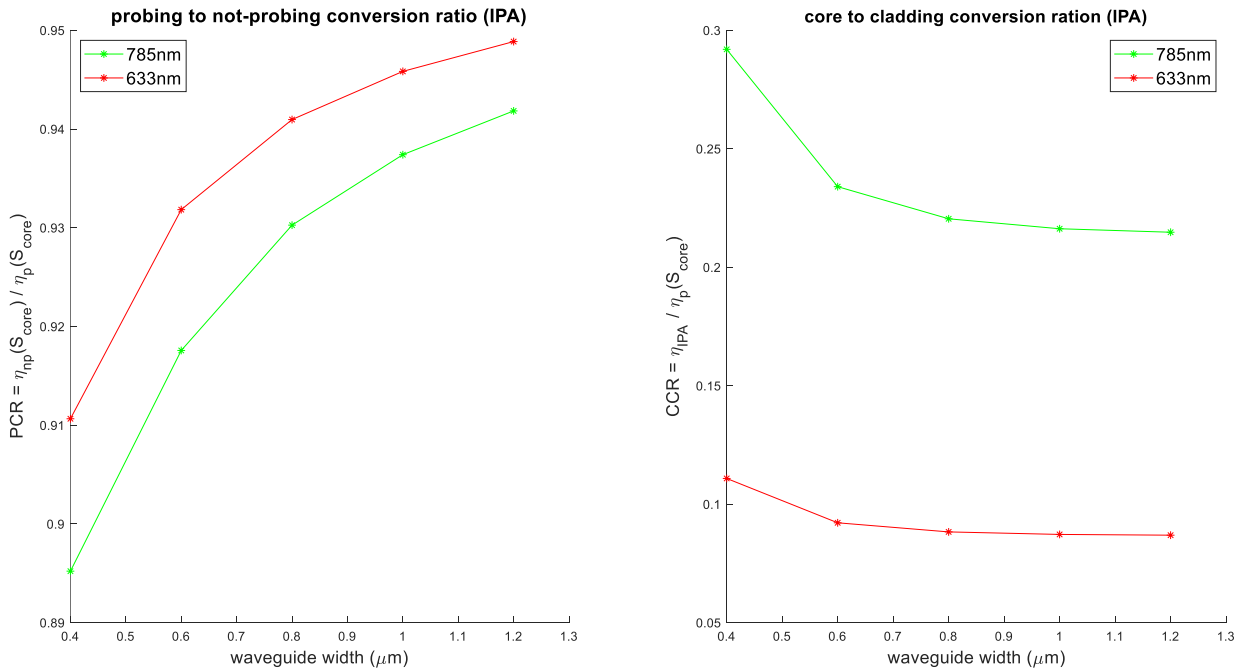


Figure 67: on the left the correction factor at the denominator of the not-probing factor ($\eta_{\text{np}}(S_{\text{core}}) / \eta_{\text{p}}(S_{\text{core}})$) in function of the waveguide width. On the right there is the coefficient the CCR ($\eta_{\text{IPA}} / \eta_{\text{p}}(S_{\text{core}})$), as we can see the distinguishable variance is given by the waveguide width of $0.4\text{ }\mu\text{m}$. These are simulation results.

5.2.2 Simulation results for PMMA

With the same approach done in the previous chapter, it has been calculated the results for poly (methyl methacrylate), PMMA. From Figure 68 on the right we can notice that:

- for pump frequency of 785nm, comparing the values for waveguides width of 1.2 and 0.4 μm , the variation of the factor CCR (core-to-cladding conversion ratio) is about 50%.
- the CCR at 785nm is around 2.5 times higher to that one at 633nm. It can be generalized that the difference between CCR from 785nm and 633nm is not dependent by the cladding refractive index (as it is reported in the appendix A.3.2).

For the PCR value (Figure 68 on the left) for both pump wavelengths the values do not change significantly for variation of the WG width (variation lower than 5%) and all the values are around 1. This can be interpreted that $\eta(\text{core})$ is not highly influenced by the cladding refractive index.

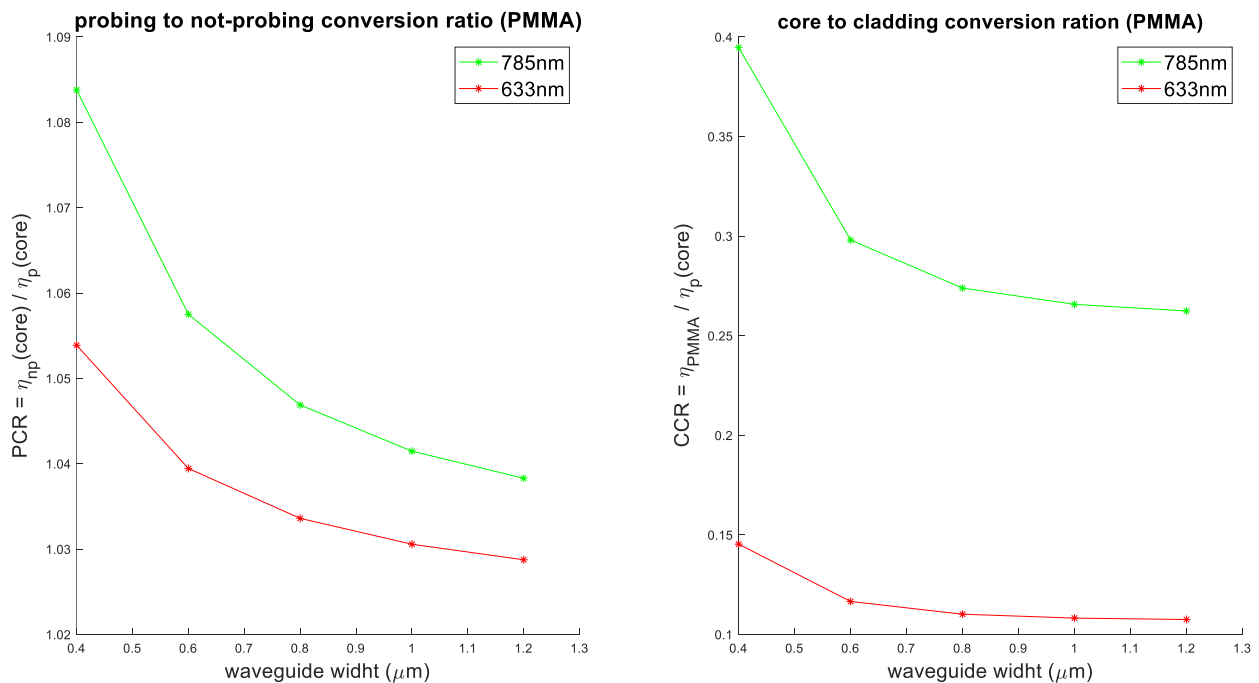


Figure 68: on the left the PCR in function of the waveguide width. On the right the CCR as function of the WG width. These values are obtained from simulation with Raman shift at 814 cm^{-1} . These are simulations result.

If we compare Figure 67 with Figure 68 we can notice that the major difference for both plot is the increase of the CCR for fixed wavelength and waveguide width. In particular, the CCR of PMMA is 40% higher with respect to CCR of IPA. This is related to the change of refractive index $n_{PMMA} = 1.48$ and for $n_{IPA} = 1.38$ which result in a decrease of the index of contrast from $\Delta n_{IPA} = 25\%$ to $\Delta n_{PMMA} = 20\%$.

In both cases with IPA and PMMA it is much more favorable the use of 785nm pump laser against 633nm laser in terms of CCR.

5.3 Scattering losses

In this chapter it will be studied how the scattering losses change as function of the WG width at 785nm wavelength. The n_w model combined with some experiemtal results will be used in order to estimate the trends and to have a rough idea of the magnitude of the loss coefficients.

5.3.1 Theoretical prediction of scattering losses

The n_w method is mentioned in chapter 2.2.2, with equation 2.38: i.e. $\alpha = A \cdot \partial n_{eff} / \partial w$. Therefore, it is firstly needed to evaluate how the effective refractive index change as function of the WG width. The results for all the possible cladding materials considered in this thesis are reported in Figure 69. It should be noticed that the WG width cut-off (i.e. the smallest WG width below which no propagating modes are allowed) is well below $0.4 \mu m$, which is the lowest WG width in our design.

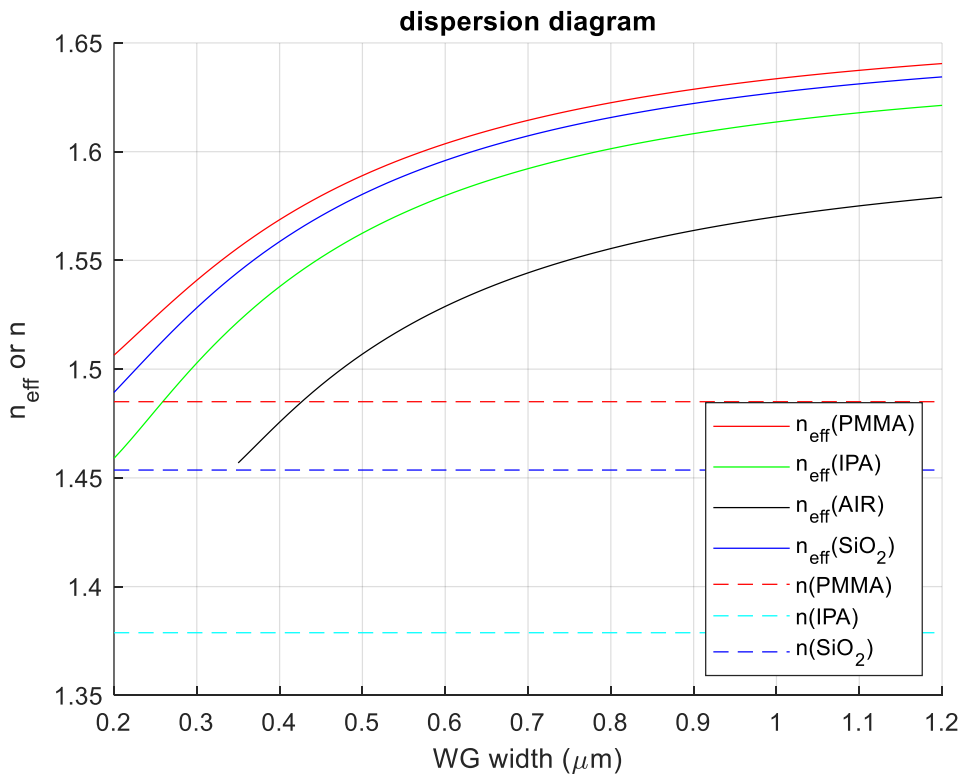


Figure 69: dispersion diagram for *a*-SiN WGs for different widths and cladding materials at 785nm wavelength for TM00 mode. These are simulations result.

From equation 2.38, it is possible to calculate the partial derivative from the dispersion diagram. The results are shown in Figure 70. As we can see by decreasing the WG width the scattering losses increases. This can be attributed to the increased interaction of the modal filed with the side wall surface, increasing the scattering losses. The influence of the refractive index result in an increase of the losses if the refractive index of contrast increase. Figure 70 capture well this trend, for example it can be noticed that at fixed WG width the $\partial n_{eff} / \partial w$ is higher for air with respect to PMMA. In particular α is proportional to the index difference $\Delta n^2 = n_{core}^2 - n_{clad}^2$ (125-

127). It should be reported that A of equation 2.38 is unknown but far from the cut-off it is not influenced by the WG width (80).

In addition, it should be underlined that α decreases as increasing the mode number (125-127). Therefore, for multimode WGs the coupling procedure is critical, since if there is a misalignment a high order mode could be preferentially excited leading to higher and unwanted losses.

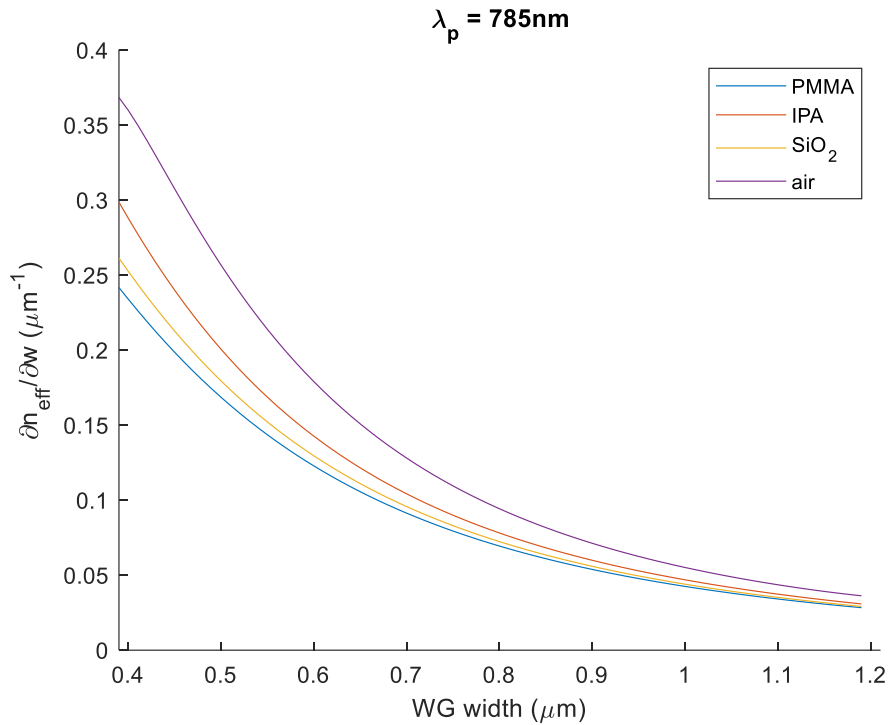


Figure 70: partial derivative of the dispersion diagram of the effective index against the WG width for different cladding materials. The $\partial n_{eff}/\partial w$ is proportional to the WG losses. These are simulations result.

5.3.2 Measurements of scattering losses

There are in the literature many different methods to estimate the scattering losses (128, 129). One of the most common is the cut back method (130). It requires WGs of different lengths and it is influenced by coupling losses (131). To overcome this limitation Regener et al. have exploited a Fabry- Pérot cavity (132).

A simple method for measuring the WG scattering losses is by direct observation with a camera on top of the WGs as reported by Yasuyuki et al. (133). It assumes that the scattered light intensity is proportional to that one propagating in the WG (134). This method has the advantage to be easily combined during the Raman measurements in the experiments. There are two main practical limitations to this approach:

1. The first one is related to the design itself of the WGs. As we can see in Figure 71 (subplot on the bottom right), the two red rectangles are the only 2 regions for each WG that can be taken into consideration, since the remaining part the losses overlap too much.
2. The second limitation is the evaluation of the losses from a length less than 0.8 *cm*. If the scattering losses are too low it will be not possible to appreciate a change in the intensity recorded.

The scattering losses are estimated for both samples, IPA and PMMA, with the 785nm laser. In Figure 71 is reported the fit to estimate the losses coefficients for IPA. In Table 10 there is the summary of the results obtained. It can be noticed that there are some loss coefficients that are negative. This is associated to the low length over which the measurement is performed. Although the high error on the estimated values, these are in line with the order of magnitude that researchers have found (61, 125).

For PMMA, the experimental scattering losses are not well estimated since most of them are negative and for 3E WG the α_p is much higher than the others. There is a common trend for which decreasing the WG width the scattering losses increases. This is in line with what expected.

Comparing PMMA and IPA loss coefficients it can be noticed that α_{PMMA} is lower with respect to α_{IPA} (most of the times). This is in line on what should be expected since the scattering losses should be proportional to Δn^2 .

For 3E WG the α_p is 11dB/cm much higher with respect to that one with IPA, 3.6dB/cm. This could be associated to some defect of that WG but looking at the image no particular local increase of the WG losses is present. Instead, there is a distributed increase of the scattering losses of the spiral, therefore it could be associated to a design limitation of the WG. This is further supported if is taken into consideration the scattering losses coming from "2" WGs series in Table 10. As it can be seen these results are like those obtained from "3" WGs series, with a high increase of the 2E WG. Therefore, it is more reasonable that the reason of the increase of the WG losses should be attributed to the decrease of the WG width to 0.4 μm . Taking into account this this abrupt increase could be attributed to the vicinity of the WG width to the cut-off width for which no propagating modes could exist in the WG. In this case the calculation performed are no longer valid and there is an exponential increase of the scattering losses.

Finally, it should notice that the mean of the errors associated to the fit is around 1.9 dB/cm. this error is in line on other paper (61) which used the same approach. A rule of thumb is that for scattering losses lower than 1 dB/cm this method gives negative results. So, we can interpret the negative values obtained experimentally as low loss WGs.

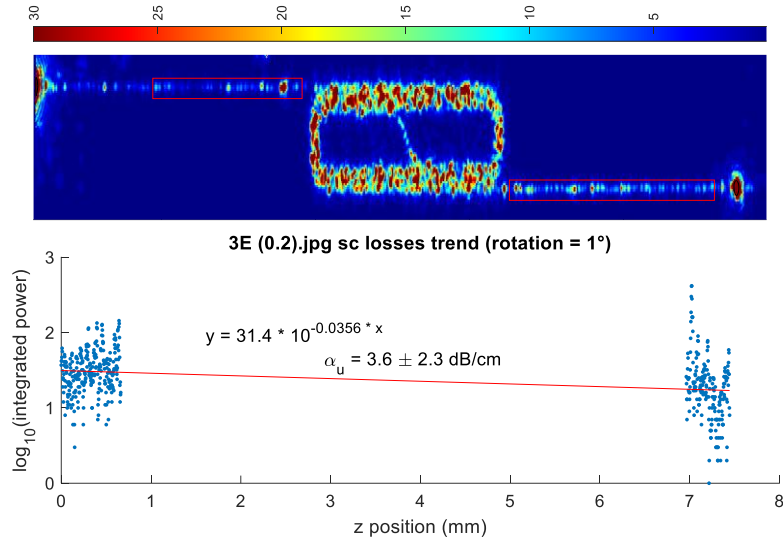


Figure 71: The top image shows an intensity map from of the scattering losses. The two red rectangles delimit the area over which the calculation is performed. The bottom plot represents the log10 of the scattered power integrated over one line (perpendicular over the propagation direction in the red rectangles) versus the z position, i.e. the WG length.

Table 10: summary of the scattering losses for IPA and PMMA as function of the WG width at 785 nm. The first two experimental values are obtained form 3 WGs, the last column refers to 2 WGs. It should be noted that 3WGs have lower uncertainty since loner portion of the WG can be used to evaluate the scattering losses. In the last column there is an estimation of the loss coefficients with the n_w model. It should be noticed that have a wide uncertainty.

WG width (um)	WG	Loss (IPA) [dB/cm]	Loss (PMMA) [dB/cm]	WG	Loss (PMMA) [dB/cm]	n_w model (PMMA) [dB/cm]
1.2	3A	-0.1±2.0	-2.8±1.7	2A	-0.7±3.8	0.14
1.0	3B	-1.8±2.2	0.0±1.6	2B	-0.7±3.6	0.2
0.8	3C	1.2±2.3	-0.6±1.7	2C	-0.2±3.8	0.3
0.6	3D	2.9±1.9	0.7 ±1.6	2D	-0.9±3.9	0.7
0.4	3E	3.6±2.3	11.2±1.9	2E	12.9±4.3	//

5.3.3 Comparison n_w model to scattering losses trends

It is interesting to compare the trend of the scattering losses measured experimentally with the simulations results obtained from the n_w model.

For example, in the case of IPA cladding, taking as reference 3E scattering losses, it can be estimated the A coefficient of the n_w model. It results $A = 12 \text{ dB/cm} * \mu\text{m}$. In Figure 72 the experimental data and the n_w model are plotted together. It can be seen a good agreement between the two trends, where the values of the WGs 3C and 3A almost overlap.

It should be noticed that for 3A loss coefficient the experimental value is negative (-0.1 dB/cm) and has a wide range of uncertainty (± 2.0 dB/cm). Therefore, to have an estimation of the loss coefficient for the 3A WG the most reasonable result is to use the n_w model prediction. It should be kept in mind that there is a wide uncertainty on this value.

With a similar approach the scattering losses of PMMA can be estimated. But PMMA most of the values are negative. Therefore, if we are sufficiently far from the cut-off, the A coefficient can be estimated (80). As said before the "E" WGs shows very high losses, which can be the results of excitation of leaky modes, since it is near or below the cut-off. The experimental result coming from 3D WGs has been chosen to calculate A factor. The n_w model together with the α_p values measured are shown in Figure 73. It is a rough estimation but at least we can capture both the trends and have an idea of the magnitude of the scattering losses. The estimated scattering losses are: 0.7 dB/cm; 0.3 dB/cm; 0.2 dB/cm and 0.14 dB/cm for the WGs 3D; 3C; 3B and 3A respectively. The last column of Table 10 reports these data. It should be noted that the results obtained suffer of a high uncertainty.

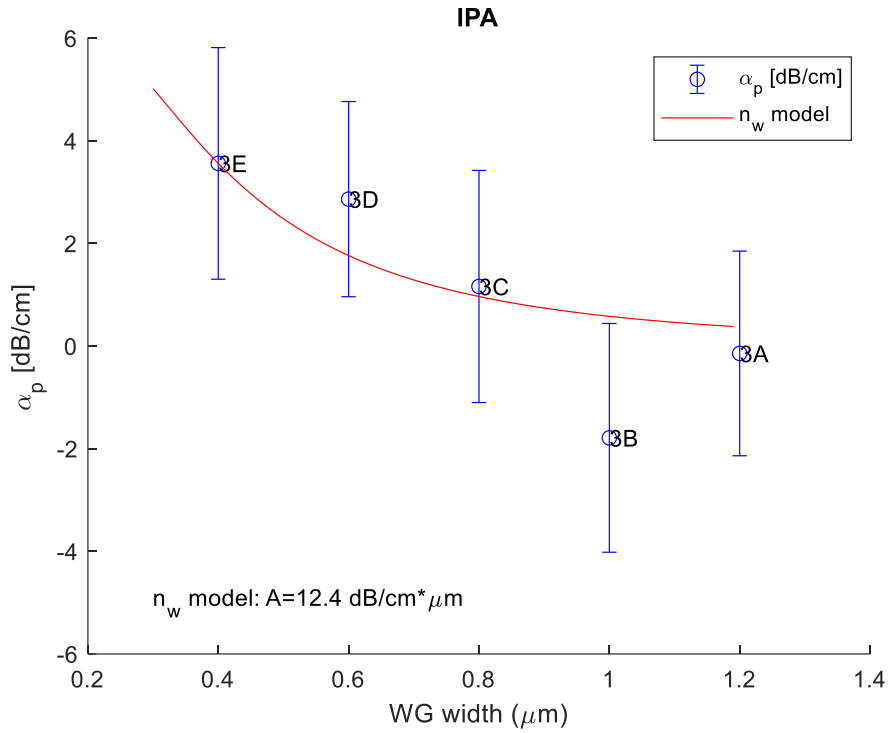


Figure 72: scattering losses experimentally determined (α_p) or simulated (with n_w model) of WGs with different width, with IPA cladding and 785nm laser. The A factor is estimated with 3E WG as reference (lowest relative error).

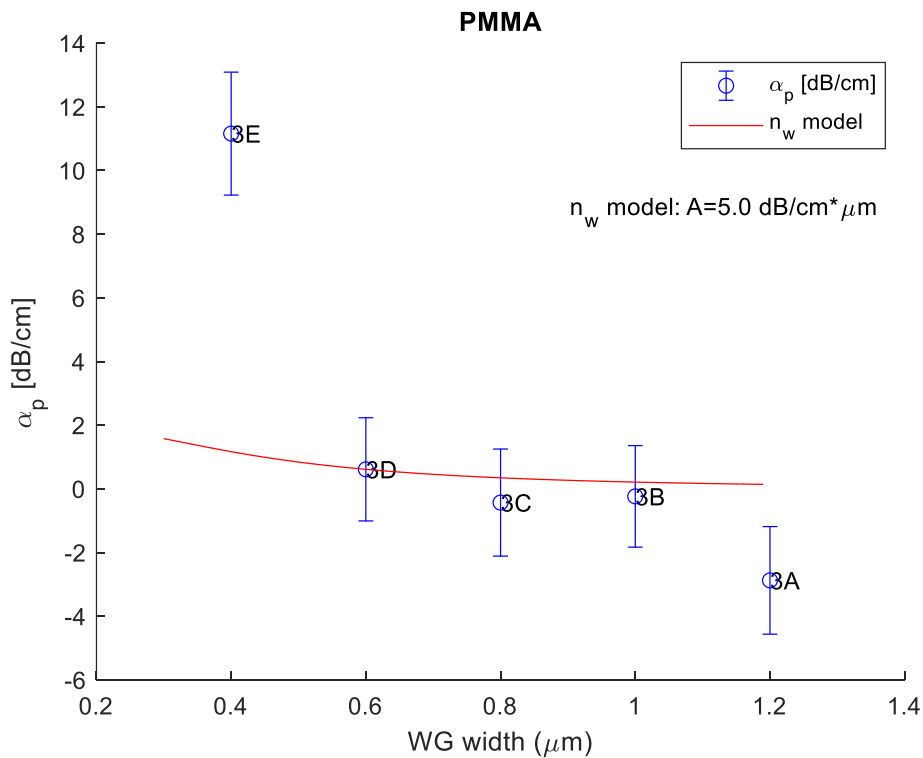


Figure 73: scattering losses experimentally determined (α_p) or simulated (with n_w model) of WGs with different width, with PMMA cladding and 785nm laser. The A factor is estimated from the experimental value obtained from 3D WG.

5.4 Influence of the probing length and cladded length on the SBR

5.4.1 Theoretical prediction

SBR can be estimated as function of the WG probing length (L) and cladded length (L'). The sample used is isopropyl alcohol (IPA), since it is cheap, easily available and other studies has been already used with this analyte. The SBR can be estimated from equation:

$$SBR = \frac{\rho_{IPA}\sigma_{IPA}}{\beta_{BG}} \eta_{S/B} \frac{1}{e^{2\alpha_{np}L'} \eta_{nP/P} \frac{\alpha_p}{\alpha_{np}} \frac{1 - e^{-2\alpha_{np}L'}}{1 - e^{-2\alpha_p L}} + 1} \quad 5.17$$

Where $\beta_{BG} = \rho_{BG}\sigma_{BG}$ can be found in literature (59) and at 822 cm^{-1} the $\beta_{BG} = 2.03 \cdot 10^{-9} \text{ sr}^{-1} \text{ cm}^{-1}$. Then IPA scattering cross section is $\sigma_{819} = 7.7 \cdot 10^{-31} \text{ cm}^2/\text{sr}/\text{molecule}$ and $\rho_{IPA} = 7.87 \cdot 10^{21} \frac{\text{molecules}}{\text{cm}^3}$. Therefore: $\sigma_{IPA}\rho_{IPA} = 6.07 \cdot 10^{-9} \text{ sr}^{-1} \text{ cm}^{-1}$. Combining the simulations results found in Figure 67 and the experimental one in Table 10 for a D WG (width $0.6 \mu\text{m}$), it results in $\eta_{nP/P} = 0.918$, $\eta_{S/B} = 0.234$, $\alpha_p = 2.9 \text{ dB/cm}$ (for 785nm pump laser). Finally, the loss coefficient of the not probing factor is taken from literature (125, 134): $\alpha_{np} = 0.6 \text{ dB/cm}$. It has been considered two cases on which $L' = [0.3, 1.7] \text{ cm}$.

The results in Figure 74 shows the trend of the SBR over the x , the ration cladded-detection length ($x = L'/L$). The order of magnitude of the SBR is 10^{-1} . In Figure 74 on the left shows that the experimental data are expected to lie on the transition region from a linear trend and a plateau one. In Figure 74 on the right shows that for $x=2$ ($L' = 1.7 \text{ cm}$) the SBR is 0.14 and for $x=0.4$ ($L' = 0.3 \text{ cm}$) the SBR is 0.38 (for $L = 0.8\text{cm}$). Therefore, it should be expected an increase in the SBR of 2.7 times if the chip is cleaved from a $x=2$ to $x=0.4$.

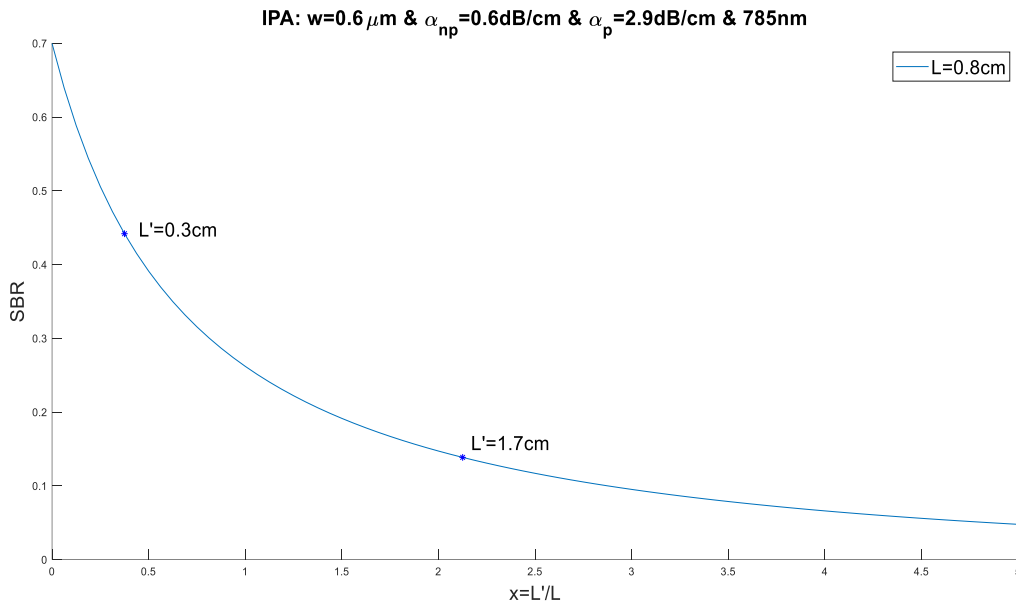


Figure 74: the SBR as function of the ratio not-probing/probing length ($x=L'/L$). In the title there are more info about the input values. There are some "*" highlighting the expected experimental data.

5.4.2 Raman spectra from IPA sample

The first measurements were performed with IPA sample. It was chosen IPA since it has been extensively used in literature. Unfortunately, all the measurements performed over all the WGs and with different chips no signal were recorded. In Figure 75 there are two examples of spectra collected. The characteristic IPA peak at 822 cm^{-1} (135) is not detected. It can be noticed that the spectrum obtained with laser full power results in a peak that could be assigned to IPA. But that signal suffers of poor signal to noise ratio (SNR). The SBR results equal to 0.15. Although higher power seems to increase the SBR it should be noticed that the noise is increased too.

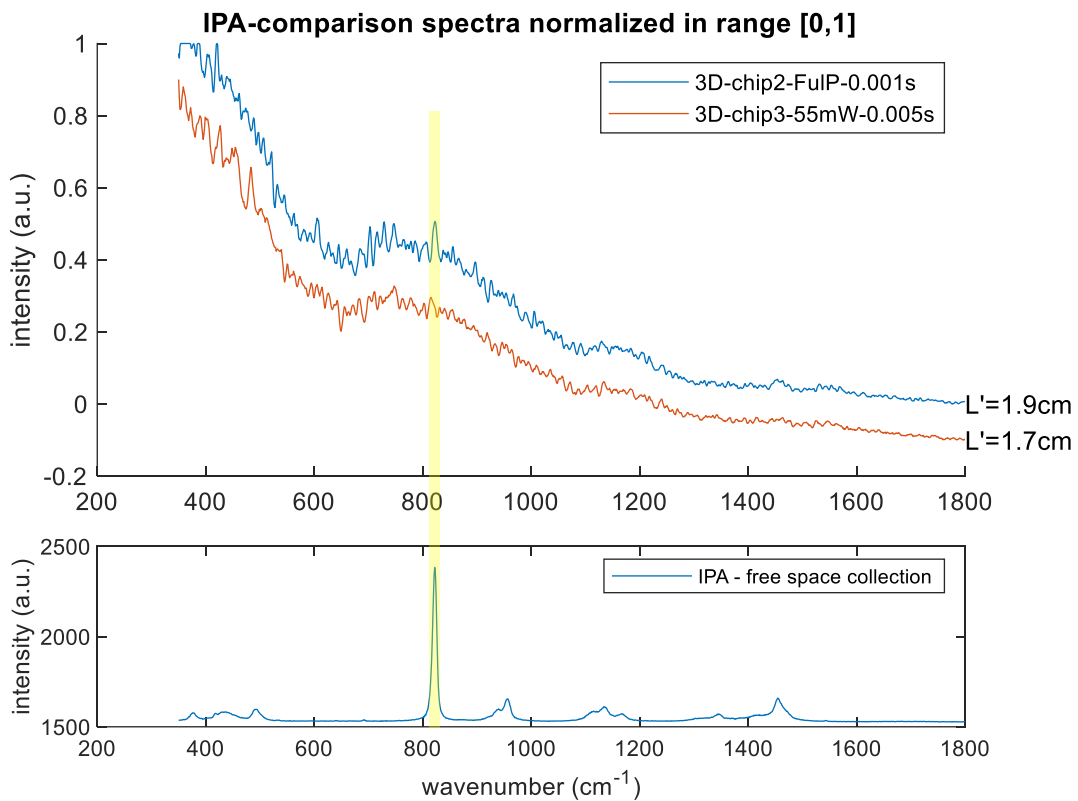


Figure 75: spectra obtained with 785nm pump laser and 40x objective, the other specifications are reported in the legend. The spectrum from chip3 is downshifted by 0.1. In yellow is highlighted the region where the most intense IPA peak is expected to be. $SBR(3D\text{-chip2-FulIP-}0.001s) = 0.17$ and $SBR(3D\text{-chip3-}55mW\text{-}0.005s) = 0.0$. In the bottom plot there is IPA Raman signal collected with 10x objective without the chip.

Then, it has been taken a new chip and cleaved in order to reduce the cladded length to $L' = 0.2\text{cm}$. The resulting spectrum obtained is reported in Figure 76 and compared to a signal one coming from a chip with $L' = 1.7\text{cm}$. It can be seen a much larger increase of the IPA peak, with respect to the other chip with $L' = 1.7\text{cm}$, and the resulting SBR is about 0.27. This result is sufficient to understand that the decision of reducing as much as possible the not-probing region is the correct one.

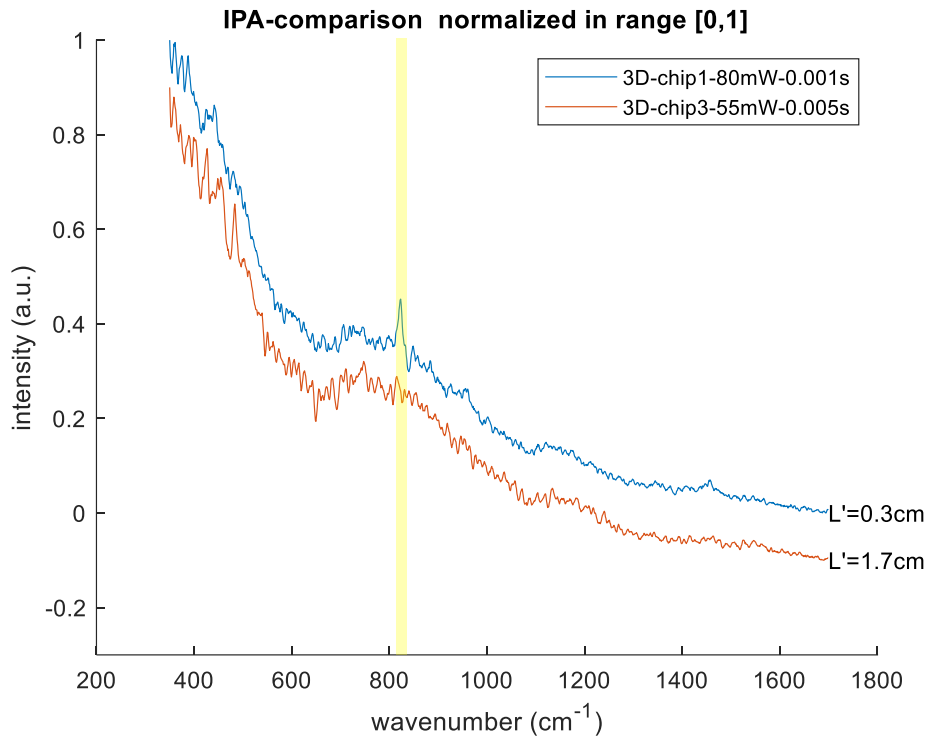


Figure 76: spectra obtained with 785nm pump laser and 40x objective, the other specifications are reported in the legend.

It can be noticed that the two spectra in Figure 76 are collected with different power and integration time, therefore it is not ideal to compare to each other. In my opinion this result is still remarkable since represents the first time that it can be clearly distinguishable the IPA peak over the background (i.e. with high signal to noise ratio).

In the last measurements there were some problems related to IPA evaporation that made much more difficult the measurements with such small chip with the current set up. Therefore, even though it could have created an improved set up it was preferred to change the sample used in the experiments.

In the next paragraph it will be presented experimental results with PMMA. The main advantage in using this kind of sample is that we do not need a liquid container for the experiments. The PMMA was deposited on the chip by using spin coating and the resulting thickness was measured with the confocal Raman microscope by z-scan, the resulting thickness is about $1 \mu\text{m}$.

5.5 WG width influence on the SBR

From this chapter PMMA spin coated will be used as sample under study. There were 5 chip spin-coated, among them two have been wasted due to bad cleavage. It should be noted that cleavage step even if simple is critical and fundamental in order to have good laser coupling. Among the 3 chips remaining one was studied with both 633nm and 785nm, with $L' = 1.5\text{ cm}$, and both strip and slot designs have been studied. No signal was detected from all of them. A second chip has been cleaved in order to reduce the not-probing length to $L' = 0.3\text{ cm}$. It has been studied only strip WGs, with 785nm laser wavelength, 40x/0.65NA objective but no signal has been recorded. By observation with Thor camera, it has been recorded high and anomalous scattering losses in correspondence of the first bending. This could be the origin of the no signal detection for the second chip. The last chip, cleaved at $L' = 0.2\text{ cm}$ resulted with good signal and the data obtained from that chip will be exposed.

5.5.1 Simulation

The WG width influence the SBR because of two factors:

- As the WG width decrease the scattering losses increase.
- As the WG width decrease the core to cladding conversion ratio decrease.

Therefore, it exists an optimal WG width which maximize the SBR. It should be noticed that the PCR is almost not affected by the WG width. The $\eta_{S/B}$ and $\eta_{nP/P}$ have been calculated for PMMA and the results are reported in Figure 68. The scattering cross section is evaluated from the literature, knowing that $\sigma \sim 1/\lambda_s^4$, it results that $(\rho\sigma)_{PMMA} = 2.88 \cdot 10^{-9}\text{ cm}^{-1}\text{ sr}^{-1}$ (136, 137) at 811 cm^{-1} with pump wavelength of 785nm (value similar to $\beta_{BG} = 2.03 \cdot 10^{-9}\text{ sr}^{-1}\text{ cm}^{-1}$).

The losses coefficients for the probing region the results taken from Table 10. The not-probing scattering losses, α_{np} , should be influenced by the WG width, too. Therefore, it has been estimated with the n_w model the values: 1.5 dB/cm; 0.8 dB/cm; 0.4 dB/cm; 0.3 dB/cm and 0.2 dB/cm for E, D, C, B, A WGs respectively (for more info about the calculations look at appendix chapter A.4.2).

The input can be found in Table 11. The results are shown in Figure 77. It can be noticed that due to the high scattering losses of the E WG series should have much lower SBR compared to the others. The order of magnitude of the SBR is around 0.3. The influence of the WG width on the SBR shows, as expected, an optimal width. The highest SBR predicted is 4D WGs.

Table 11: summary of the main input for the model of the SBR.

WG width (μm)	α_p (dB/cm)	α_{np} (dB/cm)	CCR	PCR	$\frac{(\rho\sigma)_{PMMA}}{\beta_{BG}}$	L' (cm)
1.2	0.13	0.14	0.26	1.0	1.42	0.2
1.0	0.2	0.3	0.27	1.0		
0.8	0.3	0.4	0.27	1.0		
0.6	0.5	0.6	0.30	1.0		
0.4	11	1.5	0.39	1.1		

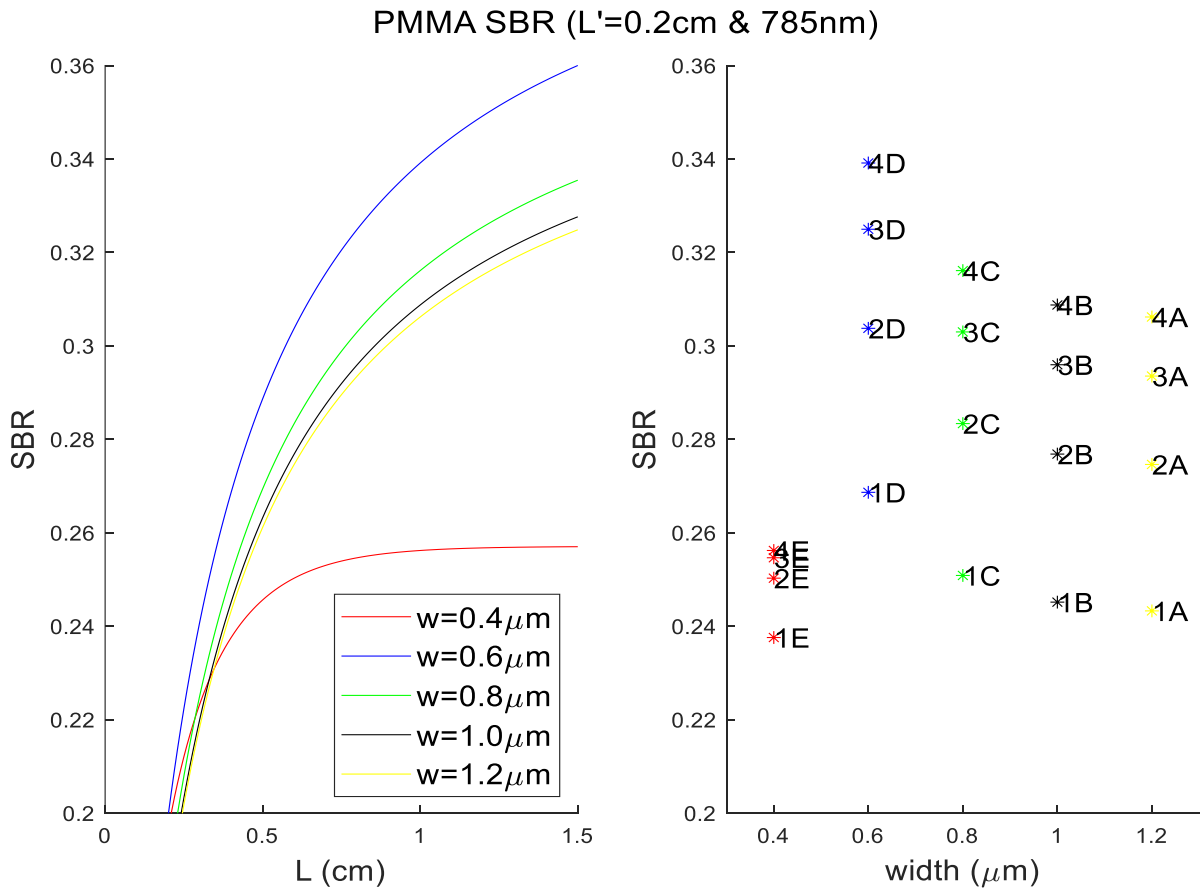


Figure 77: on the left the SBR as function of the probing length for different WG widths. On the right the SBR as function of the WG width (each colour defines the WG width), for different WGs. It should be noted that all the data plotted are simulations results.

5.5.2 Experimental results

From experiments it has been estimated the SBR as function of the WG width and probing length. The chip used was with PMMA spin coated on top. Raman spectra were collected from 20 different WGs two times. Unfortunately, due to technical problems the two set of measurements were performed with 25 days of distance, but still they can provide a reinforcement of the theory used and can give some insight of the time evolution of the PMMA coated. In Figure 78 is reported one example of one measurement of a 3D WG. More info about the single Raman spectra and some additional information's are reported in the appendix A.5. The peaks studied are at 814 cm^{-1} assigned to C-O-C symmetric stretching vibration (of the group C-COOCH₃) and at 1455 cm^{-1} assigned to C-H vibration (138). The standard procedure for evaluation of the SBR is reported in appendix "A.5.4 Standard procedure for evaluation the SBR". In Figure 78 on the right it is shown an example of the fitting procedure, the signal to background ratio is given by $SBR = S/B$.

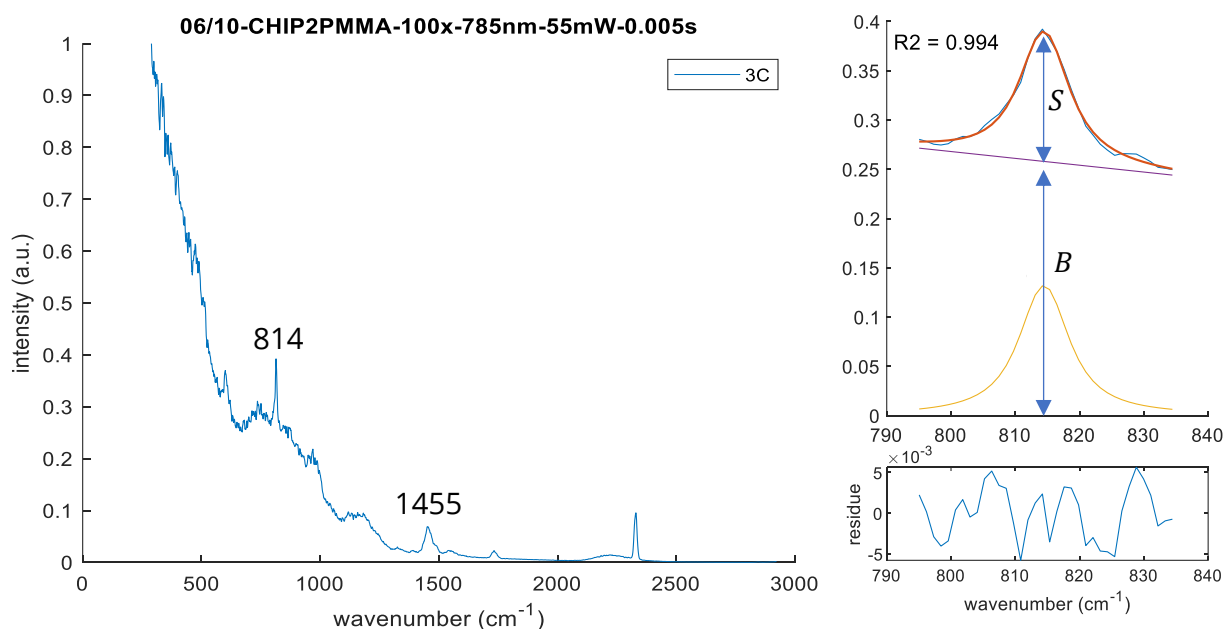


Figure 78: on the left the Raman spectra obtained from 3C WG coated with PMMA. All the parameters used to measure these spectra are reported in the title. On the right an example of the fitting procedure for the peak at 814 cm^{-1} and estimation of the signal intensity (S) and background (B). In yellow is the peak estimated, violet the linear background and in orange the sum of them.

The calculation results of the SBR are reported in Figure 79:

- The two plots on the left show SBR as function of the probing length. It can be noticed that SBR increases with increasing of L_{probe} . This demonstrate that the introduction of the not-probing factor in equation 5.11 for our model is fundamental to explain the experimental data.
- In both left plots, at fixed WG width (i.e. same color), the trend of the SBR as function of the WG probing length it is almost linear. This can suggest that the probing length could be increased much more. Considering the loss coefficient estimated $\alpha_p = 0.8dB/cm$ the probing length could be extended to 9 cm, such that the length factor is approximately at its plateau value (where $1 - e^{-2\alpha_p L} \approx 0.95$, the trend of the length factor is in Figure 26).
- Some deviations of the expected trend are associated to WGs 3D and 4D on the data collected the 06/07/2021. Up to now no logical explanation has been found to justify this behavior.
- For both plots the WG 4E has a clear deviation from the linear trend of the others E WGs. This could be explained by looking at previous measurements of the scattering losses (chapter 5.3.3). These high losses have been attributed to bending losses of the spirals. Looking at Figure 35 (page 49) if we consider that only the straight WG that connects the spiral collects Raman signal and after the power goes to zero, it is clear that the length of that path is given for each WG the sum of the length of the previous WGs and the length of the WG itself. For example, if WG number 1E has a length of 1cm and WG 2E has a length of 3cm so on the resulting probing length will be: 1,3,6,10 cm. There is a nonlinear increase of the probing length resulting in a high increase of the 4E SBR. This could be an explanation but no other data can support this idea, therefore it should be taken only as an hint.
- The two plots on the right shows how the SBR change as function of the WG width. If we compare with Figure 77 on the right it can be noticed a well agreement with the trend predicted by simulations. If we look the graph on the left the WGs with width of $0.6\mu m$ are the most efficient in terms of signal collection at 814 cm^{-1} wavenumbers.
- the values of SBR ranges from 0.13 to 0.63, with a mean value of 0.35. If compared to our simulation results in Figure 77, the SBR was underestimated. The origin of this error is not only associated to errors in the not-probing factors. If $F_{np} = 1$ the SBR predicted for D series is about 0.42, that is much lower than the maximum SBR registered of 0.63.

Finally, it should be noted that in principle the variation associated to the SBR is not affected by coupling losses, and therefore the variation between 2 equivalent measurements should be limited. Therefore, by comparing between two sets of measurements made on 10/06 and on 06/07 it could be noticed a general decrease of the SBR from a mean value of 0.4 to 0.3 after 25 days. This could be associated to a progressive oxidation of the C-O-C bonds with the environment, but more studies should be done.

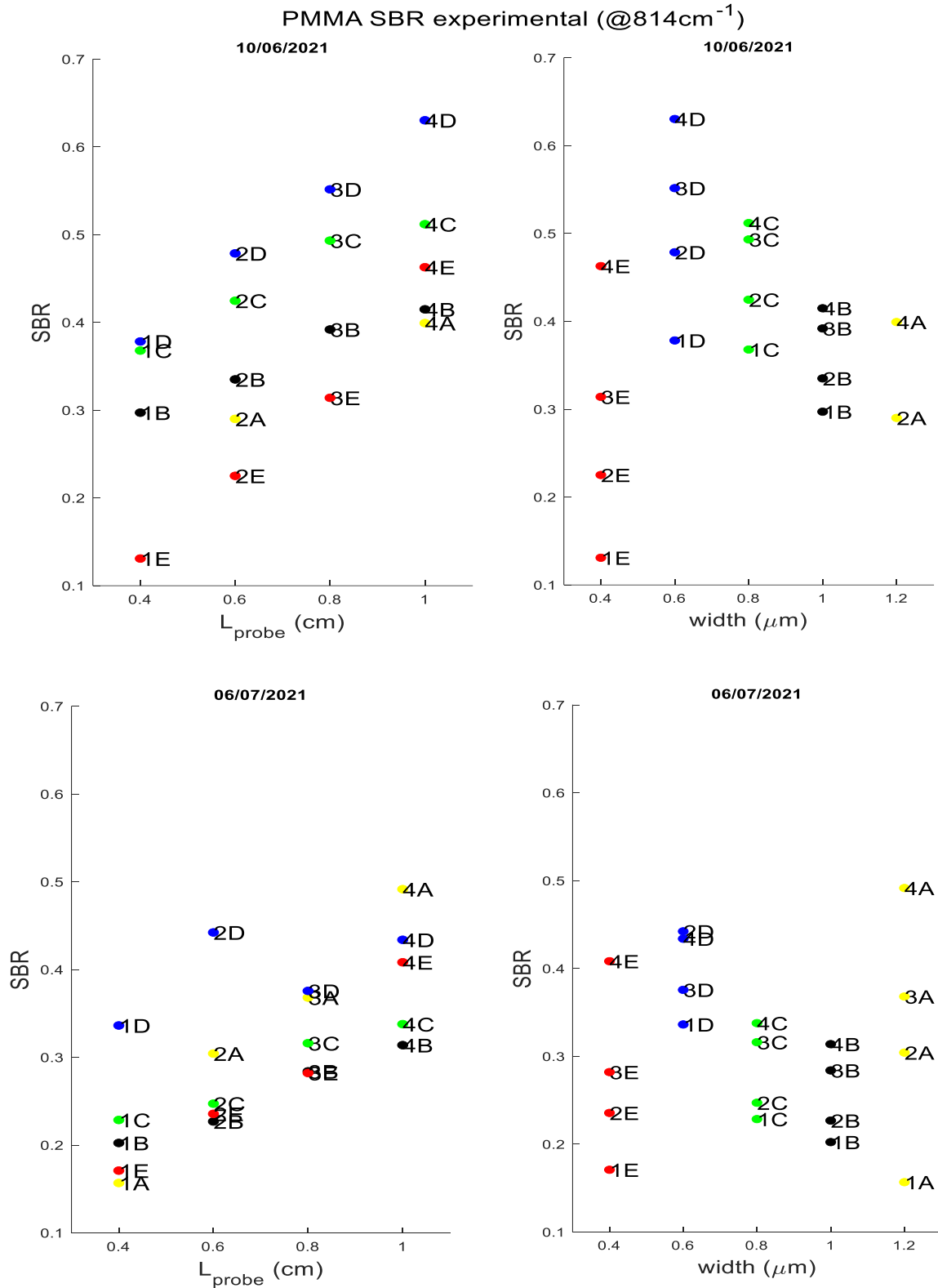


Figure 79: the two left show the SBR as function of the probing length for respectively data sets collected on 10/06/2021 and 06/07/2021. The two plots on the right there are the same SBR data but there is the WG width on the x axis. Each colour defines the WG width: 0.4 μm in red, 0.6 μm in blue, 0.8 μm in green, 1.0 μm in black and 1.2 μm in yellow.

5.6 Influence of the scattering wavelength

5.6.1 Experimental results

From experiments it has been calculated the SBR obtained from the same set of spectra of the previous chapter but evaluated on the peak at 1455 cm^{-1} . In this case the difference between the SBR of the two data set collected on the different dates is much lower, this reinforces the idea of possible degradation process of the PMMA. Therefore, both datasets have been plotted together. From plot on the right, the data shows, at fixed WG width, a linear trend. Therefore, longer WGs could be made. Relevant comments can be made:

- Firstly, it can be noted that the mean value of the SBR is much higher, $\text{SBR}=1.80$, with respect of the before that one coming from the peak at 814 cm^{-1} ($\text{SBR}=0.35$). Therefore, there is an increase of 410%.
- On the right plot it shows that for 1455 cm^{-1} Raman shift the best WGs for Raman collection are the D WGs series, with WG width correspondent to $0.8\mu\text{m}$. This is a relevant result since it shows how each WG should be optimized for the specific wavelength region of Raman signal collection enhancement. With a 785nm laser wavelength the 1455 cm^{-1} Raman shift correspond to a scattered wavelength of 886nm . On the other hand, from the previous data, for a peak at 814 cm^{-1} , the optimal WG width of $0.6\mu\text{m}$ is for scattered wavelength around 839 nm .

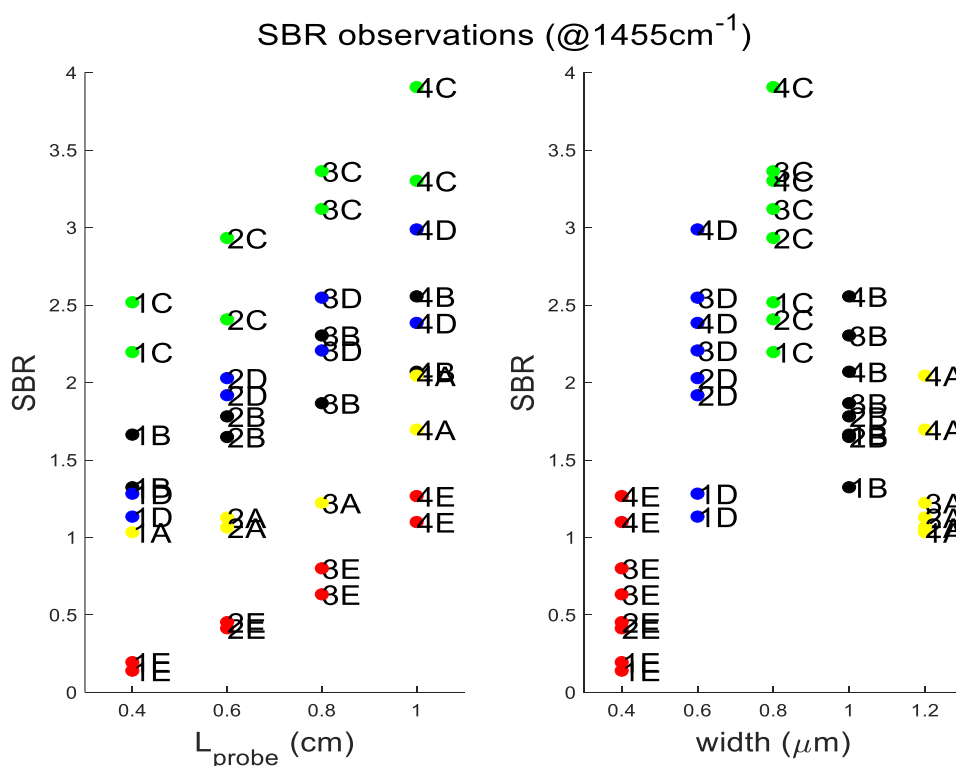


Figure 80: SBR of peak 1455 cm^{-1} of PMMA sample deposited on the chip. Each colour defines the WG width: $0.4\mu\text{m}$ in red, $0.6\mu\text{m}$ in blue, $0.8\mu\text{m}$ in green, $1.0\mu\text{m}$ in black and $1.2\mu\text{m}$ in yellow.

5.6.2 Simulation

To better understand the origin of the change in the trend of the SBR as function of the WG width extra simulations has been performed. The three parameters that can be influenced by the wavenumber change are:

- The scattering cross section of the background and the PMMA: $\beta_{BG}(1455cm^{-1}) = 0.23 \cdot 10^{-9}sr^{-1}cm^{-1}$. If compared to the $\beta_{BG}(814cm^{-1})$ there is a decrease of 780%. This is the main contribution of that increase in the mean SBR. To be more precise the PMMA the scattering cross section decreases to $(\rho\sigma)_{PMMA} = 1.56 \cdot 10^{-9}cm^{-1}sr^{-1}$. Therefore, the beta ration increases from $\beta_{S/B}(814cm^{-1}) = 1.42$ to $\beta_{S/B}(1455cm^{-1}) = 6.8$. i.e. a variation of 380%.
- The CCR changes but not as much as the $\beta_{S/B}$ (Figure 81). We have a mean increase of 11% going from 814 cm^{-1} to 1455 cm^{-1} . The general trend does not change significantly. As reported in the subplot it can be noticed the increase in the CCR is slightly higher for smaller WGs it is not relevant.
- The scattering losses can change. Unfortunately, with the Thor camera it is possible to measure only the losses associated to 785nm wavelength if any filter is applied (most of the scattering losses are associated to the pump wavelength). By calculating with the n_w model the scattering losses (Figure 82) it can be noticed that for an increase in wavelength (i.e. an increase of Raman wavenumber), the losses decrease. This is in line on what measured by Tyndall et al. (55). Therefore, the relative increase of the C WGs over the D WGs can not be explained by the influence in the scattering losses.
- For exclusion, the main reason why there is a change in the trend, resulting as best WG the C series, it can associate to other sources of losses which will be discussed in the next paragraph.

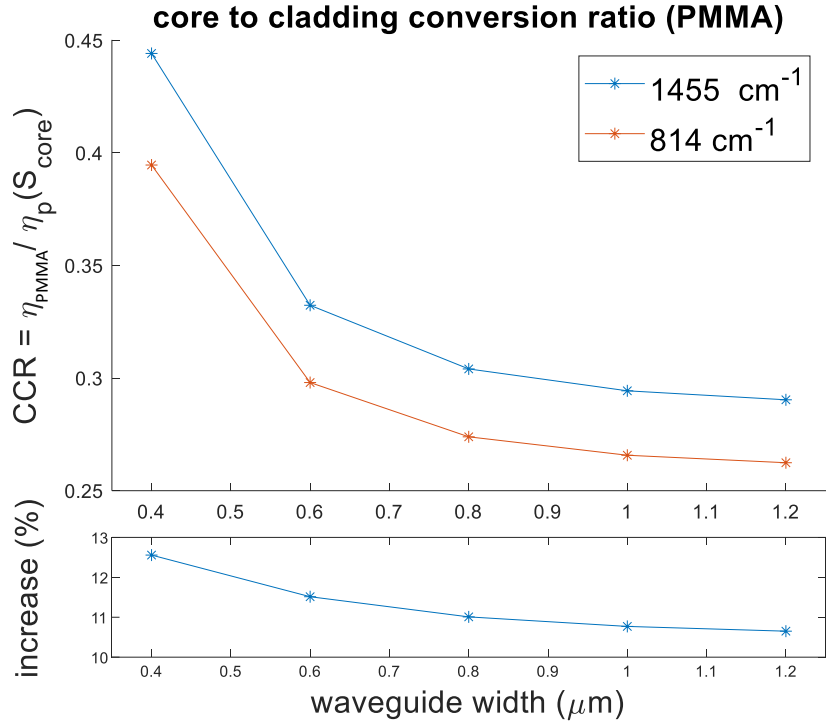


Figure 81: CCR as function of the WG width for PMMA cladded WG evaluated at two different Raman shift (1455 cm^{-1} and 814 cm^{-1}). In the subplot at the bottom the increase in % going from 814 cm^{-1} to 1455 cm^{-1} .

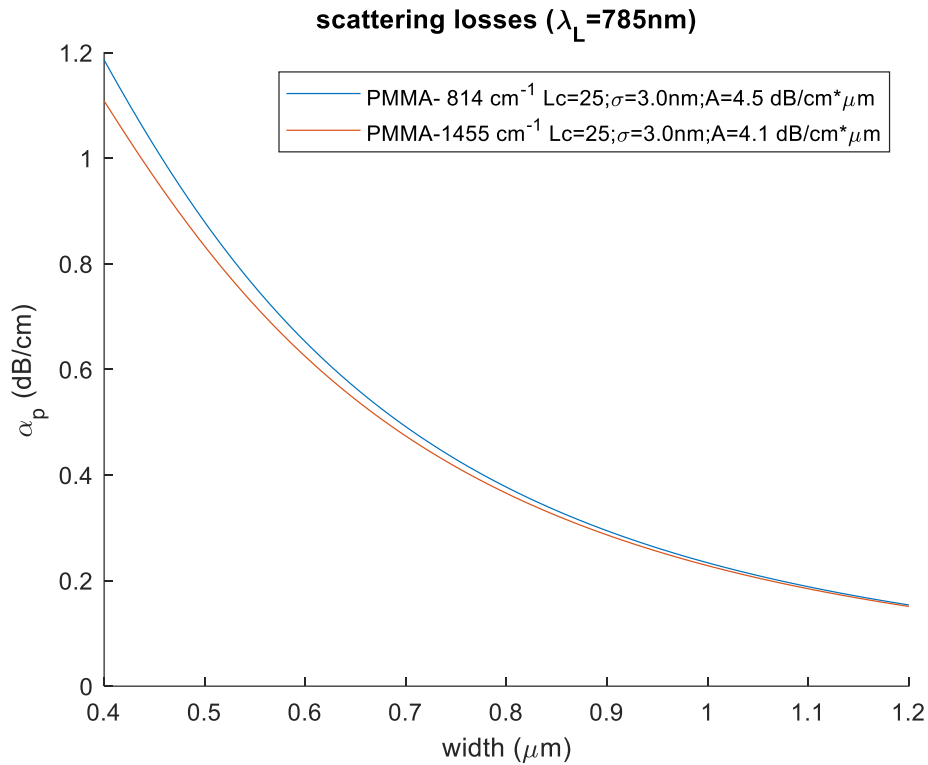


Figure 82: simulated scattering losses with n_w model under the hypothesis of $L_c = 25 \text{ nm}$ and $\sigma = 3 \text{ nm}$ for 3 different Raman wavenumber with laser wavelength at 785 nm.

5.6.3 Additional losses

In previous chapter it has been shown the need of further details in the description of the SBR to explain the change in the trend. Therefore, it will be discussed qualitatively other sources of losses. In between of the not-probing and probing region there are two bends. These two have been designed to have minimum bending losses characterized by a bending radius of $35 \mu\text{m}$. It should be noted that although the large bending radii, it has been recorded losses associated to those features, as shown in Figure 83. This could be associated to the not well design of the mode matching between bent mode and straight mode (139). It should be noted that in the example in the figure on the left the bending losses were much larger than the usually observed bending losses. Another source of losses is the transition from SiO_2 cladding and the probing region. The modal properties discontinuity due to the change of refractive index result in a high localized point of light scattering. To consider of these losses the χ factor should be introduced.

Therefore, the wavelength shift could result in change of the losses in those regions, that results in a change in the best WG width. Lumerical mode solver offer an easy tool for evaluating the bending losses based on the paper (140). As can be seen from Figure 84, there is an increase of 15% of the losses associated to D WGs, and of 3% for B WGs. Therefore, there is an increase of losses for D WGs compared to B WGs and this explains why at 1455 cm^{-1} B WGs have higher SBR.

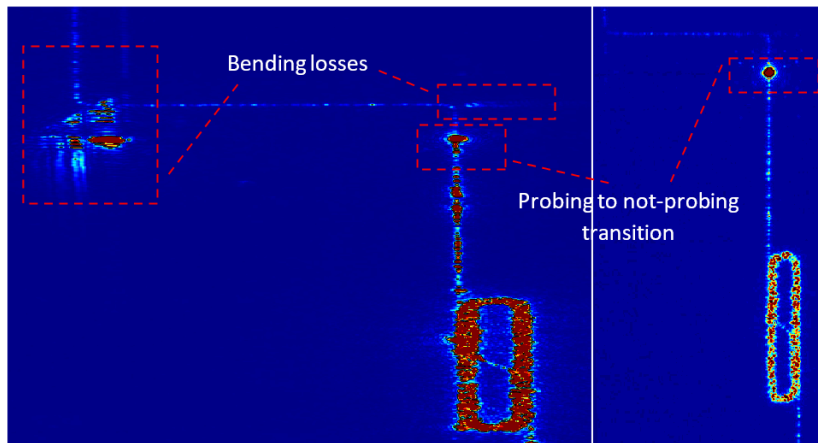


Figure 83: two different images reporting the scattering intensity coming from two WGs. There are two critical point where the losses are more intense, and these are highlighted in the image. The colours and size are changed to have better evidence of the scattering losses.

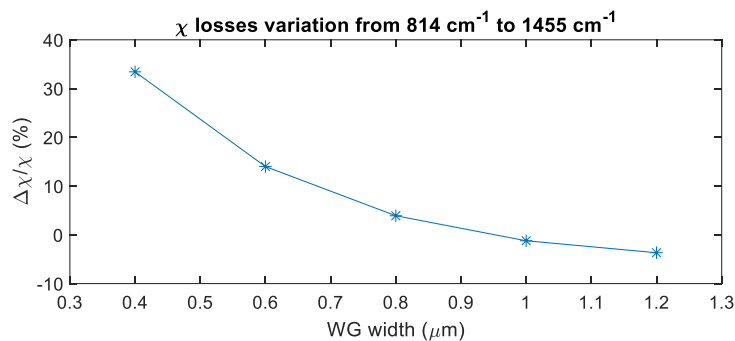


Figure 84: χ losses variation going from 814 cm^{-1} to 1455 cm^{-1} for PMMA at pump wavelength of 785 nm .

5.7 Influence of the laser wavelength

In this last chapter the influence of the laser wavelength will be briefly discussed.

In Figure 85 is reported the measurements among different WGs done with 633nm laser wavelength. It is well visible the peak associated to C-H vibration and the study of the SBR over that peak is performed. By comparing the Figure 85 and Figure 78 it can be noted that as already said in chapter 4.4.4 the spectra collected with 633nm pump wavelength have much higher noise in low Raman shift region. This result in the almost no detectable C-O-C symmetric stretching peak at 814cm^{-1} . It should be also noticed that the N_2 peak has a much higher intensity with respect to 785nm laser wavelength spectrum.

The SBR evaluated are reported in Figure 86. If we look at figure on the right the SBR as function of the WG width we can notice that the best WG width result the E series ($0.4\ \mu\text{m}$) but also the B WGs ($1.0\ \mu\text{m}$ width) have high SBR. Therefore, there are two “local maxima” in the plot SBR as function of the WG width. By looking on Figure 86 on the right the typical trend of SBR increase as increasing the probing length remains also for 633nm pump laser. Also, in this case most of the WGs at fixed width series have a linear trend.

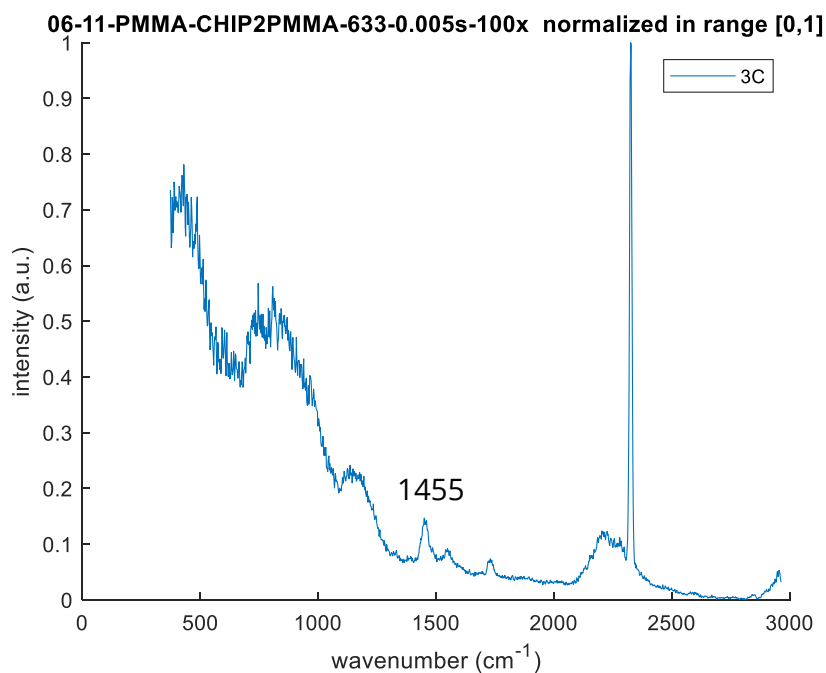


Figure 85: Raman spectra obtained from WGs coated with PMMA. All the parameters used to measure these spectra are reported in the title.

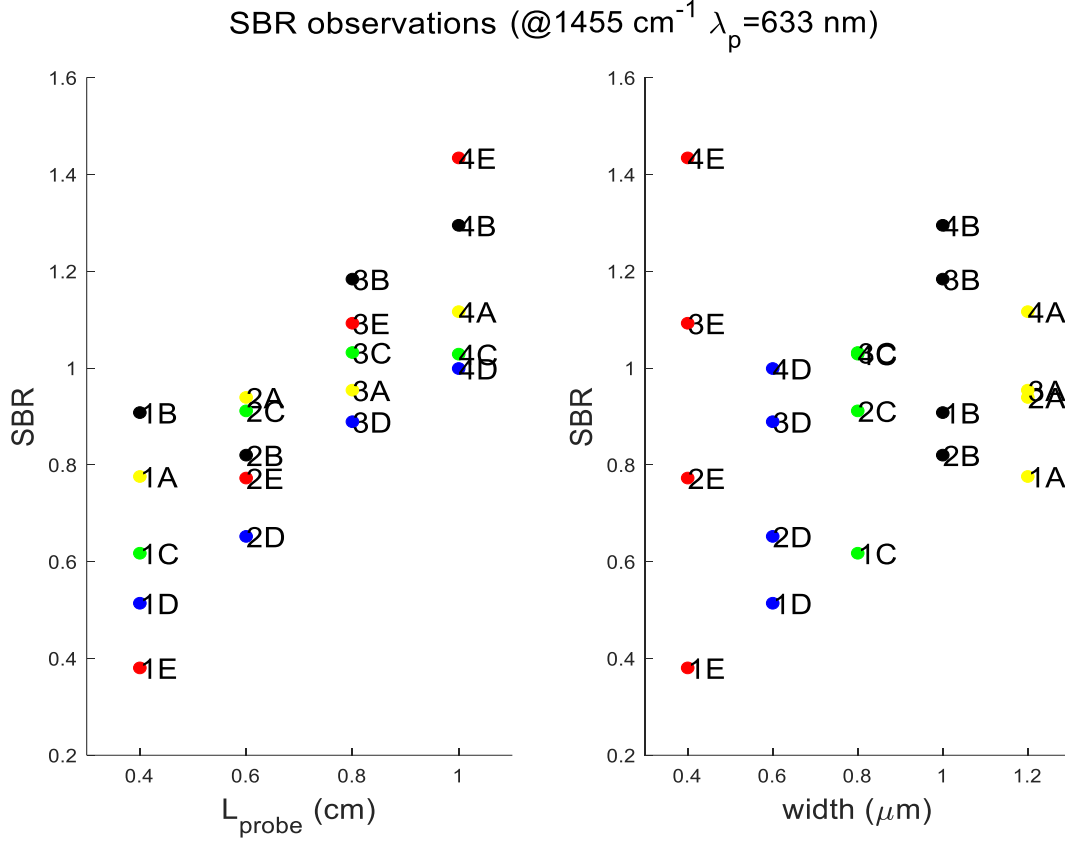


Figure 86: SBR of peak 1455 cm⁻¹ of PMMA sample deposited on the chip obtained with 633nm laser wavelength. Each colour defines the WG width: 0.4 μm in red, 0.6 μm in blue, 0.8 μm in green, 1.0 μm in black and 1.2 μm in yellow.

Now it will be made a comparison between the two plots on the left of Figure 80 and Figure 86 which can further sustain the idea of the need to add an extra loss factor. To simplify the comparison the two data, both figures are reported in an additional graph in Figure 87. If curves are drawn connecting constant WG widths (same color), it can be noticed that in Figure 87 on the left the different color lines do not cross, but in Figure 87 on the right they do. For example, by looking at E WGs series, it can be noticed a very high angular coefficient (follow the red line). As seen previously, it seems that the χ loss factor is predominant factor when the wavelength changes with respect to $\alpha_p(\lambda)$ and $\alpha_{np}(\lambda)$. Therefore, from equation 5.13, if we simplify $\alpha_{np}L' \sim 0$ and $\alpha_p L \sim 0$, then it results ($\eta_{np/P} \approx 1$, as previously calculated for 633nm):

$$SBR \approx \beta_{S/B} \cdot \eta_{S/B} \cdot \frac{\chi L}{L' + \chi L} \quad 5.25$$

The SBR has a linear trend if $L' \gg \chi L$:

$$SBR \approx \beta_{S/B} \cdot \eta_{S/B} \cdot \chi \cdot L/L' \quad 5.26$$

in which the angular coefficient is given by the product of: χ and $\eta_{S/B}$ ($\beta_{S/B}$ and L' are constants with respect to changes in WG width). The CCR ($\eta_{S/B}$) trend is unchanged as we change the laser wavelength from 633nm to 785nm (Figure 68). Therefore, comparing plot on the left of Figure 80 and Figure 86 it should not be expected a change in the trend. The χ loss factor, as shown previously in Figure 84, shows an increase for E WGs as the wavelength decrease. Therefore, the

introduction of the χ can justify this change in the trend. E WGs has higher angular coefficients with respect to A WGs and this is in line on the behavior recorded in Figure 84 whereas the wavelength decreases the χ increases for lower WGs width.

We have shown that the introduction of the χ loss factor is fundamental. And therefore, improvements in the design of the probing to not-probing transition and bending is needed.

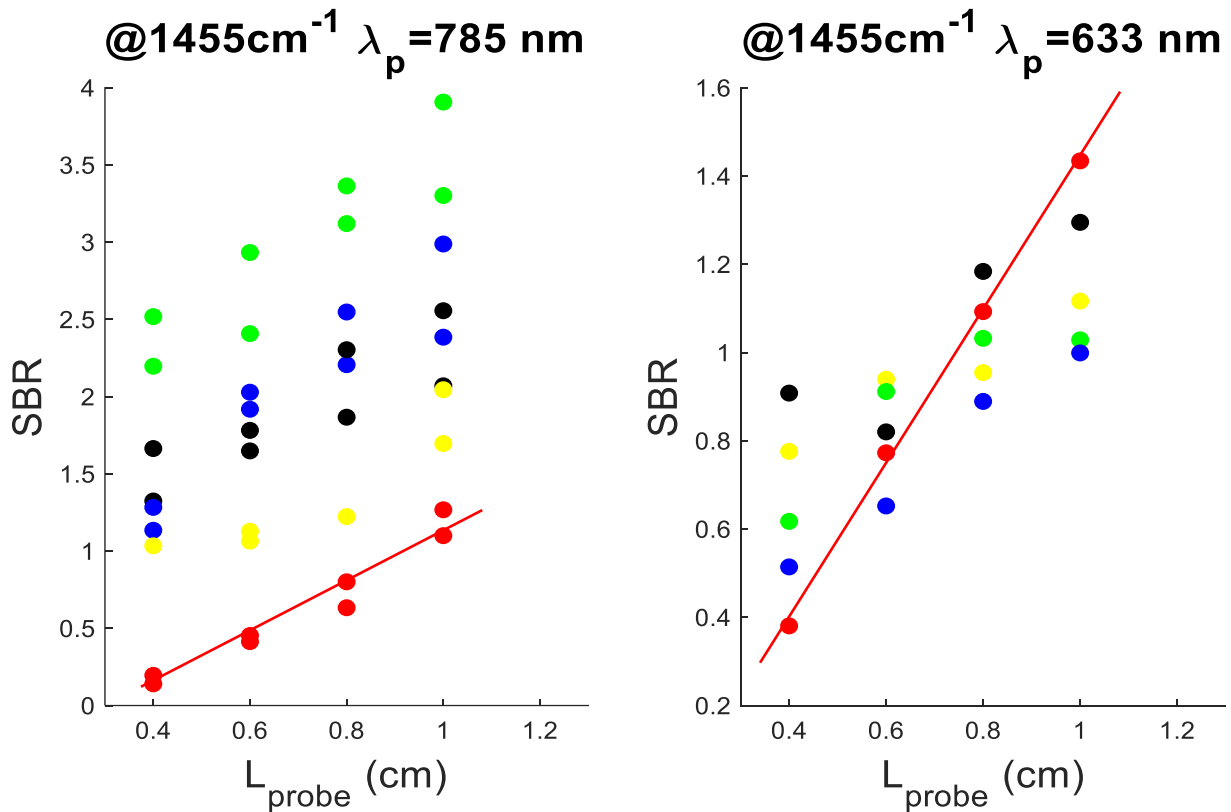


Figure 87: SBR of peak 1455 cm⁻¹ of PMMA sample deposited on the chip. On the left measurements are performed with 785nm laser wavelength and on the right with 633nm. Each colour defines the WG width: 0.4 μm in red, 0.6 μm in blue, 0.8 μm in green, 1.0 μm in black and 1.2 μm in yellow. The two red lines fits the red dots (0.4 μm WG width). The data are taken from figures on the left of Figure 80 and Figure 86.

6 Conclusion and Prospective

6.1 Set-up designs

The first objective of this master thesis was the development of a set-up for light coupling into clean edge WERS chip.

Many problems have been pointed out and solved, leading to the development of a **coupling procedure** for reliable testing using confocal Raman microscope. With this procedure it has been possible to consistently measure Raman spectra with 100x/0.9NA objective with xy precision of 0.1 μm .

For the design of the **set-up** modelling with SolidWorks software were made. Three different set-ups were made: the N0 set-up is suitable for no-sample or coating-solid sample; the N1 set-up can hold liquid samples with simple change between different chips, the N2 chip set-up is good for highly volatile liquids, with closed liquid holder, and simple change between different liquid samples. Future evolution of these set-up is needed to open the possibility to further studies and more importantly to decrease the time spent for experiment. For example, up to now under confocal microscope was possible to study only WGs with TM polarization mode. Therefore, TE polarization set-up should be included for TE experiments. Secondly, it would be interesting to include in the N0 set-up the possibility to include measurements of transmitted light as WiTec confocal microscope includes transmission analysis. Finally, it could be useful the development of a flat platform without using confocal microscope or complex stages. Kit et al. (49) proposed the most straightforward solution to this problem by using optical fibers. Gratings or inverse taper couplers should be developed to further improve the coupling procedure for real applications.

Finally, the **Thor camera** has been mainly used to help the coupling procedure. But it can provide insight in terms of WG losses, and the improvement of the existing scattering losses procedure is useful to critically discuss the experimental results. It has been implemented a Matlab script for picture analysis, but improved software analysis is needed to have much faster quantitative estimation.

6.2 Background signal Raman spectrum

The second objective of this master thesis was the in depth understanding of the background Raman scattering signal coming from SiN core and SiO₂ substrate WGs.

In this framework an automatic **fitting script** in Matlab have been developed for quick signal fitting. This program includes the possibility to normalize the spectra, remove polynomial baseline and fit the spectra with Fytik software. It has been included also the possibility to perform principal component analysis data. This study could help in the development of artificial background subtraction. Since the background spectrum from a given WG is almost fixed, for future applications it would be interesting to have a simple method to remove it without the need of recording the no-sample spectrum. This can help to detect components at low concentration in the spectral region of [0-600] cm⁻¹ for which the background is very steep. In particular this method can substitute the spectral subtraction method (66), which can give good results only for high SNR and no chemical interactions. For example, Kita et al. (49) have been publish a paper in which their only Raman experimental result relied on spectral subtraction.

From the results obtained the SiO₂ Raman signal cannot be excluded form the background signal. This is particularly true for the spectral region [600-1300] cm⁻¹. This is not completely in line on what Dhakal et al. (59) have been reported. More studies on the effect of the production process on the background Raman spectrum could be interesting.

The presence of the **exponential decreasing background** at low wavenumbers has been measured for both 785nm and 633nm and at different powers. The exponential background it is clearly present in all the spectra: $P_{LFD C} \sim e^{-\tau \cdot \omega}$. This is a peculiar line shape for a Raman peak, and it is characteristic of Raman spectra collected form WGs (this is further demonstrated in the appendix A.5.2). Further studies of the influence of the exponential shape, in particular on τ could be relevant in order to provide novel strategy to reduce this signal. The theory proposed to explain such line shape have been developed by Thomas et al. (27, 60). I am not able to debate on this field, but it is not clear to me if it has been widely accepted.

Finally, I would like to report this idea. Scattering losses due to side wall roughness can be seen as dipoles which excited by evanescent fields produces Rayleigh scattering (84, 85). It would be interesting to understand which would be the Raman signal associated to the surface of these systems where the surface can have relevant effects on the device performances.

6.3 Optimal WERS design

The **enhancement in WERS** is controlled by the scattering losses (α) and conversion efficiency (η). The η have been simulated at different WG width, laser wavelength and cladding refractive index (i.e. IPA and PMMA refractive index). In order to consider the presence of the background it has been introduced the core to cladding conversion ratio (CCR) as figure of merit. The simulation shows an increase of CCR of 40% and 50% going from 0.4 μm to 1.2 μm WG width for IPA and PMMA cladding samples respectively. CCR is around 2.5 higher for 785 nm laser wavelength with respect to 633nm. The α have been estimated with the n_w model combined to experiments. α it is greatly influenced by the sample refractive index and by the WG width and these possible generalizations. For example, for IPA a change in WG width of 0.4 μm to 1.2 μm result in a loss coefficient 7 times lower. But for small WG length this contribution can be neglected. With the estimated values of α and η it has been developed a model to predict the SBR as function of the WG parameter designs.

The first parameter studied is the **not-probing length**. It has been shown with simulations and experimentally that it is deleterious for the device performances. Some design solutions in order to still use a long not-probing length to deliver light but avoiding the collection of the Raman scattered power from the not-probing region can be the use of a multi modal interferometer (MMI) (62) or using a 2x2 directional couplers (49). Kita et al. (49) has been proposed further possible improvements by using broadband adiabatic coupler or wavelength-selective filters which (141-143) have not been already studied in WERS devices, as far as I know. These can be used to remove pump wavelengths power when it is no more needed.

Secondly, it has not been reported the results for **slot WGs**, but I would report that the slot WGs were not working well. The reason why for that can be attributed to the strip-slot converter that probably was not well design. Therefore, it has been chosen to not further report those study. I would report for the future designs that it can be used a MMI for strip-slot conversion (53). As reported by Kita et al. (49) back reflection of MMI need to be reduced as much as possible the signal background.

The second parameter studied was the **WG width**. To evaluate the best WG width it has been chosen the signal to background ratio (SBR) as the figure of merit. The advantage in using SBR is the possibility to neglect the coupling efficiencies. Therefore, it has been both theoretically and then experimentally. It has been obtained a good agreement at least in the trend of the SBR vs the WG width change (Figure 88). The major discrepancies were associated to the estimation of scattering cross section of PMMA and scattering losses estimation.

The best WG is 0.6 μm width for a fixed probing length. This should be noted that cannot really tells if 0.6 μm width WGs are the best design in general, since if lower losses are obtained with 1.2 μm width WGs it could be designed longer WGs for those WGs resulting in higher SBR. As reported in the paper (49), for backward losses the figure of merit (f.o.m.) in terms of signal to noise ratio (SNR) should be:

$$f.o.m.SNR \sim \frac{\eta_{clad}}{\sqrt{\alpha_p \eta_{core}}}$$

Further studies about the best WG width should be performed by taking into account the f.o.m. reported. It would be possible to recycle the current chip design for studying η_{clad} and η_{core} as function of the WG width, but at the same time there is the need to evaluate α_p too.

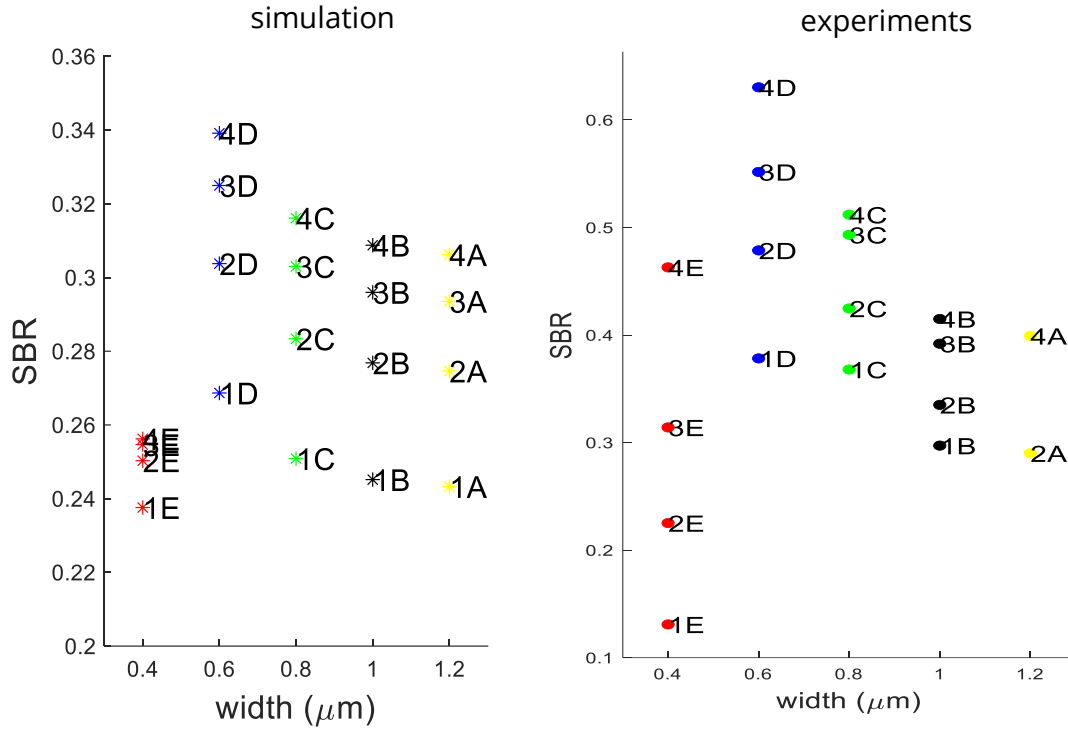


Figure 88: on left the simulation results and on the right the experimental of SBR as function of the WG width. SBR coming from strip WGs coated with PMMA analyzed with 785nm laser.

In the end, it has been studied the SBR as function of the WG width for **different Raman peak** ($\tilde{\nu}_s$ or λ_s) and **pump wavelengths** (λ_p). This underlines the importance to consider that $\alpha_p = \frac{\alpha_p(\lambda_p) + \alpha_p(\lambda_s)}{2}$, $\eta(\lambda_p; \lambda_s)$ and $\sigma(\lambda_p; \tilde{\nu}_s)$. The change in the best WG width at fixed length results in the understanding of a not well-designed bending. Therefore, for next generation devices an extensive simulation before production should be needed. For design a well written paper for simulation has been written by Melloni et al. (139). In addition the interface between pronging and not-probing region need to be improved, to reduce WG losses. Kita et al. proposed to reduce these losses by letting the WG enter the probing region at shallow angle (instead of normal angle as in our design (49)).

Up to now all the **simulations** have been done for separated components and then the results loaded on Matlab for final calculations (e.g. SBR) but to further improve the simulation framework a network between all the different separated simulations (e.g. scattering losses, η , bending losses, mode coupling,...) could be useful to simplify the study process.

Up to now there is still not leading design between strip and slot WGs. These two designs favour the two different WERS enhancement factors: increased probing length design and WG enhancement. It should be noted a possible limitation of slot WGs: the most important region for detection is in between the two rectangular cross sections, therefore it could be critical the filling of those regions if bad wettability occurs. On the other hand, strip WGs can have increase detection length resulting in less prone of local inhomogeneities.

6.4 Next generation samples

If improvements in the detection limit will be made there is a huge range of possibilities for applications of WERS. WERS devices has been studied mainly with standard liquid samples. Some works has been done to demonstrate the possibility to apply WERS also for gas detection by exploiting hyper absorbent coatings (41, 42). For example, surface functionalization has been used for DNA hybridization (40). But there are wide range of possible studies for WERS surface functionalization that can be found in (23). Since WERS is on chip, it is a 2D sensor. Due to its shape, it would be interesting to study 2D materials or thin films with WERS to have increased Raman signal.

Possible samples in which WERS could applied are drugs and proteins, in which Raman it has been always of interest. Such systems are studied in solution and therefore a starting point should be the studies of WERS in different solvents. In my work the main experimental results have been obtained with PMMA sample, which it is a good starting point for dye embedded studies.

6.5 Final overview on the thesis work

In this master thesis the development of set-up, coupling procedure, data analysis software has been developed to collect Raman spectra and scattering losses pictures as experimental data. The critical review of different components of the current design have been done with conjunction with Lumerical simulation software. In depth study of the background limiting signal have been performed showing the presence of signal coming from: exponential decreasing background, amorphous silicon nitride core and amorphous silicon dioxide substrate and cladding. The influence of different parameters has been studied, the main of interest were the strip WG width, the pump wavelength and scattered wavelength. The current design of the chip resulted in great limitation for determining a clear relationship between those parameters and the efficiency of the collection of the signal. Therefore, a review of all the possible solutions for improving the current design has been proposed for next generation devices.

It has been already demonstrated how promising WERS as future Raman sensing device (1, 2) but many different aspects need to be improved to have access to mass production.

Bibliography

References

1. Peyskens F, Dhakal A, Van Dorpe P, Le Thomas N, Baets R. Surface Enhanced Raman Spectroscopy Using a Single Mode Nanophotonic-Plasmonic Platform. *ACS Photonics*. 2016;3(1):102-8.
2. what is integrated photonics? [Internet].; 2021 []. Available from: <https://www.aimphotonics.com/what-is-integrated-photonics>.
3. Morris K. No More Nanometers It's Time for New Node Naming. *Electron.Eng.J.* 2020.
4. European Technology Platform Photonics21. Europe's age of light! Photonics21 Multiannual Strategic Roadmap 2021–2027. . 2019.
5. European Investment Bank. Financing the digital transformation – Unlocking the value of photonics and microelectronics. ; 2018.
6. Ramos IRM, Malkin A, Lyng FM. Current advances in the application of Raman spectroscopy for molecular diagnosis of cervical cancer. *BioMed research international*. 2015;2015.
7. Alessandri I, Lombardi JR. Enhanced Raman scattering with dielectrics. *Chem Rev*. 2016;116(24):14921-81.
8. Pilot R, Signorini R, Durante C, Orian L, Bhamidipati M, Fabris L. A review on surface-enhanced Raman scattering. *Biosensors*. 2019;9(2):57.
9. Ashurov M, Baranchikov A, Klimonsky S. Photonic crystal enhancement of Raman scattering. *Physical Chemistry Chemical Physics*. 2020;22(17):9630-6.
10. Cheng, J.-X., & Xie, X.S. *Coherent Raman Scattering Microscopy*. 1st ed. CRC Press.; 2012.
11. Cialla D, März A, Böhme R, Theil F, Weber K, Schmitt M, et al. Surface-enhanced Raman spectroscopy (SERS): progress and trends. *Analytical and bioanalytical chemistry*. 2012;403(1):27-54.
12. Kneipp J, Kneipp H, Kneipp K. SERS—a single-molecule and nanoscale tool for bioanalytics. *Chem Soc Rev*. 2008;37(5):1052-60.
13. Kneipp K, Kneipp H, Itzkan I, Dasari RR, Feld MS. Ultrasensitive chemical analysis by Raman spectroscopy. *Chem Rev*. 1999;99(10):2957-76.
14. Costa MD, Cançado LG, Jorio A. Event chronology analysis of the historical development of tip-enhanced Raman spectroscopy. *J Raman Spectrosc*. 2021;52(3):587-99.

15. Frosch T, Knebl A, Frosch T. Recent advances in nano-photonic techniques for pharmaceutical drug monitoring with emphasis on Raman spectroscopy. *Nanophotonics*. 2020;9(1):19-37.
16. Markin AV, Markina NE, Goryacheva IY. Raman spectroscopy based analysis inside photonic-crystal fibers. *TrAC Trends in Analytical Chemistry*. 2017;88:185-97.
17. Huang W, Li Z, Cui Y, Zhou Z, Wang Z. Efficient, watt-level, tunable 1.7 μm fiber Raman laser in H₂-filled hollow-core fibers. *Opt Lett*. 2020;45(2):475-8.
18. Almohamed Y, Barille R, Vodchits AI, Voinov YP, Gorelik VS, Kudryavtseva A, et al. Reduction of the threshold of stimulated Raman scattering in Raman-active media introduced into pores of a globular photonic crystal. *JETP Letters*. 2015;101(6):365-70.
19. Benabid F, Knight JC, Antonopoulos G, Russell PS. Stimulated Raman scattering in hydrogen-filled hollow-core photonic crystal fiber. *Science*. 2002 Oct 11;298(5592):399-402.
20. Yan H, Gu C, Yang C, Liu J, Jin G, Zhang J, et al. Hollow core photonic crystal fiber surface-enhanced Raman probe. *Appl Phys Lett*. 2006;89(20):204101.
21. Dinish U, Beffara F, Humbert G, Auguste J, Olivo M. Surface-enhanced Raman scattering-active photonic crystal fiber probe: Towards next generation liquid biopsy sensor with ultra high sensitivity. *Journal of biophotonics*. 2019;12(11):e201900027.
22. Pérez-Jiménez AI, Lyu D, Lu Z, Liu G, Ren B. Surface-enhanced Raman spectroscopy: benefits, trade-offs and future developments. *Chemical science*. 2020;11(18):4563-77.
23. Ettabib MA, Marti A, Liu Z, Bowden BM, Zervas MN, Bartlett PN, et al. Waveguide Enhanced Raman Spectroscopy for Biosensing: A Review. *ACS sensors*. 2021.
24. Subramanian AZ, Ryckeboer E, Dhakal A, Peyskens F, Malik A, Kuyken B, et al. Silicon and silicon nitride photonic circuits for spectroscopic sensing on-a-chip. *Photonics Research*. 2015;3(5):B47-59.
25. Wuytens P. Surface-enhanced Raman spectroscopy for intracellular sensing and protease activity detection: from chip technology to applications. 2017.
26. Dhakal A, Peyskens F, Clemmen S, Raza A, Wuytens P, Zhao H, et al. Single mode waveguide platform for spontaneous and surface-enhanced on-chip Raman spectroscopy. *Interface focus*. 2016;6(4):20160015.
27. Le Thomas N, Liu Z, Lin C, Zhao H, Baets R. Raman on-chip: current status and future tracks. *Integrated Optics: Devices, Materials, and Technologies XXV*; International Society for Optics and Photonics; 2021.
28. Walrafen G, Stone J. Intensification of spontaneous Raman spectra by use of liquid core optical fibers. *Appl Spectrosc*. 1972;26(6):585-9.

29. Levy Y, Imbert C, Cipriani J, Racine S, Dupeyrat R. Raman scattering of thin films as a waveguide. *Opt Commun.* 1974;11(1):66-9.
30. Kanger JS, Otto C, Slotboom M, Greve J. Waveguide Raman spectroscopy of thin polymer layers and monolayers of biomolecules using high refractive index waveguides. *J Phys Chem.* 1996;100(8):3288-92.
31. Dhakal A, Subramanian AZ, Wuytens P, Peyskens F, Le Thomas N, Baets R. Evanescent excitation and collection of spontaneous Raman spectra using silicon nitride nanophotonic waveguides. *Opt Lett.* 2014;39(13):4025-8.
32. Dhakal A, Wuytens P, Peyskens F, Subramanian A, Skirtach A, Le Thomas N, et al. Nanophotonic Lab-On-A-Chip Raman sensors: a sensitivity comparison with confocal Raman microscope. 2015 International Conference on BioPhotonics (BioPhotonics); IEEE; 2015.
33. Y. Li, H. Zhao, A. Raza, S. Clemmen, R. Baets. Surface-Enhanced Raman Spectroscopy Based on Plasmonic Slot Waveguides With Free-Space Oblique Illumination. *IEEE Journal of Quantum Electronics.* 2020;56(1):1-8.
34. Van Daele M, Griffiths MBE, Raza A, Minjauw MM, Solano E, Feng J, et al. Plasma-Enhanced Atomic Layer Deposition of Nanostructured Gold Near Room Temperature. *ACS Applied Materials & Interfaces.* 2019;11(40):37229-38.
35. Raza A, Clemmen S, Wuytens P, Muneeb M, Van Daele M, Dendooven J, et al. ALD assisted nanoplasmonic slot waveguide for on-chip enhanced Raman spectroscopy. *APL Photonics.* 2018;3(11):116105.
36. Raza A, Clemmen S, Van Daele M, Dendooven J, Griffiths MB, Barry ST, et al. On-chip surface enhanced Raman spectroscopy using ALD grown plasmonic nanotrenches integrated with a silicon nitride slot waveguide. 21st European Conference on Integrated Optics (ECIO 2019); ; 2019.
37. Turk N, Raza A, Wuytens P, Demol H, Van Daele M, Detavernier C, et al. Comparison of free-space and waveguide-based SERS platforms. *Nanomaterials.* 2019;9(10):1401.
38. Zhao H, Clemmen S, Raza A, Baets R. Stimulated Raman spectroscopy of analytes evanescently probed by a silicon nitride photonic integrated waveguide. *Opt Lett.* 2018 Mar;43(6):1403-6.
39. Reynkens K, Clemmen S, Zhao H, Raza A, Vanackere T, Stassen A, et al. Gold-induced photothermal background in on-chip surface enhanced stimulated Raman spectroscopy. *Opt Lett.* 2021;46(5):953-6.
40. Dhakal A, Wuytens PC, Peyskens F, Jans K, Thomas NL, Baets R. Nanophotonic Waveguide Enhanced Raman Spectroscopy of Biological Submonolayers. *ACS Photonics.* 2016;3(11):2141-9.

41. Holmstrom SA, Stievater TH, Kozak DA, Pruessner MW, Tyndall N, Rabinovich WS, et al. Trace gas Raman spectroscopy using functionalized waveguides. *Optica*. 2016;3(8):891-6.
42. Zhao H, Baumgartner B, Raza A, Skirtach A, Lendl B, Baets R. Multiplex volatile organic compound Raman sensing with nanophotonic slot waveguides functionalized with a mesoporous enrichment layer. *Opt Lett*. 2020;45(2):447-50.
43. Liu Z, Zhao H, Baumgartner B, Lendl B, Stassen A, Skirtach A, et al. Ultra-sensitive slot-waveguide-enhanced Raman spectroscopy for aqueous solutions of non-polar compounds using a functionalized silicon nitride photonic integrated circuit. *Opt Lett*. 2021;46(5):1153-6.
44. Raza A, Clemmen S, Wuytens P, Goede Md, Tong ASK, Thomas NL, et al. High index contrast photonic platforms for on-chip Raman spectroscopy. *Opt.Express*. 2019 Aug;27(16):23067-79.
45. Wuytens PC, Skirtach AG, Baets R. On-chip surface-enhanced Raman spectroscopy using nanosphere-lithography patterned antennas on silicon nitride waveguides. *Opt.Express*. 2017 May;25(11):12926-34.
46. Wang Z, Zervas MN, Bartlett PN, Wilkinson JS. Surface and waveguide collection of Raman emission in waveguide-enhanced Raman spectroscopy. *Opt Lett*. 2016;41(17):4146-9.
47. Ettabib MA, Liu Z, Zervas MN, Wilkinson JS. Optimized design for grating-coupled waveguide-enhanced Raman spectroscopy. *Optics Express*. 2020;28(25):37226-35.
48. Subramanian AZ, Selvaraja S, Verheyen P, Dhakal A, Komorowska K, Baets R. Near-infrared grating couplers for silicon nitride photonic wires. *IEEE Photonics Technology Letters*. 2012;24(19):1700-3.
49. Kita DM, Michon J, Hu J. A packaged, fiber-coupled waveguide-enhanced Raman spectroscopic sensor. *Optics express*. 2020;28(10):14963-72.
50. Losada J, Raza A, Clemmen S, Serrano A, Griol A, Baets R, et al. SERS Detection via Individual Bowtie Nanoantennas Integrated in Si₃N₄ Waveguides. *IEEE Journal of Selected Topics in Quantum Electronics*. 2019;25(3):1-6.
51. Nie X, Turk N, Li Y, Liu Z, Baets R. High extinction ratio on-chip pump-rejection filter based on cascaded grating-assisted contra-directional couplers in silicon nitride rib waveguides. *Opt Lett*. 2019;44(9):2310-3.
52. Mere V, Kallega R, Selvaraja SK. Efficient and tunable strip-to-slot fundamental mode coupling. *Optics express*. 2018;26(1):438-44.
53. Deng Q, Yan Q, Liu L, Li X, Michel J, Zhou Z. Robust polarization-insensitive strip-slot waveguide mode converter based on symmetric multimode interference. *Optics express*. 2016;24(7):7347-55.

54. A. Z. Subramanian, P. Neutens, A. Dhakal, R. Jansen, T. Claes, X. Rottenberg, et al. Low-Loss Singlemode PECVD Silicon Nitride Photonic Wire Waveguides for 532–900 nm Wavelength Window Fabricated Within a CMOS Pilot Line. *IEEE Photonics Journal*. 2013;5(6):2202809-.
55. Tyndall NF, Stievater TH, Kozak DA, Pruessner MW, Rabinovich WS, Fahrenkopf NM, et al. A low-loss SiN photonic integrated circuit foundry platform for waveguide-enhanced Raman spectroscopy. *Smart Photonic and Optoelectronic Integrated Circuits XXIII; International Society for Optics and Photonics*; 2021.
56. Dhakal A, Raza A, Peyskens F, Subramanian AZ, Clemmen S, Le Thomas N, et al. Efficiency of evanescent excitation and collection of spontaneous Raman scattering near high index contrast channel waveguides. *Optics Express*. 2015;23:27392-404.
57. Stievater TH, Khurgin JB, Holmstrom SA, Kozak DA, Pruessner MW, Rabinovich WS, et al. Nanophotonic waveguides for chip-scale raman spectroscopy: Theoretical considerations. *Chemical, Biological, Radiological, Nuclear, and Explosives (CBRNE) Sensing XVII; International Society for Optics and Photonics*; 2016.
58. Dhakal A, Raza A, Peyskens F, Subramanian AZ, Clemmen S, Thomas NL, et al. Efficiency of evanescent excitation and collection of spontaneous Raman scattering near high index contrast channel waveguides. *Opt.Express*. 2015 Oct;23(21):27391-404.
59. Dhakal A, Wuytens P, Raza A, Le Thomas N, Baets R. Silicon Nitride Background in Nanophotonic Waveguide Enhanced Raman Spectroscopy. *Materials*. 2017;10(2).
60. Thomas NL, Dhakal A, Raza A, Peyskens F, Baets R. Impact of fundamental thermodynamic fluctuations on light propagating in photonic waveguides made of amorphous materials. *Optica*. 2018 Apr;5(4):328-36.
61. Lee W, Muñoz-Galindo P, Hegeman I, Yong Y, Dijkstra M, García-Blanco SM, et al. Study on multiple waveguide platforms for waveguide integrated Raman spectroscopy. *OSA Continuum*. 2020 May;3(5):1322-33.
62. Reynkens K, Clemmen S, Raza A, Zhao H, Peñaranda JS, Detavernier C, et al. Mitigation of photon background in nanoplasmonic all-on-chip Raman sensors. *Opt.Express*. 2020 Oct;28(22):33564-72.
63. Steglich P, Hülsemann M, Dietzel B, Mai A. Optical biosensors based on silicon-on-insulator ring resonators: A review. *Molecules*. 2019;24(3):519.
64. Kita DM, Michon J, Johnson SG, Hu J. Are slot and sub-wavelength grating waveguides better than strip waveguides for sensing? *Optica*. 2018;5(9):1046-54.
65. Raza A. Raman spectroscopy enhanced by on-chip dielectric and metal waveguides. 2019.

66. Ferraro J, Nakamoto K, Brown C. Introductory Raman Spectroscopy. Second Edition ed. Amsterdam, Boston, London, New York, Oxford, Paris, San Diego, San Francisco, Singapore, Sidney, Tokyo: Academic Press; 2003.
67. Raman CV, Krishnan KS. A new type of secondary radiation. Nature. 1928;121(3048):501-2.
68. Hand LN, Finch JD. Analytical mechanics. Cambridge University Press; 1998.
69. Dhakal A. Nanophotonic waveguide enhanced Raman spectroscopy. 2016.
70. Bradley M. Curve Fitting in Raman and IR Spectroscopy: Basic Theory of Line Shapes and Applications. ; 2007.
71. Shuker R, Gammon RW. Raman-Scattering Selection-Rule Breaking and the Density of States in Amorphous Materials. Phys Rev Lett. 1970 Jul;25(4):222-5.
72. Ando MF, Benzine O, Pan Z, Garden J, Wondraczek K, Grimm S, et al. Boson peak, heterogeneity and intermediate-range order in binary SiO₂-Al₂O₃ glasses. Scientific reports. 2018;8(1):1-14.
73. Ivanda M, Clasen R, Hornfeck M, Kiefer W. Raman spectroscopy on SiO₂ glasses sintered from nanosized particles. J Non Cryst Solids. 2003 15 July 2003;322(1):46-52.
74. Chen C. Foundations for guided-wave optics. John Wiley & Sons; 2006.
75. Saleh BE, Teich MC. Fundamentals of photonics. John Wiley & sons; 2019.
76. Zhu Z, Brown TG. Full-vectorial finite-difference analysis of microstructured optical fibers. Opt.Express. 2002 Aug;10(17):853-64.
77. Understanding the mode overlap calculation [Internet].; 2021 []. Available from: <https://support.lumerical.com/hc/en-us/articles/360034396834-Understanding-the-mode-overlap-calculation>.
78. Melati D, Melloni A, Morichetti F. Real photonic waveguides: guiding light through imperfections. Adv.Opt.Photon. 2014 Jun;6(2):156-224.
79. Payne F, Lacey J. A theoretical analysis of scattering loss from planar optical waveguides. Opt Quant Electron. 1994;26(10):977-86.
80. Melati D, Morichetti F, Melloni A. A unified approach for radiative losses and backscattering in optical waveguides. Journal of Optics. 2014;16(5):055502.
81. Wang Y, Kong M, Xu Y, Zhou Z. Analysis of scattering loss due to sidewall roughness in slot waveguides by variation of mode effective index. Journal of Optics. 2018;20(2):025801.

82. Bogaerts W, Selvaraja SK. Compact single-mode silicon hybrid rib/strip waveguide with adiabatic bends. *IEEE Photonics Journal*. 2011;3(3):422-32.
83. Liu Y, Sun W, Xie H, Zhang N, Xu K, Yao Y, et al. Very sharp adiabatic bends based on an inverse design. *Opt Lett*. 2018 Jun;43(11):2482-5.
84. Grillot F, Vivien L, Cassan E, Laval S. Influence of waveguide geometry on scattering loss effects in submicron strip silicon-on-insulator waveguides. *IET optoelectronics*. 2008;2(1):1-5.
85. Bogaerts W, Bienstman P, Baets R. Scattering at sidewall roughness in photonic crystal slabs. *Opt Lett*. 2003;28(9):689-91.
86. Jun YC, Briggs RM, Atwater HA, Brongersma ML. Broadband enhancement of light emission in silicon slot waveguides. *Optics Express*. 2009;17(9):7479-90.
87. Subramanian A, Neutens P, Dhakal A, Jansen R, Claes T, Rottenberg X, et al. Low-loss singlemode PECVD silicon nitride photonic wire waveguides for 532–900 nm wavelength window fabricated within a CMOS pilot line. *IEEE Photonics Journal*. 2013;5(6):2202809-.
88. WITec. WITec alpha300+ User Manual. 2007.
89. raman spectrometer presentation [Internet].; 2021 []. Available from: https://www.horiba.com/en_en/ramanspectrometerpresentation/.
90. CCD camera andor oxinst [Internet].; 2021 []. Available from: <https://andor.oxinst.com/assets/uploads/products/andor/documents/andor-newton-ccd-specifications.pdf>.
91. emccd specifications andor oxinst [Internet].; 2021 []. Available from: <https://andor.oxinst.com/assets/uploads/products/andor/documents/andor-newton-emccd-specifications.pdf>.
92. Shinya I. Foundations of Confocal Scanned Imaging in Light Microscopy. In: Pawley JB, editor. *Handbook Of Biological Confocal Microscopy*. Boston, MA: Springer US; 2006. p. 1-19.
93. Pinhole Effect in Confocal Microscopes [Internet].; 2017 []. Available from: <https://www.leica-microsystems.com/science-lab/pinhole-effect-in-confocal-microscopes/>.
94. Epilog Laser. Laser System Manual. 2021.
95. Lei W, Kumar A, Yalamanchili R. Die singulation technologies for advanced packaging: A critical review. *Journal of Vacuum Science & Technology B*. 2012 07/01; 2021/10;30(4):040801.
96. Haupt O, Schuetz V, Schoonderbeek A, Richter L, Kling R. High quality laser cleaving process for mono- and polycrystalline silicon. *Laser-based Micro- and Nanopackaging and Assembly III; International Society for Optics and Photonics; SPIE*; 2009.

97. Soudi A, Khan E, Dickinson J, Gu Y. Observation of unintentionally incorporated nitrogen-related complexes in ZnO and GaN nanowires. *Nano letters*. 2009;9(5):1844-9.
98. Richter H, Wang Z, Ley L. The one phonon Raman spectrum in microcrystalline silicon. *Solid State Commun*. 1981;39(5):625-9.
99. Gogotsi Y, Baek C, Kirscht F. Raman microspectroscopy study of processing-induced phase transformations and residual stress in silicon. *Semiconductor Science and Technology*. 1999;14(10):936.
100. Zhang YX, Kang RK, Guo DM, Jin ZJ. Raman Microspectroscopy Study on the Ground Surface of Monocrystalline Silicon Wafers. *Advances in Grinding and Abrasive Technology XIII*; 1; Trans Tech Publications Ltd; 2006.
101. Zhang Y, Kang RK, Guo DM, Jin ZJ. Raman microspectroscopy study on the ground surface of monocrystalline silicon wafers. *Key Engineering Materials*; Trans Tech Publ; 2006.
102. Yadav AK, Singh P. A review of the structures of oxide glasses by Raman spectroscopy. *RSC advances*. 2015;5(83):67583-609.
103. McMillan PF, Remmele RL. Hydroxyl sites in SiO₂ glass: A note on infrared and Raman spectra. *Am Mineral*. 1986;71(5-6):772-8.
104. Di Francesca D, Boukenter A, Agnello S, Alessi A, Girard S, Cannas M, et al. Resonance Raman of oxygen dangling bonds in amorphous silicon dioxide. *J Raman Spectrosc*. 2017;48(2):230-4.
105. Gunde MK. Optical effects in IR spectroscopy: thickness-dependent positions of absorbance lines in spectra of thin films. *Appl Spectrosc*. 1992;46(2):365-72.
106. Lippincott ER, Van Valkenburg A, Weir CE, Bunting EN. Infrared studies on polymorphs of silicon dioxide and germanium dioxide. *Journal of Research of the National Bureau of Standards*. 1958;61(1):61-70.
107. Mazet V, Carteret C, Brie D, Idier J, Humbert B. Background removal from spectra by designing and minimising a non-quadratic cost function. *Chemometrics Intellig Lab Syst*. 2005 28 April 2005;76(2):121-33.
108. Ahmed N, Singh CB, Bhattacharya S, Dhara S, Bhargav PB. Raman and FTIR studies on PECVD grown ammonia-free amorphous silicon nitride thin films for solar cell applications. *Conference Papers in Science*; Hindawi; 2013.
109. Giorgis F, Giuliani F, Pirri C, Tresso E, Summonte C, Rizzoli R, et al. Optical, structural and electrical properties of device-quality hydrogenated amorphous silicon-nitrogen films deposited by plasma-enhanced chemical vapour deposition. *Philos Mag B*. 1998;77(4):925-44.

110. Narikawa S, Kojima Y, Ehara S. Investigations of NH and Si-N bonding configurations in hydrogenated amorphous silicon nitride films by infrared absorption spectroscopy. *Japanese journal of applied physics*. 1985;24(11A):L861.
111. Smith DL, Alimonda AS, Chen C, Ready SE, Wacker B. Mechanism of SiN_xH_y Deposition from NH₃-SiH₄ Plasma. *J Electrochem Soc*. 1990;137(2):614.
112. Tsu DV, Lucovsky G, Mantini M. Local atomic structure in thin films of silicon nitride and silicon diimide produced by remote plasma-enhanced chemical-vapor deposition. *Physical Review B*. 1986;33(10):7069.
113. Molinari M, Rinnert H, Vergnat M. Evolution with the annealing treatments of the photoluminescence mechanisms in a-SiN_xH alloys prepared by reactive evaporation. *J Appl Phys*. 2007;101(12):123532.
114. Gunde MK. Optical effects in IR spectroscopy: thickness-dependent positions of absorbance lines in spectra of thin films. *Appl Spectrosc*. 1992;46(2):365-72.
115. Gunde MK. Vibrational modes in amorphous silicon dioxide. *Physica B: Condensed Matter*. 2000;292(3-4):286-95.
116. McMillan P. Structural studies of silicate glasses and melts—applications and limitations of Raman spectroscopy. *Am Mineral*. 1984;69(7-8):622-44.
117. Bell R, Dean P, Hibbins-Butler D. Localization of normal modes in vitreous silica, germania and beryllium fluoride. *Journal of Physics C: Solid State Physics*. 1970;3(10):2111.
118. Bauters JF, Heck MJ, John DD, Barton JS, Bruinink CM, Leinse A, et al. Planar waveguides with less than 0.1 dB/m propagation loss fabricated with wafer bonding. *Optics express*. 2011;19(24):24090-101.
119. Henry CH, Kazarinov RF, Lee HJ, Orlosky KJ, Katz L. Low loss Si₃N₄-SiO₂ optical waveguides on Si. *Appl Opt*. 1987;26(13):2621-4.
120. Shaw MJ, Guo J, Vawter GA, Habermehl S, Sullivan CT. Fabrication techniques for low-loss silicon nitride waveguides. *Micromachining Technology for Micro-Optics and Nano-Optics III*; International Society for Optics and Photonics; 2005.
121. Germann R, Salemink H, Beyeler R, Bona G, Horst F, Massarek I, et al. Silicon oxynitride layers for optical waveguide applications. *J Electrochem Soc*. 2000;147(6):2237.
122. Pfeiffer MH, Liu J, Raja AS, Morais T, Ghadiani B, Kippenberg TJ. Ultra-smooth silicon nitride waveguides based on the Damascene reflow process: fabrication and loss origins. *Optica*. 2018;5(7):884-92.
123. Sani E, Dell'Oro A. Spectral optical constants of ethanol and isopropanol from ultraviolet to far infrared. *Optical Materials*. 2016;60:137-41.

124. Sultanova N, Kasarova S, Nikolov I. Dispersion properties of optical polymers. *Acta Physica Polonica-Series A General Physics*. 2009;116(4):585.
125. Subramanian A, Neutens P, Dhakal A, Jansen R, Claes T, Rottenberg X, et al. Low-loss singlemode PECVD silicon nitride photonic wire waveguides for 532–900 nm wavelength window fabricated within a CMOS pilot line. *IEEE Photonics Journal*. 2013;5(6):2202809-.
126. Tien Pv. Light waves in thin films and integrated optics. *Appl Opt*. 1971;10(11):2395-413.
127. Yap KP, Delage A, Lapointe J, Lamontagne B, Schmid J, Waldron P, et al. Correlation of Scattering Loss, Sidewall Roughness and Waveguide Width in Silicon-on-Insulator (SOI) Ridge Waveguides. *J Lightwave Technol*. 2009;27:3999-4008.
128. Ramponi R, Osellame R, Marangoni M. Two straightforward methods for the measurement of optical losses in planar waveguides. *Rev Sci Instrum*. 2002;73(3):1117-20.
129. Tittelbach G, Richter B, Karthe W. Comparison of three transmission methods for integrated optical waveguide propagation loss measurement. *Pure and Applied Optics: Journal of the European Optical Society Part A*. 1993;2(6):683.
130. Keck D, Tynes A. Spectral response of low-loss optical waveguides. *Appl Opt*. 1972;11(7):1502-6.
131. De Rossi A, Ortiz V, Calligaro M, Lanco L, Ducci S, Berger V, et al. Measuring propagation loss in a multimode semiconductor waveguide. *J Appl Phys*. 2005;97(7):073105.
132. Feuchter T, Thirstrup C. High precision planar waveguide propagation loss measurement technique using a Fabry-Perot cavity. *IEEE photonics technology letters*. 1994;6(10):1244-7.
133. Okamura Y, Yoshinaka S, Yamamoto S. Measuring mode propagation losses of integrated optical waveguides: a simple method. *Appl Opt*. 1983 Dec;22(23):3892-4.
134. N. Daldosso, M. Melchiorri, F. Riboli, M. Girardini, G. Pucker, M. Crivellari, et al. Comparison among various Si₃N₄ waveguide geometries grown within a CMOS fabrication pilot line. *Journal of Lightwave Technology*. 2004;22(7):1734-40.
135. A. Dhakal, P. Wuytens, F. Peyskens, A. Subramanian, A. Skirtach, N. Le Thomas, et al. Nanophotonic lab-on-a-chip Raman sensors: A sensitivity comparison with confocal Raman microscope. - 2015 International Conference on BioPhotonics (BioPhotonics); ; 2015.
136. Thomas K, Sheeba M, Nampoori V, Vallabhan C, Radhakrishnan P. Raman spectra of polymethyl methacrylate optical fibres excited by a 532 nm diode pumped solid state laser. *Journal of optics a: pure and applied optics*. 2008;10(5):055303.
137. Xu X. Stimulated Raman spectrum threshold in poly (methyl methacrylate) optical fibers. *Opt Commun*. 2001;199(1-4):89-93.

138. Xingsheng X, Hai M, Qijing Z, Yunsheng Z. Properties of Raman spectra and laser-induced birefringence in polymethyl methacrylate optical fibres. *Journal of Optics A: Pure and Applied Optics*. 2002;4(3):237.
139. Melloni A, Monguzzi P, Costa R, Martinelli M. Design of curved waveguides: the matched bend. *JOSA A*. 2003;20(1):130-7.
140. Sakai A, Go H, Baba T. Sharply bent optical waveguide silicon-on-insulator substrate. *Physics and Simulation of Optoelectronic Devices IX; International Society for Optics and Photonics*; 2001.
141. Nie X, Turk N, Li Y, Liu Z, Baets R. High extinction ratio on-chip pump-rejection filter based on cascaded grating-assisted contra-directional couplers in silicon nitride rib waveguides. *Opt Lett*. 2019;44(9):2310-3.
142. Oser D, Mazeas F, Le Roux X, Pérez-Galacho D, Alibart O, Tanzilli S, et al. Coherency-broken Bragg filters: overcoming on-chip rejection limitations. *Laser & Photonics Reviews*. 2019;13(8):1800226.
143. Tyndall NF, Stievater TH, Kozak DA, Pruessner MW, Holmstrom SA, Rabinovich WS. Ultrabroadband lattice filters for integrated photonic spectroscopy and sensing. *Optical Engineering*. 2018;57(12):127103.
144. Ledinský M, Paviet-Salomon B, Vetushka A, Geissbühler J, Tomasi A, Despeisse M, et al. Profilometry of thin films on rough substrates by Raman spectroscopy. *Scientific reports*. 2016;6(1):1-7.
145. Xu Z, He Z, Song Y, Fu X, Rommel M, Luo X, et al. Topic review: application of Raman spectroscopy characterization in micro/nano-machining. *Micromachines*. 2018;9(7):361.
146. Kushwaha A, Kumar I, Khare A. Laser Induced Breakdown of Poly (Methyl Methacrylate (PMMA)) in Air. *Journal of Physical Science and Application*. 2014;4(7).
147. Wojdyr M. \it Fityk: a general-purpose peak fitting program. *Journal of Applied Crystallography*. 2010 Oct;43(5 Part 1):1126-8.

A. Appendix A

A.1 Electromagnetic spectrum

It is important to have in mind the electromagnetic spectrum and the possible phenomena involved for its interaction with the material (Figure 89). For Raman scattering it is useful to take into account the correspondence between scattered wavelength and Raman shift for both 633nm and 785nm pump laser (Figure 90). The relation is given by the formula:

$$\lambda_s(\text{nm}) = \frac{1}{\frac{1}{\lambda_L(\text{nm})} - \frac{\bar{\nu}(\text{cm}^{-1})}{10^7}}$$

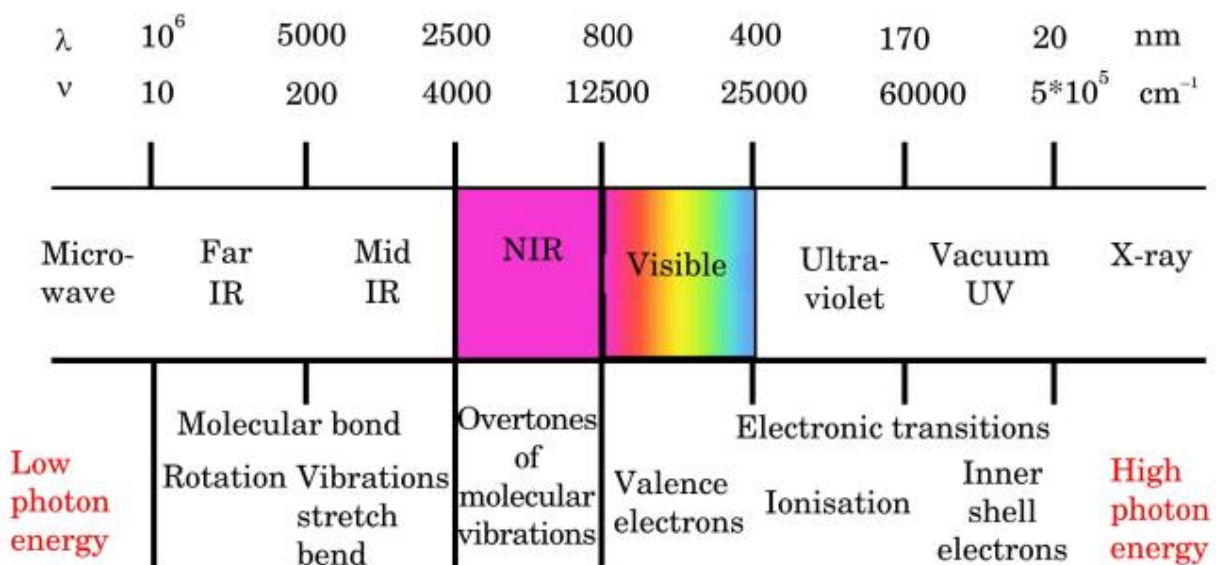


Figure 89: electromagnetic spectrum.

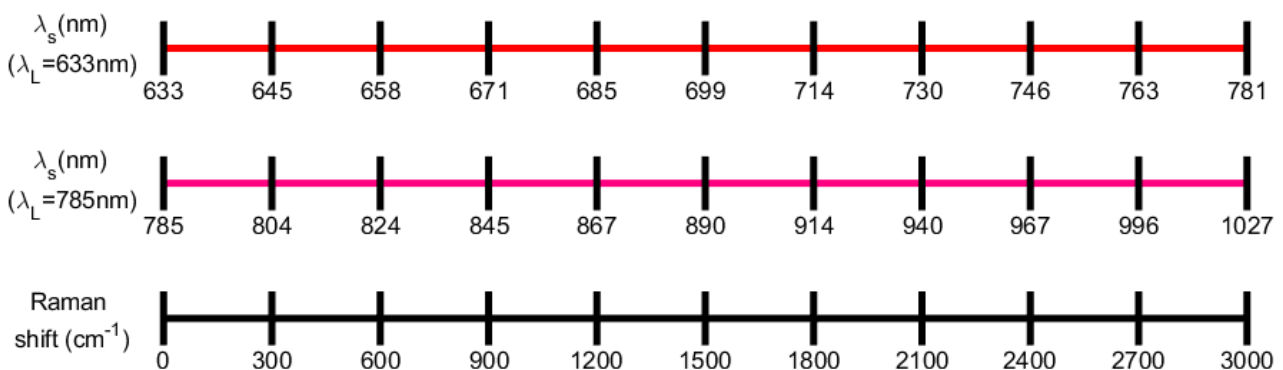


Figure 90: correspondence between Raman shift and scattered wavelength. It is useful to have it in mind to have the correspondence between the Raman peak observed on the spectrum and the scattered light wavelength travelling back in the WG.

A.2 Overlap analysis for waveguide-objective coupling

To have a rough idea of the power couple in the WGs, it is estimated the power coupling efficiency (γ) for different WG width. The $\gamma(\omega_p)$ into the WG is affected by two main factors:

1. The losses related to reflection at the interface air-SiN.
2. The overlap, between the gaussian beam coming from the objective and the mode of the WG.

Lumerical FDE solver offers the possibility to calculate the overlap between a waveguide mode and the gaussian beam coming from an objective. The input for the calculation of the waveguide mode is given by the refractive index map and the objective numerical aperture. The SiN WG is surrounded by silicon dioxide of the cladding and substrate.

It has been performed 2 different simulations: the first one with NA=0.65, for variable WG width from $0.5 \mu\text{m}$ to $0.7 \mu\text{m}$. The waveguide cross section can be variable due to the cleavage of the chip not at a well-fixed position. It should be considered the two different excitation lines that we can use, 785 nm and 633 nm, and the polarization (TE and TM). In *Figure 91* are reported the results of the simulation: as we can see there is a general trend where the increase of waveguide width leads to increase of the coupling efficiency. The power coupling efficiency is around 70%, therefore the losses are 30% or 5.2 dB/facet which are in line to those calculated by (44). The influence of the WG width on the coupling efficiency is negligible, as can be seen the standard deviation reported for each curve is much lower with respect to the mean value (e.g. $\langle \gamma_{TE,785\text{nm}} \rangle = 0.786 \pm 0.005$). The major influence on γ are the polarization of the light and the pump laser wavelength. TE polarization and 785 nm has the highest overlap, with a mean value of $\langle \gamma_{TE,785\text{nm}} \rangle = 0.786$.

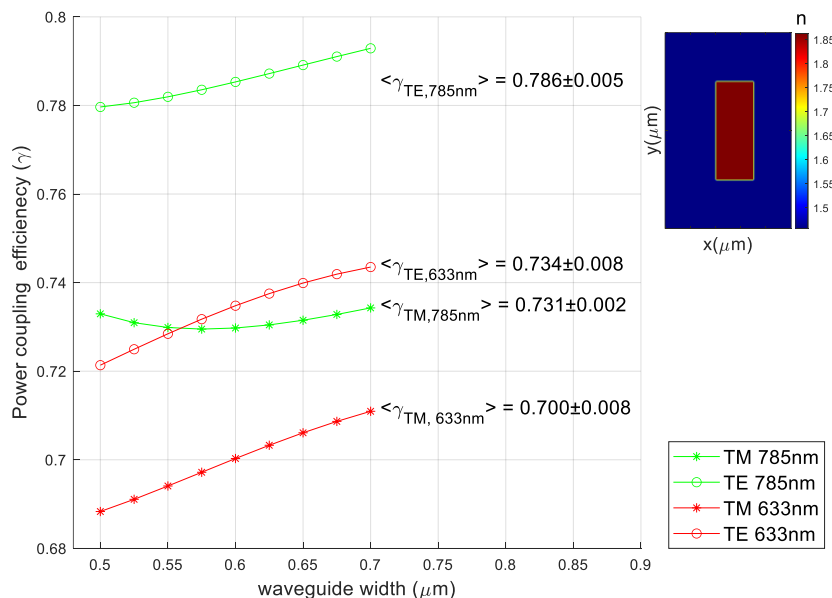


Figure 91: power coupling efficiency in function of the WG width for TM - TE modes and 633 - 785 nm pump wavelength. On top right there is an example of refractive index map over which the calculation is evaluated with an objective with NA = 0.65.

A second simulation it has been performed considering only TM mode and 785nm laser wavelength. It has been compared two different objectives with NA=0.65 and NA=0.9, for variable WG width from 0.4 μm to 1.2 μm . The coupling coefficient as function of the WG width is reported in Figure 92. It is shown an optimal coupling efficiency at around 0.6 μm for NA=0.9 with a value of 0.78. For NA=0.65 the optimal coupling efficiency is at higher WG width, as expected since for higher NA the gaussian open space mode will be larger and therefore the coupling will result optimal for larger WG width. There is a considerable drop in coupling efficiency for NA=0.9 at WG width of 1.2 μm .

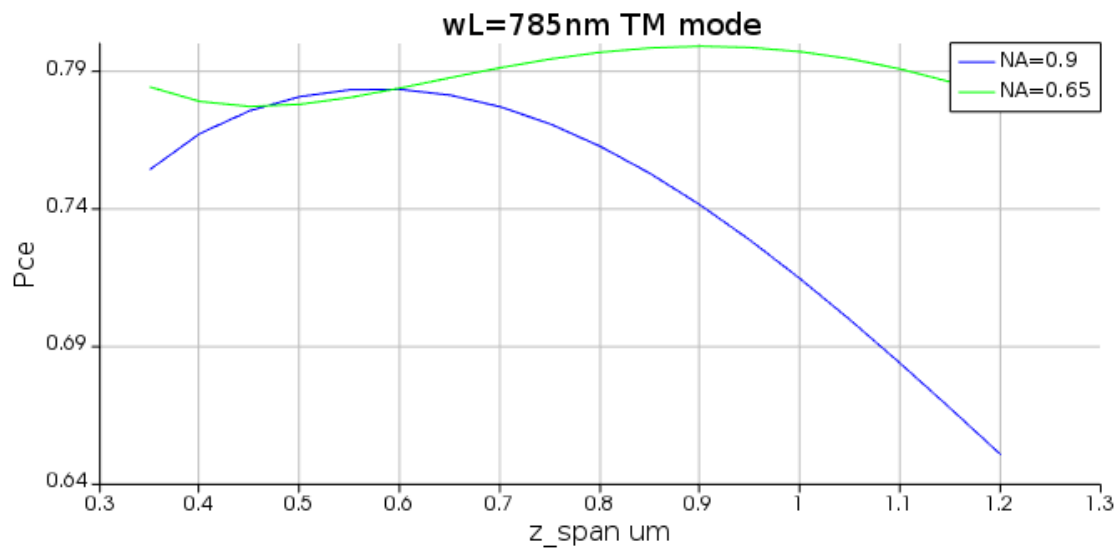


Figure 92: the power coupling efficiency (Pce) estimated by Lumerical simulations as function of the WG width for two different NA objectives: 0.9 NA and 0.65 NA. The only mode analyzed is the TM mode at wavelength 785nm.

A.3 Conversion efficiency (Lumerical)

A.3.1 Convergence testing

The mesh size and the simulation region dimension will need to be determined by different convergence testing. Both should be optimized considering that in Lumerical 2D simulations the memory requirements go as $\sim A(\lambda/dx)^2$ and the simulation time goes as $\sim A(\lambda/dx)^3$, where A is the simulation area, dx is the mesh size and λ is the wavelength. On the other hand, the simulation region dimension should be large enough to include the entire mode and the mesh size should be smaller enough to get precise and reliable results.

To determine the solver region dimension it has been performed a simulation with:

- z_span and y_span large enough to be sure to get very low field intensity at the boundary: $y_span \times z_span = 3 \times 5 \mu m^2$.
- The waveguides of reference that I have used are those with width $0.4 \mu m$ and $1.2 \mu m$.
- The wavelength chosen to correspond to the two-laser used in the experiments, 633nm and 785nm, and the 1000nm which correspond to a Raman shift in the order of 2800 cm^{-1} , which represent one of the longest wavelength collected from Raman scattering in my experiments.

Therefore, it has been performed 6 different simulations at 3 different wavelength and 2 different waveguide widths. It has been plotted the field intensity profile along the y and z directions passing through the origin Figure 93. It has been chosen to consider the boundary of the solver region on which the field intensity is less then 10^{-3} (with normalized units), the blue dashed lines in Figure 93 represent where the field intensity is in the order of 10^{-3} for the 1000 nm wavelength. The solver region taken for all the following simulations is:

$$y_span \times z_span = 2 \times 3 \mu m^2$$

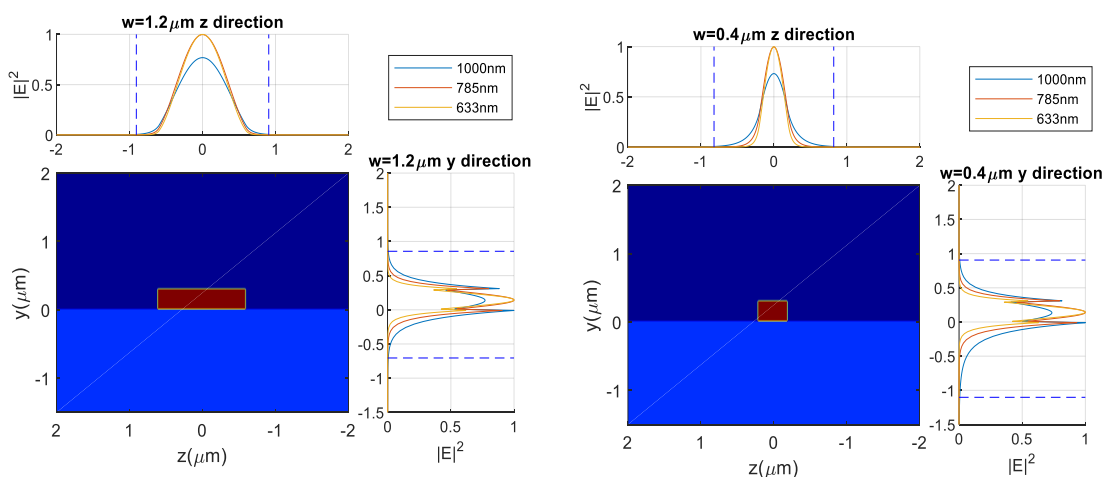


Figure 93 on the left normalized electric field square modulus profiles resulting from 3 simulations at 3 different wavelengths are plotted around the refractive index map of a strip waveguide with width $1.2 \mu m$. The blue dotted lines correspond to a value of $|E|^2(\lambda = 1000nm) \sim 5 \cdot 10^{-3}$. The 0 point of the two lateral plots correspond to the (0,0) point of the refractive index map. On the right it is like the left image but with a waveguide width of $0.4 \mu m$. TBN the field intensity plotted correspond to the TM01 mode.

From Figure 93, looking at the graph in the y direction, we can notice that the evanescent tails of the modes with wavelength 633nm and 785nm extend in the positive y direction till +0.5 μm and +0.7 μm respectively. This means that the interaction length between the electric field and the analyte extends into a region of approximately 0.2 μm and 0.4 μm over the waveguide.

Now I have to decide the mesh input. It is important to notice that in correspondence to the refractive index discontinuities the control of the mesh is crucial. This can be shown with the results obtained from two different mesh size sweep that differs by the presence of a mesh override region which refine the mesh around the boundary of the silicon nitride waveguide, Figure 94. Therefore, the region over which there are cell with intermediate refractive index is reduced, as can be seen in the insets in Figure 94. So, by the introduction of a mesh override the convergence is achieved without reducing too much the mesh size of the FDE region reducing the simulation time and memory requirements. The input for the next simulations are:

- FDE mesh: $dz = dy = 0.05 \mu\text{m}$
- Mesh override: $z_span = 1.4\mu\text{m}$ and $y_span = 0.4\mu\text{m}$; $dz = dy = 0.005 \mu\text{m}$

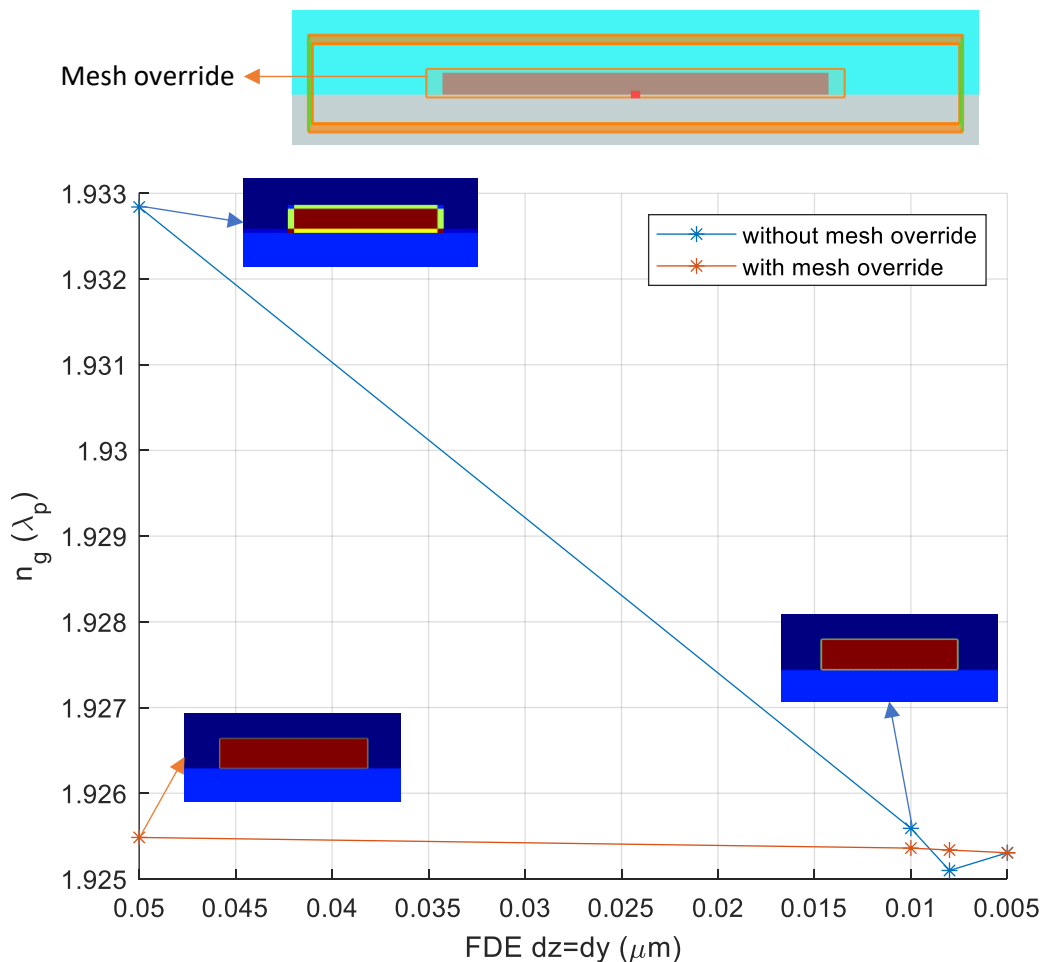


Figure 94 The group index as function of the mesh size of the FDE solver region. The blue curve is the simulation without mesh override and the orange one is with (on the top there is a representation YZ view of the simulation with mesh override). The insets are the refractive index maps which are the input to each data point obtained.

Finally, the choice of the boundary condition should be considered. It is possible to choose between Metal and PML boundary conditions. The metal ones are recommended in case of

negligible fields at the boundary because are fastest. Since the simulations time was not a limiting factor, it has been preferred to use PML boundary conditions, since are in line with the physics of the problem.

The solver will only determine propagation loss due to the materials (absorption) or radiative loss (for example in a bent waveguide), it do not account the losses due to roughness.

A.3.2 Additional simulations

The ratio $\frac{\eta_{SiN}}{\eta_{SiO_2}}$ is evaluated for TM00 and PMMA cladding. In our hypothesis this ratio should not change greatly with the WG width. This is a good assumption as can be evinced from the figure below. But in the paper, they have been used a WG with width $0.22 \mu m$ but our WGs have $0.3 \mu m$. The difference between these two cases results in a change in the $\frac{\eta_{SiN}}{\eta_{SiO_2}}$. The experimental value for $\beta_{BG}(\tilde{\nu})$ is for $0.22 \mu m$ height and $0.7 \mu m$ width.

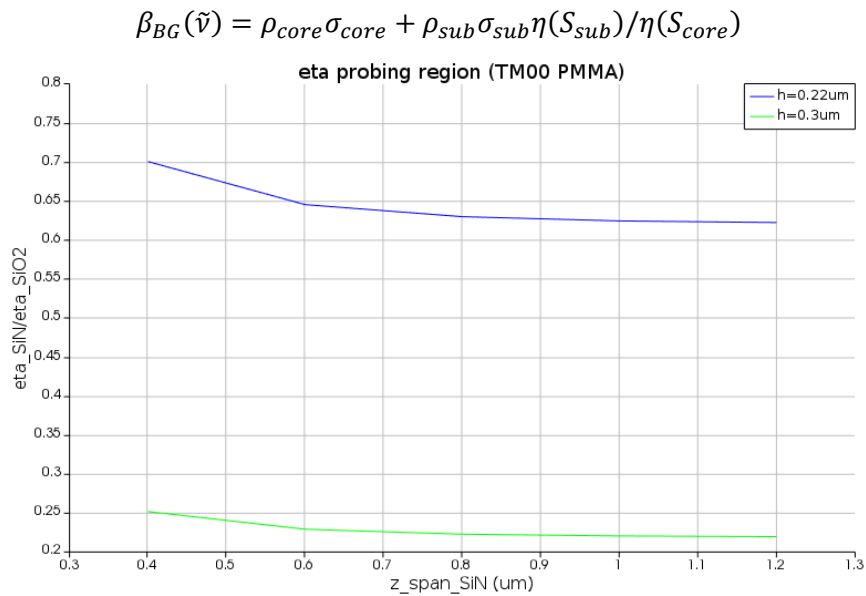


Figure 95: ratio between $\eta(S_{sub})/\eta(S_{core})$ as function of the WG width (z_span_SiN) for two different WG height. The strip WGs are with cladding PMMA and the simulation is performed at 785nm and TM00 mode.

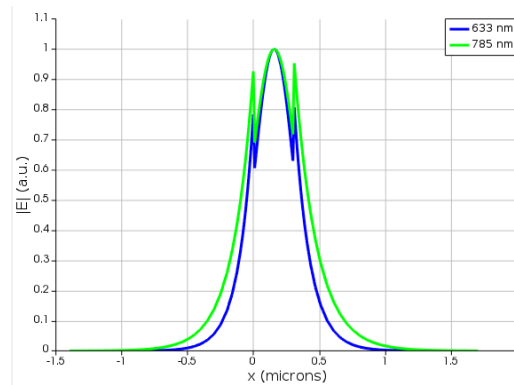


Figure 96: mode intensity as function of the x direction. The intensity plotted is a slice of the y axis at the correspondence of the axis of symmetry of the WG.

Influence of the CCR on the cladding refractive index is reported in Figure 97. In the bottom graph it can be clearly seen that the ratio $CCR(785nm)/CCR(633nm)=2.5$ is constant for every cladding refractive index.

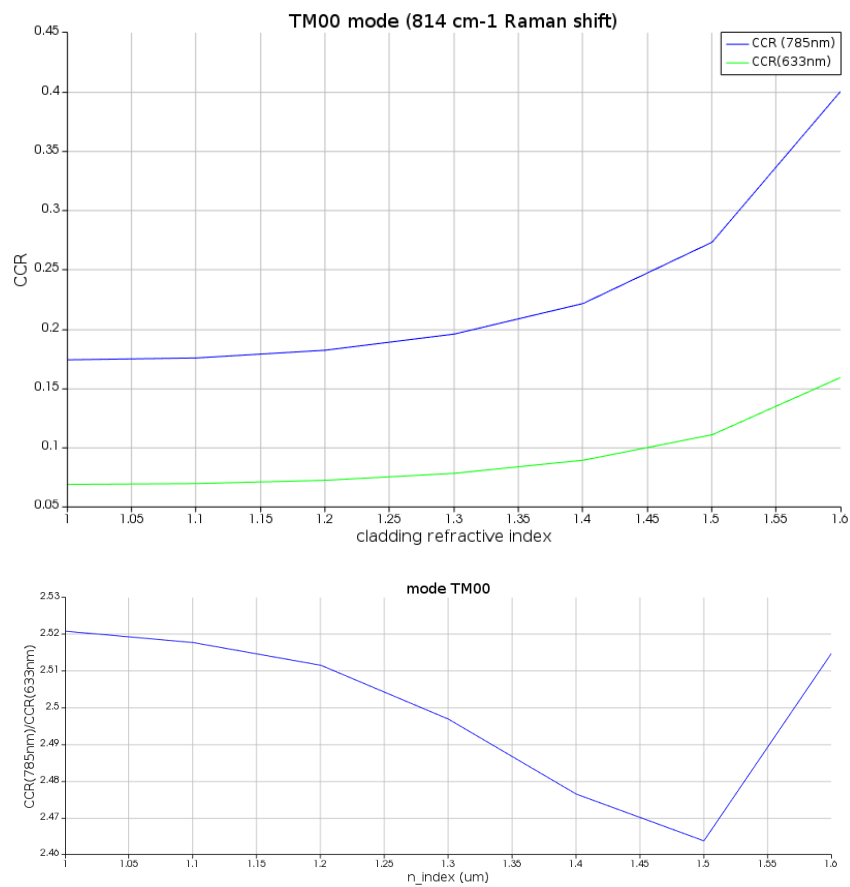


Figure 97: top image the CCR as function of the cladding refractive index at different laser wavelengths. On the bottom the ratio between CCR of the two lines in the upper graph.

Influence of the Raman shift to CCR is reported in Figure 98. As can be seen at higher wavenumbers this value increases.

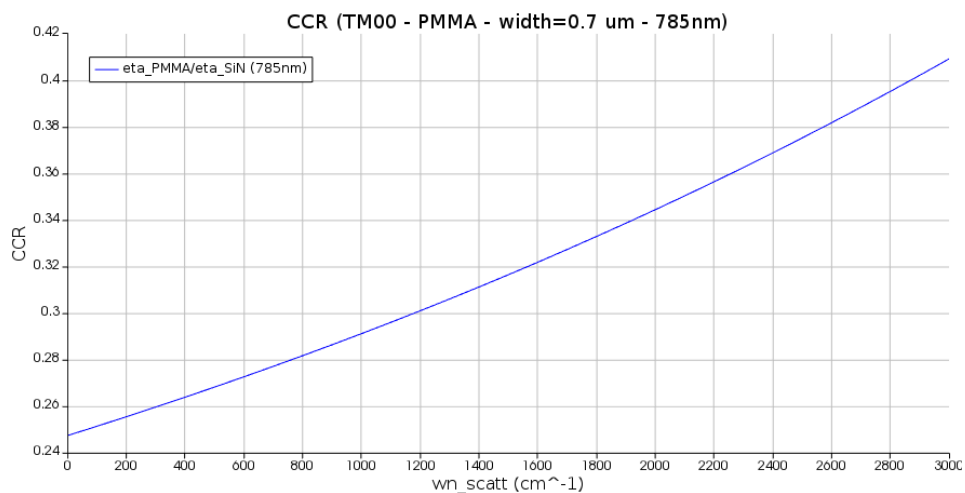


Figure 98: the CCR as function of the wavenumber Raman scattering.

A.3.3 Script: conversion efficiency probing region

```
##### main parameters #####
#height of the WG
y_span_SiN = 0.3*10^-6;
#FDE simulation region
FDE_y_span = 2*10^-6;   FDE_z_span = 3*10^-6;
#mesh
FDEdzdy = 0.05*10^-6;
MESHon = 1;             MESHdzdy = 0.005*10^-6;
switchtolayout;
select("PMMA");        set("enabled",1);
select("IPA");          set("enabled",0);
analyte = 'PMMA';

#####
switchtolayout;
#components dimension
select("SiO substrate");
set("y min", -10*10^-6); set("y max", 0); set("z span", 10*10^-6);
select("SiN waveguide");
set("y min", 0.0);      set("y max", y_span_SiN);
select("IPA");
set("y min", 0.0);      set("y max", 10*10^-6); set("z span", 10*10^-6);
select("PMMA");
set("y min", 0.0);      set("y max", 10*10^-6); set("z span", 10*10^-6);

select("FDE");
#geometry
set("y", 0.15*10^-6); set("z", 0);
set("y span", FDE_y_span); set("z span", FDE_z_span);
#mesh
set("define y mesh by",1); set("define z mesh by",1);
set("dy",FDEdzdy);        set("dz",FDEdzdy);
set("mesh refinement", "conformal variant 1");

#mesh Override
select("WG mesh");
set("enabled",MESHon); set("directly defined", 1);
set("dy", MESHdzdy);   set("dz", MESHdzdy);

##### parameters #####
wL = [785, 633]*10^-9; #in m
wn_scatt = 822;        #in cm^-1
z_span_SiN = [0.4:0.2:1.2]*10^-6; # the waveguide width in m
#z_span_SiN = 0.7*10^-6;
eta_Analyte = zeros(length(z_span_SiN),length(wL));
eta_SiN = zeros(length(z_span_SiN),length(wL));
eta_SiO = zeros(length(z_span_SiN),length(wL));

#####
#mode and boundary conditions
slect_mode = "model1"; # we consider the TM01 mode we need z symmetric BC
mode_chosen = "FDE::data::"+slect_mode;
select("FDE");
set("y max bc", "PML");
set("y min bc", "PML");
set("z max bc", "PML");
set("z min bc", "Symmetric");
```

```

for (o = 1:length(wL)){
  for (k=1:length(z_span_SiN)){
    #####
    #change the geometry
    switchtolayout;
    select("FDE");          set("wavelength", wL(o)); #change wavelength
    select("SiN waveguide"); set("z span", z_span_SiN(k)); #change width
    findmodes;
    y = getdata(mode_choosen,"y"); # m z = getdata(mode_choosen,"z"); # m
    n = getresult("FDE::data::material","index");
    relpe_p = pinch((n.index_x)^2);
    ng_p = getresult(mode_choosen,"ng");
    Ex = getresult(mode_choosen,"Ex"); Ey = getresult(mode_choosen,"Ey");
    Ez = getresult(mode_choosen,"Ez"); E2=abs(Ex)^2+abs(Ey)^2+abs(Ez)^2;
    #####
    switchtolayout;      wL_scatt =1/(1/wL(o) - wn_scatt*(10^2));
    select("FDE");      set("wavelength", wL_scatt); #change wavelength
    findmodes;
    n = getresult("FDE::data::material","index");
    relpe_s = pinch((n.index_x)^2);
    n_Analyte_s = relpe_s(end,end)^0.5; n_SiO_s = relpe_s(1,1)^0.5;
    n_SiN_s = relpe_s(end/2,end/2)^0.5; ng_s = getresult(mode_choosen,"ng");
    Ex = getresult(mode_choosen,"Ex"); Ey = getresult(mode_choosen,"Ey");
    Ez = getresult(mode_choosen,"Ez"); E2=abs(Ex)^2+abs(Ey)^2+abs(Ez)^2;
    #####
    en_density_int_p = relpe_p*E2_p;
    integral_p = integrate(en_density_int_p,[1,2],y,z);
    en_density_int_s = relpe_s*E2_s;
    integral_s = integrate(en_density_int_s,[1,2],y,z);
    Nx = size(relpe_p,1);      Ny = size(relpe_p,2);
    int_limit = zeros(Nx, Ny); int_limit_SiN = zeros(Nx, Ny);
    int_limit_SiOunder = zeros(Nx, Ny);
    for (i=1:Nx){ for (j=1:Ny){
      if (relpe_p(i,j)==relpe_p(end,end)){int_limit(i,j) = 1;}
      else {int_limit(i,j) = 0;}
      if (relpe_p(i,j)==relpe_p(end,end)){int_limit_SiN(i,j) = 0;}
      else if (relpe_p(i,j)==relpe_p(1,1)){int_limit_SiN(i,j) = 0;}
      else {int_limit_SiN(i,j) = 1;}
      if (relpe_p(i,j)==relpe_p(1,1)){int_limit_SiOunder(i,j) = 1;}
      else {int_limit_SiOunder(i,j) = 0;}
    }}
    #####
    en_density_int2 = int_limit*(E2_p*E2_s);
    integral2 = integrate (en_density_int2,[1,2],y,z);
    ?eta_Analyte(k,o) = real(ng_p) * real(ng_s) * integral2 * wL_scatt^2 /
(n_Analyte_s*integral_p*integral_s);

    en_density_int2_SiN = int_limit_SiN*(E2_p*E2_s);
    integral2_SiN = integrate (en_density_int2_SiN,[1,2],y,z);
    ?eta_SiN(k,o) = real(ng_p) * real(ng_s) * integral2_SiN * wL_scatt^2 /
(n_SiN_s*integral_p*integral_s);

    en_density_int2_SiO = int_limit_SiOunder*(E2_p*E2_s);
    integral2_SiO = integrate (en_density_int2_SiO,[1,2],y,z);
    ?eta_SiO(k,o) = real(ng_p) * real(ng_s) * integral2_SiO * wL_scatt^2 /
(n_SiO_s*integral_p*integral_s);
  } }

```

A.3.4 Script: conversion efficiency for not-probing region

```
select("SiO substrate");
set("y min", -2*10^-6); #change heighth
set("y max", 2*10^-6); #change heighth

select("FDE");
#geometry
set("y", 0.15*10^-6);
set("z", 0);
set("y span", FDE_y_span);
set("z span", FDE_z_span);
#mesh
set("define y mesh by",1);
set("define z mesh by",1);
set("dy",FDEdzdy);
set("dz",FDEdzdy);
set("mesh refinement", "conformal variant 1");
#mesh Override
select("WG mesh");
set("enabled",MESHon);
set("dy", MESHdzdy);
set("dz", MESHdzdy);
set("directly defined", 1);

##### parameters #####
wL =[785, 633]*10^-9; #in m (785nm and 633nm)
wL_scatt = 822;
z_span_SiN = [0.4:0.2:1.2]*10^-6; # the waveguide width in m
eta_SiO = zeros(length(z_span_SiN),length(wL));
eta_SiN = zeros(length(z_span_SiN),length(wL));
#####

#mode and boundary conditions
slect_mode = "mode1"; # we consider the TM01 mode we need z symmetric BC
mode_choosen = "FDE::data::"+slect_mode;
select("FDE");
set("y max bc", "PML");
set("y min bc", "PML");
set("z max bc", "PML");
set("z min bc", "Symmetric");
```

```

for (o = 1:length(wL)){
  for (k=1:length(z_span_SiN)){
    #####
    #change the geometry
    switchtolayout;
    select("FDE");
    set("wavelength", wL(o)); #change the wavelength
    select("SiN waveguide");
    set("z span", z_span_SiN(k)); #change the waveguide width
    findmodes;
    y = getdata(mode_choosen,"y"); # m
    z = getdata(mode_choosen,"z"); # m
    n = getresult("FDE::data::material","index");
    rel_perm_p = pinch((n.index_x)^2);
    ng_p = getresult(mode_choosen,"ng");
    Ex = getresult(mode_choosen,"Ex"); Ey = getresult(mode_choosen,"Ey");
    Ez=getresult(mode_choosen,"Ez");E2 =(abs(Ex))^2+(abs(Ey))^2+ (abs(Ez))^2;
    #####
    switchtolayout;
    select("FDE");          wL_scatt = 1/(1/wL(o) - wn_scatt*(10^2));
    set("wavelength", wL_scatt); #change the wavelength
    findmodes;
    n = getresult("FDE::data::material","index");
    rel_perm_s = pinch((n.index_x)^2);
    n_IPA_s = rel_perm_s(end,end)^0.5;
    #image(y,z,rel_perm);
    ng_s = getresult(mode_choosen,"ng");
    Ex = getresult(mode_choosen,"Ex"); Ey = getresult(mode_choosen,"Ey");
    Ez=getresult(mode_choosen,"Ez");E2 =(abs(Ex))^2+(abs(Ey))^2+ (abs(Ez))^2;
    #####
    en_density_int_p = rel_perm_p*E2_p;
    ?integral_p = integrate(en_density_int_p,[1,2],y,z);
    en_density_int_s = rel_perm_s*E2_s;
    ?integral_s = integrate(en_density_int_s,[1,2],y,z);

    Nx = size(rel_perm_p,1); Ny = size(rel_perm_p,2);
    int_limit = zeros(Nx, Ny);
    int_limit_SiN = zeros(Nx, Ny);
    for (i=1:Nx){
      for (j=1:Ny){
        if (rel_perm_p(i,j)==rel_perm_p(end,end)){int_limit(i,j) = 1;}
        else {int_limit(i,j) = 0;}
        if (rel_perm_p(i,j)==rel_perm_p(end,end)){int_limit_SiN(i,j)= 0;}
        else if (rel_perm_p(i,j)==rel_perm_p(1,1)){int_limit_SiN(i,j)= 0;}
        else {int_limit_SiN(i,j) = 1;}
      } }

    en_density_int2 = int_limit*(E2_p*E2_s);
    ?integral2 = integrate (en_density_int2,[1,2],y,z);
    ?eta_SiO(k,o) = real(ng_p) * real(ng_s) * integral2 * wL_scatt^2 /
(n_SiO_s*integral_p*integral_s);

    en_density_int2_SiN = int_limit_SiN*(E2_p*E2_s);
    ?integral2_SiN = integrate (en_density_int2_SiN,[1,2],y,z);
    ?eta_SiN(k,o) = real(ng_p) * real(ng_s) * integral2_SiN * wL_scatt^2 /
(n_SiN_s*integral_p*integral_s);
  } }

```

A.4 Scattering losses

A.4.1 Experiments procedure

Procedure for estimation of scattering losses (Figure 99):

1. Image acquisition from the Thor camera while the laser is coupled in the WG.
2. Since the chip sometimes has a small rotation of 1° the images have been firstly rotated all by that amount to simplify the calculation and data elaboration.
3. The angle of rotation is estimated by minimizing the absolute value of the angular coefficient of a linear fit of the line resulting from the scattered power of the WG.
4. For each WG there are two red rectangle which delimits the area over which the experimental data are extracted.
5. Integration line by line of the scattered intensity and plot on the y axis. On the x axis the z-position is reported. Fitting of the log scale.

In Figure 100 is reported the MATLAB scripts for the WG losses estimation.

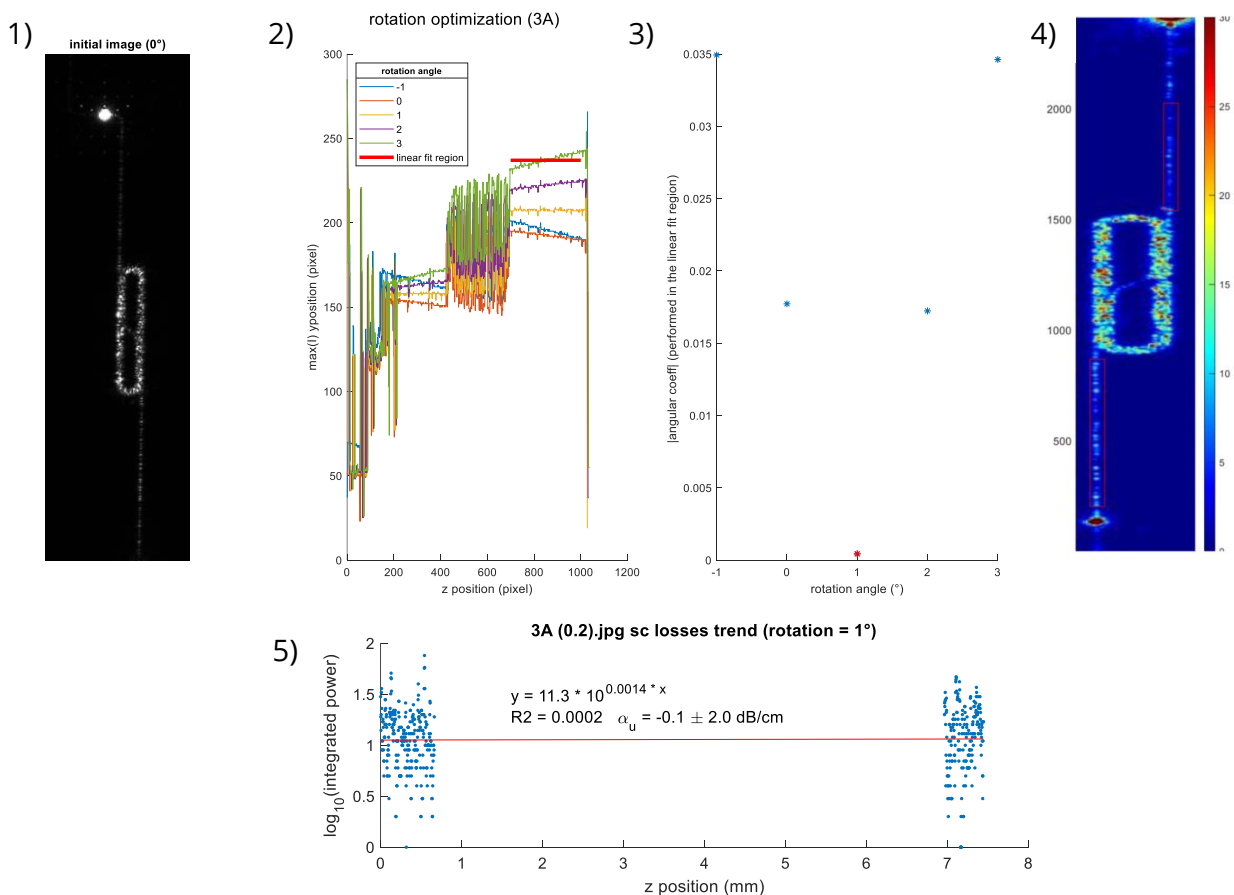


Figure 99: it is applied an initial rotation of the image. 1): To estimate the best rotational angle the black and white image is converted in a vector line for which only the position of the maximum intensity (along y direction) is recorded. 2): A linear fit of the “linear fit region” displaced. 3): the absolute value of the angular coefficient is plotted as function of the rotation angle. 4): picture obtained from the top camera on the WG correctly rotated. There are two red rectangle which delimits the area over which we are taking the measurements. 5): the \log_{10} of the scattered power integrated over one line (one horizontal line delimited by the red rectangles) versus the z position, i.e. the WG length.

```

%-----total integration of the scattering intensity-----
.
.
.
% cutting the data in the region for the integration
doub_Int_Img2 = doub_Int_Img2(y_lim,x_lim);
%removal background
doub_Int_Img2 = doub_Int_Img2 - 1*(doub_Int_Img2~=0);
.
.
% integration of the intensity from all the area
tot_power_sc = sum(sum(doub_Int_Img2));
tot_power_sc_vec(file_n) = tot_power_sc;

%----Scattering losses coeff estimated with top camera-----
.
.
.
% cutting the data in the region for the integration
doub_Int_Img2 = doub_Int_Img2(y_lim,x_lim);
%removal background
doub_Int_Img2 = doub_Int_Img2 - 1*(doub_Int_Img2~=0);
.
.
.
% data point integration first rectangle
for i = 1:Np1
    y = doub_Int_Img2(intervl1(i), ycut1);
    integral_vec(i) = sum(y);
end
% data point integration second rectangle
for i = 1:Np2
    y = doub_Int_Img2(intervl2(i), ycut2);
    integral_vec(Np1+i) = sum(y);
end
.
.
.
% fit
y0 = log10(integral_vec);
x1 = linspace(min(z),max(z));
[p,S] = polyfit(z,y0,1);
y1 = polyval(p,x1);
plot(x1,y1, 'r');

```

Figure 100: script of the main step for calculation of WG losses.

In Figure 101 and Figure 102 are reported the scattering intensity coming from WG spirals covered by PMMA. It can be noticed that the highest scattering intensity is coming from 3E and 2E WGs. Under the hypothesis that similar amount of power is coupled in it can be understood that 3E and 2E WGs have higher loss coefficients.

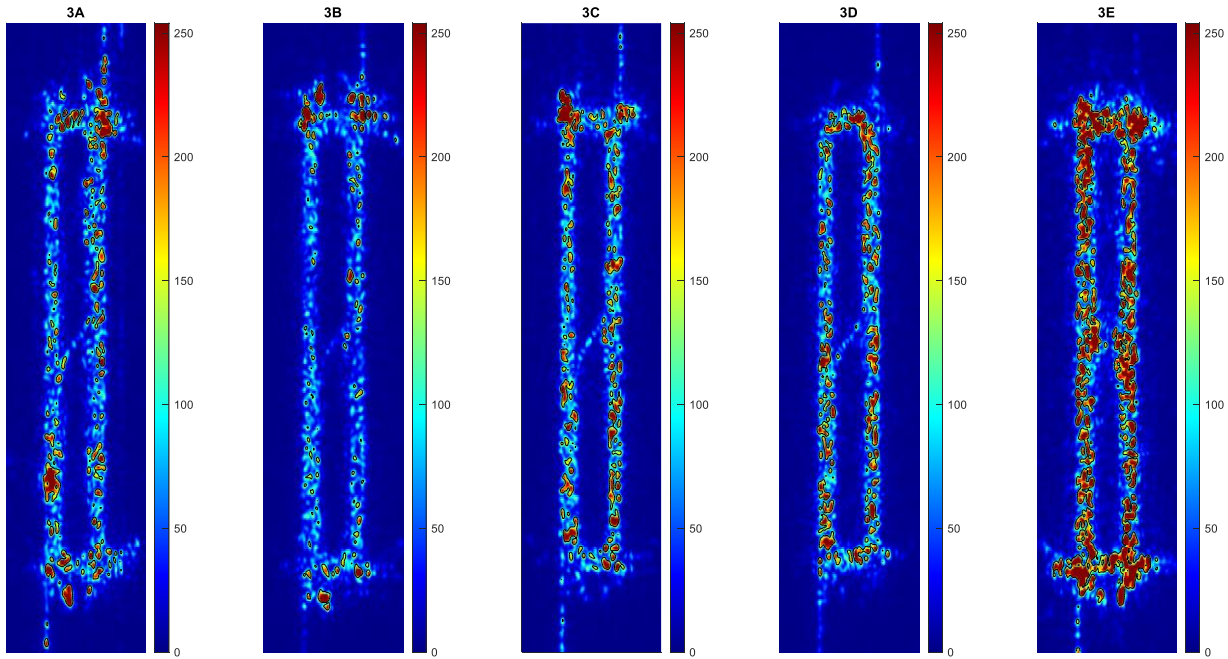


Figure 101: scattering intensity of spirals of WGs number "3".

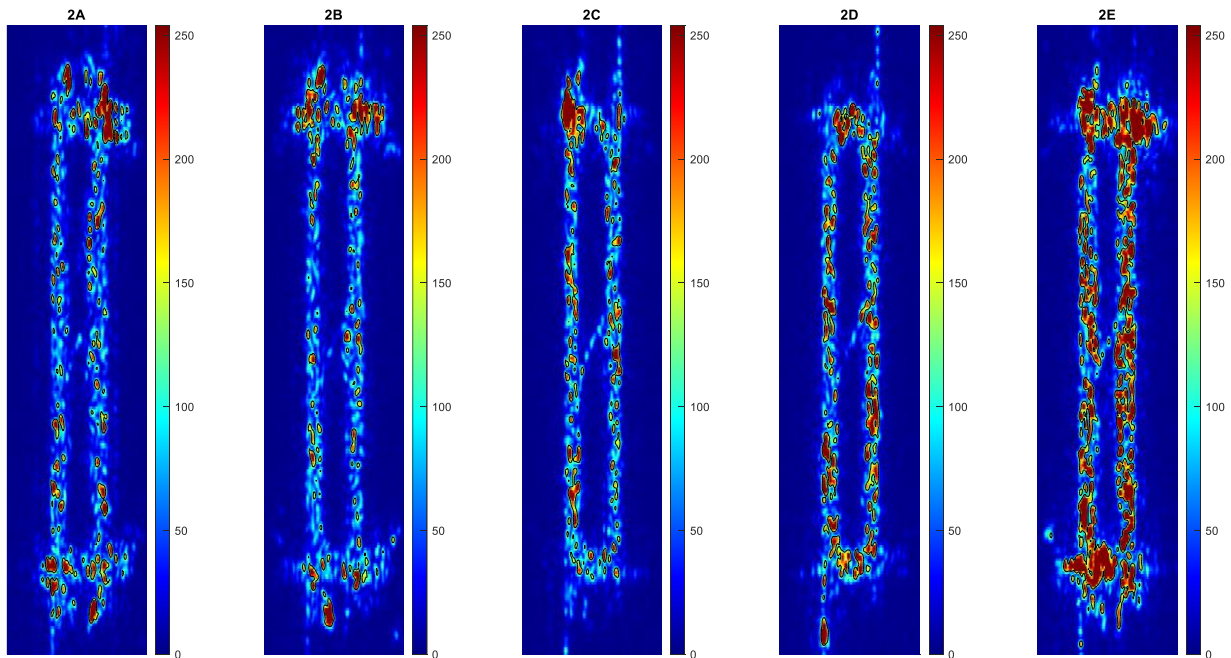


Figure 102: scattering intensity of spirals of WGs number "2".

A.4.2 Comparison n_w model with volume-current method

In Figure 103 is shown the comparison between the volume current method and n_w model. The data of the volume-current method are taken from (49). As can be seen there is a good agreement between the two methods. For higher WG width the n_w model has higher values with respect to the volume-current method.

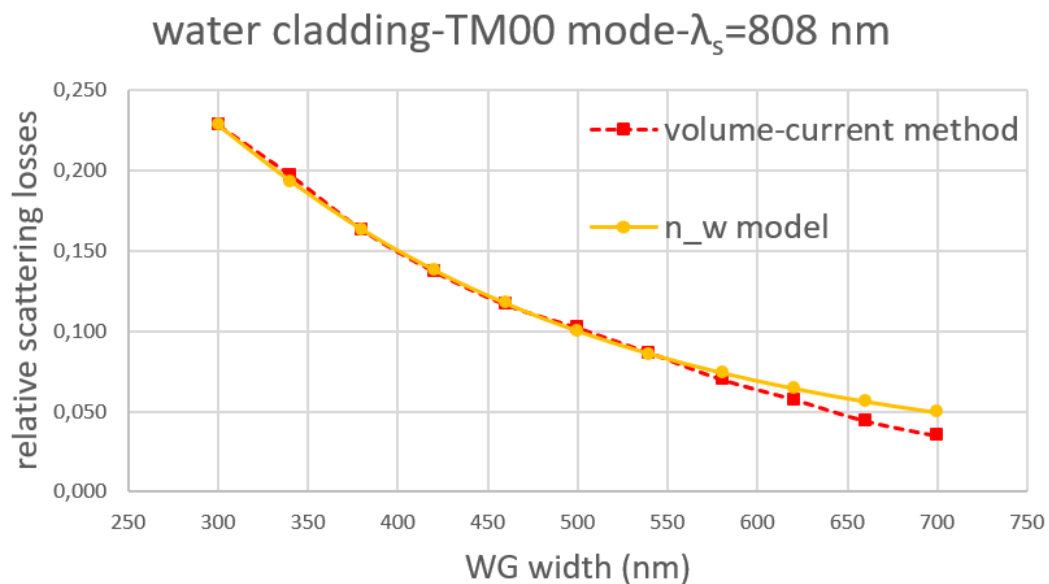


Figure 103: relative scattering losses as function of the WG width. All the specific of the simulation are reported in the title. The strip WGs used are with height $0.4 \mu\text{m}$. The volume current data are taken from article (49).

A.4.3 WG losses simulation for not-probing region

In the n_w model, from the formula of A coefficient (81):

$$A = \sigma^2 L_c k_0^2 \frac{n_{core}^2 - n_{clad}^2}{n_{core}^2} n_{eff} \tilde{f} \quad 0.1$$

$$\tilde{f} = \sqrt{\frac{\sqrt{y} + 1 - L_c^2 k_0^2 (n_{eff}^2 - n_{clad}^2)}{y}} \quad 0.2$$

$$y = \left(1 + L_c^2 k_0^2 (n_{eff}^2 - n_{clad}^2)\right)^2 + 16 L_c^2 k_0^2 n_{clad}^2 \quad 0.3$$

Where $k_0 = 2\pi/\lambda_p$ is the vacuum wavenumber, n_{eff} is the effective refractive index, L_c is the correlation length and σ is the roughness, n_{core} and n_{clad} are the core and cladding refractive indexes respectively. It can be noticed that:

- $A \sim \sigma^2$, for fixed values of correlation length (L_c).
- For $L_c < \lambda_p$ increases A increases too but more slowly with respect to the case of σ (fixed σ).
- Finally, it should be noticed that generally the larger the σ , the shorter the L_c (81). From values taken from the literature (80, 81) the relation could be: $L_c = \frac{C}{\sigma}$ with $C \in [70; 100] nm^2$

In general, knowing the value of A it is not possible to find both (L_c, σ) but it will be found a set of points (in Figure 104 is highlighted in red for PMMA). It could be guessed both roughness and correlation length if the $L_c = \frac{C}{\sigma}$ relation is valid. For example, for PMMA it was found $A = 5.0 \frac{dB}{cm} * \mu m$, a map in Figure 104 which the points near that value are highlighted in red. Therefore, it results $L_c = 29 nm$ and $\sigma = 2.7 nm$.

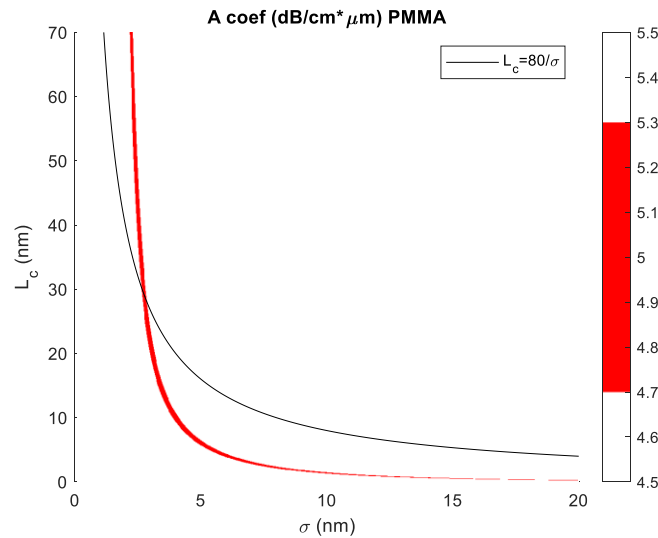


Figure 104: A factor map as function of σ and L_c for PMMA at 785 nm wavelength. The colour scale is such that only values in between [4.7:5.3] are in red and the others are white. It is also reported the function: $L_c = 80/\sigma$ in black.

Knowing the values of correlation length and root mean square roughness it is possible to estimate the scattering losses for PMMA cladding at different wavelengths. The results are

reported in Figure 105 and shows how the α_p decreases as the Raman shift moves from 0 cm^{-1} to 1455 cm^{-1} (i.e. 866 nm). The scattering losses decrease. Therefore, it should be noted that in the equation of SBR the scattering coefficient is the mean between the α_p at the pump and scattered wavelengths: $\alpha_p = \frac{(\alpha_p(\lambda_p) + \alpha_p(\lambda_s))}{2}$, the results are reported in Table 11.

These values of roughness and correlation length have been obtained from strip WGs with PMMA cladding. For the same chip it is reasonable to consider the same values of L_c and σ also for the not-probing region with SiO_2 cladding. Under this hypothesis it is possible to evaluate the α_{np} with the n_w model. The results are reported in Figure 106. Therefore, it results that the not-probing loss coefficients are: 1.3 dB/cm; 0.7 dB/cm; 0.4 dB/cm; 0.3 dB/cm and 0.15 dB/cm for E, D, C, B, A WGs respectively.

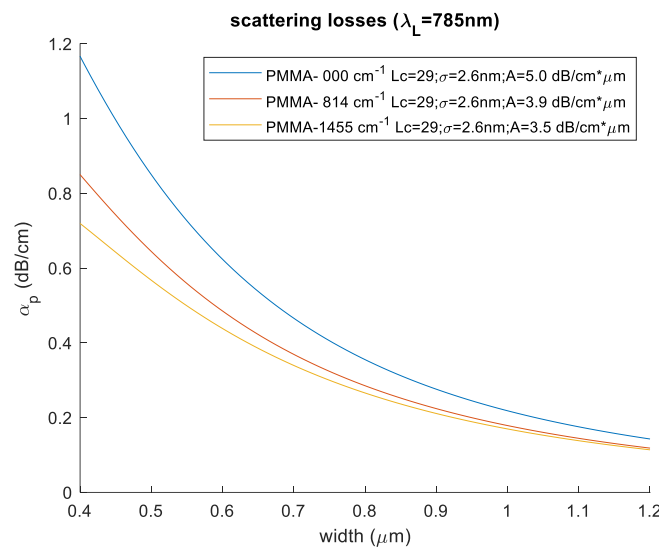


Figure 105: scattering loss coefficients as function of the WG width predicted from n_w model.

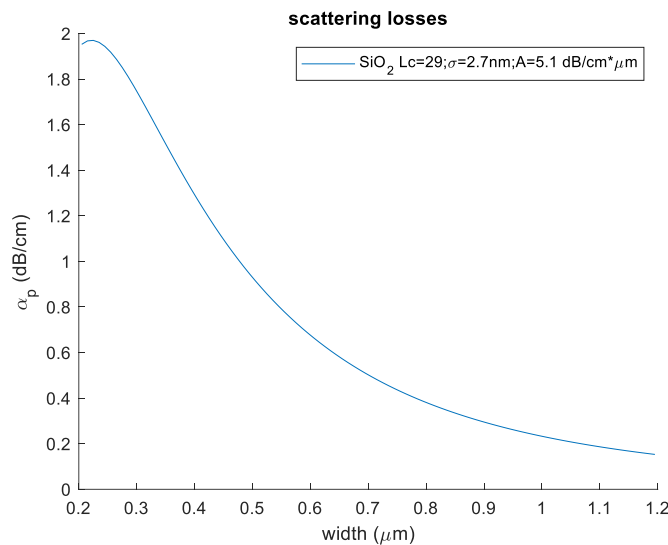


Figure 106: scattering losses predicted by the n_w model of strip WGs with SiO_2 cladding and $L_c = 29\text{ nm}$ and $\sigma = 2.7\text{ nm}$.

A.5 Raman spectra of PMMA

A.5.1 Height of PMMA spin coated film

To roughly evaluate the height of PMMA film deposited on the chip it was performed a z-scan with 633nm laser and 100x/0.95NA objective. The technique used is similar to what reported by M. Ledinský et al. (144). The final film height is approximately $1\mu\text{m}$.

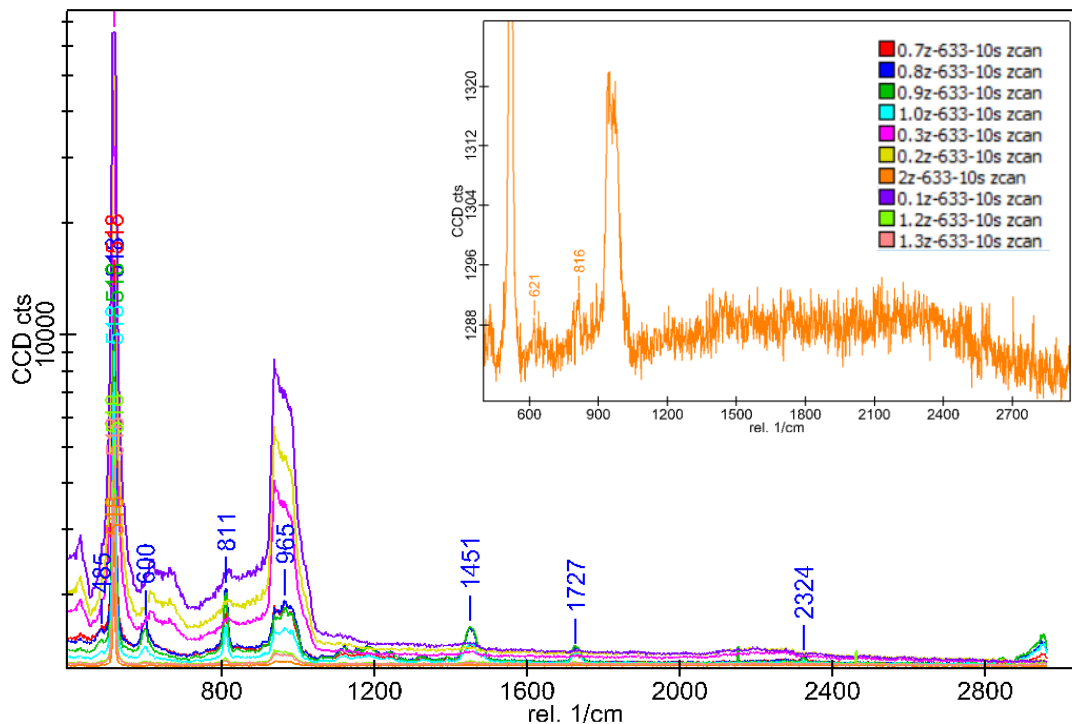


Figure 107: Raman spectra of PMMA sample spin coated on the chip at different z position.

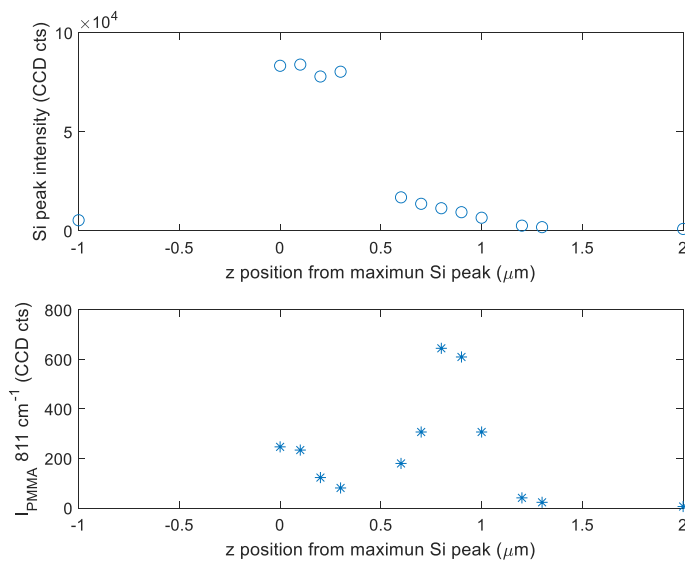


Figure 108: top image intensity of Si peak (518 cm^{-1}) as function of the z position of the objective. It should be taken into account the penetration depth of $3\mu\text{m}$ for wavelength of 638nm (145), therefore if the focal plane is $1.5\mu\text{m}$ under the Si surface the Si peak should be decreased by $1/e$. This could help to find the position of the Si/PMMA interface. On the bottom PMMA peak intensity as function of z position of the maximum of intensity of the Si peak.

A.5.2 Thin film PMMA Raman spectrum

In Figure 109 the Raman spectrum of PMMA spin coated on the SiN WG. It is collected on the zy chip plane. The peak at 811 cm^{-1} is the most intense one and it can be assigned the C-O-C symmetric stretching vibration. Most of the peaks are similar to what founded by (136, 138, 146). It is really interesting to compare that spectrum with that one collected from the same film but collected from the xy face Figure 110. The main difference is the presence of the low frequency dominant component with its characteristic exponential decreasing feature.

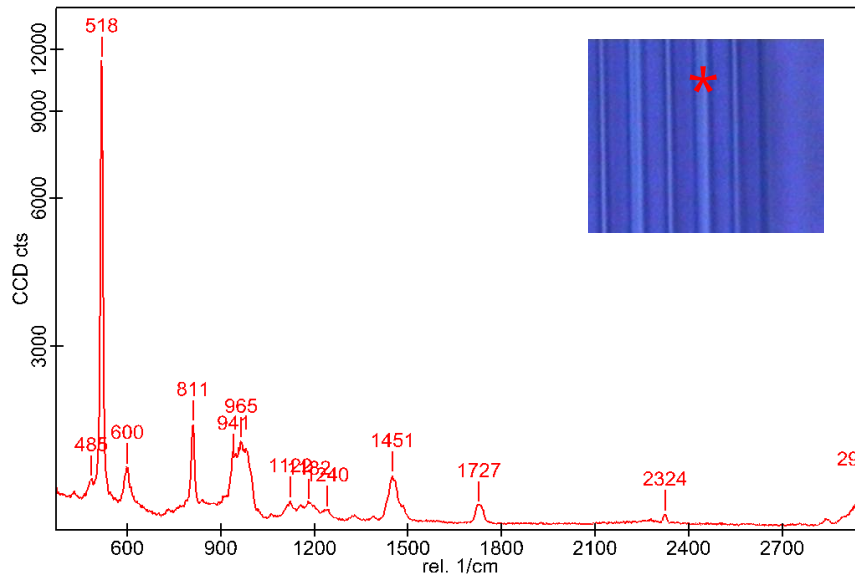


Figure 109: Raman spectrum of PMMA spin-coated on the chip. The laser used is 633nm with 100x/0.9NA objective, 10s integration time and 10 accumulation number. The laser hit the sample perpendicular to the chip surface (as shown in the inset, the laser spot is highlighted with an *). It can be noticed the 518 cm^{-1} peak associated to Si and the 2325 cm^{-1} peak of N_2 molecules in the WGs.

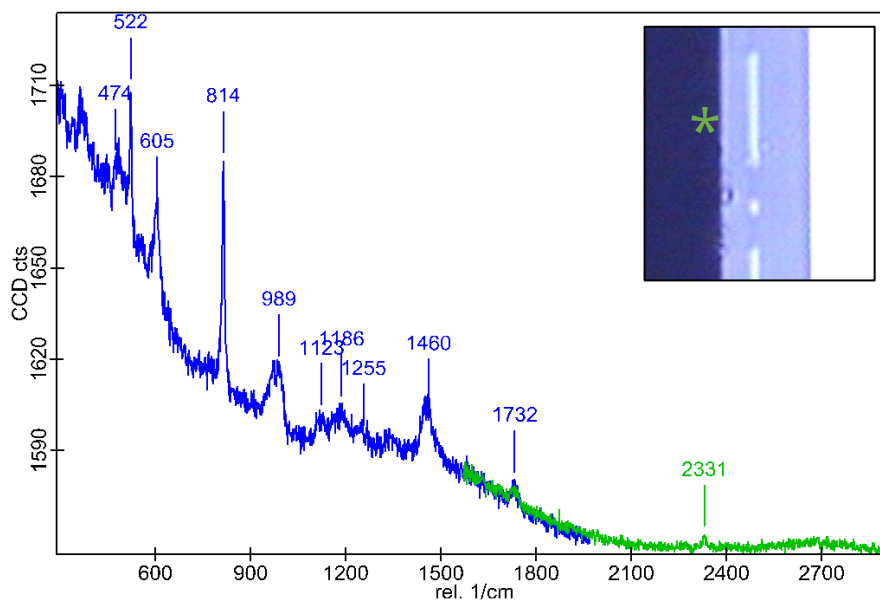


Figure 110: Raman spectra of PMMA thin film collected from a lateral face of the chip. The laser hit the sample perpendicular to the chip surface (as shown in the inset, the laser spot is highlighted with an *). TBN it is only a schematic indication and not the real picture of the PMMA film). The laser used is 785nm with 100x/0.9NA objective, 0.005s integration time and 20 accumulation number.

6.5.1 Exponential decreasing component

It is interesting to report the measured characteristic times coming from all the experimental spectra that has been shown in the previous chapters ($P_{LDFDF} \sim e^{-\omega \cdot \tau}$). To briefly summarize those results for the set of 20 spectra, with different WG width and length, in Table 11, it has been reported only the range over which the different characteristic times have been found.

It can be noticed that there is a noticeable increase of τ as the laser wavelength increase from 785nm to 633nm. Therefore, it is more advantageous to use 785nm laser since the exponential decreasing background becomes zero much faster.

Also, by decreasing the cladding refractive index τ decreases. Therefore, it seems that lower refractive index contrast is beneficial.

Table 12: characteristic time estimated from different WGs and under different laser wavelength. In the last line there is the

	Characteristic time (fs)				
	785nm			633nm	
	<i>SiO₂</i>	PMMA		<i>SiO₂</i>	PMMA
Cladding material					
Date of collection		10/06	06/07		
range	[11; 15]	[14; 16]	[15; 17]	//	[8; 12]
mean	13	15	16	//	10
3D WG	12	15	16	11	10

A.5.3 PCA for extraction PMMA signal

In this chapter it is shown an interesting result in which by application of principal component analysis (PCA) it is possible to extract the PMMA spectra separated from the background and noise too. The procedure consisted in spectra collection from all the WGs and normalization of all the spectra in the range of intensity [0;1]. After that the PCA is applied.

The PCA aim is to reduce the dimensionality of the data set (66). Starting from 20 Raman spectra it finds a set of orthogonal representation (loadings L or principal component PC) in which each spectrum deviation from the mean can be decomposed. In practice we represent the variance from the mean of each spectrum o ($S_o(\bar{\nu}) - S_{mean}(\bar{\nu})$) as a linear combination of loadings ($L_{i,o}$) multiplied by a coefficient (score $s_{i,o}$):

$$S_o(\bar{\nu}) - S_{mean}(\bar{\nu}) = \sum_i s_{i,o} L_{i,o}(\bar{\nu})$$

Therefore, from a set of complex spectra coming from samples composed by different materials mixed with different concentrations it would be possible to extract the original spectra coming of isolated materials¹. More information can be found in the book (66). Below are reported some useful equations used to perform the PCA:

$$\Sigma = \frac{\chi' * \chi}{\sqrt{N-1}} \rightarrow \text{covariance matrix} \quad \text{with } \chi = y - \text{mean}(y)$$

$$[L, \sigma] = \text{eig}(\Sigma) \rightarrow \text{eigenevalues and vectors of the covariance matrix}$$

$$s = \frac{\chi * L}{\sqrt{N-1}} \rightarrow \text{scores} \quad s' = s * \frac{1}{\text{diag}(\sqrt{\sigma})} \rightarrow \text{normalized scores}$$

the score s is the weight of each loading (L) for one spectrum. The eigenvalue σ is the weight of the L over the variation in all the data: $\Sigma = \sum_i \sigma_i L_i$.

The spectra collected from different WGs are characterized by different interaction length, which would lead to an increase of both background signal (mostly coming from a-SiN and on a small extent from $a - SiO_2$) and sample signal. On the other hand, the WG width variation should result in a variation of the relative intensity of the background signal and the sample one, opening the possibility to separate these two signals. Since the huge impact of the SiN background signal on the overall variance, the normalization of the intensities between [0;1] of each spectrum is beneficial in order to moderate this contribution to the total variance. By doing so it is found as the second principal component (PC2) surprisingly similar to PMMA Raman signal (Figure 111 Principal components plot). It is interesting to note that the PC2 is almost completely speared by the noise. It results in a great increase of the signal to noise ratio. This procedure has been done also to Raman spectra collected with 633nm and it is reported in Figure 112. It should be noted that the firsts PC gives useful indications on the main variation in the dataset, the most relevant.

¹ This is true as long as the two materials do not interact between each other's. For real mixtures PCA is still valid but the principal components would take into account the interaction. Furthermore the nonlinearities could be captured by third or fourth loading (66).

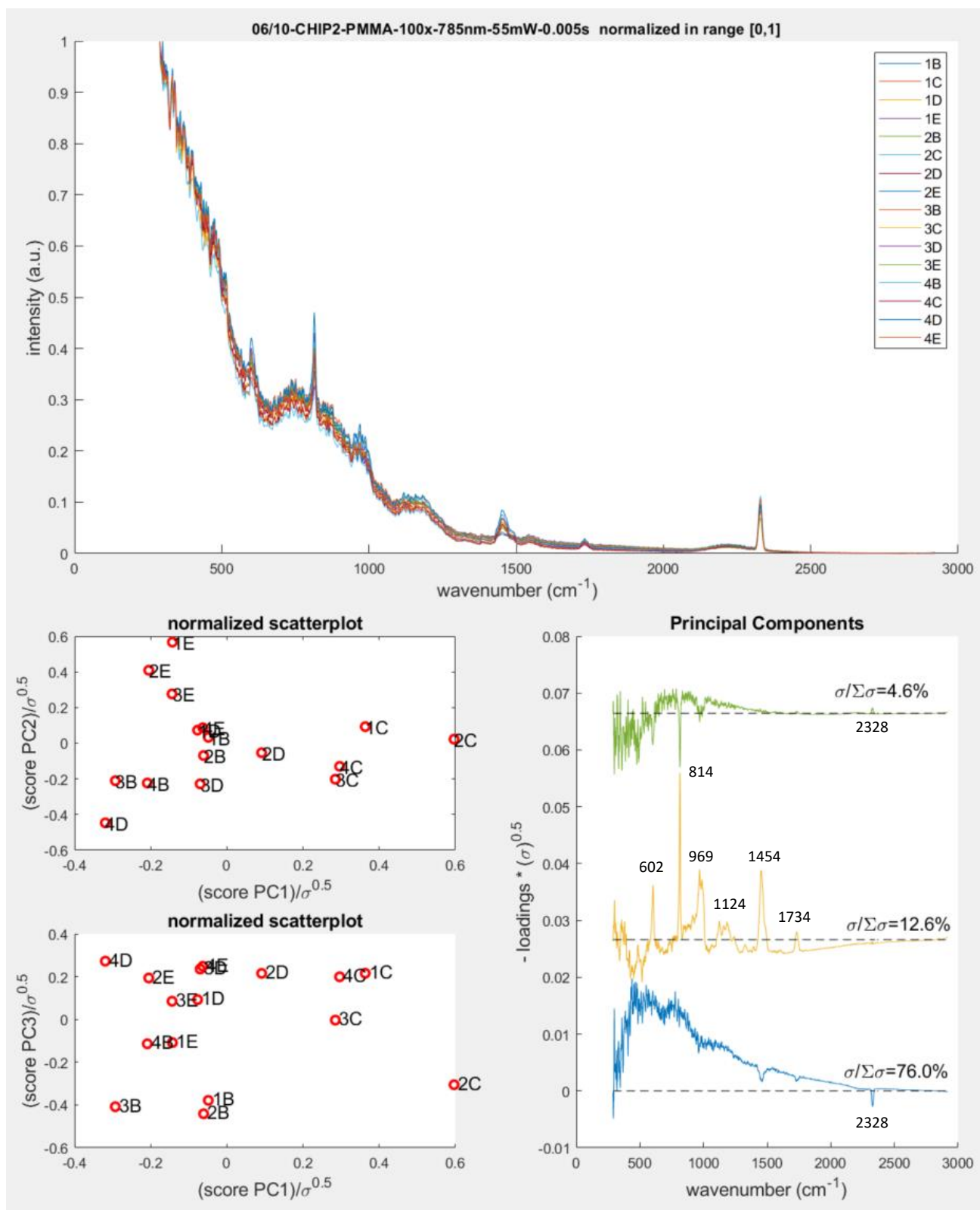


Figure 111: on the top plot the complete data set already normalized of Raman spectra obtained with 785nm laser wavelength. Each spectrum is labelled by a letter and number associated to the width and length of a strip WG. On the left two normalized scatter plot PC2 vs PC1 and PC3 vs PC1 showing for each spectrum its score normalized to their absolute relevance on the total variance ($\sigma^{0.5}$). On the right the PC plot. It shows also the $\sigma/\Sigma\sigma_i$ shows the relative impact on the total variance ($\Sigma\sigma_i$). TBN the minus in the y axis of the "Principal Components" plot.

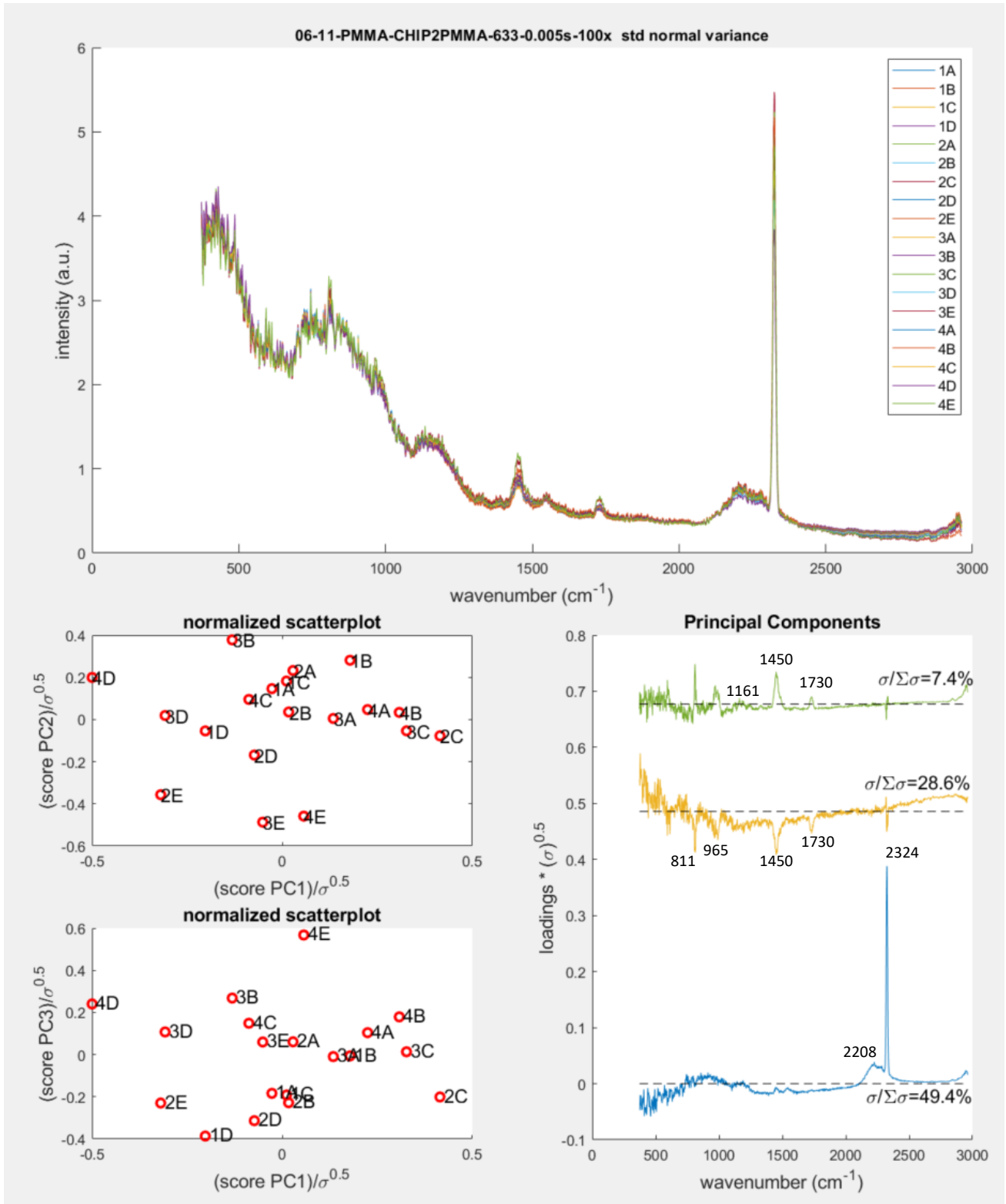


Figure 112: on the top plot the complete data set already normalized of Raman spectra obtained with 633nm laser wavelength. Each spectrum is labelled by a letter and number associated to the width and length of a strip WG. On the left two normalized scatter plot PC2 vs PC1 and PC3 vs PC1 showing for each spectrum its score normalized to their absolute relevance on the total variance ($\sigma^{0.5}$). On the right the PC plot. It shows also the $\sigma/\Sigma\sigma_i$ shows the relative impact on the total variance ($\Sigma\sigma_i$).

A.5.4 Standard procedure for evaluation the SBR

Here it is reported the procedure for the evaluation of the SBR:

1. Recording of Raman spectrum in the range $200\text{-}2700\text{ cm}^{-1}$ ($y(\tilde{\nu})$). With the 785nm laser two spectra have been collected for each WG with different grating positions and then they are merged.
2. dark signal elimination: $y_1 = y - \min(y)$.
3. Normalization the maximum signal to 1: $y_2 = y_1 / \max(y_1)$.
4. Cut in the region of the peak of interest, given by: $[\tilde{\nu}_{peak} - \Delta\tilde{\nu}; \tilde{\nu}_{peak} + \Delta\tilde{\nu}] \text{ cm}^{-1}$.
5. The spectrum is fitted with a Voigt profile, $f_V(\tilde{\nu})$, and a linear function, $f_L(\tilde{\nu})$. The program used was Fityk (147). The procedure is automated and a fraction the script is the evolution of a script written by Thomas Nuytten.
6. From the Voigt profile the intensity and the center of the peak $\tilde{\nu}_0$ are estimated and therefore calculate the SBR as:

$$SBR = \frac{f_V(\tilde{\nu}_0)}{f_L(\tilde{\nu}_0)}$$

An example is reported in Figure 113.

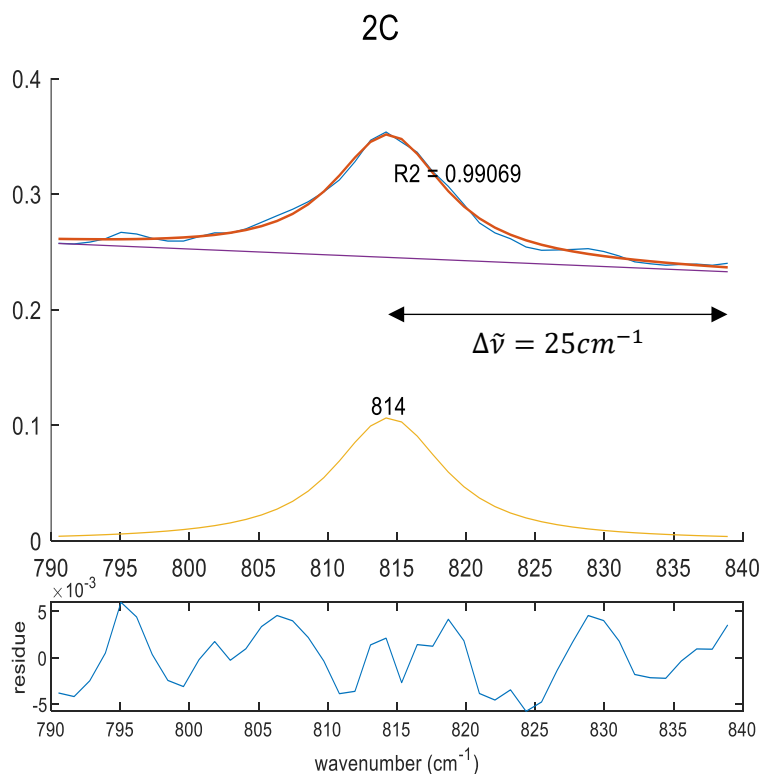


Figure 113: fitting of the spectrum 2D at the peak 814 cm^{-1} . The spectrum is catted in a region $[815-\Delta\tilde{\nu}; 815+\Delta\tilde{\nu}] \text{ cm}^{-1}$.

Since the spectra are noisy, it has been studied the effect of the region dimension over which perform the fitting of the peak. Figure 114 shows the influence of the variation of the cut $\Delta\tilde{\nu}$. As can be seen in the figure on the left, the cutting region fortunately does not influence too much the overall trend of the SBR changing the WGs. Therefore, by looking at figure on the right, the best mean R2 value is achieved when $\Delta\tilde{\nu} = 20\text{cm}^{-1}$, corresponding to 4 times larger of the mean HWFM (half width full maximum).

$\Delta\tilde{\nu} = 20\text{cm}^{-1}$ has been chosen for peak at 814cm^{-1} . Similarly, for the peak at 1455cm^{-1} a $\Delta\tilde{\nu} = 70\text{cm}^{-1}$ has been chosen.

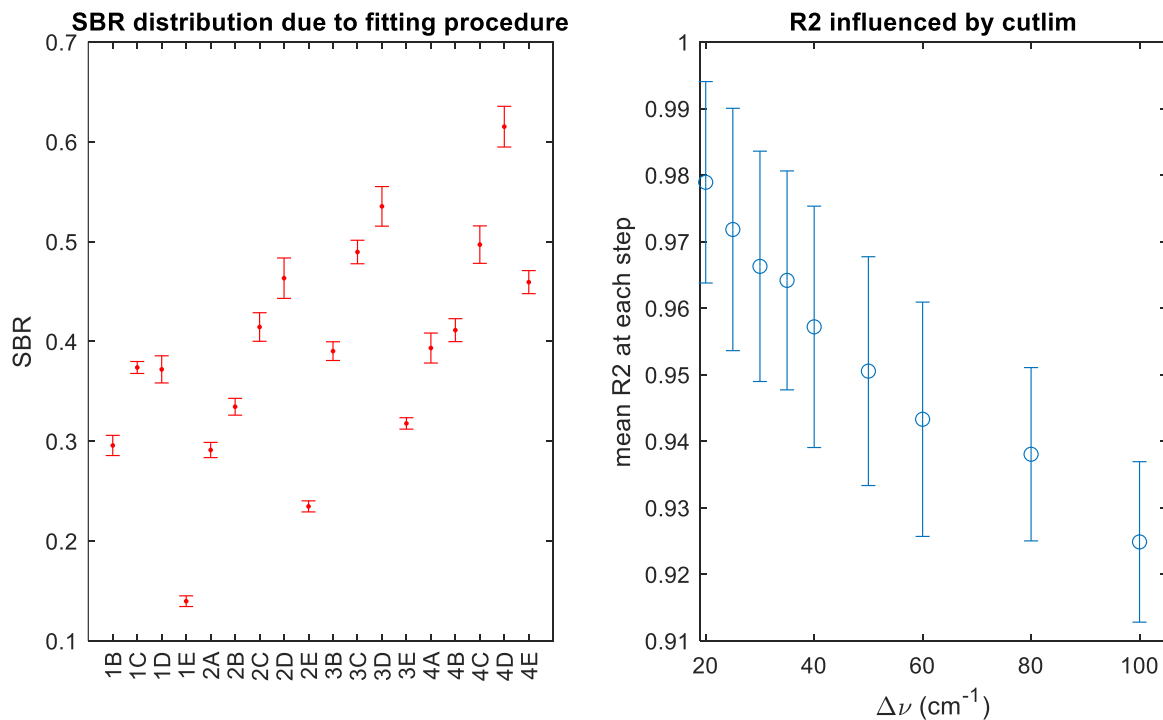


Figure 114: on the left the SBR distribution due to the fitting procedure: for each single WG the fitting is performed varying $\Delta\tilde{\nu}$, the resulting mean and standard deviation are reported. On the right is calculated the mean and standard deviation of the R2 value among all the WGs at each step of $\Delta\tilde{\nu}$. As expected, if $\Delta\tilde{\nu}$ increases the R2 decreases, as more noisy background is considered.

A.6 Additional observation during experiments

A.6.1 Slot WGs Raman spectra

It will be reported some examples of bad Raman spectra. We wanted to collect some spectra coming from SLOT WGs. But due to the design of the chip there is the risk to couple in between the two WGs, the slab region (shown in the insets on the top left in Figure 115). In Figure 115 is shown of a collection of Raman spectra coming from the slab region.

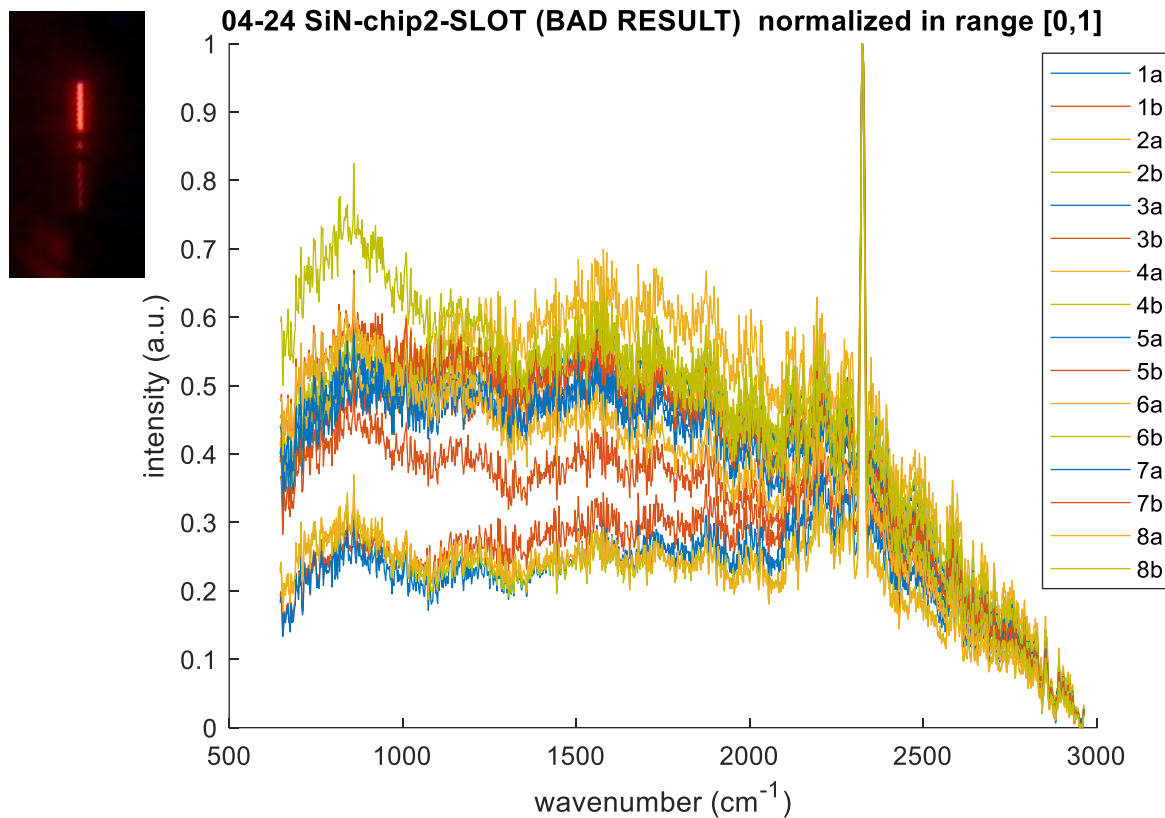


Figure 115: spectrum claimed to be come form the SLOT WGs but actually they comes from the slab WGs in between the slots.

A.6.2 Strange coupling effect

It has been recorded a “strange effect” associated to the change in the z position of a 100x objective while coupling in the 3B WG. By increasing of $0.05\mu\text{m}$ the distance of the objective from the chip surface a significative change of the scattering losses is recorded, as reported in Figure 116. It is interesting to see how a little change in the z direction drastically change the WG scattering losses. In picture (2) these is a clear increase of the scattering losses with respect to picture (1), highlighted with \star .

To explain this effect, it could be possible to think that, due to a change in the coupling condition, there is the excitation of a different guiding mode which result in an increase of the losses. This observation is important since it can highlight that even though the SBR should not be influenced by the coupling losses, still the coupling procedure is a key step and could influence the SBR through the change in scattering losses coefficients. To increase the precision in the measurements the use of a 100x objective can be beneficial but on the other hand using the 100x the system is much more sensible to possible drift (chapter 4.3.2 Data acquisition and Drift).

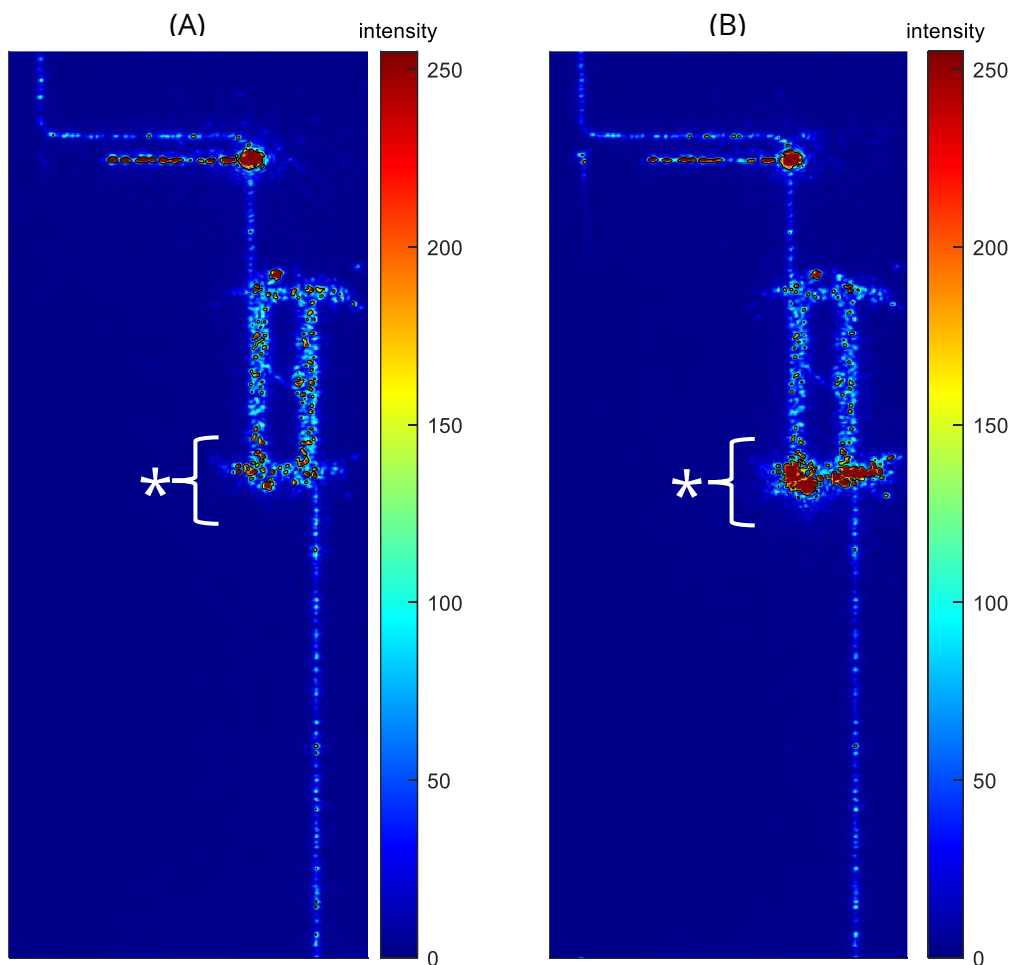


Figure 116: scattering losses coming from the same WG but at two different z -positions of the objective with a 785nm laser. The image (A) is at reference position of $z = 0\mu\text{m}$ and (B) is with objective up shifted of $0.05\mu\text{m}$.

List of figures

Figure 1: Global Market of Healthcare Photonics Systems. TBN Raman spectroscopy can be allocated in the analytical sensing field.	9
Figure 2: Raman spectrum example to highlight the two different regions of it. Fingerprint region is one of the most of interest in drug monitoring field (6).	10
Figure 3: collection of figures for each techniques: 1) Coherent Raman scattering (10); 2) Surface enhanced Raman scattering (22); 3) Photonic crystal for enhancement Raman scattering (9); 4) Fibre enhanced Raman spectroscopy (15) and 5) photonic crystals fibers for Raman spectroscopy (16).	11
Figure 4: citation and publications per year. Results taken from Web of Science by searching: "Waveguide Enhanced Raman"	12
Figure 5: Image and text caption taken from (25). "Conceptual view of a fully integrated Raman system on a nanophotonic chip. Insets (a) and (b) show the two contributions to the waveguide enhanced excitation and collection: An efficient coupling of dipole radiation to the waveguide and the collection of Stokes power over a long interaction length".	13
Figure 6: scheme of the light path into the WG for Raman detection. In red the Raman scattered light and green the laser light. P_{in} is the input power, P_b is the backward Raman scattered power and P_{br} is the backward scattered power, P_{tr} is the power transmitter at pump wavelength and P_f is the forward power Raman scattered.	15
Figure 7: a) schematic of a fraction of the setup with objective coupling (50). b) Experimental apparatus with prism coupling in a slab WG. Broken blue lines: waveguide surface collection configuration; solid green lines: waveguide end collection configuration. L1 and 2, lenses; LPF, long pass filter (46). c. top-view schematics of the fiber-bonding region. The glass V-groove block is bonded to the chip with epoxy at the tip of the fiber in the etched groove, and with larger volumes of cured epoxy on the sides of the block for improved robustness. Image and caption taken from (49).	16
Figure 8: Theoretical and experimental values of η obtained for (a) TE modes and (b) TM modes of Si_3N_4 waveguides. The markers represent the estimated experimental values obtained from the least square error fit of the experimental data. The error bars represent the measurement and estimation errors. Lines represent the theoretical curves. The red solid lines are the theoretical curve for slot waveguides with $s = 150$ nm. The blue and black dashed lines are the theoretical curves for TE and TM polarizations, respectively, for strip waveguides. Circle: TE polarization, strip waveguides. Left-handed triangles: TM polarization, strip waveguides. Right-handed triangles: TM polarization, slot waveguides. Square: TE polarization, slot waveguides. Image and caption taken from (58).	17
Figure 9: Background scattering spectra for the four material platforms studied by (44).	18
Figure 10: Propagation loss vs. wavelength for the TE_{00} and TM_{00} modes in the i/z bands (750 nm to 1000 nm) of four wafer builds: MPW, PPA, TLN, and TLA (the first letter refers to the production process of the SiO_2 P=PEVEC and T=Thermal, M=P+T; the second letter refers to the production process of SiN: L=LPCVD and P=PEVEC; the third letter refers if it is annealed or not: A=yes, N=no, W=N+A). The light gray and light red shaded regions indicate the standard error in the linear fit.	

Note the different y-axis scales in the plots. Image and caption taken from (55). The WGs used were 220 nm thick, 0.5 μm width and top and bottom cladding are 5 μm thick.18

Figure 11: on the top: comparison between slot, strip and WERS-SERS (metal slot) WGs signal vs shot noise (65). on the bottom influence of the WG on the waveguide sensitivity and loss (63).
.....20

Figure 12: Scheme of Raman scattering process.22

Figure 13 Schematic representation of the normal stretching mode of nitrogen molecule (Q_{vib}), with Rt nuclei distance.23

Figure 14 representation of the solutions of the quantum harmonic oscillator for one vibrational mode.25

Figure 15: Comparison between a harmonic potential (blue) and anharmonic potential (red). Where A, B and C are constants. As can be noticed the energy levels are no more equidistant.
.....26

Figure 16: Scheme of the transitions involved in Raman anti-Stokes, Rayleigh, Raman Stokes, Resonance Raman scattering and IR absorption. The last phenomena is characterized by photon energies in the order of the electronics transitions ($S_0 \rightarrow S_1$) and this leads to an increase of the Raman scattering intensity in the order of $10^3 - 10^5$. In the schematic spectrum at the bottom is reported also the intensities normalized to the incident radiation (image inspired by (69)).27

Figure 17 Characteristic features in the polarized Raman spectra of a-SiO₂ (73). The peaks D1 and D2 are the defects bands.30

Figure 18: a-SiN background Raman signal coming from a WG with different pump laser wavelength: 633nm in blue and 785 nm in red. The plot is taken from (44).31

Figure 19: scheme of the cross section of strip WG (translationally invariant on the not shown direction). The refractive index of the WG made by a-SiN is $n_w = 1.852$, then we distinguish two region s: the cladding (n_c : H₂O = 1.3296 PMMA = 1.4850281701926) and the substrate (if SiO₂ $n_s = 1.454$).32

Figure 20: lateral view of a WG and representation of two confined waves in the ray theory. To have propagation, the phase shift related to AB segment should be equal to that on related to CD segment (considering the phase shift due to reflection).32

Figure 21: representation of many possible radiation losses in the WG due to contamination, crystalline defects, surface roughness and bending (R is the bending radius). A model for describing surface roughness is given by the exponential correlation function: $h_z = \sigma 2 \exp - z/L_c$ where σ is the standard deviation of the surface with respect to the mean line (blue dotted line on the left figure) and L_c is the correlation length, above which the surface profile is random. L_c and σ are shown in the figure.35

Figure 22: schematic working principle of WERS (23).36

Figure 23: scheme of a $a - SiN$ strip WG on SiO₂ substrate and a diatomic molecule in harmonic approximation.37

Figure 24: Strip waveguide made by amorphous silicon nitride with uniformly distributed molecules in the cladding.38

Figure 25 zy sketch of a generic waveguide of length L and width w . In a backward configuration we collect the power, P_b , from at the same side of the incoming power, P_{in} . At the end of the

WG it can be collected the transmitted power P_{tr} and the forward Raman scattered signal P_f39

Figure 26 length factor in function of the waveguide length with $\alpha = 2.5 \text{ dB} \cdot \text{cm}^{-1}$. It is also reported $1/\alpha$ line which correspond to the saturation limit or maximum LF for respectively the backward and forward collection.....40

Figure 27: schematic of the xy plane of the chip, i.e. the cleaved face. The lighter blue is Si, then the SiO_2 is the darkest blue and then there is the $\alpha - \text{SiN}$ waveguides. The vector r_{obj} connects the $\alpha - \text{SiN}$ WG to the laser spot.....41

Figure 28 Schematic illustration of the beam path for Confocal Raman Microscopy in green (88). The main components are highlighted in blue. Scattered and pump light are unfortunately shown with the same colour: green.....42

Figure 29: Czerny Turner design (89).43

Figure 30 Internal and external coordinate systems in WITec Control (88).45

Figure 31 a) Principal setup of a confocal microscope (92) b) Pinhole diameter and diffraction pattern, the red circle indicates a circular pinhole adjusted to 1 Airy Unit (93).46

Figure 32 scheme of an ideal strip waveguide on the left, and of an ideal slot waveguide on the right. The thickness are not in scale.48

Figure 33 On the left the real image of a xy cleaved surface taken with the microscope with a 100x/0.9NA objective. We can notice that between each waveguides of our interest (small dots) there is a $\alpha - \text{SiN}$ slab waveguide much wider that is not designed for guiding the light to the probe region. On the left the scheme of the cross section of the coupling region of the red dotted region.....48

Figure 34: scheme of the chip used in the experiments with some details regarding its dimensions and regions: probing regions in green and SiO_2 cladded areas in blue.49

Figure 35: T1 design. With capital letter we distinguish the difference in width and with numbers the different probing length. The spirals bends have bending radius of 35, 40, 45, 50, 55 μm ...49

Figure 36: T2 design. With letter we distinguish between slot and strip and with numbers the different geometry.50

Figure 37: instruments for cleavage the chips.51

Figure 38: difference between 2 cleavage procedure: diamond saw for chip1 and diamond tip for chip2. Pictures taken with 40x objective except for the chip2-xy plane taken with 10x, to show better the presence of defects highlighted with red circles. Both cannot be used in the experiments.52

Figure 39: appearance of the side wall of the cleaved die form a (100) wafer at different angles. Taken from article (96). To be noted the length scale of these two phenomena.52

Figure 40: example of complete set up for a general experiment.53

Figure 41: scheme of the how measurements are done. P_{in} is the incoming power and P_b is the backscattered collected power.....53

Figure 42: images of the space near by the objective with two additional components used for building the set up: the metallic plate and the tilt stage. The last one was not used in all the set up. On the top image the 5 cm refers to the constrains of the maximum height reachable by the objective.54

Figure 43: complete set up N1 on the left. On the right image is shown how the chip is anchored to the PMMA laser cut holder that subsequently will be inserted in the set up N1. Therefore, it is very important the accurate study of all the tolerances. This set up is directly mounted on the metallic plate.....55

Figure 44: set up N2. It is composed by two plane of acrylic, allowing light transmission, connected by 2 layers of double side tape and 4 screws. A fluidic channel is built for liquid sample delivery. A tilt stage is used to connect the box to the metallic plate.....55

Figure 45: the image A) is the xy surface where is indicated the region where scan image was done. On the top right there are two scan images (B and C) with two different filters, i.e. the colour of the images range from 0 to 1 intensity of a certain quantity, in this case is the standard deviation with centre at Si peak (B image) and N2 at 2329 cm^{-1} (C image). The four spectra reported are numbered and their position is shown in the scan images (A, B, C). Raman acquisition with excitation wavelength: 785nm, integration time: 0.005s, objective 100x/0.9...56

Figure 46: a spectrum taken at position 5 of Figure 45-A) with laser 785nm with 55mW power, integration time of 0.1s and accumulation number of 100. As we can see the clear peak of Si-Si stretching and a peak at 609 cm^{-1} it could be related to defects in the a-SiO₂ network.57

Figure 47 Pictures of a chip xy surface. The two images on the left were taken with 40x objective of two different chip, one of them not well cleaned and with some cladding of the slab WG broken. On the right image is the same chip of the central image but taken with 100x objective.58

Figure 48 images obtained with 40x objective in camera mode and edge filter on for 633nm laser.58

Figure 49: Raman spectra of collected at different position on the x axis from the SiN WGs air cladded maximum intensity. The pump laser wavelength is 785 nm.....59

Figure 50 on the left one picture of the xy plane captured with 100x objective. On right the position map on the xy plane of one feature of the chip, each point is labelled with the time at which was recorded, and is reported in [mm:ss].....60

Figure 51: on the top figure, the normalized spectrum between [0,1], *SWG*, and the low frequency dominant component. *PLFDC*. *PLFDC* is estimated by a 5th order polynomial with an asymmetric truncated quadratic cost function ('atq') with threshold 0.021 (reported in the title). In the bottom the difference is reported. The result of the fitting of the 5th order polynomial with an exponential function is written in the bottom subplot along with the characteristic time τ of the fluctuations of the refractive index.62

Figure 52: fit of the resulting spectrum after low frequency dominant component subtraction $SWG_v - PLFDC_v$. The spectrum refers to the WG type 3D. In the bottom figure the residue is reported. The coloured lines are the 7 peaks used in the fitting.63

Figure 53: original spectrum obtained from 3D waveguide with 40x objective, 785 nm laser, 0.3s integration time and 20 accumulation number. in orange the total fit curve is represented. In the bottom subplot the residue is given by the fit and experimental data difference.63

Figure 54: The total fitting spectrum for each WG. There are also reported the assignments where (s), (b) stays for stretching and bending vibrations. The mean R2 value and standard deviation over all the spectra are reported in the top left of the graph. The spectra have been taken at 785nm laser wavelength, full power, 40x objective and 0.3s of accumulation time64

Figure 55: on the left: different spectra of SiN coming taken with different pump power. On the right: rescaled spectra by a coefficient to the 55mW spectrum as reference. The mean distance between 55mW and the rescaled spectra is also reported in % in the labels of the right image.

.....65

Figure 56: estimation of the PLFDC with a 5th order polynomial fitted with an asymmetric cost function with threshold=0.016. in the bottom subplot the resulting spectrum obtained from the subtraction of SWG – PLFDC. The text shows results of the fitting of the PLFDC with an exponential decreasing function.....66

Figure 57: results of the fitting of the spectrum SWG – PLFDC. In the bottom subplot the residue is shown.....67

Figure 58: original spectrum obtained from 3D waveguide. in orange the total fit curve is represented. In the bottom subplot the residue is given by the fit and experimental data difference.67

Figure 59: scheme of the chip design. L_{tot} is the total length, L is the probing length and L' is the not-probing SiO₂ cladded length. P_{in} and P_{col} are the incoming and collected power respectively. On the left and right insets two cross section of the WG are represented in order to underline the difference of the two regions and recall the different regions: cladding, core and substrate.68

Figure 60: the SBR (RS/B) experimentally evaluated as function of the probing length (59).....69

Figure 61 on the left not-probing factor (F_{np}) as function of the detection length (L). The arrows show the trend due to the increase of L' , the decrease of the plateau limit is shown with an orange arrow. On the right image F_{np} as function of the SiO₂ cladded length (L') for two different probing length. It clearly shows the exponential decrease of F_{np} vs L' . The blue arrow highlights the effect of the increase of L . It is important to remind that $SBR \propto F_{np}$72

Figure 62: refractive index map of probing region in brown a-SiN, light blue is SiO₂, in blue the analyte76

Figure 63: refractive index map of not-probing region.76

Figure 64: $|E|$ map of TM₀₁ mode. The arrows indicate the major E-field direction.....76

Figure 65: materials dielectric coefficients real components of silicon dioxide (Material data taken from Lumerical library), IPA and PMMA (Material data taken from (123, 124)) and silicon nitride (Material data taken from imec library). For the simulation a polynomial fit of the Material data is performed in order to obtain the Eigensolver model (blue line). The mean refractive index are: $n_{SiO_2} = 1.46$, $n_{SiN} = 1.85$, $n_{IPA} = 1.38$ and $n_{PMMA} = 1.48$ ($n_{H_2O} = 1.33$).76

Figure 66: two plots of Raman conversion efficiency evaluated at 822 cm⁻¹ Raman shift with light in TM₀₁ polarization mode. On left the plot of η for the probing region with IPA on upper cladding in function of the waveguide width. On right the plot of η for the SiO₂ cladding region in function of the waveguide width. In each plots the η are evaluated for pump wavelength of 785nm and 633nm. Near the titles of the graphs on the top right and top left there are the two representations of the two regions respectively the SiO₂ cladding region and the probing region with IPA. These are simulation results.....78

Figure 67: on the left the correction factor at the denominator of the not-probing factor ($\eta_{npScore}/\eta_{pScore}$) in function of the waveguide width. On the right there is the coefficient the

CCR ($\eta_{pSclad}/\eta_{pScore}$), as we can see the distinguishable variance is given by the waveguide width of $0.4 \mu\text{m}$. These are simulation results.78

Figure 68: on the left the PCR in function of the waveguide width. On the right the CCR as function of the WG width. These values are obtained from simulation with Raman shift at 814 cm^{-1} . These are simulations result.....79

Figure 69: dispersion diagram for a-SiN WGs for different widths and cladding materials at 785nm wavelength for TM00 mode. These are simulations result.....80

Figure 70: partial derivative of the dispersion diagram of the effective index against the WG width for different cladding materials. The $\partial n_{eff}/\partial w$ is proportional to the WG losses. These are simulations result.81

Figure 71: The top image shows an intensity map from of the scattering losses. The two red rectangles delimit the area over which the calculation is performed. The bottom plot represents the \log_{10} of the scattered power integrated over one line (perpendicular over the propagation direction in the red rectangles) versus the z position, i.e. the WG length.83

Figure 72: scattering losses experimentally determined (α_p) or simulated (with n_w model) of WGs with different width, with IPA cladding and 785nm laser. The A factor is estimated with 3E WG as reference (lowest relative error).....85

Figure 73: scattering losses experimentally determined (α_p) or simulated (with n_w model) of WGs with different width, with PMMA cladding and 785nm laser. The A factor is estimated from the experimental value obtained from 3D WG.85

Figure 74: the SBR as function of the ratio not-probing/probing length ($x=L'/L$). In the title there are more info about the input values. There are some "*" highlighting the expected experimental data.86

Figure 75: spectra obtained with 785nm pump laser and 40x objective, the other specifications are reported in the legend. The spectrum from chip3 is downshifted by 0.1. In yellow is highlighted the region where the most intense IPA peak is expected to be. SBR(3D-chip2-FullIP-0.001s) = 0.17 and SBR(3D-chip3-55mW-0.005s) = 0.0. In the bottom plot there is IPA Raman signal collected with 10x objective without the chip.87

Figure 76: spectra obtained with 785nm pump laser and 40x objective, the other specifications are reported in the legend.....88

Figure 77: on the left the SBR as function of the probing length for different WG widths. On the right the SBR as function of the WG width (each colour defines the WG width), for different WGs. It should be noted that all the data plotted are simulations results.....90

Figure 78: on the left the Raman spectra obtained from 3C WG coated with PMMA. All the parameters used to measure these spectra are reported in the title. On the right an example of the fitting procedure for the peak at 814 cm^{-1} and estimation of the signal intensity (S) and background (B). In yellow is the peak estimated, violet the linear background and in orange the sum of them.....91

Figure 79: the two left show the SBR as function of the probing length for respectively data sets collected on 10/06/2021 and 06/07/2021. The two plots on the right there are the same SBR data but there is the WG width on the x axis. Each colour defines the WG width: $0.4 \mu\text{m}$ in red, $0.6 \mu\text{m}$ in blue, $0.8 \mu\text{m}$ in green, $1.0 \mu\text{m}$ in black and $1.2 \mu\text{m}$ in yellow.93

Figure 80: SBR of peak 1455 cm^{-1} of PMMA sample deposited on the chip. Each colour defines the WG width: $0.4\ \mu\text{m}$ in red, $0.6\ \mu\text{m}$ in blue, $0.8\ \mu\text{m}$ in green, $1.0\ \mu\text{m}$ in black and $1.2\ \mu\text{m}$ in yellow.94

Figure 81: CCR as function of the WG width for PMMA cladded WG evaluated at two different Raman shift (1455 cm^{-1} and 814 cm^{-1}). In the subplot at the bottom the increase in % going from 814 cm^{-1} to 1455 cm^{-1}96

Figure 82: simulated scattering losses with *nw* model under the hypothesis of $L_c = 25\text{ nm}$ and $\sigma = 3\text{ nm}$ for 3 different Raman wavenumber with laser wavelength at 785 nm96

Figure 83: two different images reporting the scattering intensity coming from two WGs. There are two critical point where the losses are more intense, and these are highlighted in the image. The colours and size are changed to have better evidence of the scattering losses.97

Figure 84: χ losses variation going from 814 cm^{-1} to 1455 cm^{-1} for PMMA at pump wavelength of 785 nm97

Figure 85: Raman spectra obtained from WGs coated with PMMA. All the parameters used to measure these spectra are reported in the title.98

Figure 86: SBR of peak 1455 cm^{-1} of PMMA sample deposited on the chip obtained with 633 nm laser wavelength. Each colour defines the WG width: $0.4\ \mu\text{m}$ in red, $0.6\ \mu\text{m}$ in blue, $0.8\ \mu\text{m}$ in green, $1.0\ \mu\text{m}$ in black and $1.2\ \mu\text{m}$ in yellow.99

Figure 87: SBR of peak 1455 cm^{-1} of PMMA sample deposited on the chip. On the left measurements are performed with 785 nm laser wavelength and on the right with 785 nm . Each colour defines the WG width: $0.4\ \mu\text{m}$ in red, $0.6\ \mu\text{m}$ in blue, $0.8\ \mu\text{m}$ in green, $1.0\ \mu\text{m}$ in black and $1.2\ \mu\text{m}$ in yellow. The two red lines fits the red dots ($0.4\ \mu\text{m}$ WG width). The data are taken form figures on the left of Figure 80 and Figure 86.100

Figure 88: on left the simulation results and on the right the experimental of SBR as function of the WG width. SBR coming from strip WGs coated with PMMA analyzed with 785 nm laser. ...104

Figure 89: electromagnetic spectrum.117

Figure 90: correspondence between Raman shift and scattered wavelength. It is useful to have it in mind to have the correspondence between the Raman peak observed on the spectrum and the scattered light wavelength travelling back in the WG.117

Figure 91: power coupling efficiency in function of the WG width for TM - TE modes and $633 - 785\text{ nm}$ pump wavelength. On top right there is an example of refractive index map over which the calculation is evaluated with an objective with $NA = 0.65$118

Figure 92: the power coupling efficiency (Pce) estimated by Lumerical simulations as function of the WG width for two different NA objectives: 0.9 NA and 0.65 NA . The only mode analyzed is the TM mode at wavelength 785 nm119

Figure 93 on the left normalized electric field square modulus profiles resulting from 3 simulations at 3 different wavelengths are plotted around the refractive index map of a strip waveguide with width $1.2\ \mu\text{m}$. The blue dotted lines correspond to a value of $E^2\lambda = 1000\text{ nm} \sim 5 \cdot 10 - 3$. The 0 point of the two lateral plots correspond to the (0,0) point of the refractive index map. On the right it is like the left image but with a waveguide width of $0.4\ \mu\text{m}$. TBN the field intensity plotted correspond to the TM01 mode.120

Figure 94 The group index as function of the mesh size of the FDE solver region. The blue curve is the simulation without mesh override and the orange one is with (on the top there is a

representation YZ view of the simulation with mesh override). The insets are the refractive index maps which are the input to each data point obtained.....121

Figure 95: ratio between η_{Ssub}/η_{Score} as function of the WG width (z_span_SiN) for two different WG height. The strip WGs are with cladding PMMA and the simulation is performed at 785nm and TM00 mode.....122

Figure 96: mode intensity as function of the x direction. The intensity plotted is a slice of the y axis at the correspondence of the axis of symmetry of the WG.122

Figure 97: top image the CCR as function of the cladding refractive index at different laser wavelengths. On the bottom the ratio between CCR of the two lines in the upper graph.....123

Figure 98: the CCR as function of the wavenumber Raman scattering.123

Figure 99: it is applied an initial rotation of the image. 1): To estimate the best rotational angle the black and white image is converted in a vector line for which only the position of the maximum intensity (along y direction) is recorded. 2): A linear fit of the "linear fit region" displaced. 3): the absolute value of the angular coefficient is plotted as function of the rotation angle. 4) picture obtained from the top camera on the WG correctly rotated. There are two red rectangle which delimits the area over which we are taking the measurements. 5): the log10 of the scattered power integrated over one line (one horizontal line delimited by the red rectangles) versus the z position, i.e. the WG length.128

Figure 100: script of the main step for calculation of WG losses.129

Figure 101: scattering intensity of spirals of WGs number "3".130

Figure 102: scattering intensity of spirals of WGs number "2".130

Figure 103: relative scattering losses as function of the WG width. All the specific of the simulation are reported in the title. The strip WGs used are with height $0.4 \mu m$. The volume current data are taken from article (49).131

Figure 104: A factor map as function of σ and L_c for PMMA at 785 nm wavelength. The colour scale is such that only values in between [4.7:5.3] are in red and the others are white. It is also reported the function: $L_c = 80/\sigma$ in black.132

Figure 105: scattering loss coefficients as function of the WG width predicted from n_w model.133

Figure 106: scattering losses predicted by the n_w model of strip WGs with SiO_2 cladding and $L_c = 29nm$ and $\sigma = 2.7 nm$133

Figure 107: Raman spectra of PMMA sample spin coated on the chip at different z position. .134

Figure 108: top image intensity of Si peak ($518 cm^{-1}$) as function of the z position of the objective. It should be taken into account the penetration depth of $3\mu m$ for wavelength of 638nm (145), therefore if the focal plane is $1.5\mu m$ under the Si surface the Si peak should be decreased by $1/e$. This could help to find the position of the Si/PMMA interface. On the bottom PMMA peak intensity as function of z position of the maximum of intensity of the Si peak.....134

Figure 109: Raman spectrum of PMMA spin-coated on the chip. The laser used is 633nm with 100x/0.9NA objective, 10s integration time and 10 accumulation number. The laser hit the sample perpendicular to the chip surface (as shown in the inset, the laser spot is highlighted with an *). It can be noticed the $518 cm^{-1}$ peak associated to Si and the $2325 cm^{-1}$ peak of N_2 molecules in the WGs.135

Figure 110: Raman spectra of PMMA thin film collected from a lateral face of the chip The laser hit the sample perpendicular to the chip surface (as shown in the inset, the laser spot is highlighted with an *.TBN it is only a schematic indication and not the real picture of the PMMA film). The laser used is 785nm with 100x/0.9NA objective, 0.005s integration time and 20 accumulation number.....135

Figure 111: on the top plot the complete data set already normalized of Raman spectra obtained with 785nm laser wavelength. Each spectrum is labelled by a letter and number associated to the width and length of a strip WG. On the left two normalized scatter plot PC2 vs PC1 and PC3 vs PC1 showing for each spectrum its score normalized to their absolute relevance on the total variance ($\sigma/0.5$). On the right the PC plot. It shows also the $\sigma/\sum\sigma_i$ shows the relative impact on the total variance ($\sum\sigma_i$). TBN the minus in the y axis of the "Principal Components" plot.138

Figure 112: on the top plot the complete data set already normalized of Raman spectra obtained with 633nm laser wavelength. Each spectrum is labelled by a letter and number associated to the width and length of a strip WG. On the left two normalized scatter plot PC2 vs PC1 and PC3 vs PC1 showing for each spectrum its score normalized to their absolute relevance on the total variance ($\sigma/0.5$). On the right the PC plot. It shows also the $\sigma/\sum\sigma_i$ shows the relative impact on the total variance ($\sum\sigma_i$).139

Figure 113: fitting of the spectrum 2D at the peak 814 cm^{-1} . The spectrum is catted in a region $[815-\Delta\nu; 815+\Delta\nu]\text{ cm}^{-1}$140

Figure 114: on the left the SBR distribution due to the fitting procedure: for each single WG the fitting is performed varying $\Delta\nu$, the resulting mean and standard deviation are reported. On the left is calculated the mean and standard deviation of the R2 value among all the WGs at each step of $\Delta\nu$. As expected, if $\Delta\nu$ increases the R2 decreases, as more noisy background is considered.....141

Figure 115: spectrum claimed to be come form the SLOT WGs but actually they comes from the slab WGs in between the slots.142

Figure 116: scattering losses coming from the same WG but at two different z-positions of the objective with a 785nm laser. The image (A) is at reference position of $z = 0\mu\text{m}$ and (B) is with objective up shifted of $0.05\mu\text{m}$143

List of tables

Table 1 laser property.	43
Table 2: summary of the objective specifications for confocal Raman.....	45
Table 3 xy positioner and scan stage properties.	45
Table 4 Property of Thor Camera.....	47
Table 5: summary of the settings for Epilog laser cutter.	47
Table 6: Summary of the geometries of the T1 design.	50
Table 7: summary of the geometries of the T2 design.....	50
Table 8: mean values of the fit of 16 WGs with their standard deviation and relative error. For each spectrum a fit is performed. For example, the $FWHM_{ij}$ of the spectrum i and peak j and the fitting error $FitErr_{ij}$ are evaluated. For each peak is reported the mean $FWHM$ over all the spectra and the associated standard deviation in the form: $FWHM_{iji} \pm stdFWHM_{iji}$. In the row below is also reported the relative error in %: $stdFWHM_{iji}/FWHM_{iji}$ and in the parenthesis is reported the mean of the fitting error over all the spectra divided by $FWHM_{iji}$ in %: $FitErr_{iji}/FWHM_{iji}$. For peak Center is not reported the fitting error since is negligible. (n.u.= normalized units).....	64
Table 9: Input for evaluation of the Raman conversion efficiency η . Each column shows which are the values used, some of the values are in common therefore for some rows, the columns are joint.	76
Table 10: summary of the scattering losses for IPA and PMMA as function of the WG width at 785 nm. The first two experimental values are obtained form 3 WGs, the last column refers to 2 WGs. It should be noted that 3WGs have lower uncertainty since loner portion of the WG can be used to evaluate the scattering losses. In the last column there is an estimation of the loss coefficients with the n_w model. It should be noticed that have a wide uncertainty.....	83
Table 11: summary of the main input for the model of the SBR.....	90
Table 12: characteristic time estimated from different WGs and under different laser wavelength. In the last line there is the	136

List of symbols and Abbreviations

Abbreviations	symbols	
	σ	Raman scattering cross-section or eigenvalues of covariance matrix
	λ_s	Scattered wavelength
	λ_p	Pump or laser wavelength
	$\tilde{\nu}$	Wavenumber
	τ	Characteristic time
	W	Radial half-width of gaussian approximated mode profile
	α	Loss coefficient
<i>a – SiN</i> or <i>SiN</i>		Amorphous silicon nitride
<i>a – SiO₂</i> or <i>SiO₂</i>		Amorphous silicon dioxide
	w	Waveguide width
	Λ_{wg}	Integrated luminosity
	η	Raman conversion efficiency
	ξ	Raman collection efficiency
	LF	Length factor
SBR		Signal to background ratio
SNR		Signal to noise ratio
	γ	Coupling efficiency
	χ	Loss factor not-probing region
	α_{np}	Loss coefficient of not-probing region
	α_p	Loss coefficient of probing region
	L	Probing length
	L'	Not-probing length
	F_{np}	Not-probing factor
CCR	$\eta_{S/B}$	Core-to-cladding conversion ratio
PCR	$\eta_{nP/P}$	Probing to not-probing conversion ratio

Acknowledgements

I thank a lot to my parents, my sisters, Riccardo, Mauro and professor Carlo Casari. Even if with different awareness they helped me a lot. Without them I do not know If I were able to continue with my thesis work during the pandemic. The first period of my thesis work was brutal: the combination of covid isolations, empty laboratories, my first experience in a real research environment abroad, the distance from my colleagues in PoliMi and the quite hard work required by the thesis made the working at imec extremely tough. It should be noted that in correspondence of the starts of the thesis work it is usually the last semester for master students after that no simple choice about the future can be done. This spontaneously increased in me the anxiety towards the future. These people really help me in different times during my work. Therefore, I would again deeply says thank you.²

I would like also to express my special thanks to Aadhar Jain, he introduced me in the amazing word of photonics and followed me during my work.

I also express deep sense of gratitude to professor Pol Van Dorpe, for his guidance and for giving me the opportunity to do my thesis in imec.

This thesis would also not have been possible without the support of some other people from imec. Thank you, Stefanie, you give the help for development of data elaboration software (shearing me the file of Thomas which indirectly helped me too). Thank you, Kathrin and Shahriar, you were very nice people that I can meet on few occasions during my work.

This thesis became reality with kind support and help of many individuals. I would like to extend my sincere thanks to all of them not explicitly mentioned.

² I would like not to provoke compassion towards me by saying these things but only to remind a possible guy in the future who may read my thesis to keep going even if many problems arise. Keep going, be strong, ask for help to someone else!